Title

Studies of Ionosphere/Thermosphere Plasma-Neutral Coupling in Response to Various Energy Drivers

Author

Gasque, Lilias Claire

Publication Date

2024

Peer reviewed|Thesis/dissertation

Studies of Ionosphere/Thermosphere Plasma-Neutral Coupling in Response to Various Energy Drivers

by

L. Claire Gasque

A dissertation submitted in partial satisfaction of the

requirements for the degree of

Doctor of Philosophy

in

Physics

in the

Graduate Division

of the

University of California, Berkeley

Committee in charge:

Professor Stuart Bale, Co-chair
Dr. Thomas Immel, Co-chair
Professor Jonathan Wurtele
Professor William Collins

Spring 2024

Studies of Ionosphere/Thermosphere Plasma-Neutral Coupling in Response to Various Energy Drivers

Abstract

Studies of Ionosphere/Thermosphere Plasma-Neutral Coupling in Response to Various Energy Drivers

by

L. Claire Gasque

Doctor of Philosophy in Physics

University of California, Berkeley

Professor Stuart Bale, Co-chair

Dr. Thomas Immel, Co-chair

Extending from approximately 85 to 1,000 km above Earth's surface, the terrestrial ionosphere-thermosphere (I-T) system holds growing significance as we increasingly rely on space-based infrastructure. The I-T system comprises a mixture of ionized and neutral gases whose dynamics are tightly coupled, generating a variety of complex phenomena, some of which remain poorly characterized and understood. This dissertation presents studies investigating three of the most enigmatic I-T phenomena, each driven by a distinct energy source. Specifically, we examine:

1. rapid electrodynamic changes and plasma redistribution following explosive events in the lower atmosphere, with a particular focus on the 2022 eruption of the Hunga Tonga-Hunga Ha'apai (hereafter 'Tonga') volcano,
2. thermospheric wind perturbations linked to the abrupt changes in solar inputs triggered daily by the setting sun, and
3. aurora-like glows in the subauroral ionosphere associated with rapid ion flows in the upper ionosphere during geomagnetically active periods.

Each study employs both observational data and theoretical modeling to examine the coupled plasma-neutral response to the energy driver and to characterize and explain the ensuing phenomenon.

The first study delves into the ionospheric effects of the 2022 Tonga volcanic eruption. This eruption drove global-scale atmospheric waves that propagated into space and propelled

ionospheric disturbances. This dissertation investigates the ionospheric consequences of the eruption within about 5,000 km of the volcano. The study demonstrates the immediate large-scale electrodynamic effects of the eruption using observations from NASA's Ionospheric Connection Explorer (ICON) satellite. Extreme (>100 m/s) east-west and vertical ion drifts are observed thousands of kilometers away from the volcano within an hour of the eruption, before the arrival of any known neutral atmospheric wave. The measured ion drifts are magnetically conjugate to the ionospheric E region about 400 km from Tonga. A theoretical calculation shows that the observed ion drifts are consistent with the ionospheric E region dynamo effects of an expanding neutral atmospheric wavefront with a large (>200 m/s) neutral wind amplitude. The analysis suggests that the thermospheric neutral winds initiated by the eruption interacted with the E Region ionospheric plasma and created strong electric potentials which propagated along Earth's magnetic field via Alfvén waves and caused the observed plasma drifts in the opposite hemisphere. These observations are the first direct detection in space of the rapid and extreme electrodynamic consequences of a volcanic eruption and contributes to our understanding of the coupling between the lower atmosphere and I-T system following explosive events such as this eruption.

The second study considers the daily effect of the setting sun on the I-T system. The moving solar terminator (ST) generates atmospheric disturbances, broadly termed solar terminator waves (STWs). Despite theoretically recurring daily, STWs remain poorly understood, partially due to measurement challenges near the ST. By presenting analysis of neutral wind data from the Michelson Interferometer for Global High-resolution Thermospheric Imaging (MIGHTI) onboard the ICON satellite, this dissertation reveals observations of STW signatures in thermospheric neutral winds, including the first observed meridional wind signatures. Seasonal analysis demonstrates that STWs are most prominent during solstices, when they intersect the ST about $\sim 20^\circ$ latitude from the equator in the winter hemisphere and have phase fronts inclined at a $\sim 40^\circ$ angle to the ST. This work provides the first observed STW altitude profiles, revealing large (>200 km) vertical wavelengths above 200 km. Comparing these observations to four different models suggests the STWs likely originate directly or indirectly with waves from below 97 km. These results indicate that STWs may play an under-recognized role in the daily variability of the I-T system, warranting further study.

Finally, this dissertation considers aurora-like emissions which arise equatorward of the auroral oval in conjunction with extremely fast ionospheric ion flows. The 'picket fence' is a captivating visual phenomenon featuring vibrant green streaks. It is often observed concurrently with and at lower altitudes than the rare purpleish-white arc called STEVE (Strong Thermal Emission Velocity Enhancement). Despite its aurora-like appearance, recent studies suggest that the picket fence may not be driven by magnetospheric particle precipitation but instead by local electric fields parallel to Earth's magnetic field. This dissertation evaluates the parallel electric fields hypothesis by quantitatively comparing picket fence spectra with the emissions generated in a kinetic model driven by local parallel electric fields energizing ambient electrons in a realistic neutral atmosphere. The results demonstrate that, at

a typical picket fence altitude of 110 km, parallel electric fields between 40 and 70 Td (∼80 to 150 mV/m at 110 km) energize ambient electrons sufficiently so that, when they collide with neutrals, they reproduce the observed ratio of N_2 first positive to atomic oxygen green line emissions, without producing N_2^+ first negative emissions, consistent with the features observed in picket fence spectra. These findings establish a quantitative connection between ionospheric electrodynamics and observable picket fence emissions, offering verifiable targets for future models and experiments.

The work presented in this dissertation has contributed to ongoing I-T research as well as spawned new research directions, including providing benchmarks for more detailed modeling studies of the Tonga volcanic eruption, demonstrating the need for in-depth modeling follow-up studies to examine the origin of STWs and their effects on the ionosphere, and leading to a proposal for a rocket campaign to measure the parallel electric fields that may drive picket fence emissions for the first time.

Contents

Contents **i**

List of Figures **iii**

List of Tables **ix**

1 Dissertation Goals and Impact **1**
1.1 Earth's Upper Atmosphere: Impacts on Infrastructure in the Space Age . . . 1
1.2 Case Studies: I-T Drivers and Associated Plasma-Neutral Coupling Phenomena 6
1.3 Outline of the Dissertation 13
1.4 Contributions 14

2 The Coupled Ionosphere/Thermosphere System **16**
2.1 Earth's Atmosphere: Structure and Composition 17
2.2 Disturbances in the Upper Atmosphere: An Overview of Oscillations and Wave Phenomena 21
2.3 Plasma-Neutral Coupling: An Exploration of the Ion Continuity Equation . 27
2.4 Ionospheric Phenomena Across Different Latitudinal Regions: The Equatorial, Subauroral, and Auroral Ionospheres 37
2.5 Summary: Plasma/Neutral Interactions in the Coupled Ionosphere/Thermosphere System 44

3 Rapid Volcanic Modification of the E Region Dynamo: ICON's First Glimpse of the Tonga Eruption [108] **46**
3.1 Introduction 47
3.2 Data and Methods 50
3.3 Results and Discussion 52
3.4 Conclusion 56

4 Evening Solar Terminator Waves: Neutral Wind Signatures Observed by ICON-MIGHTI [106] **58**
4.1 Introduction: Solar Terminator Waves in the Terrestrial Thermosphere . . . 60
4.2 Methods: Observations and Modeling 61

4.3 Results . . . 64
4.4 Discussion . . . 70
4.5 Conclusion . . . 74

5 It's Not Easy Being Green: Kinetic Modeling of the Emission Spectrum Observed in STEVE's Picket Fence [107] 76
5.1 Introduction: Debate Over the Picket Fence's Origin . . . 78
5.2 Picket Fence Spectral Observations . . . 79
5.3 Kinetic Modeling of Emissions Driven by Parallel Electric Fields . . . 83
5.4 Comparison with Observations . . . 86
5.5 Discussion and Conclusion . . . 88

6 Conclusion and Directions for Future Work 91
6.1 Ionospheric Effects of the 2022 Tonga Volcanic Eruption . . . 91
6.2 Solar Terminator Waves in the Terrestrial Thermosphere . . . 92
6.3 Picket Fence Optical Emissions . . . 94
6.4 Overarching Conclusions . . . 96

Bibliography 98

A Appendix for Chapter 2 125
A.1 Derivation: Ionospheric Conductivity and Ohm's Law in the Ionosphere . . . 125

B Appendix for Chapter 3 129
B.1 The Ionospheric Connection Explorer: Mission and Instrumentation . . . 129
B.2 Dynamo Calculation and Comparison with Whole-Atmosphere Model Results 133

C Appendix for Chapter 4 139
C.1 MIGHTI Neutral Wind Observations . . . 139
C.2 Identifying the Solar Terminator as a Function of Altitude . . . 142
C.3 Description of STW Parameters Using all Three Years of ICON Neutral Wind Data . . . 146

D Appendix for Chapter 5 151
D.1 The TREx Spectrograph . . . 151
D.2 Are Picket Fence Emissions Consistent with Magnetospheric Particle Precipitation? . . . 152
D.3 Calculating Electron Impact Excitation Rate Constants . . . 154
D.4 Detailed Steady State Kinetic Calculations of N_2 1P, GL, and N_2^+ 1N VERs 155
D.5 Comparison with the Results from Yonker and Bailey (2020) [379] . . . 159
D.6 Calculating VERs for Various UV Emissions . . . 164

List of Figures

1.1 An Extreme-Ultra Violet (EUV, 195 Å) view of the sun captured by the Sun Earth Connection Coronal and Heliospheric Investigation (SECCHI) EUV imager on board the Solar TErrestrial RElations Observatory (STEREO-A) at 23:55 UT on January 29, 2022. The CME responsible for the loss of 38 Starlink satellites emanated from the active region circled in red (Gopalswamy et al., 2023) [113]. . 2
1.2 The number of objects >10 cm in LEO, determined by the NASA Orbital Debris Program Office. 3
1.3 Illustration of the many of the potential impacts of space weather on modern infrastructure. Credit: European Space Agency (ESA). 4
1.4 Effects of the 15 January 2022 Tonga volcanic eruption. (a) The plume from the volcanic eruption, captured by the Advanced Baseline Imager (ABI) aboard NASA's GOES-West satellite. Credit: NASA. (b) Atmospheric waves emanating from the eruption site, captured by NASA's GOES-West satellite. Credit: Mathew Barlow/University of Massachusetts Lowell. (c) Cartoon illustrating some of the upper atmospheric effects of the eruption, highlighting findings from Harding et al. (2022) [127]. Credit: NASA's Goddard Space Flight Center/Mary Pat Hrybyk-Keith. 8
1.5 View of the terrestrial solar terminator from space, as observed by the Meteosat-9 satellite. From the left, the images were captured on the June solstice, September equinox, December solstice, and March equinox, showing the varying angle of the terminator due to Earth's axial tilt. Credit: NASA Earth Observatory. 10
1.6 Photograph of STEVE (mauve arc) and the picket fence (green streaks) taken around 05:53 UT on 16 September 2017 by Robert Downie, reproduced from Archer et al. (2019)a [10]. 12

2.1 Altitude profiles characterizing the thermosphere and ionosphere under midlatitude, daytime, equinox conditions. Neutral density, composition, and temperature profiles were calculated with the MSIS model, while ionospheric density, composition, and temperature profiles were calculated using the International Reference Ionosphere 2016 (IRI16) (Bilitza et al., 2017; Ilma, 2017) [31, 153]. (a) Thermospheric and ionospheric density profiles, highlighting the dominant neutral species and the plasma density. (b) Atmospheric temperature profiles for neutrals (black), ions (blue), and electrons (red), with major atmospheric regions highlighted and labeled. (c) Ionospheric composition profile, showing the densities of dominant ion species. 18
2.2 Schematic showing the heating resulting in solar thermal tides, reproduced from Figure 11 of Forbes (1995) [85]. (a) Vertical heating variations associated with the absorption of solar radiation by different atmospheric constituents. (b) Latitudinal heating variations associated with changing solar inclination angle. (c) Local time heating variations. 22
2.3 (a) Typical values of the Pedersen (σ_P), Hall (σ_H) and parallel ($\sigma_\parallel$) conductivity in the mid-latitude daytime ionosphere. (b) Representative mid-latitude profiles of ionospheric gyrofrequencies and plasma-neutral collisional frequencies, inspired by Figure 4.10 of Baumjohann and Treumann (2012) [18]. 33
2.4 Diagram of Earth's magnetic field and magnetosphere. Close to Earth, the magnetic field is approximately dipolar, and the ionosphere can be divided into equatorial, subauroral, and auroral regions, distinguished by the varying orientation of the magnetic field with latitude. Credit: ESA (original picture courtesy C. Russel). 38

3.1 (a) ICON's geographic and south magnetic footpoint positions relative to the Tonga volcano. Also shown are wavefronts for disturbances traveling from the eruption site at 310 m/s (yellow), 600 m/s (purple) and 900 m/s (green). The wavefronts are assumed to propagate isotropically at constant velocity, and are shown at the moment that the IVM south footpoint is at the same longitude as the wavefront. (b) The magnetic field line connected to ICON at its closest approach to Tonga, showing the IVM south magnetic footpoint. A simple spherical wavefront model shows that when the IVM south magnetic footpoint is north of the volcano, the normal to it points mostly northward. 51
3.2 IVM ion density and drift measurements during ICON's orbit following the Tonga eruption. The data taken when the south footpoint was within nominal wavefronts moving at 900 m/s, 600 m/s, and 310 m/s are highlighted in green, purple, and yellow, respectively. The SLT climatologies are shown in gray, with light gray bounding the 10th to 90th quantiles, dark gray bounding the 25th to 75th quantiles, and the median shown as the darker gray line. Note the extreme vertical and zonal ion drifts in the region affected by the volcano. 53

3.3 Predictions from a simplified slab model of Hall region currents driving the ionospheric dynamo (see text for details). (a) The locations of the ICON observatory and IVM south footpoint with respect to the expanding 600 m/s (purple) and 310 m/s (yellow) wavefronts at times which correspond to the westward, northward, and eastward neutral winds. (b) A chart showing predicted ion drifts given the assumed neutral wind input. The top row shows the neutral wind input, the middle shows the determination of the ion drift direction from PEF established by the Hall region current. The bottom two rows show the theoretically predicted vertical and zonal ion drifts. (c) The IVM drift data with a linear trend removed aligned with the columns of the chart above. Upward pointing arrows represent upward perturbation drifts and rightward pointing arrows represent eastward perturbation drifts. These observations show good agreement with the theoretical results. 55

4.1 Meridional winds during NH winter as observed by MIGHTI, presented as a function of latitude and SLT. In the first row, (a) shows the binned and averaged data prior to the removal of tidal components. The second row displays the fits for the (b) diurnal, (c) semidiurnal, and (d) terdiurnal tidal components. The final row shows the data residuals after successively removing the (e) diurnal, (f) semidiurnal, and (g) terdiurnal tides. Note that the colorbar amplitude varies between subfigures. 65
4.2 Same as Figure 4.1, but for the observed zonal wind component. 66
4.3 Binned and averaged MIGHTI meridional (left column) and zonal (right column) neutral winds for NH winter (top row), combined equinox (middle row), and NH summer (bottom row). Diurnal tides have been removed. Northward and eastward winds are positive. The gray shading shows the portion of the latitude/SLT space that is in darkness for each season. Clear STW features are marked by a black dotted line for the solstice cases ((a), (b), (e), and (f)). 68
4.4 Each panel shows NH winter meridional winds binned by latitude and SLT with diurnal tides removed (the same as Figure 4.3(a)), but for (a) TIEGCM simulations without HME inputs, (b) TIEGCM simulations with HMEs derived from MIGHTI observations, (c) SD-WACCM-X simulations, and (d) HIAMCM simulations. The first three simulation results incorporate winter 2019 and 2020, while the HIAMCM result is for 15 January 2022. 70
4.5 Same as Figure 4.4, but for the modeled zonal wind component. 71
4.6 NH winter meridional (left) and zonal (right) winds averaged between 10° and 20° latitude as a function of altitude and SLT for (top) MIGHTI data (winter 2019 and 2020), (middle) SD-WACCM-X simulations (winter 2019 and 2020), and (bottom) HIAMCM simulations (15 January 2022). Diurnal tides have been removed. The gray shading shows the portion of the altitude/SLT space that is in darkness. Northward and eastward winds are defined to be positive. 72

4.7 NH summer meridional (left) and zonal (right) winds averaged between -10° and 0° latitude as a function of altitude and SLT for (top) MIGHTI data (winter 2019 and 2020), (bottom) SD-WACCM-X simulations (winter 2019 and 2020). Diurnal tides have been removed. The gray shading shows the portion of the altitude/SLT space that is in darkness. Northward and eastward winds are defined to be positive. 73

5.1 (a) Keogram of total TREx luminosity between 6:15 and 8:00 UT on April 10, 2018, showing STEVE emissions and stellar contamination. A full spectrum (385-801 nm) is available at every point. (b) Keogram of TREx GL observations (555.2-560.7 nm) during the same period, highlighting the picket fence observations. (c) Picket fence and background spectra extracted between 6:49 and 7:00 UT. Some spectra were removed due to stellar contamination. See text for details of selection process. (d) Approximate observation geometry for picket fence observed at 6:52 UT. The sample picket shown is only a representation as the altitude of the emissions is unknown. 80

5.2 (a) Median picket fence spectrum (black) and poleward (blue) and equatorward (red) background spectra. (b) Median picket fence spectrum after background subtraction. Inset: N_2 1P spectrum (642-700 nm). (c) Ratio of N_2 1P (642-700 nm) to GL luminosity from the TREx observations, scaled to account for atmospheric transmission. 82

5.3 Modeling process flowchart of steps (a) - (d), with subfigures to further elucidate steps (b) and (d). (b) EEDFs at 110 km for different parallel electric field strengths, overlaid with electron impact excitation cross sections for $O(^1S)$, $N_2\,(B^3\Pi_g)$, and $N_2^+\,(B^2\Sigma_u^+)$. (d) VERs at 110 km for GL, N_2 1P, and N_2^+ 1N calculated with the steady state kinetic model. 84

5.4 (a) Calculated N_2 1P (642-700 nm) to GL VER ratios. Observed luminosity ratios and margins of error are indicated by the black dotted line and shaded region, respectively. (b) The same as (a), but with parallel electric field strength in mV/m. (c) Calculated N_2^+ 1N (421-431 nm) to GL VER ratios. 87

6.1 Images of two types of aurora, both captured by Vincent Ledvina (theauroraguy.com). (Left) A 'typical' aurora which has a smooth brightness profile with altitude. (Right) An 'enhanced' aurora, which shows a sharp discontinuity in the brightness profile with altitude that cannot be explained by traditional magnetospheric particle precipitation models. 96

B.1 Schematic of measurements made by the ICON satellite, reproduced from Immel et al., (2018) [156]. The satellite follows the orbit shown in green, making in situ plasma measurements near the apex of the equatorial field lines (shown in white). Simultaneously, ICON remotely measures the horizontal neutral wind profile, combining measurements $\sim$ 7 minutes apart both ahead of and behind the satellite track to resolve the 2D vector winds. 130

B.2 ICON IVM climatologies for 8-13 January 2022, the period used to evaluate the background conditions in Gasque et al. (2022) [108]. Northward, upward, and eastward are defined to be positive for the ion drifts. The black line indicates the median at each solar local time (SLT), the dark grey shading spans the 25th to 75th percentiles, and the light grey shading spans the 10th to 90th percentiles. . 132
B.3 Diagram of the slab geometry and coordinate system used in the dynamo calculation described in the text. We use a field-aligned slab of the atmosphere with footpoints $\sim 20^\circ$ on either side of the equator. The coordinate system is aligned such that the y-axis points along the magnetic field direction, the z-axis points vertically at the magnetic equator, and the x-axis points eastward to complete the right-handed coordinate system. 134
B.4 Modeled horizontal winds following the Tonga volcanic eruption at 150 km at both (a) 5:15 UT and (b) 8:00 UT. The color bar displays the horizontal wind magnitude and the black arrows indicate the direction of the wind. The HIAMCM model simulation data is described in detail in Vadas et al., (2023) [346]. 136

C.1 MIGHTI green and red line horizontal averaging kernels for day (solid lines) and night (dashed lines) modes as a function of the tangent altitude of the observation. Figure courtesy of Brian Harding, using the same analysis described in the Appendix of Harding et al. (2021) [129]. 142
C.2 World maps showing the illuminated and dark parts of the atmosphere at 5 UT on December 21, 2020 at (a) 0 km, (b) 120 km, (c) 550 km, and (d) 10,000 km, calculated using the Python functions included in the text. 143
C.3 Meridional winds during NH winter as observed by MIGHTI (full mission), presented as a function of latitude and SLT. In the first row, (a) shows the binned and averaged data prior to the removal of tidal components. The second row displays the fits for the (b) diurnal, (c) semidiurnal, and (d) terdiurnal tidal components. The final row shows the data residuals after successively removing the (e) diurnal, (f) semidiurnal, and (g) terdiurnal tides. Note that the colorbar amplitude varies between subfigures. 148
C.4 Same as Figure C.3, but for the observed zonal wind component. 149
C.5 Binned and averaged MIGHTI meridional (left column) and zonal (right column) neutral winds for NH winter (top row), combined equinox (middle row), and NH summer (bottom row) for the full ICON mission. Diurnal tides have been removed. Northward and eastward winds are positive. The gray shading shows the portion of the latitude/SLT space that is in darkness for each season. Clear STW features are marked by a black dotted line for the solstice cases ((a), (b), (e), and (f)). 150

D.1 GLOW model simulation results of the N_2^+ 1N to GL VER ratio as a function of altitude and characteristic electron beam energy. The region labelled 'Observable GL' is where the GL emissions are bright enough to be observed, as defined in the text. Since there is no electron beam energy for which GL emissions are produced without N_2^+ 1N emissions at picket fence altitudes, this shows that the picket fence cannot be replicated by particle precipitation models. 153
D.2 Modeled atmospheric and ionospheric profiles from the time and location of the TREx observations. (a) Neutral atmospheric density profiles from MSIS. (b) Electron density profile from IRI. (c) Magnetic field strength profile obtained from IGRF. 156
D.3 Comparing the N_2 ($A^3\Sigma_u^+$) state density between our steady-state model and the model described in Yonker and Bailey (2020) [379] as a function of altitude and parallel electric field strength. 161
D.4 Comparing the VER of N_2 1P emissions between our steady-state model and the model described in Yonker and Bailey (2020) [379], looking at (a) the percentage difference between the two models as a function of altitude and parallel electric field strength and (b) the modeled VERs as a function of parallel electric field strength at 110 km, a typical picket fence altitude. 162
D.5 Comparing the N_2 1P to GL VER ratio obtained by our steady-state model and the model described in Yonker and Bailey (2020) [379] as a function of altitude and parallel electric field strength. 162
D.6 N_2 1P fraction of emissions in the 642 - 700 nm band, as modeled by Yonker et al., (2020) [379] 163
D.7 Calculated VER Ratios of various UV emissions to GL as a function of altitude and parallel electric field strength. (a) O 1356 $\mathring{A}$ (b) VK Bands (c) N_2 2P (d) N_2 LBH. 165

List of Tables

D.1 Radiative Transition Rates. Transition rates were obtained from Eyler and Pipkin (1983) [77] and Grubbs et al. (2018) [116]. 157
D.2 Quenching Reaction Rate Constants. Reaction rates were obtained from Grubbs et al. (2018) [116], Campbell et al. (2006) [36], and Strickland et al. (1999) [333]. [a] $\chi = e^{-\left(6750-0.0151T_n^2\right)/8.314T_n}$ where T_n is the neutral temperature in K. 158

Acknowledgments

This dissertation, which motivates and details all of the published work that I have produced over the past five years, would not have been possible without the tremendous support that I received from my community. This work has been a product of steady progress at weekly research meetings, many hours spent fighting with Python, solo slogging through countless research papers, hurried conversations at copious conferences, long form email discussions and hastily sent Slack messages, and slightly tipsy after-work rambling sessions. It, of course, would also not have been possible without the off-the-job support from my friends and family, who were always willing to lend a supportive ear and help to keep the burnout at bay. This acknowledgements section is my brief attempt to thank as many of the wonderful people who helped me through this journey as possible.

First, to get it out of the way, thank you to the funding agencies without whom I would not have been able to feed or house myself throughout this process. In particular, I was supported by the UC Berkeley Physics Department, the Parker Solar Probe FIELDS experiment (which was developed and is operated under NASA contract NNN06AA01C), the Robert P. Lin Fellowship, the ICON satellite (which was supported by NASA's Explorers Program through contracts NNG12FA45C and NNG12FA42I), and the Future Investigators in NASA Earth and Space Science and Technology (FINESST) program (award #80NSSC21K1386).

Next, thank you so much to my official advisors for shepherding me through the degree program, and seeing me through to the other side. First, a massive thank you to Thomas! You taking a chance on the random PhD student who approached you to ask if you were hiring students from out of the blue was a turning point in my career. Thank you for being so excited and welcoming, even in the middle of a global pandemic. I've learned a tremendous amount from you, certainly about ionospheric physics, but also about how to pose and pursue a research question, how to navigate the strange politics of research and funding agencies, and how to be resilient when faced with setbacks. Also, thank you to Stuart, who first brought me into the fold at the lab and welcomed me as a brand new graduate student. I greatly appreciate how willing you always were to support my goals and ideas, and how you helped teach me to advocate for myself. Thank you also to my other committee members, Jonathan and Bill, for offering valuable feedback, and to Forrest for asking great questions during my qual. Thanks also to the staff of the physics department, including Joelle, Roia, Claudia, and Christian.

Next, I'd like to thank all of my unofficial advisors at the lab, who helped me purely out of their kindness and interest in working with students, and whom I am deeply indebted to. A big thank you first to John Bonnell, for your constant and remarkable support, despite being perpetual bogged down with who knows how many projects! From bringing me under your wing during our early work on RBSP, to your general advice throughout my career and unfailing willingness to offer insight, to inspiring me with your unique and in depth perspective on the science and deep natural curiosity, thank you for everything. Also thank you to Brian Harding, who continues to be a model of the kind of early career researcher I hope to grow into. Thanks for inspiring me with your constant curiosity, relentless pursuit of

scientific knowledge, and enduring willingness to help out and pass it forward. And thanks for suffering through the worst of my puns (and even somehow being coerced into letting me pick an amusing name for the rocket proposal!). Next, thanks to Joanne Wu, a complete inspiration and utter workhorse. I appreciate your fantastic suggestions during our research meetings, and also that you believed in me enough to bring me into the early stages of the CINEMA team - I can't wait to work with you more! I wish the best for you and your growing family! Thanks also to Colin Triplett, who has provided great and candid advice not just on the science, but also on the way things work in academia and how to navigate it. Even though you've been working remotely for the majority of my time at the lab, you've been an integral part of the team! Thanks also for being the first one to read through this dissertation in its entirety!

Thank you also to the rest of the ICON science team, at Berkeley and beyond, and everyone who made this extraordinary mission possible. This is an incomplete list, but thank you to Scott, Astrid, Rod, Mike, Ken, Jeff, Gilda, and Stephen for their support on the weekly ICON calls and at conferences. Thanks to Mateo for being the first student almost completely under my mentorship. I've learned just as much from you as you have from me about how to be a good research advisor. I wish you the best for your future career and hope you keep in touch. Thank you also to the ICON satellite itself for collecting such a rich and compelling data set. Even though you ghosted us when I was still in the 'getting-to-know-you' phase, your legacy lives on, in part through this dissertation. Rest in peace, ICON!

I'd like to thank all of my co-authors and collaborators who have helped me shape and refine the work presented in this dissertation and at various conferences through the years. I've already thanked some of them above, but for those that I haven't, thanks to Sharon, Erich, Justin, Meg, Forrest, Jamey, David, Glyn, and Heli for being wonderful collaborators! Also, thanks to Reza, who helped spearhead one of the works that I'm most proud of in this dissertation and whose sarcasm and attention to detail both helped push the paper along in different ways.

Thank you to my community of contemporaries at the lab, who have shown me the way, offered camaraderie, and swapped tales of woe. Thanks Orlando, Milo, Tamar, Meredith, Chris, and Savannah! Also, thanks in particular to Sam Badman for being my PhD guru, and my first friend in Berkeley, starting from admitted student's day when you hosted me and another prospective grad student air mattresses in your living room! Thanks to Hilary for being a great office mate, and to Kyung-Eun for all of our great conversations (and for letting me try so many Korean snacks!). Thanks to Roger for always providing office entertainment, and for being a good sport about my sarcasm! Thanks also to everyone who has helped make the ASSURE program possible, for creating one of the most personally fulfilling parts of my time at Berkeley. In particular, Matt, Trevor, and Sam, who worked tirelessly with me to resurrect the program back in 2020!

Thank you to everyone who mentored me while I was an undergraduate, and helped form my aspirations to attend graduate school, including Phil Erickson, Rob Pfaff, Robyn Millan, John Thorstensen, Shun-rong Zhang, Bill Rideout, and Anthea Coster. You were

the ones who set me on this remarkable path, and I am immensely grateful for your generous support and encouragement. Also thanks to the community at large for bringing the field to the point where these studies made sense as the next logical steps. I also looked at so many dissertations while I was writing this one, to help me get a sense of the genre and learn more about the field. In particular, I drew inspiration from the dissertations by Brian Harding, Matt Zettergren, Nick Pedatella, Sam Badman, Colin Triplett, Katy Greer, Lindsay Goodwin, Gareth Perry, Mack Jones Jr., and Federico Gasperini.

Finally, thanks to all the friends and family members who were there for me throughout this time, and even through a global pandemic. Thanks to my wonderful mom, who has stood by me the entire time, who followed me into a scientific career and so is able to understand a good amount of what I'm doing, and who is a constant inspiration. Thanks also to my fantastic dad, who helped me develop my communication skills from a very young age, is endlessly supportive of everything I do, and gives some of the best advice I've ever received. Thank you to my loving partner Kia, who is always there to provide a friendly ear to the ups and downs of each day of work, to support me during my dissertation milestones, and to show genuine interest in my work despite it being so far outside of your field. I can't wait for us to be Dr. & Dr.! Thanks to the kitties Piccolo and Aria (aka Mao Mao and Tiny Kitty), who always meow for food the minute I get home. Thank you also to Grandma Get, who was calling me 'Dr.' long before I got to this point, and who would have been so proud if she had gotten to see this moment. Thank you also to the rest of my family, including Lora, Aunt Susan, Uncle Rob, Cheryl, Papa Richard, and Uncle Bro. Thank you to Felicia, for being an amazing and generous support system for me when I was far from home in the middle of a pandemic. Thanks to Megan for being my first friend in life and reconnecting with me out here. Thanks also to my string quartet QinQin, Jacqie, and Kristin, for bringing some wonderful music in the depth of the pandemic.

That's probably enough thanking for one dissertation. I am sincerely grateful to everyone mentioned here, and quite a few folks not mentioned here as well. I could not have completed this work without you all! Now, without further ado, on to the dissertation!

Chapter 1

Dissertation Goals and Impact

1.1 Earth's Upper Atmosphere: Impacts on Infrastructure in the Space Age

On January 29, 2022, an active region on the sun's surface (Figure 1.1[1]) erupted, propelling a coronal mass ejection (CME) towards Earth (Gopalswamy et al., 2023) [113]. The Space Weather Prediction Center (SWPC) promptly issued an alert,[2] warning that a geomagnetic storm triggered by the CME might induce power grid fluctuations, disrupt high-frequency (HF) radio communications, or increase atmospheric drag on low Earth-orbit (LEO) satellites. Upon reaching Earth on February 3, however, the CME induced only a 'minor' geomagnetic storm, which was not expected to cause major infrastructure disturbances (Berger et al., 2023) [28].

On the warm, nearly cloudless afternoon of February 3, 2022, a SpaceX rocket launched from Florida's Kennedy Space Center and injected 49 Starlink satellites into an initial orbit at 210 km.[3] Following their successful launch and injection, the satellites should have ascended to their designated 500 km operational altitude using their electric thrusters (Hapgood et al., 2022) [124]. However, the ongoing geomagnetic storm heated the upper atmosphere, enhancing the atmospheric density and increasing the atmospheric drag on the satellites to unexpected levels (Oliveira & Zesta, 2019, Y. Zhang et al., 2022; Berger et al., 2023) [251, 386, 28]. Despite mitigation efforts, within days, 38 of the satellites had re-entered the atmosphere and subsequently burned up, an estimated financial loss of tens of millions of dollars.[4]

[1]The solar data shown here was retrieved from `https://stereo.gsfc.nasa.gov/cgi-bin/images`.

[2]Warnings are issued from `https://www.swpc.noaa.gov/products/alerts-watches-and-warnings`. On February 1, 2022, the alert read, "A G2 (Moderate) geomagnetic storm is likely on 2 February due to the anticipated arrival of a CME from late 29 January. Any CME effects are likely to linger into 3 February at G1 (Minor) storm levels" (Fang et al., 2022) [78].

[3]The video of the launch can be viewed at `https://www.spacex.com/launches/sl4-7/`

[4]`https://www.cnbc.com/2022/02/09/spacex-losing-starlink-satellites-due-to-geomagnetic-space-storm.html`

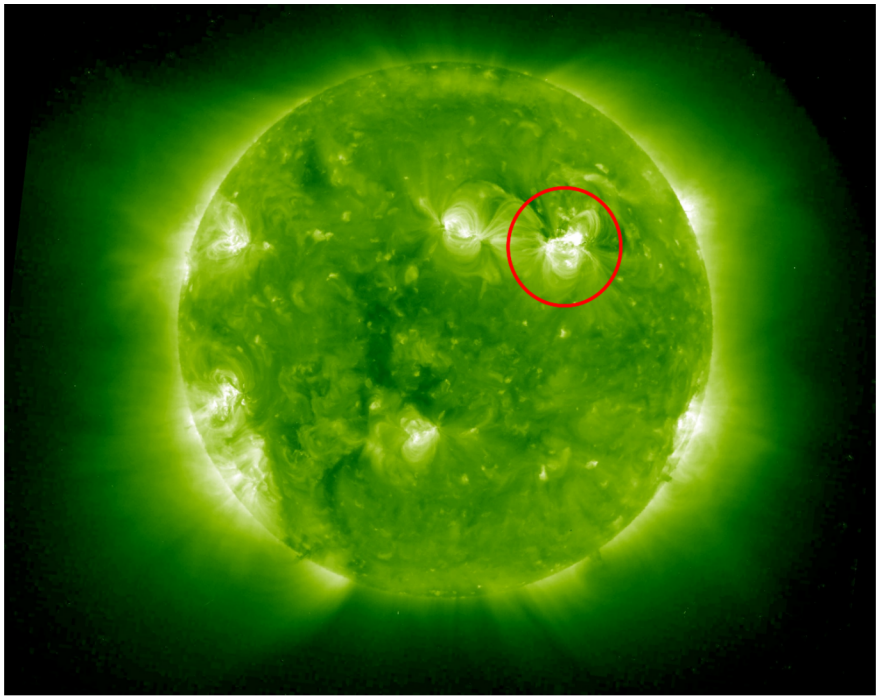

Figure 1.1: An Extreme-Ultra Violet (EUV, 195 Å) view of the sun captured by the Sun Earth Connection Coronal and Heliospheric Investigation (SECCHI) EUV imager on board the Solar TErrestrial RElations Observatory (STEREO-A) at 23:55 UT on January 29, 2022. The CME responsible for the loss of 38 Starlink satellites emanated from the active region circled in red (Gopalswamy et al., 2023) [113].

The dramatic loss of these satellites illustrates the potentially profound repercussions of space weather. **As we increasingly rely on space-based communications, navigation, and defense systems, and as we rapidly send more spacecraft into orbit (Figure 1.2)**[5]**, we become more vulnerable to space weather effects.** Only by better understanding space weather and what drives it will we be able to predict and mitigate space weather's impact on modern infrastructure. The Starlink disaster, for example, might have been prevented with an improved estimate of the incoming CME's arrival time and effect on the upper atmosphere (Fang et al., 2022) [78].

Understanding and forecasting the behavior of the ionosphere-thermosphere (I-T) system, the region of space spanning ∼85 to 1,000 km above Earth, is particularly essential for mitigating space weather effects. This region houses a diverse array of objects in Low-Earth Orbit (LEO), ranging from tiny ten centimeter cubesats to the massive football field-length International Space Station[6] (Heelis & Maute, 2020) [133]. Changes in atmospheric drag,

[5] https://orbitaldebris.jsc.nasa.gov/modeling/legend.html

[6] https://www.nasa.gov/international-space-station/space-station-facts-and-figures/

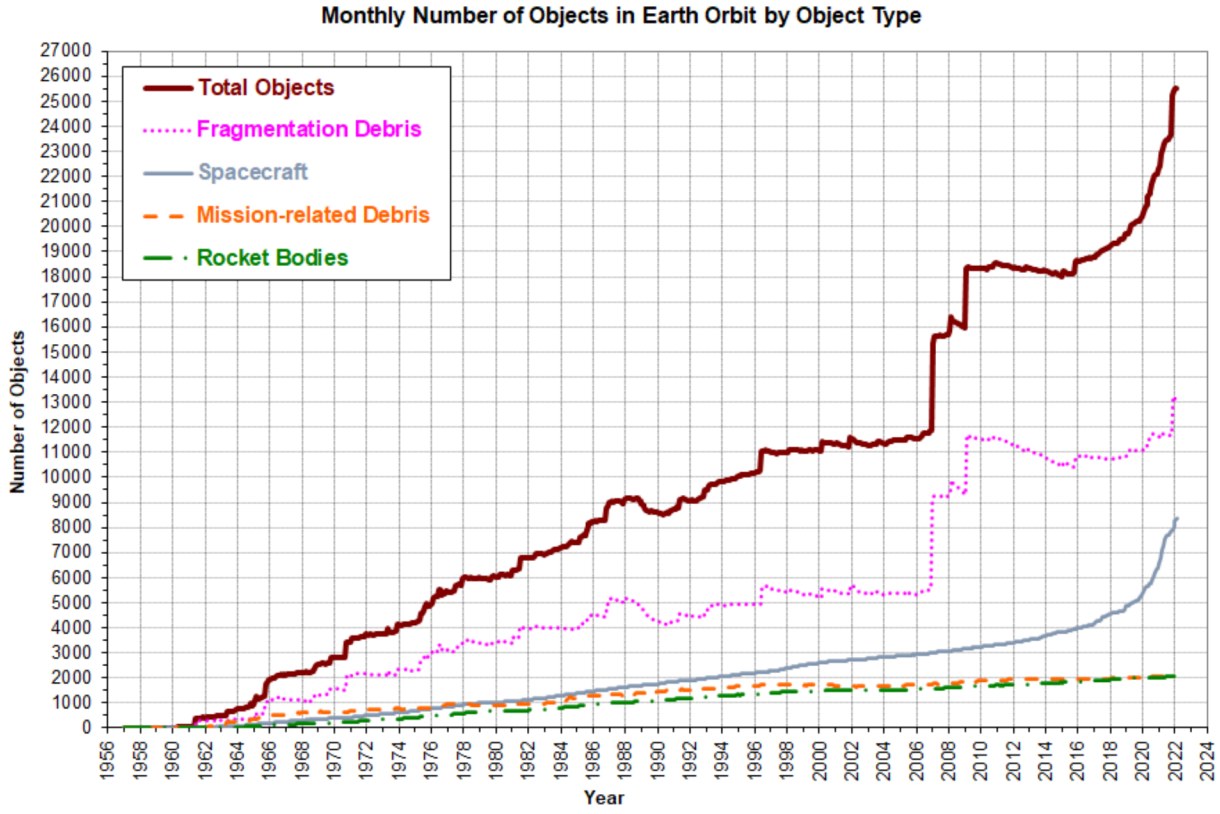

Figure 1.2: The number of objects >10 cm in LEO, determined by the NASA Orbital Debris Program Office.

whether induced by geomagnetic disturbances (e.g., Oliveira & Zesta, 2019) [251] or day-to-day I-T variations (e.g., Leonard et al., 2012) [185], alter satellite lifetimes (sometimes dramatically as in the Starlink disaster) and increase uncertainty in orbital tracking (Oliveira et al., 2021) [252]. The recent proliferation of LEO spacecraft (as illustrated in Figure 1.2) for purposes including communication, navigation, defense, and scientific research, heightens the critical need for precise orbital tracking in this region to avert catastrophic collisions, emphasizing the importance of advancing our understanding of energy dynamics in the I-T system to obtain accurate forecasts.

In addition to affecting LEO satellites, space weather in the I-T system can impair other space-dependent infrastructure, as illustrated in Figure 1.3. Ionospheric irregularities can disrupt or scatter radio waves propagating through the ionosphere (e.g., Booker & Wells, 1938) [35], including Global Positioning System (GPS) signals and long-distance radio communications. In the context of GPS navigation, these disruptions can lead to positioning errors and signal loss (e.g., Wanninger, 1993; Coster & Komjathy, 2008; Oksavik et al.,

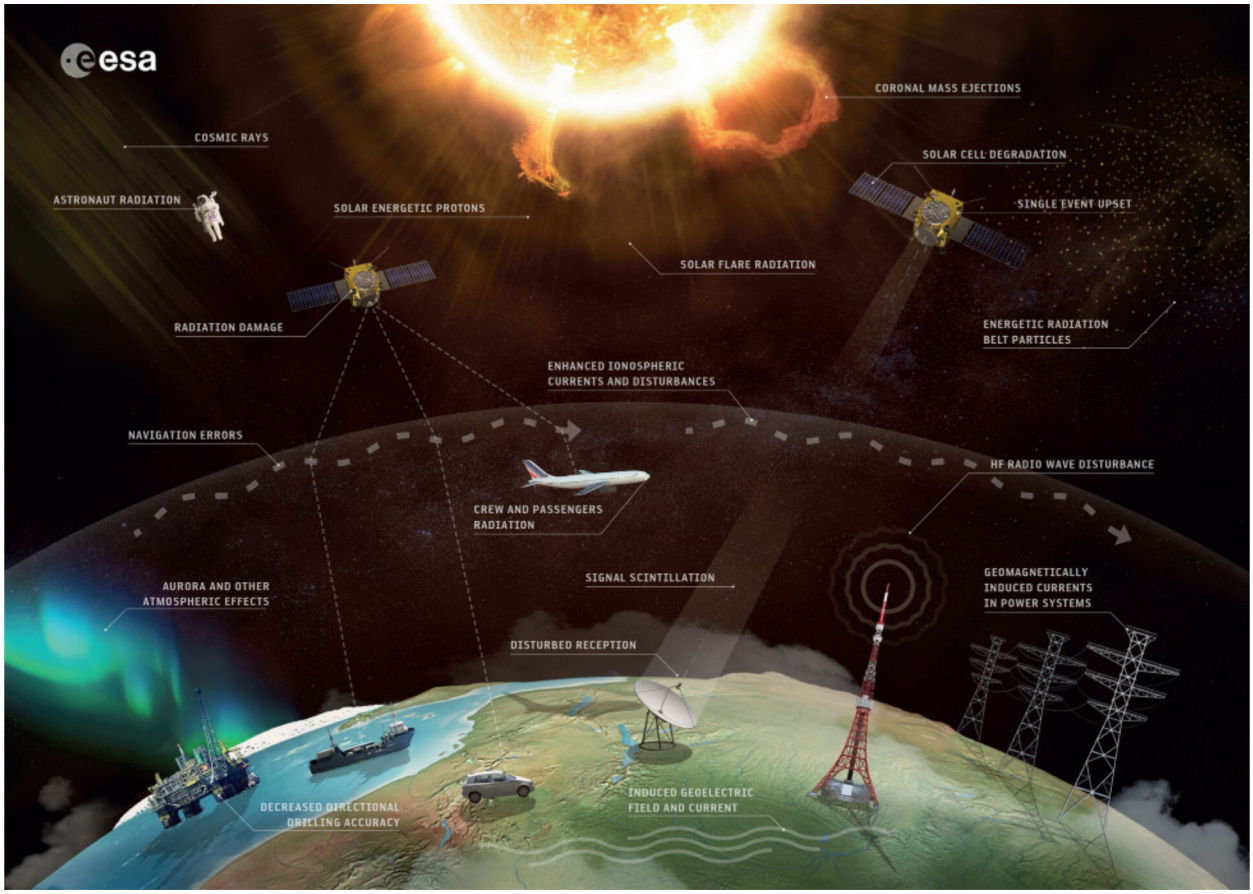

Figure 1.3: Illustration of the many of the potential impacts of space weather on modern infrastructure. Credit: European Space Agency (ESA).

2015; Demyanov & Yasyukevich, 2021) [363, 52, 250, 59]. Furthermore, during geomagnetic disturbances, rapid changes in the magnetic field at Earth's surface, often induced by ionospheric currents, can drive large currents in the ground (Viljanen et al., 2001; Viljanen et al., 2006) [357, 356]. These ground-induced currents (GICs) pose a threat to ground-based infrastructure, including power grid transformers (e.g., Kappenman, 2001; Cannon et al., 2013) [166, 37], potentially causing major power blackouts and costing billions of dollars (e.g., Eastwood et al., 2017; Space Studies and National Research Council, 2009) [67, 335].

Despite these potentially harmful impacts on infrastructure, the I-T system plays a crucial role on our planet, safeguarding complex lifeforms from harmful radiation, moderating atmospheric escape into space (e.g., Airapetian et al., 2020) [4], and supporting long-range radio communications. Scientifically, it serves as a natural laboratory for studying plasma-neutral interactions (Stubbe & Hagfors, 1997) [334]. Additionally, this atmospheric layer contains the aurora, a striking natural display that has inspired humans since ancient times

(e.g., Hamacher, 2013) [123].

While the importance of understanding the I-T system is evident, accurate and actionable space weather forecasts remain a challenge, as highlighted by recent events such as the loss of Starlink satellites. Specifically, we are still far from being able to forecast ionospheric and thermospheric behavior, and many aspects of the coupling between the thermospheric neutral gas and ionospheric plasma remain poorly understood (Schunk & Sojka, 1996; Harding, 2017; Heelis & Maute, 2020) [304, 125, 133]. As Heelis and Maute (2020) expressed in their review of current challenges in understanding Earth's I-T system:

> "To protect space-based assets and minimize the impact of space weather on society with reliable specification and forecast, it is critical that we understand how to specify its state and predict its evolution by advancing our holistic understanding of the I-T system... Understanding how the behavior of this region is controlled, by internal interactions and by the external regions to which it is coupled, is the preeminent challenge for the next generation of scientists." [133]

This dissertation takes on the challenge outlined by Heelis and Maute (2020) [133] and makes progress toward understanding how the coupling between neutral gas and plasma in the I-T system is influenced by both daily and extreme energy inputs. This exploration will focus on the coupled I-T response to three different types of drivers:

1. explosive events in the lower atmosphere, with a specific focus on the 2022 eruption of the Hunga Tonga-Hunga Ha'apai volcano,
2. abrupt changes in solar inputs triggered daily by the evening solar terminator's passage, and
3. extremely fast ion flows in the upper ionosphere during geomagnetic storms, associated with unusual optical phenomena.

This dissertation will trace how the effects of these energy inputs propagate through the I-T system, characterizing the poorly-understood ionospheric and thermospheric phenomena which result. It will additionally provide benchmarks against which to validate future I-T system models.

This chapter next provides a summary of each of the three problems that will be extensively addressed later in this dissertation (Section 1.2). Subsequently, an outline of the dissertation is presented (Section 1.3), followed by a discussion of the specific contributions that this dissertation makes to our understanding of I-T coupling and the field of space physics more broadly (Section 1.4).

1.2 Case Studies: I-T Drivers and Associated Plasma-Neutral Coupling Phenomena

This dissertation investigates the impact of three types of energy inputs into the I-T system. In this section, we offer a brief overview of each source, the associated plasma-neutral coupling phenomena, and their integration into our understanding of the broader I-T system. For each case, we will also outline the science questions that this dissertation aims to address.

Explosive Lower Atmospheric Energy Inputs: The 2022 Tonga Volcanic Eruption

Sandwiched between Earth's dense lower atmosphere and its magnetosphere,[7] the I-T system responds to energy inputs from both below and above. Daily and seasonal variations in ionospheric structure are broadly attributable to solar, geomagnetic, and lower atmospheric drivers (e.g., Rishbeth et al., 2006) [290]. Studies of ionospheric variability have generally concluded that while long-term variations are mostly driven by changes in solar inputs connected to the 11-year solar cycle, geomagnetic activity has a greater effect on daily variability (e.g., Forbes et al., 2000; Fuller-Rowell et al., 2000) [86, 96]. On shorter timescales, solar flares generate ionospheric variations by rapidly enhancing ionospheric plasma production rates (e.g., Qian et al., 2011) [275]. Recently, however, it has become clear that lower atmospheric coupling to the I-T system via atmospheric waves also plays a significant role in daily variations in ionospheric and thermospheric structure and behavior, potentially comparable to the effects of geomagnetic activity (Forbes et al., 2000; Fuller-Rowell et al., 2000; Rishbeth & Mendillo, 2001; Rishbeth et al., 2006; Goncharenko et al., 2010; Liu, 2016; Pedatella & Liu, 2018) [86, 96, 294, 290, 112, 194, 262]. The waves responsible for this coupling are surveyed in more detail in Chapter 2.2.

Significant progress has been made in recent years in understanding the lower atmosphere's influence on the I-T system (e.g., Forbes et al., 2009; Gasperini et al., 2015; Liu, 2016; Gasperini et al., 2022) [87, 105, 194, 104]. Despite this recent progress, understanding the ionospheric response to lower atmospheric forcing remains an open and active research area, including studying how the changing thermospheric wind state affects the ionosphere (Immel et al., 2021) [155].

The first science topic addressed in this dissertation investigates the mechanisms of energy transfer upward into space from explosive lower atmospheric events. These impulsive energy inputs can arise from natural phenomena, such as earthquakes and volcanic eruptions, or human-generated phenomena, such as nuclear explosions. While it has long been recognized that such events lead to disturbances in the ionosphere (e.g., Dieminger & Kohl, 1962; Leonard & Barnes, 1965; Roberts et al., 1982) [60, 186, 297], only recently, aided by more abundant observations and more sophisticated modeling, have we begun disentangling the

[7] Earth's *magnetosphere* is the part of near-Earth space dominated by Earth's magnetic field and coupled to the solar wind and interplanetary magnetic field.

various I-T coupling mechanisms at play during these events (e.g., Zettergren et al., 2017; Aa et al., 2022; Vadas et al., 2023) [381, 2, 352]. However, there remain many open questions, particularly regarding how the thermospheric disturbances from these events couple to and disturb the ionosphere.

In this dissertation, we focus on demonstrating and explaining the mechanisms influencing the ionospheric impact of the Hunga-Tonga Hunga-Ha'pai (hereafter referred to as 'Tonga') volcanic eruption, which occurred on 15 January 2022 (Figure 1.4(a)[8]). This event was the largest volcanic eruption in at least 30 years (Duncombe et al., 2022) [65], sending ash at least 55 km into the atomsphere (Carr et al., 2022) [40], producing lightning at the highest rate ever documented (Van Eaton et al., 2023) [354], and triggering a tsunami which devastated the nation of Tonga (Pakoksung et al., 2022) [256]. This eruption detonated with an energy blast comparable to the largest nuclear explosions (Astafyeva et al., 2022; Garvin, 2022; Kulichkov et al., 2022; Vergoz et al., 2022) [13, 103, 179, 355], and the resulting tsunami's effects were felt across the Pacific (Caravajal et al., 2022) [41].

Beyond the energy it sent rippling through the earth and the ocean, the eruption deposited a significant amount of energy in the atmosphere, generating a spectrum of atmospheric waves that traversed the globe (Wright et al., 2022) [371]. Although the eruption occurred in a part of the Pacific with few ground-based observatories, the recent proliferation of space-based research assets offers an unprecedented opportunity to observe the atmospheric effects of this event. For example, Figure 1.4(b)[9] shows these atmospheric disturbances as captured by Geostationary Operational Environmental Satellites (GOES) West Infrared data, which, after smoothing and taking the difference between consecutive images, reveals lower atmospheric temperature variations.

Some of the eruption's energy propagated vertically through the atmosphere, causing disturbances in the I-T system (e.g., Ghent & Crowell, 2022; Wright et al., 2022; Zhang et al., 2022; Vadas et al., 2023) [109, 371, 383, 352]. Waves propagated globally in the ionosphere (Zhang et al., 2022) [383], contributing to the formation of large equatorial ionospheric instabilities (Aa et al., 2022; Rajesh et al., 2022) [2, 277], which interfered with GPS signals over the Asian sector (e.g., Ke et al., 2023) [170]. As illustrated in Figure 1.4(c)[10], the electrodynamics of the ionosphere were also disrupted after the eruption, with extreme winds in the thermosphere producing unusual electric currents over South America (Harding et al., 2022) [127].

While many studies have focused on the global or far-field ionospheric effects of this event, relatively fewer studies have examined the near-field ionospheric effects: drastic changes that occurred rapidly in the I-T system within ∼5,000 km of the eruption. The near-field serves as a laboratory for studying the plasma-neutral coupling resulting from an extreme, impulsive

[8] https://www.earthdata.nasa.gov/worldview/worldview-image-archive/explosive-eruption-of-hunga-tonga-hunga-ha-apai-volcano

[9] For an animated version of this figure, showing the waves propagating over time, visit https://github.com/mathewbarlow/animations/blob/main/tonga_wave_labeled.gif

[10] https://www.nasa.gov/missions/icon/nasa-mission-finds-tonga-volcanic-eruption-effects-reached-space/

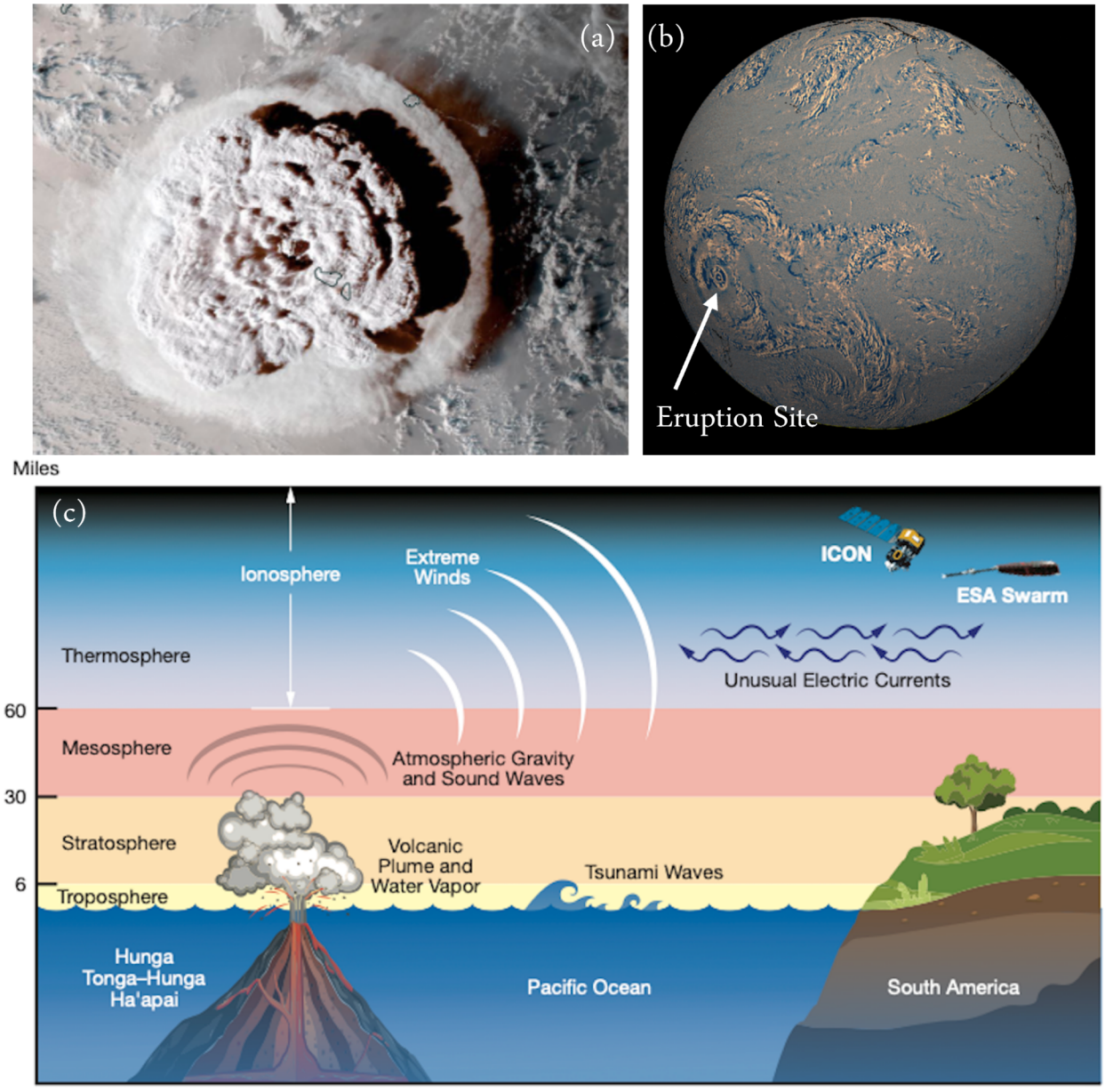

Figure 1.4: Effects of the 15 January 2022 Tonga volcanic eruption. (a) The plume from the volcanic eruption, captured by the Advanced Baseline Imager (ABI) aboard NASA's GOES-West satellite. Credit: NASA. (b) Atmospheric waves emanating from the eruption site, captured by NASA's GOES-West satellite. Credit: Mathew Barlow/University of Massachusetts Lowell. (c) Cartoon illustrating some of the upper atmospheric effects of the eruption, highlighting findings from Harding et al. (2022) [127]. Credit: NASA's Goddard Space Flight Center/Mary Pat Hrybyk-Keith.

energy input, much of which remains poorly characterized.

In this dissertation, we aim to address the following science questions on this topic:

- How did the ionosphere in the near-field (within ∼5,000 km) of the Tonga volcano evolve over time following the eruption?
- What were the thermospheric drivers of these ionospheric changes?
- What were the dominant near-field plasma-neutral coupling mechanisms during this event?

This dissertation will address these questions by using near-field satellite measurements of the ionosphere and thermosphere following the Tonga eruption. In particular, leveraging data from NASA's Ionospheric Connection Explorer (ICON), which measures both ionospheric plasma drifts and neutral winds along the same magnetic field line, offers an unprecedented look at plasma-neutral coupling following explosive events in the lower atmosphere.

Daily Effect of the Setting Sun: Thermospheric Solar Terminator Waves

The second I-T driver considered in this dissertation is the solar terminator, which marks the division between illumination and darkness, as shown Figure 1.5. In contrast to the extreme but solitary energy impulse in the lower atmosphere caused by a volcanic eruption, the solar terminator sweeps across the Earth twice daily–once in the morning and once in the evening–introducing gradients in atmospheric solar energy inputs.

Despite occurring daily, the solar terminator's effect on the I-T system has received little scientific attention. In the early 1970s, Chimonas and Hines (1970) [46] first theorized that the heating gradients produced during a solar eclipse would generate a spectrum of waves in the upper atmosphere. Later, Beer (1973) [25] suggested that the daily motion of the solar terminator would do the same. Subsequent theoretical studies generally confirmed that it was possible for the moving solar terminator to generate waves (Beer, 1978; Cot & Teitelbaum, 1980; Somsikov, 1987; Somsikov & Ganguly, 1995) [26, 53, 322, 324], but few observations were available to test their theoretical predictions.

In the decades since, numerous papers have reported observations of these waves, broadly termed 'solar terminator waves' (STWs) in the ionosphere, typically near the morning solar terminator (e.g., Galushko et al., 1998; Afraimovich, 2008; Song et al., 2013; Ding et al., 2014; Zhang et al., 2021) [101, 3, 325, 61, 384]. However, only three studies to date have reported observations of these waves in the thermosphere (Forbes et al., 2008; Liu et al., 2009; Bespalova et al., 2016) [89, 199, 30], finding them to be prominent only near the evening solar terminator and to have longer wavelengths than their reported morning ionospheric counterparts. This discrepancy between ionospheric and thermospheric observations remains unresolved, and will be discussed in more detail in Chapter 4.

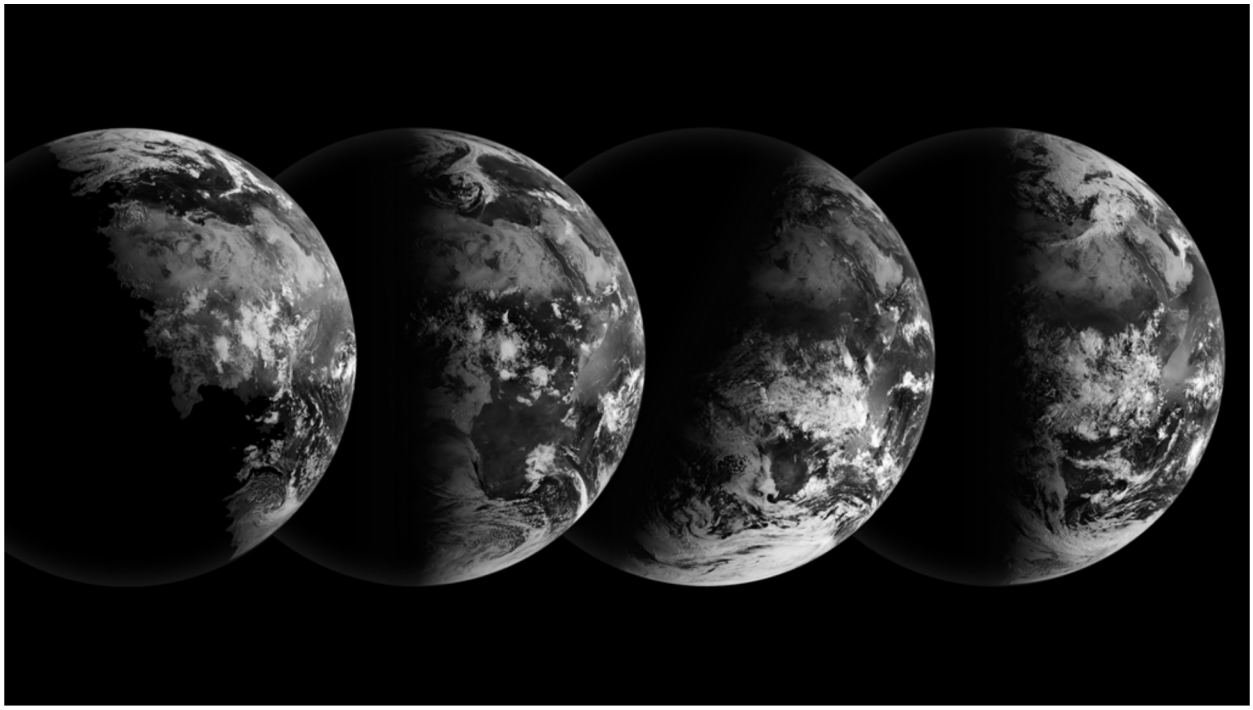

Figure 1.5: View of the terrestrial solar terminator from space, as observed by the Meteosat-9 satellite. From the left, the images were captured on the June solstice, September equinox, December solstice, and March equinox, showing the varying angle of the terminator due to Earth's axial tilt. Credit: NASA Earth Observatory.

Recent whole-atmosphere modeling studies (Vadas et al., 2023; Chou et al., 2022) [352, 47] have suggested that thermospheric STWs may be more prominent than previously thought, and that they may consequently exert considerable influence on thermospheric and ionospheric dynamics. However, these suggestions have yet to be verified observationally. In particular, the northward component of the STW winds, which could play an important role in ionospheric plasma redistribution, has never been measured. Additionally, the altitude profile of these winds has never been observed, which could help identify where in the atmosphere these waves originate, which remains an open question.

This dissertation will attempt to fill these observational gaps and advance our understanding of these waves. The specific science questions addressed are:

- What is the daily effect of the solar terminator on Earth's upper atmosphere? In particular, what is the effect on the thermospheric north/south (meridional) winds, and how does the effect vary with altitude in the thermosphere?
- Do observations of solar terminator waves in thermospheric winds agree with whole atmosphere model results? Which whole atmosphere models agree best with the obser-

vations, and how can we use the model agreement to learn about the physics of these waves?

- Where do thermospheric solar terminator waves originate in the atmosphere? Are they generated in-situ or do they propagate up from the lower atmosphere?

This dissertation will address these questions using ICON neutral wind observations in combination with the outputs of various whole-atmosphere models, including the Thermosphere-Ionosphere-Electrodynamics General Circulation Model for the Ionospheric Connection Explorer (TIEGCM-ICON) (Maute, 2017) [217], the HIgh Altitude Mechanistic general Circulation Model (HIAMCM) (Becker & Vadas, 2020; Becker, Vadas, et al., 2022; Becker, Goncharenko, et al., 2022) [20, 23, 24], and the Specified Dynamics Whole Atmosphere Community Climate Model with thermosphere-ionosphere eXtension (SD-WACCM-X) (Liu et al., 2018) [198].

This work will compare these results with the previous observations presented in Forbes et al. (2008) [89] and Liu et al. (2009) [199] as well as the modeling results in Chou et al. (2022) [47] and Vadas et al. (2023) [352] and suggest avenues for further study of STWs.

Coupling to the Magnetosphere During Substorms: Aurora-like Emissions in the Subauroral Ionosphere

While there has been growing interest in the impact of coupling from the lower atmosphere on the I-T system, there are also still unresolved questions regarding coupling to the magnetosphere above (e.g., Heelis & Maute, 2020) [133]. The magnetosphere is the region of space dominated by Earth's magnetic field, shielding Earth from the solar wind (e.g., Kelley, 2009) [172]. Coupling between the magnetosphere and the ionosphere, via particle precipitation and electromagnetic forcing, results in electrical currents, frictional and Joule heating, and drifts in ionospheric plasma (e.g., Killeen et al., 1982; Ridley et al., 1998; Kelley, 2009) [176, 288, 172]. The plasma can exchange momentum with the neutral gas in the thermosphere, affecting the circulation of the neutral atmosphere (e.g., Conde et al., 2018; Heelis & Maute, 2020) [50, 133]. Notably, the aurora is a visual manifestation of the magnetosphere's effect on the ionosphere, and is often used to trace and investigate the relationship between solar wind forcing and magnetospheric dynamics (e.g., Akasofu, 1964; Birn et al., 2012; Forsyth et al., 2020) [5, 32, 91].

Recently, MacDonald et al. (2018) [210] brought a new "aurora-like form" to the attention of the scientific community. The mauve arc now known as 'STEVE' (defined below) and the associated green streaks of the 'picket fence' (Figure 1.6) were identified by citizen scientist "aurora chasers," although records of similar phenomena appear in historical observations back to the eighteenth century (Hunnekuhl, 2019; Hunnekuhl & MacDonald, 2020) [149, 150].

Initially believed to be a new type of aurora, formed when particles accelerated in the magnetosphere or topside ionosphere collide with the upper atmosphere, it soon became clear

Figure 1.6: Photograph of STEVE (mauve arc) and the picket fence (green streaks) taken around 05:53 UT on 16 September 2017 by Robert Downie, reproduced from Archer et al. (2019)a [10].

that STEVE likely had a different origin, as satellites transiting over STEVE sightings did not observe any particle precipitation (MacDonald et al., 2018; Gallardo-Lacourt et al., 2018a; Gillies et al., 2019) [210, 99, 110]. STEVE occurs in the subauroral ionosphere, equatorward of the regular aurora (Gallardo-Lacourt et al., 2018b) [100], and is associated with extremely fast (>5 km/s) ion drifts, called Sub-Auroral Ion Drifts (SAIDs), which inspired the name 'Strong Thermal Emission Velocity Enhancement' (STEVE) (MacDonald et al., 2018) [210]. Furthermore, unlike regular aurora, STEVE's optical emission spectrum consists mainly of broadband, continuum emissions (Gillies et al., 2019) [110]. A modeling study conducted by Harding et al. (2020) [126] suggested that this unique spectrum might arise as a consequence of the fast SAID flows colliding with and vibrationally exciting N_2 molecules, setting off a chemical cascade which results in the production of NO_2 and spectrally broad light.

However, there is ongoing debate regarding whether the green streaks of the picket fence are generated by particle precipitation, similar to regular aurora, or by another mechanism. In their recent review paper on STEVE and the picket fence, Nishimura et al. (2023) [249] wrote:

"How the magnetosphere plays a role in the generation of the picket fence is

> another important question. Although the green ray structure resembles rayed auroral arcs that are created by energetic electrons precipitating from the magnetosphere, so far there is no consensus about whether electron precipitation is involved in the picket fence." [249]

While early studies suggested that the picket fence might be generated by particle precipitation (Nishimura et al., 2019; Bennett & Bourassa, 2021) [248, 27], the spectrum of the picket fence is different from that of green aurora (Gillies et al., 2019; Mende et al., 2019) [110, 228]. Recently, it has been suggested that the emissions are a consequence of instabilities which arise from extremely fast ion flows (Lynch et al., 2022; Mishin & Streltsov, 2022) [208, 235]. In particular, these theories suggest that the light might be generated when electrons energized by electric fields parallel to Earth's magnetic field collide with the local atmosphere, but it was not shown that the spectrum of light produced by such a mechanism would be consistent with the observed picket fence spectrum.

This dissertation will take up this question, investigating how extremely fast ion flows driven by magnetospheric activity might result in the optical signatures of the picket fence. Specifically, this work addresses the questions:

- Can local parallel electric fields energize ionospheric electrons to energies which, upon colliding with the neutral atmosphere, result in emissions that are spectrally consistent with picket fence observations?
- Can we constrain the expected magnitude of parallel electric fields which can generate picket fence emissions?
- Is this phenomenon limited to the picket fence in the subauroral region, or might it be a more important coupling process than previously considered?

To address these questions, this work includes a model of the optical emissions produced in the lower I-T system under the influence of local parallel electric fields and compares the model results with spectral observations of the picket fence.

1.3 Outline of the Dissertation

To address the science questions laid out in the previous section, this dissertation is organized as follows:

Chapter 2 will review the background material necessary to fully understand this dissertation, describing the I-T system, its underlying structure and main drivers, as well as a broad overview of ionospheric physics and phenomena.

Chapter 3 explores the near-field ionospheric impact of the Tonga volcanic eruption within the first hour of the eruption. The results of this chapter are published in Gasque et al. (2022) [108].

Chapter 4 moves to studying a more quotidian phenomenon: the daily effect of the setting sun on the I-T system. This chapter presents some of the first measurements of STWs in the thermosphere, including the first reports of the meridional wind effects and the first observed altitude profiles. By comparing these with the results of several whole-atmosphere models, this work assesses the models' ability to capture observed features, allowing speculation on the origin of these waves. The results of this chapter are published in Gasque et al. (2024) [106].

In Chapter 5, the focus of this work moves to subauroral latitudes to study the origin of the picket fence. This dissertation reviews current theories behind the picket fence and describes the development of a model to use its optical spectrum as a diagnostic tool for studying the physics of its formation. This chapter is based on work published in Gasque et al. (2023) [107].

Chapter 6 summarizes the results of this work and lists remaining open questions, pointing the way to future studies and missions which could further illuminate the explored phenomena.

Following the main text, there are appendices for Chapters 2 through 5 which contain further details about the data sources, models, and methods used to arrive at the results.

1.4 Contributions

This dissertation advances our understanding of the I-T system response to three energy inputs, presenting studies which characterize, model, and analyze I-T plasma-neutral coupling and the resulting phenomena.

This dissertation's studies of the Tonga volcanic eruption offer the first direct, in-situ detection of the swift and intense ionospheric electrodynamic consequences of a volcanic eruption. The observations and analysis presented in this dissertation will serve as pivotal benchmarks for future modeling efforts seeking to accurately capture the ionospheric effects of this nd future explosive lower atmospheric events.

The study of thermospheric STWs presented herein is, to date, only the fourth observational investigation of those features, and is the first study to reveal their meridional wind signatures and altitude profiles. This dissertation demonstrates that solar terminator waves are a dominant feature in the solstice thermospheric meridional winds, potentially influencing daily I-T system variability. By investigating the results of whole-atmosphere simulations, this work finds that thermospheric solar terminator waves originate below 97 km and that gravity waves may play an important role in their formation. However, several mysteries remain, including the waves' increased prominence during solstice over equinox, the asymmetry between evening and morning terminator features, and the tilt of solar terminator wave features approximately 40° from the terminator line. This work has therefore demonstrated the need for observational and modeling follow-up studies to resolve these open questions.

Finally, this dissertation concludes that the picket fence optical emissions are not caused by particle precipitation like auroras, but may rather be excited by electrons energized

by local parallel electric fields, resolving a longstanding debate. This study shows that a kinetic model of a realistic atmosphere and ionosphere driven solely by parallel electric fields produces emissions that are quantitatively consistent with picket fence observations, contributing to the development of a unified model of subauroral optical phenomena. It also identifies similar spectral features within some auroral structures, suggesting that parallel electric fields may play a role in auroral emissions as well. As a result, this dissertation was heavily influential in the development of a rocket proposal to attempt to make the first in-situ measurements of parallel electric fields in the collisional base of the ionosphere. The proposal was submitted fall of 2023, and, as of the time of this writing, we have not yet received a funding decision.

Chapter 2

The Coupled Ionosphere/Thermosphere System

This dissertation advances our scientific understanding of how three different energy inputs give rise to various phenomena within the coupled ionosphere-thermosphere (I-T) system. As explored in Chapter 1, a more detailed grasp of the behavior of this system is essential for predicting and mitigating space weather effects on modern infrastructure. Unlike the lower atmosphere, which is composed of a dense neutral gas, and much of the rest of space, which consists of collisionless and fully ionized plasma, the I-T region contains a relatively dense blend of neutral and ionized gases. The complex interactions, or 'coupling,' between these two gases give rise to the various phenomena which will be explored in subsequent chapters.

This chapter provides a foundational overview of the I-T system's fundamental structure and governing physics, emphasizing the concepts which will form the background needed to understand the results presented in later chapters. Since the core of this dissertation concerns physical processes within the I-T system, Section 2.1 begins with a broad overview of the structure and composition of Earth's atmosphere, briefly describing the lower atmosphere before focusing on the I-T system itself.

When the system experiences a perturbation from its steady state, induced, for instance, by various energy inputs considered in this dissertation, different oscillations or wave modes are excited, all capable of transporting energy and momentum within the system. The types of oscillations most relevant to this work are described in Section 2.2. These include gravity waves generated by thermospheric displacements (as observed following the Tonga volcanic eruption, pertinent to Chapter 3, and likely generated by the passage of the solar terminator, discussed in Chapter 4), tidal signatures that must be considered when examining solar terminator wave effects (Chapter 4), traveling ionospheric disturbances (observed in connection with both volcanic eruptions and solar terminator effects), plasma motions influencing whether the ionosphere is magnetized or collisional (pertinent to the modeling in Chapter 5), and plasma wave modes facilitating the rapid propagation of electromagnetic signals along magnetic field lines (an effect which enabled the Tonga eruption to swiftly have a global impact, as discussed in Chapter 3).

Following the discussion of oscillations and wave modes, Section 2.3 will explore the mechanisms of plasma-neutral coupling in the ionosphere. Specifically, this section examines the ion continuity equation to understand how local plasma density changes, influenced by the dynamics of the neutral gas. In Chapter 3, when investigating the mechanisms responsible for the electrodynamic changes following the Tonga eruption, this section's discussion of ionospheric conductivity and dynamo effects will be particularly relevant. A derivation for ionospheric conductivity and Ohm's law in the ionosphere complements this section (Appendix A.1).

Section 2.4 explores how Earth's magnetic field topology creates distinct ionospheric regions, each hosting unique phenomena. This dissertation's work on the volcanic eruption's effects and solar terminator waves presented in Chapters 3 and 4 predominantly concerns the equatorial region, while the picket fence phenomenon discussed in Chapter 5 lies in the subauroral region. To provide sufficient background for distinguishing picket fence emissions from regular auroral emissions, this section also includes a description of the high-latitude ionosphere and the primary mechanisms of particle acceleration that generate auroras.

Finally, Section 2.5 concludes this introduction. While I have aimed to include background information most relevant for contextualizing later chapters, this chapter is not intended to be an exhaustive survey of everything known about the I-T system. Excellent texts, including Rishbeth and Garriott (1969) [295], Prölss (2004) [273], Schunk and Nagy (2009) [303], Kelley (2009) [172], and Baumjohann and Treumann (2012) [18] can provide the interested reader with additional details about the physics of the I-T system.

2.1 Earth's Atmosphere: Structure and Composition

The terrestrial atmosphere comprises a thin (compared to Earth's radius) shell of gas gravitationally bound to the planet. Earth's atmosphere is loosely divisible into layers based on its temperature profile, since the temperature gradient with respect to altitude is determined by the dominant physical processes occurring within each layer (e.g., Wallace & Hobbs, 2006; Kelley, 2009) [359, 172]. The boundaries between these regions as depicted in Figure 2.1(b) are approximate, varying with latitude, local time, season, and solar cycle phase. The neutral atmospheric profiles shown in Figure 2.1(a) and 2.1(b) are for midlatitude, daytime, equinox conditions, as calculated by the Mass Spectrometer Incoherent Scatter Radar (MSIS) model version 2.1 (Picone et al., 2002; Emmert et al., 2021, 2022; Lucas, 2023) [266, 70, 71, 205].

As the closest layer to Earth's surface, the *troposphere* contains most of what we think of as "weather" – thunderstorms, tornadoes, blizzards, hurricanes, and cyclones all inhabit this region. The tropospheric temperature diminishes with increasing altitude as it becomes increasingly rarefied, until the *tropopause*, a local minimum in temperature located approximately 10 km above the surface. Above the tropopause, in the *stratosphere*, the temperature increases primarily due to the absorption of solar ultraviolet (UV, ∼250-315 nm) radiation by ozone (O_3) (Prather, 1981) [271]. The *stratopause*, situated at around 50 km, is a local maximum in temperature, dividing the stratosphere from the *mesosphere* above. In the

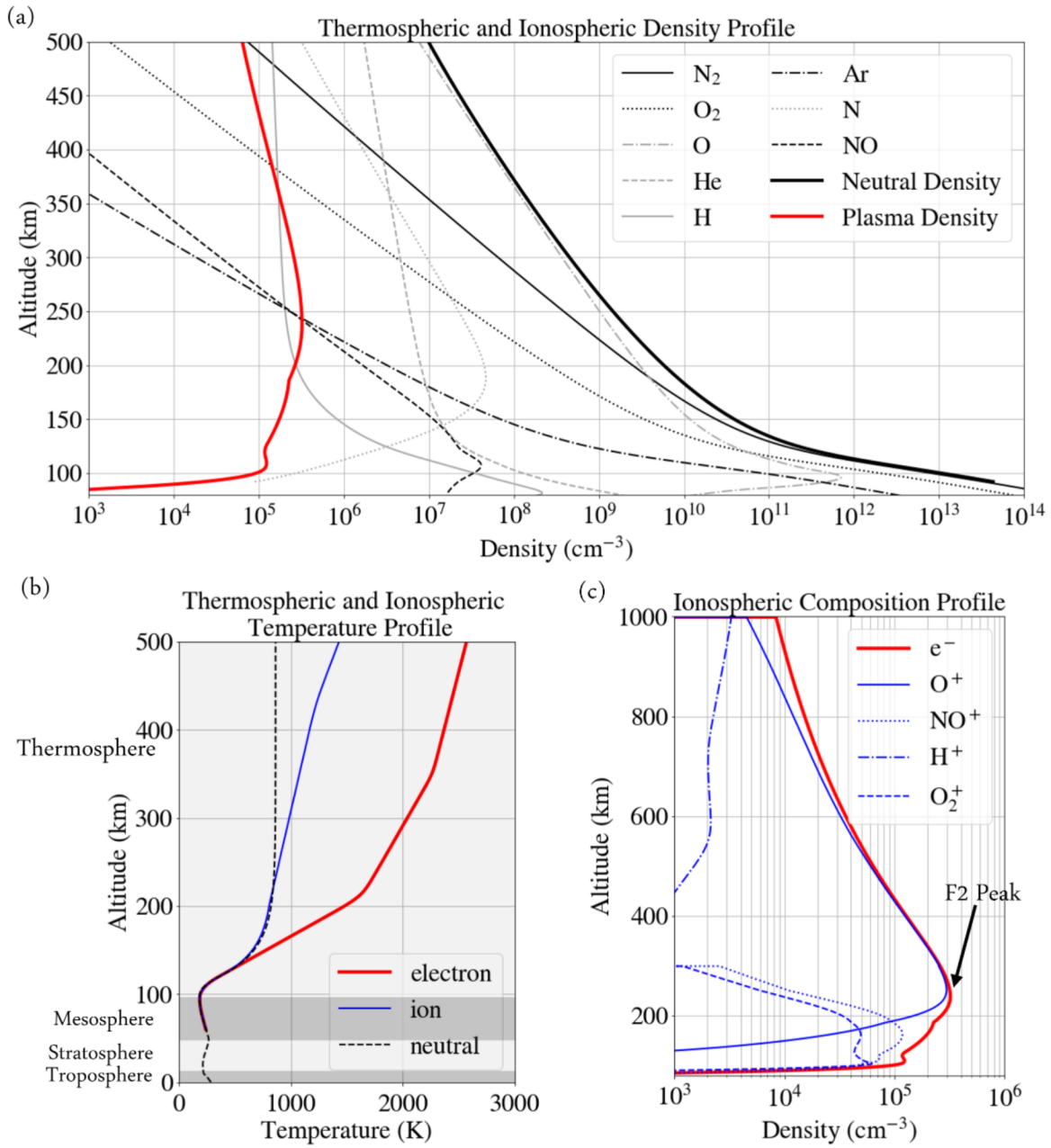

Figure 2.1: Altitude profiles characterizing the thermosphere and ionosphere under midlatitude, daytime, equinox conditions. Neutral density, composition, and temperature profiles were calculated with the MSIS model, while ionospheric density, composition, and temperature profiles were calculated using the International Reference Ionosphere 2016 (IRI16) (Bilitza et al., 2017; Ilma, 2017) [31, 153]. (a) Thermospheric and ionospheric density profiles, highlighting the dominant neutral species and the plasma density. (b) Atmospheric temperature profiles for neutrals (black), ions (blue), and electrons (red), with major atmospheric regions highlighted and labeled. (c) Ionospheric composition profile, showing the densities of dominant ion species.

mesosphere, the temperature decreases with increasing altitude due a decreased concentration of ozone as well as radiative cooling by carbon dioxide (CO_2). The atmosphere reaches its coldest point at the *mesopause*, located approximately 90 km above the surface. Above the mesopause, in a layer aptly termed the *thermosphere*, the temperature rapidly increases due to absorption of high-energy solar radiation (primarily extreme UV (EUV) with wavelengths less than 102.5 nm and UV in the Schumann-Runge continuum range below 175 nm), typically reaching temperatures over 1,000 K (Roble & Emery, 1983) [298]. Finally, above the *exobase* between approximately 500 and 1,000 km, the density in the *exosphere* is so low that the air can no longer be treated as a fluid dominated by collisional diffusion, but is rather a collection of particles each on their own ballistic trajectories.

Additional reviews of these atmospheric layers can be found in texts including Holton (1973), Curry and Webster (1999), Prölss (2004), and Kelley (2009) [143, 56, 273, 172]. This dissertation primarily focuses on the thermosphere, stretching from the mesopause to the exobase, so this region will be explored in greater detail. The following discussion draws from detailed descriptions in texts by Prölss (2004), Kelley (2009), Schunk and Nagy (2009), and Baumjohann and Treumann (2012) [273, 172, 303, 18].

Close to the base of the thermosphere, approximately aligned with the mesopause, the *turbopause* delineates the boundary below which turbulence predominantly influences atmospheric mixing, and above which diffusion plays the dominant role in determining composition. Below this boundary, the atmosphere is well-mixed, with a largely uniform composition of $\sim 78\%$ N_2, $\sim 21\%$ O_2 and $\sim 1\%$ other species. However, above this boundary, atmospheric constituents become increasingly separated by the mass of each constituent. This distinction is evident in Figure 2.1(a), in which the densities of heavier species (dark grey lines) such as N_2 and O_2 decrease much more rapidly with altitude than those of the lighter species (light grey lines) such as O and H. Above 200 km, O becomes the dominant neutral species, primarily formed when photons with energies of 5.12 eV or above (wavelengths below 242.2 nm) are absorbed by O_2, leading to photodissociation (Rees, 1989) [279].

The elevated temperature in the thermosphere compared to the lower atmospheric regions, depicted in Figure 2.1(b), is primarily due to the thermospheric absorption of solar radiation at EUV and shorter wavelengths. In the polar regions, energetic particle bombardment also contributes to thermospheric heating through collisional momentum exchange. These processes can also ionize the neutral atmosphere through photoionization and impact ionization, respectively (Yonezawa, 1966) [378]. Further discussion of these plasma production mechanisms will be provided in Section 2.3.

This plasma, collocated with the thermosphere, is referred to as the *ionosphere*. The region of the ionosphere with the highest density, which is known as the F2 peak (identified in Figure 2.1(c)), harbors the densest plasma in geospace. This peak density is typically observed at around 300 km and is governed by the altitude-dependent balance between plasma production rates and the rate at which plasma recombines into neutral gas. However, as evident in Figure 2.1(a), the thermospheric neutral density (black line) remain orders of magnitude higher than the plasma density (red line) at all ionospheric altitudes. Thus, the ionosphere is a *weakly ionized* plasma, and the interplay between plasma and neutral

processes strongly couples ionospheric and thermospheric dynamics. This coupling, how the coupled system responds to various drivers, and the resulting phenomena is the broad topic of this dissertation, and will be explored in more detail in later sections.

The ionosphere, like the neutral atmosphere, can be divided into several layers, most of which are defined by a local peak in the plasma density. These layers form because of the varying ionization rates and plasma recombination chemistry at different altitudes. At its base, the *D Region*, which resides below 90 km, is formed primarily by photoionization of nitric oxide (NO) by Lyman α radiation ($\lambda = 122$ nm) (Kelley, 2009) [172]. Negative ions, formed via the attachment of electrons to neutrals, are important in this region, as are metallic ions such as Fe^+ deposited by meteor ablation at these altitudes. The D Region is only very weakly ionized and has dynamics dominated by collisions with the surrounding dense neutral air. Although this region contains many interesting phenomena,[1] this dissertation focuses on higher altitudes of the I-T system where the plasma plays an important role in the dynamics, so the D Region region will not be explored further in this work.

Next, the *E Region*, composed primarily of molecular ions such as O_2^+ and NO^+, extends between about 90 and 150 km. As explored in greater detail in Section 2.3, the ionospheric plasma density at a specific location in space is regulated by the balance between plasma production (via photoionization or impact ionization), destruction (via recombination), and transport. During nighttime, when the dominant source of plasma production vanishes, the ionospheric E Region plasma density is reduced by several orders of magnitude due to the rapid recombination rates for molecular ions.

Above about 150 km, the *F Region* is mainly composed of O^+ ions due to the dominance of atomic oxygen in the neutral atmosphere at these altitudes. The F Region, where the dominant O^+ recombine more slowly than molecular ions, persists throughout the night. As evident from Figure 2.1(b), the temperatures of ions and electrons diverge from the neutral temperature in the F Region, where thermalizing collisions are less frequent. Above the F Region, in the *plasmasphere* or *protonosphere*, H^+ becomes the dominant ion. The transition height between the two regions typically lies between 500 and 1200 km, but is highly variable at different latitudes and under different solar flux conditions (Kutiev et al., 1994) [180].

Both the thermosphere and ionosphere are driven by forces from above (e.g. changes in solar and geomagnetic inputs, particle precipitation, etc.) and from below (e.g., terrestrial weather, lower atmospheric tides, etc.) (e.g., Smith, 2012; Wang et al., 2022) [318, 362]. Disturbances in the thermosphere or ionosphere, through plasma-neutral coupling, often result in oscillations propagating through the I-T system. The following section will review some of the wave phenomena which will be relevant to this dissertation.

[1] For example, this region strongly affects the propagation of radiowaves, absorbing most AM radio signals during the day. Furthermore, charged dust and ice particles in this region lead to interesting dusty and icy plasma physics behavior (e.g., Kelley, 2009) [172].

2.2 Disturbances in the Upper Atmosphere: An Overview of Oscillations and Wave Phenomena

Below the exosphere, where the atmosphere is dense and there are frequent collisions between particles, neutral air behaves collectively, allowing it to be meaningfully described using average quantities including temperature and bulk flow velocity. Here, for most applications[2], the neutral atmosphere can be described as a fluid and can sustain a variety of atmospheric oscillations (e.g., Greer, 2013) [114]. These oscillations arise when the equilibrium state of the atmosphere is perturbed and a restoring force acts to bring it back into equilibrium. For example, *acoustic waves* (also known as sound waves) in the atmosphere are pressure oscillations which propagate through the air, carrying energy as they compresses and decompresses the air periodically (with frequencies higher than the acoustic cutoff frequency of ∼3.3 mHz in the lower thermosphere) along the propagation direction (e.g., Blanc, 1985; Astafyeva, 2019) [33, 12]. Another example more relevant to this dissertation, *gravity waves* (discussed in more detail below) arise when part of the atmosphere is vertically displaced (such as when wind passes over a mountain range) and then oscillates up and down due to the competing influences of gravity and buoyancy at frequencies lower than the Brunt-Väisälä frequency (typically ∼2.9 mHz in the lower atmosphere) (e.g., Astafyeva, 2019) [12]. Similarly, the ionized part of the upper atmosphere supports various oscillations, some of which are driven by interactions with the neutral atmosphere. This briefly describes the wave modes in the I-T system that are relevant to the work presented in later chapters. This is by no means an exhaustive survey of the plasma and neutral wave modes that one might encounter in the I-T system.

Upper Atmospheric Tides and Planetary-Scale Waves

Colloquially, the term 'tide' evokes the regular changes in sea level along the local shoreline caused by the gravitational pull of the Moon on the Earth's oceans. Earth's atmosphere also experiences tidal variations, manifesting as regular, periodic oscillations in the temperature, winds, density, and pressure of the neutral atmosphere (Chapman & Lindzen, 1970) [42]. Like ocean tides, some atmospheric tides are generated by the Moon's gravitational pull, and therefore have periods which are subharmonics of a lunar day. However, the strongest tides in the middle and upper atmosphere are solar thermal tides, with periods that are subharmonics of a solar day and which result from the periodic heating of the atmosphere by solar radiation (e.g., Kelley, 2009) [172]. A tutorial of much of the pertinent mathematics and nomenclature describing these waves can be found in Forbes (1995) [85], and will not be replicated here.

[2]For applications requiring detailed atmospheric chemistry, a kinetic approach (which focuses on individual particles or reactions rather than average quantities) is essential. In Chapter 5, a kinetic approach is used to study the chemistry resulting in picket fence optical emissions in the subauroral ionosphere.

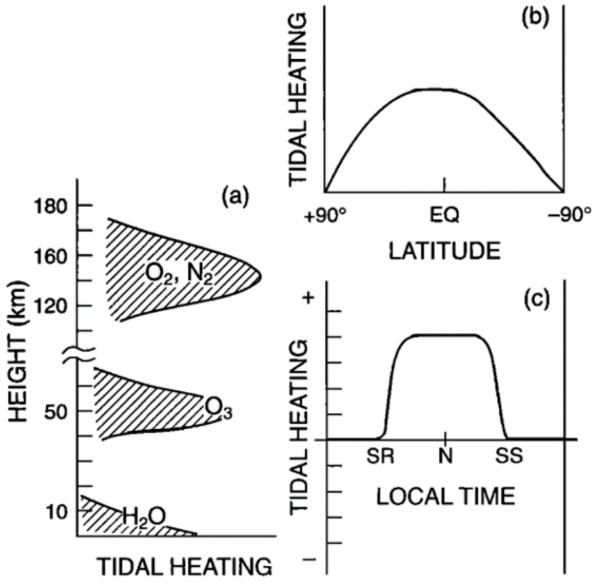

Figure 2.2: Schematic showing the heating resulting in solar thermal tides, reproduced from Figure 11 of Forbes (1995) [85]. (a) Vertical heating variations associated with the absorption of solar radiation by different atmospheric constituents. (b) Latitudinal heating variations associated with changing solar inclination angle. (c) Local time heating variations.

Figure 2.2 depicts a schematic of atmospheric heating which generates solar thermal tides (Forbes, 1995) [85]. The heating rate varies with latitude (Figure 2.2(b)) and local time (Figure 2.2(c)). As solar radiation impinges on the atmosphere, different atmospheric constituents absorb and are heated by parts of the solar spectrum, as shown in Figure 2.2(a). Some of this radiation is absorbed directly in the thermosphere by O_2 and N_2, generating an in-situ tide. The radiation absorbed by ozone (O_3) and water vapor (H_2O) in the lower atmosphere periodically heats the atmosphere and generates tidal oscillations, some of which can then propagate vertically to thermospheric altitudes.[3] As tides propagate vertically, the associated wind amplitude grows exponentially since energy is conserved while the neutral atmosphere's density decreases exponentially. The tides eventually break due to their large amplitudes or the effect of kinematic viscosity (e.g., Kelley, 2009) [172]. These tides act as an important pathway for transporting energy and momentum from the lower atmosphere into the I-T system (e.g., Jones Jr., 2015) [164].

As shown in Figure 2.2(c), the heating from incoming solar radiation rises sharply at sunrise (SR), is most intense at solar noon (N), and falls off sharply at sunset (SS). This

[3]Not all tides can propagate vertically; some remain trapped below the thermosphere. For details, see Chapman and Lindzen (1970) [42].

periodic heating structure sets the period of the tides. Near the equator, the dominant tidal mode is the *migrating diurnal tide*, which has a 24 hour period and migrates westward with the apparent motion of the sun. Tides with periods of 12 hours and 8 hours are referred to as *semidiurnal tides* and *terdiurnal tides*, respectively. The tidal forcing decreases at higher latitudes with the changing angle at which solar radiance is incident upon the atmosphere. This introduces latitudinal and seasonal variations to tidal amplitudes and structure.

In addition to the migrating tides, which appear fixed in local time, *non-migrating tides* vary in longitude, and may propagate either eastward or westward (e.g., Pedatella, 2011) [261]. These can be generated by localized sources in the troposphere, such as latent heat released by tropical convection (Hagan & Forbes, 2002) [119] or by nonlinear interactions between tides and other upper atmospheric waves (McLandress & Ward, 1994; Miyahara & Miyoshi, 1997; McLandress, 2002; Lieberman et al., 2015) [225, 238, 224, 191]. One of these other wave modes, *planetary* or *Rossby* waves, are global-scale atmospheric oscillations arising naturally as normal modes in the rotating atmosphere (e.g., Pogoreltsev et al., 2007) [268]. These have periods longer than a day, and can propagate zonally or remain stationary (Forbes, 1995) [85].

Despite abundant observations of tidal variations in the lower atmosphere and theoretical foundations for how these modes can propagate vertically, observations of neutral winds in the thermosphere are sparse and there remain open questions about the spectrum of waves and tides propagating in the upper atmosphere (Heelis & Maute, 2020) [133]. In Chapter 4, we present neutral wind observations of *solar terminator waves* (STWs) in the terrestrial thermosphere. Like solar thermal tides, STWs migrate with the apparent motion of the sun and are thought to be generated by the regular heating changes induced by sunrise and sunset. However, it remains unclear whether these originate in the lower atmosphere or are generated in situ in the thermosphere. The relation between STWs and solar thermal tides or smaller-scale waves which arise in the neutral atmosphere (such as gravity waves, reviewed in the next section) will be investigated in Chapter 4.

Atmospheric Gravity Waves

The term 'wave' often evokes rhythmic ocean swells crashing against the shoreline, a familiar sight to any beach-goer. The periodic crests and troughs of ocean waves travel along the air-water interface and are moderated by a gravitational restoring force, so they are referred to as 'surface gravity waves.' In contrast, 'internal gravity waves' are waves which move within a fluid, with gravity modulating the pressure, temperature, density, and bulk fluid motion. Unlike surface gravity waves, which only move horizontally along the interface between two fluids, internal gravity waves can propagate both horizontally and vertically, transporting energy and momentum between different layers within a fluid.

Scientific interest in understanding and characterizing internal gravity waves in the atmosphere first arose when worldwide pressure disturbances were observed following the eruption of the Krakatoa volcano in 1883 (Press & Harkrider, 1962) [272]. This historical context seems particularly fitting since a significant focus of this dissertation will be on examining

the ionospheric and thermospheric effects of the 2022 Tonga volcanic eruption. In 1960, Hines [140] published the foundational work in the field of upper atmospheric internal gravity waves (hereafter, AGWs). Hines (1960) [140] presented a mathematical development of AGWs, exploring their properties and showing that these waves were consistent with observations of irregularities in thermospheric winds and ionospheric plasma distributions. In the years since this work, significant progress has been made in understanding the various sources and effects of AGWs, as summarized in the review by Fritts and Alexander (2003) [93].

To elucidate the fundamental principles of AGWs, first observe that Figure 2.1(a) illustrates the exponential decrease in neutral atmospheric density with increasing altitude. In general, these vertical variations (aligned with the local gravitational force) are more significant than horizontal variations. The atmosphere is considered *stable* in the sense that, if a parcel of air is displaced vertically, it tends to return to its original position due to the effects of buoyancy and gravity (e.g., Sutherland, 2010) [336]. The largest AGWs, characterized by horizontal wavelengths ranging from 1,000s of km to ∼10,000 km, are also influenced by the Coriolis effects from Earth's rotation. These waves, which include the solar thermal tides described in the previous section, are termed 'inertial gravity waves.'

Various sources can give rise to AGWs. Commonly studied sources include tropospheric winds flowing over topographical features such as mountains (e.g., Long 1955; Nastrom & Fritts, 1992; Farmer & Armi, 1999) [202, 243, 80], tropospheric convection and weather fronts (e.g., Hung et al., 1978; Kelley, 1997; Vincent & Alexander, 2000; Walterscheid et al., 2001) [148, 171, 358, 361], and atmospheric heating in the auroral zone during periods of heightened geomagnetic activity (e.g., Richmond & Matsushita, 1975; Hunsucker, 1982; Immel et al., 2001; Oyama & Watkins, 2012; Lu et al., 2016) [284, 151, 154, 254, 204]. AGWs can also be generated by natural hazards, such as earthquakes (e.g., Mikumo & Watada, 2009) [232], tsunamis (e.g., Hickey et al., 2009) [139], and, notably for this dissertation, volcanoes (e.g., Ripepe et al., 2010) [289].

Gravity waves produced directly by these sources, often called *primary gravity waves*, can dissipate and/or break, generating forces in the atmosphere which can generate *secondary gravity waves* (e.g., Fritts et al., 2002, 2006; Becker & Vadas, 2018) [94, 95, 22]. These can propagate farther vertically than the primary waves, transporting energy and momentum to higher altitudes (Vadas & Fritts, 2002; Vadas et al., 2003; Vadas & Liu, 2009; Sutherland, 2010) [348, 349, 350, 336]. It is interesting to note that the same sources that can give rise to gravity waves can also generate *acoustic waves* (colloquially, 'sound waves'), which have much higher frequencies than gravity waves, but can also be important for energy transport in the upper atmosphere (e.g., Hickey et al., 2001; Walterscheid et al., 2003; Liu, 2016) [138, 360, 194].

In the case of the 2022 Tonga volcanic eruption, the subject of Chapter 3, the vertical updraft of air[4] following the eruption launched concentric rings of primary gravity waves, which

[4]Vadas et al. (2023) [352] were able to track these updrafts using cloud top brightness temperatures measured using NOAA's Geostationary Operational Environmental Satellite. The volcanic plumes appear

likely traveled horizontally up to ∼600 km from the volcano before breaking and/or dissipating (Vadas et al., 2023) [352]. Where the primaries dissipated and create local forces in the atmosphere, secondary gravity waves arose which propagated thousands of km, affecting the I-T system on a global scale (Vadas et al., 2023) [352].

Traveling Ionospheric Disturbances

When thermospheric waves, such as gravity waves, perturb the neutral density and winds, they can also modulate the ionospheric plasma density, resulting in traveling ionospheric disturbances (TIDs) (e.g., Hocke & Schlegel, 1996) [141]. Generally, neutral winds can move plasma either parallel to the local magnetic field (via collisional drag) or perpendicular to it (via dynamo electric fields and currents) (e.g., Heelis & Maute, 2020) [133]. Further exploration of these coupling mechanisms is detailed in Section 2.3. Electron density variations associated with TIDs are most frequently visualized using data collected by satellites and receivers in the Global Navigation Satellite System (GNSS), which measure the total electron content (TEC) along their line of sight (e.g., Rideout & Coster, 2006) [287].

TIDs are broadly divided into two categories based on their wave properties. Large-scale TIDs (LSTIDs), primarily associated with auroral heating processes during geomagnetic storms, exhibit wavelengths of approximately 1,000 - 3,000 km, horizontal velocities of 300 - 1,000 m/s, and periods ranging from one to several hours (e.g., Jonah et al., 2018; Lyons et al., 2019) [163, 209]. Medium-scale TIDs (MSTIDs), primarily generated by sources in the lower atmosphere such as tropospheric weather fronts, have horizontal wavelengths of several hundred kilometers, horizontal velocities between approximately 100 and 300 m/s, and periods ranging from about 15 minutes to one hour (e.g., Tsugawa et al., 2007) [343].

Several of the I-T energy inputs explored in this dissertation are known to generate TIDs. Prior to the Tonga eruption studied in Chapter 3, TIDs from volcanic eruptions have been identified and investigated as a means of determining the volcanic energy input into the ionosphere (e.g., Heki, 2006; Dautermann et al., 2009; Nakashima et al., 2016; Shults et al., 2016; Liu et al., 2017) [137, 57, 242, 315, 201]. Additionally, a considerable number of studies have since delved into the TIDs generated by the Tonga eruption, finding a broad spectrum of waves, some of which circled the globe multiple times (e.g., Aa et al., 2022; Amores et al., 2022; Hong et al., 2022; Kataoka etal., 2022; Kulichkov et al., 2022; Lin et al., 2022; Otsuka, 2022; Wright et al., 2022; Zhang et al., 2022) [2, 7, 144, 169, 179, 192, 253, 371, 383]. Comparatively fewer studies have investigated the plasma/neutral coupling and near-field effects of the eruption, which will be explored in this dissertation.

The moving solar terminator, the subject of Chapter 4, has also been observed to produce TIDs (Galushko et al., 1998; Afraimovich, 2008; Song et al., 2013; Ding et al., 2014; Zhang et al., 2021) [101, 3, 325, 61, 384]. Notably, many of these studies conclude that TIDs generated by the solar terminator are most prominent near the morning terminator. However, while

up to 50°K colder than the surrounding air in these images. For an interesting discussion about how volcanic plumes, which are very dense and hot upon being expelled from the volcano, become cooler than the surrounding atmosphere upon reaching their peaks, see Woods and Self (1992) [370].

investigating the thermospheric response to the solar terminator, we find a clear evening signature but no corresponding signature in the morning, consistent with Forbes et al. (2008) [89] and Liu et al. (2009) [199]. A possible explanation for this discrepancy will be discussed further in Section 4.4.

Ionospheric Plasma Wave Modes

In the absence of neutral atmospheric driving, plasma in near-Earth space can sustain a variety of wave modes. This section describes the plasma and electromagnetic oscillations relevant to this dissertation.

In a plasma, the most fundamental oscillations are known as *Langmuir waves* or simply *plasma oscillations*. These are rapid plasma density oscillations brought about when the electron gas is slightly displaced from the ion gas, and subsequently feels a Coulomb restoring force, resulting in oscillations at the *plasma frequency*. Ignoring corrections due to the thermal motion of the electrons, this frequency is given by:

$$\omega_p = \sqrt{\frac{n_e q^2}{m_e \epsilon_0}} \tag{2.1}$$

where n_e is the electron number density, q is the electron charge, m_e is the electron mass, and ϵ_0 is the permittivity of free space. Notably, the only variable quantity that this frequency depends on in the ionosphere is the electron density. Near the ionospheric F2 peak, this frequency is typically several MHz. Thus, these oscillations occur on timescales much faster than any that will be considered in this dissertation.

The Earth's ionosphere is threaded by the planet's magnetic field, which resembles a dipole in near-Earth space with its dipole axis tilted $\sim 11^\circ$ relative to Earth's rotation axis.[5] As a result, charged particles moving with a velocity component perpendicular to Earth's magnetic field experience a Lorentz force, causing them to spiral around the magnetic field line. This gyration occurs at the particles' *gyrofrequency*, which is given by:

$$\omega_g = \frac{qB}{m} \tag{2.2}$$

where B is the magnitude of the magnetic field, and m is the mass of the charge. In the absence of other forces, this *gyromotion* constrains charged particles' guiding centers to move along magnetic field lines. This limitation on plasma transport is important when considering the plasma conductivity, which will be explored more in Section 2.3 below and will play a crucial role in the analysis of the ionospheric response to the Tonga volcanic eruption presented in Chapter 3.

[5] While the dipole term of the Earth's magnetic field dominates in near-Earth space, other multipole components also exist and complicate Earth's magnetic topology. Additionally, farther away from Earth, the magnetic field is compressed on the dayside due to solar wind pressure and is stretched on the nightside, forming the *magnetotail*.

Furthermore, whether a charged particle is considered 'magnetized' depends on the ratio of the gyrofrequency to the collision frequency between charged and neutral particles. If the collision frequency is much larger than the gyrofrequency, collisions dominate the particles' motion and the particles are considered unmagnetized. This concept is important for understanding the kinetic modeling performed to study the picket fence optical phenomenon presented in Chapter 5. Typical ion and electron gyrofrequencies as well as collision frequencies with neutrals in the ionospheric E Region are shown in Figure 2.3(b), which is discussed more in Section 2.3.

The final plasma wave mode relevant to this dissertation are *Alfvén waves*. In this transverse hydrodynamic wave mode, magnetic fields and charged particles oscillate perpendicular to the direction of the unperturbed magnetic field in response to an effective magnetic tension force. The disturbance travels along the magnetic field lines at the Alfvén speed, given by:

$$v_A = \frac{B}{\sqrt{\mu_0 \rho}} \tag{2.3}$$

where μ_0 is the permeability of the vacuum and ρ is the mass density of the surrounding plasma (Alfvén, 1942) [6]. In the ionosphere, this speed is on the order of a few times 10^6 m/s, allowing the rapid transmission of electromagnetic energy along magnetic field lines. The consequences of this in regards to the ionospheric response to the Tonga volcanic eruption are explored more fully in Chapter 3.

For a much more complete description of these and other ionospheric wave modes, an excellent review and mathematical development of wave propagation in the ionosphere is given by Rawer (1993) [278]. A more general plasma physics approach, which still includes descriptions and derivations of all modes described in this section, can be found in Chen (2016) [45], which is not specific to ionospheric physics. In the following section, we will describe the coupling mechanisms between plasma and neutral gas and how it affects ionospheric dynamics.

2.3 Plasma-Neutral Coupling: An Exploration of the Ion Continuity Equation

Earth's thermosphere and ionosphere coexist in the same region of space, and their dynamics are intricately interconnected (e.g., Prölss, 2004) [273]. Density variations in both the thermospheric neutral gas and ionospheric plasma are strongly influenced by each other through physical processes including ionization, recombination, and collisions. In this section, we explore some of the main mechanisms of plasma-neutral coupling, focusing on the role of the neutral gas in driving changes in the plasma density. These fundamental concepts will serve as the basis for much of the research presented in this dissertation.

The Ion Continuity Equation

The plasma density n in a local region[6] of the ionosphere can change over time only if: (1) plasma is produced via ionization of the local neutral gas; (2) plasma is destroyed when ions and electrons recombine to form neutral particles; (3) plasma is transported parallel to the background magnetic field; or (4) plasma is transported perpendicular to the background magnetic field. This idea is expressed by the *ion continuity equation*:

$$\frac{\partial n}{\partial t} = Q - \beta n - \nabla \cdot (n\vec{v}) \tag{2.4}$$

where Q is the ion production rate, β is the loss coefficient, and $\vec{v}$ is the ion velocity. The final term is the ion transport term, which governs motion both parallel and perpendicular to the magnetic field.

Each of the terms Equation 2.4 can be driven by multiple underlying mechanisms. For instance, plasma production may occur through *photoionization*, in which a photon frees an electron from a neutral particle, or *impact ionization*, in which ionization results from collisions between a charged particle and a neutral particle. In the following subsections, we describe each of these processes and their underlying mechanisms within the ionosphere in more detail.

Plasma Production and Loss Chemistry

As described in Section 2.1, the ionosphere's existence and fundamental vertical structure depend largely on the balance between plasma production and recombination with respect to altitude. This section provides an overview of some of the main principles of ionospheric chemistry. A more comprehensive review can be found in, e.g., Torr and Torr (1979) [342].

With the notable exception of the high-latitude ionosphere, most ionospheric plasma is produced through the photoionization of thermospheric neutral gas by solar photons. To be photoionized, a neutral atom or molecule must interact with an incoming photon possessing energy greater than or equal to the neutral's ionization energy. For the most abundant thermospheric species, these photoionization reactions are:

$$\mathrm{N_2} + h\nu\,(\epsilon > 15.58\ \mathrm{eV}, \lambda < 79.6\ \mathrm{nm}) \rightarrow \mathrm{N_2^+} + \mathrm{e^-} \tag{2.5}$$

$$\mathrm{O_2} + h\nu\,(\epsilon > 12.08\ \mathrm{eV}, \lambda < 102.6\ \mathrm{nm}) \rightarrow \mathrm{O_2^+} + \mathrm{e^-} \tag{2.6}$$

$$\mathrm{O} + h\nu\,(\epsilon > 13.61\ \mathrm{eV}, \lambda < 91.1\ \mathrm{nm}) \rightarrow \mathrm{O^+} + \mathrm{e^-} \tag{2.7}$$

where h denotes Planck's constant, and ϵ, ν, and λ represent the photon's energy, frequency, and wavelength, respectively (Rees, 1989) [280]. At high latitudes, where energetic charged particles can stream down Earth's magnetic field, neutrals may undergo impact ionization

[6]Here, 'local' indicates a region large enough to contain many particles ($n^{1/3} \ll L$, where L is a length characterizing the size of the region), but still small enough that the density does not change significantly across the region and therefore represents a meaningful average.

when they are ionized after being struck by a particle with energy greater than or equal to their ionization energy.

If the photon or charged particle which ionizes a neutral atom or molecule possesses exactly the ionization energy of the neutral, the resulting ion will be produced in its ground (least energetic) state. However, if the photon or charge carries excess energy, the resulting ion may emerge in an excited electronic state. For example, the blue light used as a critical marker to distinguish picket fence emissions from auroral emissions in Chapter 5 is emitted when N_2^+ ($B^2\Sigma_u^+$), an excited electronic state of N_2^+, relaxes to its ground state. Although the ionization energy of N_2 is 15.58 eV (Equation 2.5), an electron colliding with a N_2 molecule requires a minimum of 18.75 eV to both ionize it and excite it to the N_2^+ ($B^2\Sigma_u^+$) state.

Once formed, ions may undergo charge exchange or ion-atom interchange reactions with other ambient neutral species, changing the ion composition,[7] but not the plasma number density. Common such reactions in the F Region include (Donahue, 1968; Pfaff, 2012) [62, 264]:

$$\begin{aligned} O^+ + N_2 &\rightarrow NO^+ + N \\ O^+ + O_2 &\rightarrow O_2^+ + O \end{aligned} \tag{2.8}$$

Plasma, once generated, suffers loss through recombination, which proceeds more rapidly for molecular ions than for atomic ions. For instance, a molecular O_2^+ ion in the ionospheric F region will recombine within seconds, whereas an atomic O^+ ion can persist for hours (e.g., Schunk & Walker, 1973) [305]. F region O^+ is commonly lost by first undergoing one of the reactions in Equation 2.8 and subsequently undergoing dissociative recombination through the reactions:

$$\begin{aligned} O_2^+ + e^- &\rightarrow O + O \\ NO^+ + e^- &\rightarrow N + O \end{aligned} \tag{2.9}$$

Equations 2.9 do not fully represent the physical process, as dissociative recombination reactions follow a two-step process, where the ion initially captures the electron, forming a neutral in an excited state which subsequently dissociates into its constituents (Sheehan & St. Maurice, 2004) [309]. Often, one or both of the neutral products on the right hand side of Equations 2.9 are produced in an excited state (Pavlov, 2014; Grubbs et al., 2018) [260, 116].

The ionospheric plasma density can undergo significant changes due to variations in the balance between production and recombination rates. Altering either rate can result in rapid density variations. For instance, in the low-latitude E region, rapid recombination occurs at night following sunset when the source of photoionization disappears. Combined with swift

[7]Note that this process technically alters the neutral composition as well; however, given that the plasma density is several orders of magnitude lower than the neutral density at ionospheric altitudes, the effect is significantly greater on the ion composition.

molecular ion recombination rates, this causes the E region plasma density to decrease by over an order of magnitude within a few minutes of sunset. At higher altitudes, the slower recombination rates of O^+ allow plasma to persist throughout the night even without a source of ionization. In the auroral region, where impact ionization from precipitating particles provides an additional plasma source, the E region can often be sustained throughout the night.

The ionospheric density can also be altered by changing the thermospheric composition. For instance, when rockets traverse the ionosphere, their exhaust plumes introduce substantial amounts of water vapor, leading to observed ionospheric depletions (e.g., Booker, 1961; Ozeki & Heki, 2010) [35, 255]. These depletions likely result from charge exchange between H_2O and ambient ions, followed by rapid recombination of the resulting H_2O^+ ions (e.g., Bernhardt et al., 2001) [29].

Transportation Perpendicular to the Magnetic Field

In the absence of external forces but in the presence of a background magnetic field $\vec{B}$, individual charged particles can move freely along the magnetic field while gyrating around it at their gyrofrequency (defined in Equation 2.2). Under these conditions, there is no net transport of plasma perpendicular to the magnetic field. When influenced by a force perpendicular to the magnetic field, a gyrating charge gains energy on half of its orbit (increasing the gyration radius) and loses it on the other half (reducing the radius). This process results in a net motion (drift) of the charge's guiding center, located at the center of its gyration, perpendicular to both the force and the background magnetic field (e.g., Chen, 2016) [45]. This drift $\vec{v}_d$ for a particle with charge q subjected to an arbitrary force $\vec{F}$ is given by:

$$\vec{v}_d = \frac{1}{q}\frac{\vec{F} \times \vec{B}}{B^2} \tag{2.10}$$

For example, consider the force enacted on a charged particle by an electric field, $\vec{F}_E = q\vec{E}$, where $\vec{E}$ is the electric field. In this case, the particle's guiding center will drift at velocity $\vec{v}_E$, given by:

$$\vec{v}_E = \frac{\vec{E} \times \vec{B}}{B^2} \tag{2.11}$$

This is commonly referred to as the "$\vec{E} \times \vec{B}$ drift." It's important to note that this drift is independent of the charged particle's charge or mass, meaning ions and electrons will drift together under the influence of the electric field. Consequently, electric fields in the ionosphere can lead to large-scale plasma redistribution across magnetic field lines (as observed in the fountain effect in the equatorial ionosphere, described in Section 2.4 below), but they do not induce the flow of currents.

Other forces, such as those due to gravity or pressure gradients, result in currents flowing perpendicular to the magnetic field. The gravitational force, $\vec{F}_G = m\vec{g}$, induces a drift $\vec{v}_G$ given by:

$$\vec{v}_G = \frac{m}{q}\frac{\vec{g} \times \vec{B}}{B^2} \tag{2.12}$$

The diamagnetic drift $\vec{v}_D$ due to a plasma pressure gradient ∇P is given by:

$$\vec{v}_D = -\frac{1}{nq}\frac{\nabla P \times \vec{B}}{B^2} \tag{2.13}$$

Usually, the gravitational and diamagnetic drifts are negligibly small compared to the $\vec{E} \times \vec{B}$ drift and are mainly relevant in low-latitude regions of the ionosphere where gravity and altitudinal plasma density gradients are largely perpendicular to the magnetic field (e.g., Schunk & Nagy, 2009) [303]. Other drifts may arise from curvature or other non-uniformities in the background magnetic field, but they tend not to be significant in the ionosphere.

In the absence of collisions, these drifts cause plasma redistribution or currents perpendicular to both the force and the background magnetic field. However, collisions are significant throughout the E region and lower F region of the ionosphere, and so must be considered. To understand how these collisions play a role, we next explore the concept of ionospheric conductivity.

Ionospheric Conductivity

In order to understand how electric fields and currents are established within the ionosphere (essential in particular for the work presented in Chapter 3), it is first important to understand the concept of *conductivity*. Generally, the conductivity (σ) of a medium relates to the ease with which charges can move through that medium [115]. In a perfect conductor, the conductivity is infinite ($\sigma = \infty$), meaning that the charges move freely with no resistance. Some metals, as well as collisionless plasmas without strong background magnetic fields, can be approximated as perfect conductors. In a perfect insulator, charges cannot move at all, so the conductivity is zero ($\sigma = 0$). Mathematically, the conductivity is defined as the proportionality relating an applied electric field $\vec{E}$ to the resulting current density $\vec{j}$:

$$\vec{j} = \overleftrightarrow{\sigma} \cdot \vec{E} \tag{2.14}$$

where the double arrow over $\overleftrightarrow{\sigma}$ signifies that it is a tensor quantity, which allows the conductivity to be directionally-dependent. This is important in environments with non-negligible background magnetic fields, including Earth's ionosphere, since charges can move much more easily along the magnetic field than across it, creating an anisotropy in the conductivity. If the background magnetic field is taken to lie along the $\hat{z}$-axis, the ionospheric conductivity tensor takes the form:

$$\overleftrightarrow{\sigma} = \begin{pmatrix} \sigma_P & -\sigma_H & 0 \\ \sigma_H & \sigma_P & 0 \\ 0 & 0 & \sigma_\parallel \end{pmatrix} \tag{2.15}$$

Here, the *parallel conductivity*, $\sigma_\parallel$, affects magnetic field-aligned currents. The *Pedersen conductivity*, σ_P, affects currents in the direction of the component of the electric field which is perpendicular to the magnetic field ($\vec{E}_\perp$). The *Hall conductivity*, σ_H, affects currents perpendicular to both the electric and magnetic field.

In Appendix A.1, we derive expressions for each of these conductivities in a simplified ionospheric plasma, accounting for only a single ion species. These can be expressed as:

$$\begin{aligned} \sigma_P &= \left(\frac{\nu_{en}}{\nu_{en}^2 + \omega_{ce}^2} + \frac{m_e}{m_i} \frac{\nu_{in}}{\nu_{in}^2 + \omega_{ci}^2} \right) \frac{ne^2}{m_e} \\ \sigma_H &= \left(\frac{\omega_{ce}}{\nu_{en}^2 + \omega_{ce}^2} - \frac{m_e}{m_i} \frac{\omega_{ci}}{\nu_{in}^2 + \omega_{ci}^2} \right) \frac{ne^2}{m_e} \\ \sigma_\parallel &= \left(\frac{1}{\nu_{en}} + \frac{m_e}{m_i} \frac{1}{\nu_{in}} \right) \frac{ne^2}{m_e} \end{aligned} \tag{2.16}$$

where ν_{in} and ν_{en} denote the ion-neutral and electron-neutral collision frequencies[8], respectively, ω_{ci} and ω_{ce} denote the ion and electron cyclotron frequencies, m_i and m_e are the ion and electron masses, n is the plasma density, and e is the elementary charge. For the true ionosphere, it would be necessary to sum over multiple ion species.

From these expressions, it is clear that the conductivity depends strongly on the plasma density, as well as on the neutral density through its influence on the plasma-neutral collision frequencies. Typical values of the conductivity in the mid-latitude ionosphere are displayed in Figure 2.3(a), calculated using the ionospheric and neutral profiles from Figure 2.1, with collision frequencies calculated using the empirical formulas presented in the TIEGCM V1.94 Model Description, page 125.[9] At all ionospheric altitudes, the parallel conductivity is much greater than the Pedersen and Hall conductivities.

The large ionospheric parallel conductivity allows charges to quickly respond to magnetic field-aligned forces by flowing along the magnetic field. This high charge mobility has important consequences for ionospheric electric fields. For example, consider a potential difference between two points along the same magnetic field line. Charges, influenced by the parallel electric field, quickly redistribute along the magnetic field, effectively neutralizing the potential difference. As a result, ionospheric magnetic fields lines are often treated as

[8]These collision frequencies depend on the neutral and plasma densities, masses, and temperatures (e.g., Banks and Kockarts 1973) [16].

[9]The Thermosphere Ionosphere Electrodynamic General Circulation Model (TIEGCM) is an upper atmosphere model developed by the High Altitude Observatory at the National Center for Atmospheric Research. This manual is available from `https://www.hao.ucar.edu/modeling/tgcm/doc/description/model_description.pdf`

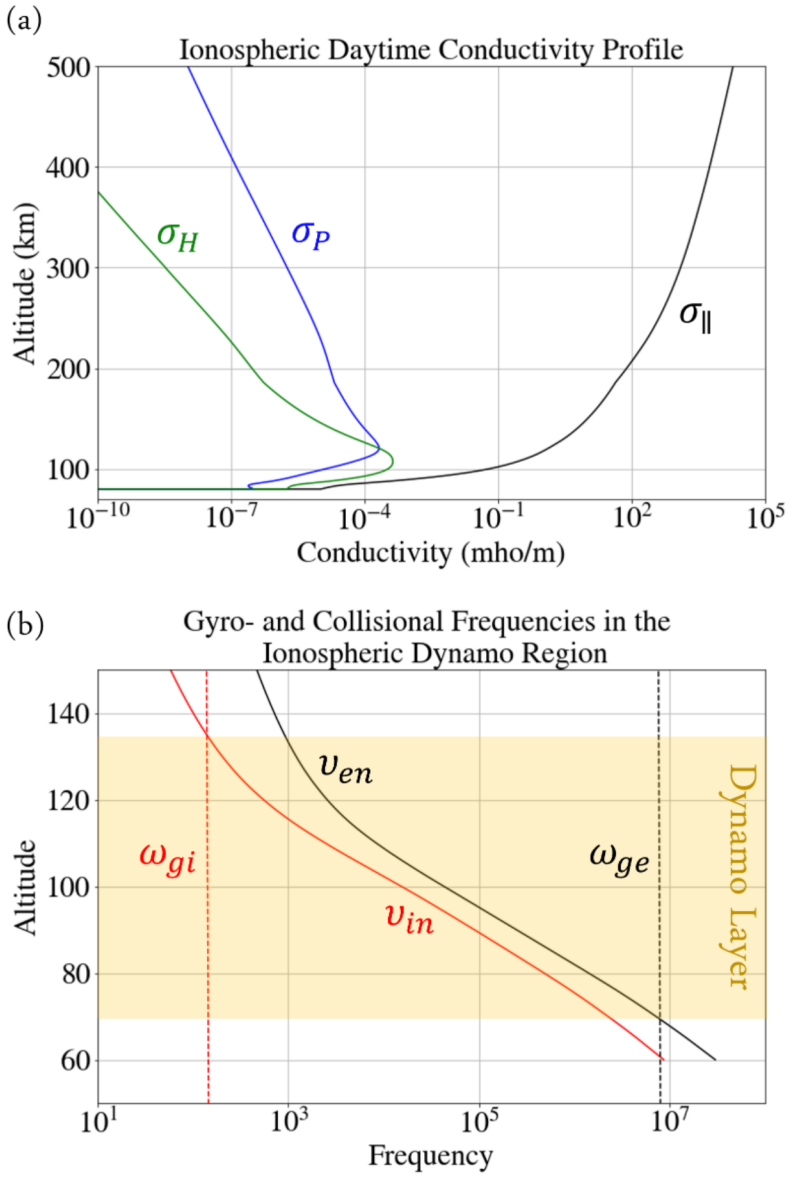

Figure 2.3: (a) Typical values of the Pedersen (σ_P), Hall (σ_H) and parallel ($\sigma_\parallel$) conductivity in the mid-latitude daytime ionosphere. (b) Representative mid-latitude profiles of ionospheric gyrofrequencies and plasma-neutral collisional frequencies, inspired by Figure 4.10 of Baumjohann and Treumann (2012) [18].

equipotentials, meaning that parallel electric fields cannot be sustained and perpendicular electric fields remain constant, mapping to all points along a given field line. This picture changes in the lower E Region, where rising collision rates and falling plasma densities cause the parallel conductivity to fall off rapidly with altitude. We will explore the consequences of a sustained parallel electric field in this region in more detail in Chapter 5.

In reality, the perpendicular electric field cannot be instantaneously transmitted to all points along a magnetic field line. If a perpendicular electric field arises at one end of the field line (potentially through the dynamo mechanisms described below), the electroquasistatic picture of the ionosphere suggests that that information is conveyed along the field line via Alfvén waves (e.g., Kelley, 2009) [172]. Moving at the Alfvén velocity $v_A = B/\sqrt{\mu_0 \rho}$, this transmission time is relatively rapid. For example, in the case of the Tonga volcanic eruption which we consider in Chapter 3, electric fields generated near the eruption site would only take a few seconds to propagate to the conjugate hemisphere travelling at the Alfvén velocity in the ionosphere,[10] which is much shorter than the timescales of interest in this dissertation.

Next, consider the plasma motion perpendicular to the magnetic field. When the electron and ion gyrofrequencies are much greater than the ion-neutral and electron-neutral collision frequencies, as occurs in the topside of the ionosphere, electrons and ions will both experience $\vec{E} \times \vec{B}$ drift, so there will be no net current. However, between about 100 and 150 km, in the region known as the 'dynamo layer,' ions and electrons collide more frequently with neutrals, leading to different dynamics.

The electron and ion gyrofrequencies as well as the electron-neutral and ion-neutral collision frequencies in the dynamo layer are depicted in Figure 2.3(b) (inspired by Figure 4.10 of Baunjohann and Treumann (2012) [18]), calculated using the ionospheric and thermospheric profiles in Figure 2.1. The gyrofrequencies appear nearly vertical in the figure as they do not vary much with altitude in this region. Below the dynamo layer, the collision frequencies are greater than the gyrofrequencies for both species, meaning that charges cannot complete one gyration around the magnetic field before colliding with a neutral particle. As a result, the plasma largely moves with the neutral bulk flow below this altitude, regardless of the direction of the magnetic field. At the base of the dynamo layer, the electron gyrofrequency is greater than the electron-neutral collision frequency but the ion gyrofrequency is less than the ion-neutral collision frequency, meaning that electrons are able to $\vec{E} \times \vec{B}$ drift relatively unimpeded but ions move with the neutrals. This differential electron/ion motion results in a Hall current perpendicular to the electric and magnetic fields. Higher in the dynamo layer, where the ion-neutral collision frequency becomes comparable to the ion gyrofrequency, ions will move in the direction of the electric field and therefore carry a Pedersen current, while electrons still carry a Hall current.

[10] While the conventional understanding suggests that Alfvén waves will reflect and bounce back and forth along the magnetic field lines until, after several bounce periods, an equilibrium is reached where the electrostatic approximation is valid (Kelley, 2009) [172], recent research questions whether such equilibrium is achievable in reality (Cosgrove, 2016) [51]. This remains an open area of investigation, not delved into further here. The history of successful application of electroquasistatics in previous ionospheric research provides a foundation for its use in this analysis.

Just as collisions can result in Pedersen currents parallel to the perpendicular component of the electric field and not just in the $\vec{E} \times \vec{B}$ direction, they can result in plasma transport in the direction of any component of a force applied perpendicular to the magnetic field. For example, the gravitational force acting on an ion in a collisional environment results in ion velocity w_{iG} given by:

$$\vec{w}_{iG} = \frac{\nu_{in}}{\nu_{in}^2 + \omega_{ci}^2} \vec{g}_\perp \tag{2.17}$$

where $\vec{g}_\perp$ denotes the component of the gravitational acceleration that is perpendicular to the magnetic field (e.g., Schunk & Nagy, 2009) [303]. The similarity between this expression and the form of the Pedersen conductivity is not coincidental.

Plasma pressure gradients, in a collisional environment, result in transport antiparallel to the direction of the gradient. For an ion, the resulting transport velocity $\vec{w}_{iD}$ can be expressed as:

$$\vec{w}_{iD} = -\frac{1}{nm_i} \frac{\nu_{in}}{\nu_{in}^2 + \omega_{ci}^2} \nabla_\perp P \tag{2.18}$$

where $\nabla_\perp$ denotes the component of the gradient perpendicular to the magnetic field (e.g., Schunk & Nagy, 2009) [303]. Again, the similarity of this expression to the Pedersen conductivity should not come as a surprise.

To conclude our discussion of the ion continuity equation, we will discuss the motion of plasma parallel to the background magnetic field.

Transportation Parallel to the Magnetic Field

As explained in the previous section and illustrated in Figure 2.3(a), the ionospheric conductivity parallel to the magnetic field is high, enabling charged particles to move freely along the magnetic field. When ionospheric plasma experiences a force with a component parallel to the magnetic field, such as gravity, plasma pressure gradients, or collisional momentum transfer from neutral winds, plasma can slide along the field.

A simplified expression for the rate of ion motion along the magnetic field can be derived using the diffusion approximation, which assumes all plasma flows are subsonic and which neglects wave phenomena (e.g., Lei et al., 2008; Schunk & Nagy, 2009) [184, 303]. Consider the effect of gravity in a region of the ionosphere where the magnetic field is nearly vertical, aligned with the gravitational force. Here, in the absence of electric forces, the lighter electrons would tend to settle vertically above the heavier ions. However, this charge separation would quickly establish a polarization electric field, drawing the electrons and ions back together. This scenario holds true for field-aligned electron and ion motion under any field-aligned forces. The rapid establishment of polarization electric fields due to any charge separation causes the combined electron and ion fluid to diffuse as a single gas, exhibiting different motion along the field lines compared to what a single fluid with the mass of either species would do alone. This collective diffusive behavior is known as *ambipolar diffusion*.

Since ions and electrons move together, this diffusion acts to transport plasma but not to induce currents.[11]

Following the development in Chapter 5 of Schunk & Nagy (2009) [303], a simplified expression for the ambipolar diffusion, neglecting terms on the order of the electron mass as well as heat flow, the effects of minor ion species, Coriolis effects, and stresses within the fluid is:

$$\vec{u_{i\parallel}} = \vec{u_{n\parallel}} - D_a \left[\frac{1}{n} \nabla_\parallel n + \frac{1}{T_p} \nabla_\parallel T_p - \frac{m_i \vec{g}}{2 k_B T_p} \right] \tag{2.19}$$

where $\vec{u_{i\parallel}}$ and $\vec{u_{n\parallel}}$ are the ion and neutral velocities along the magnetic field line, $\nabla_\parallel$ is the gradient along the direction of the magnetic field line, T_p is the plasma temperature taken as the average of the ion and electron temperatures, $\vec{g}_\parallel$ is the component of the gravitational acceleration parallel to the magnetic field, k_B is the Boltzmann constant, and the ambipolar diffusion coefficient D_a is given by:

$$D_a = \frac{2 k_B T_p}{m_i \nu_{in}} \tag{2.20}$$

From the ambipolar diffusion equation, it is evident that the field-aligned ion motion is strongly influenced by the field-aligned component of the neutral wind, but is modified by the effects of other forces regulated by ambipolar diffusion. The dominant ion species, whose density is comparable to that of the electrons, tend to drag minor ion species along with them.

The different terms of the ion continuity equation are not as independent as the presentation in this section might have suggested. For instance, the field-aligned plasma pressure gradient, which arises due to variations in plasma density along the field line, can be influenced by plasma motion perpendicular to the magnetic field. Such motion shifts plasma to different field lines, consequently affecting the pressure gradient along a given field line. Additionally, changes in production and loss rates as well as collisional momentum exchange with neutrals, can further impact the plasma pressure gradient. Furthermore, neutral winds, which typically flow from the summer to winter hemisphere, cause field-aligned plasma drift, elevating plasma to higher altitudes in the summer hemisphere and and lower altitudes in the winter winter hemisphere (Zhang, 2021; Heelis et al., 2022) [382, 136]. By moving plasma to different altitudes, at which there are different recombination rates, field-aligned plasma motions can affect plasma loss rates.

[11] If the ionospheric parallel conductivity were truly infinite, there would be no field-aligned currents. In reality, however, the conductivity is finite, so small potential differences can arise along field lines, which can then lead to field-aligned currents between hemispheres (Yamazaki & Maute, 2017) [376].

2.4 Ionospheric Phenomena Across Different Latitudinal Regions: The Equatorial, Subauroral, and Auroral Ionospheres

The plasma/neutral interactions highlighted in the previous section occur throughout Earth's ionosphere. The ionospheric response varies with latitude, primarily influenced by the consequences of Earth's changing magnetic field orientation. In this section we will describe Earth's magnetic field and how it affects the ionosphere in three sectors – equatorial, subauroral, and auroral.[12] Additionally, we will describe key phenomena occurring in each sector, laying the groundwork for the subsequent chapters of this dissertation.

The near-Earth space environment is shielded from the solar wind by a magnetic cavity maintained by Earth's intrinsic magnetic field, illustrated in Figure 2.4. This magnetic field is primarily generated by the motion of fluids deep within Earth's interior (e.g., Lanza & Meloni, 2006) [182].[13] Close to Earth's surface and throughout the I-T region, the magnetic field is predominantly dipolar. However, at greater distances from the planet, the magnetic field is compressed on its sunward side and stretched deep into the nightside, influenced by the solar wind (e.g., Thébault et al., 2015) [337].

Earth's magnetic field's dipole axis is tilted approximately 11° relative to Earth's rotational axis. Magnetic latitude is defined in reference to the magnetic poles rather than the geographic poles, making it distinct from geographic latitude. In the equatorial region, at low magnetic latitudes, ionospheric magnetic field lines are nearly horizontal. Conversely, in the auroral region at high latitudes, ionospheric magnetic field lines are nearly vertical, extending deeply into Earth's magnetosphere or even connecting to the solar wind. The subauroral region denotes the transition between these two field line orientations. The following subsections delve into the implications of these varying magnetic field orientations. The phenomena in the equatorial ionosphere will be relevant to the later exploration of the ionospheric consequences of the Tonga volcanic eruption and solar terminator waves, discussed in Chapters 3 and 4. The discussions of the auroral and subauroral regions provide important background for understanding the investigation of the picket fence optical phenomenon in Chapter 5.

The Equatorial Ionosphere

At Earth's *magnetic equator*, the roughly dipolar magnetic field lines reach their apex and consequently extend parallel to Earth's surface. The *equatorial region* of Earth's ionosphere,

[12]The midlatitude ionosphere, stretching from about 20° to 60° magnetic latitude, comprises magnetic flux tubes that reach their apex in the plasmasphere, defined further in the next section. This region of the ionosphere is not discussed further in this dissertation.

[13]Smaller contributions to Earth's magnetic field come from magnetized surface rocks, ionospheric electrical currents (including those described later in this section), magnetospheric electrical currents, and subsurface electrical currents near Earth's surface (e.g., Lanza & Meloni, 2006) [182].

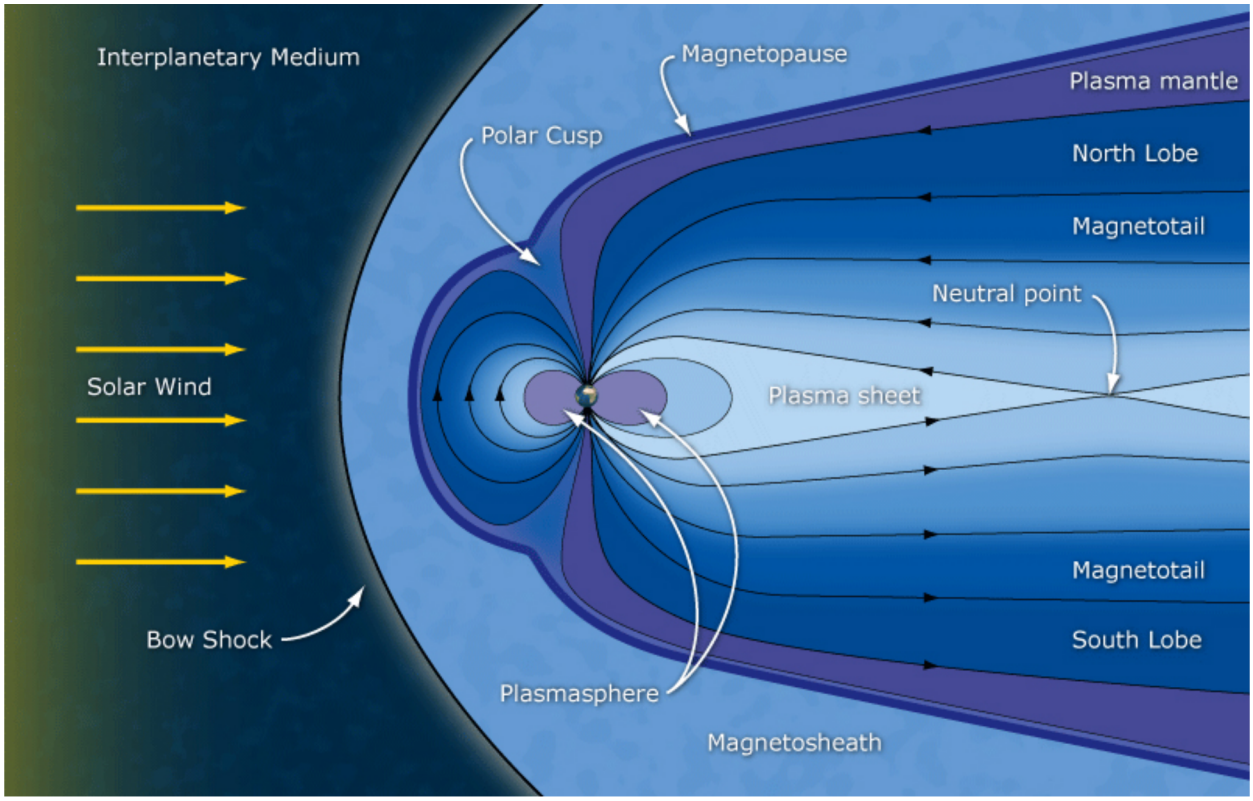

Figure 2.4: Diagram of Earth's magnetic field and magnetosphere. Close to Earth, the magnetic field is approximately dipolar, and the ionosphere can be divided into equatorial, subauroral, and auroral regions, distinguished by the varying orientation of the magnetic field with latitude. Credit: ESA (original picture courtesy C. Russel).

within approximately ±20° of the magnetic equator,[14] is characterized by a predominantly horizontal magnetic field, limiting vertical plasma transport in the absence of external forces. Moreover, the magnetic field lines in this area are closed, with both footpoints on the Earth, and peak in the ionosphere, so the equatorial ionosphere is not magnetically connected to the magnetosphere. This isolation shields it from direct magnetospheric and solar wind inputs.

At higher altitudes in the equatorial region, above the ionosphere, the *plasmasphere* is a torus of plasma extending from ∼1,000 km to four Earth radii (shown in Figure 2.4) (e.g., Carpenter & Park, 1973) [39]. It is often considered an extension of the low-latitude ionosphere (Pfaff, 2012) [264]. Similarly to the equatorial ionosphere, the plasmasphere is

[14]Magnetic field lines with their footpoints at ±20° magnetic latitude reach an apex of roughly 1,000 km at the magnetic equator. This altitude approximately represents the upper boundary of the F Region of the ionosphere. Thus, the magnetic flux tubes within ±20° magnetic latitude all reach their apex at or below ionospheric altitudes.

threaded by closed magnetic field lines which rotate with the Earth. It is primarily composed of light ions (H^+ and He^+) which flow up magnetic field lines after being generated by charge exchange with O^+ in the ionospheric F region. The plasmasphere plays a role in maintaining the ionospheric F region at night, when plasma moves back down the magnetic field to lower altitudes (e.g., Kelley, 2009) [172]. Compared to the magnetosphere beyond, it is relatively cold (∼10,000 K) and dense ($\sim 10^3/\text{cm}^3$), although it is warmer and less dense than the ionosphere (for reference, ionospheric density and temperature profiles are depicted in Figure 2.1).

Under geomagnetically quiet conditions, the equatorial ionosphere's electrodynamics and currents are primarily established by tidal neutral winds (see Section 2.2) (Forbes & Lindzen, 1976) [88]. As described in Section 2.3, neutral winds perpendicular to Earth's magnetic field in the high-conductivity ionospheric E Region drive ionospheric currents. On timescales longer than a few minutes, these currents must be divergence-free ($\nabla \cdot \vec{j} = 0$) to maintain electrical quasi-neutrality. As a result, internal polarization electric fields arise to moderate the currents, establishing a global current system known as the *Sq current*, where Sq stands for "solar quiet" (Yamazaki & Maute, 2016) [376]. The Sq current system manifests as two circulating current cells in the dayside E Region equatorial ionosphere, running counter-clockwise in the northern hemisphere and clockwise in the southern hemisphere as viewed from above (Yamazaki & Maute, 2016) [376]. Where the two cells meet along the magnetic equator, the *equatorial electrojet* (EEJ), the strongest equatorial current, flows eastward in a region of enhanced conductivity known as the Cowling channel (Lühr et al., 2004; Yamazaki & Maute, 2016) [206, 376]. The eastward electric field associated with the EEJ combined with the northward orientation of Earth's magnetic field near the magnetic equator induces an upward $\vec{E} \times \vec{B}$ plasma drift during the day, lofting ionospheric plasma to higher altitudes. Subsequently, the plasma descends poleward along the magnetic field due to gravity and plasma pressure gradients (e.g., Balan & Bailey, 1995) [14]. Termed the *fountain effect*, this process creates two plasma density crests near ±15° magnetic latitude and a density trough near the magnetic equator, collectively forming the *equatorial ionization anomaly* (EIA) (e.g., Appleton, 1946; Balan et al., 2018) [9, 15]. The location and intensity of the EIA crests depends strongly on the equatorial zonal electric field and meridional winds.

During the night, the E Region plasma density rapidly decreases due to the high recombination rates, reducing the E Region conductivity and inhibiting the currents that circulate freely there during the day (e.g., Heelis, 2004; Pfaff, 2012) [132, 264]. Since recombination rates are lower at higher altitudes, the F Region persists throughout the night, maintaining sufficient Pedersen conductivity to allow conductive current flow. Consequently, current continuity in the equatorial ionosphere is maintained at night by electrical currents in the F Region (Maute & Richmond, 2017) [220]. These currents, primarily driven by F Region neutral winds, dominate nighttime equatorial ionospheric electrodynamics, an effect termed the "F Region dynamo" (e.g., Rishbeth, 1981; Rishbeth, 1997) [292, 293]. One consequence of the difference in conductivity between the E and F Regions near sunset is an enhanced eastward electric field (and therefore vertical plasma drift) in the early evening F Region, known as the *pre-reversal enhancement* (PRE) (e.g., Rishbeth, 1971; Eccles, 1998; Scherliess

& Fejer, 1999; Eccles et al., 2015) [291, 68, 302, 69].

The evening uplift of the equatorial ionosphere, coupled with steep vertical plasma density gradients due to E Region recombination, can lead to the formation of large-scale nighttime plasma instabilities known as *equatorial plasma bubbles* (EPBs)[15] (e.g., McClure et al., 1977; Balan et al., 2018) [222, 15]. EPBs manifest as field-aligned shells of depleted plasma, one to three orders of magnitude less dense than the ambient plasma, rising through the F Region and forming depleted flux tubes measuring up to several hundred kilometers across (east-west) and thousands of kilometers in length (north-south) (e.g., Kil, 2015) [175]. Generally attributed to a Rayleigh-Taylor-like instability where a heavy plasma layer overlies a lighter one, the triggering mechanisms for this instability are still debated (e.g., Woodman & La Hoz, 1976) [369]. Suggested mechanisms important for EPB formation include gravity wave seeding (e.g., Huba & Liu, 2020) [147], neutral wind forcing (e.g., Kudeki et al., 2007) [178], shear instabilities (Hysell & Kudeki, 2004) [152], and even the solar terminator waves, which will be the subject of Chapter 4 (Chou et al., 2022) [47]. Following the 2022 Tonga volcanic eruption, "super plasma bubbles" were observed up to ∼40°N geographic latitude over eastern Asia, likely seeded by the atmospheric disturbances launched by the eruption (Aa et al., 2022; Huba et al., 2022; Rajesh et al., 2022) [2, 146, 277].

Since the electrodynamics and current systems in the equatorial ionosphere are highly dependent on the neutral winds, disruptions in the these winds can lead to altered circulation patterns, modifying previously described phenomena. For instance, following the Tonga volcanic eruption, once the disturbances in neutral winds reached the dayside, the EEJ in the American sector initially intensified and then reversed direction, flowing westward instead of eastward (Harding et al., 2022) [127]. Moreover, following the arrival of volcanically-disturbed winds, the crests of the EIA were observed to erode and collapse equatorward (Aa et al., 2022) [1].

Despite lacking a direct magnetic connection to the magnetosphere or solar wind, the equatorial ionosphere can undergo significant modifications during geomagnetic disturbances (e.g., Fejer, 2002) [81]. During these events, energy transferred from the magnetosphere to the high-latitude ionosphere generates large-scale gravity waves and corresponding TIDs. These disturbances propagate equatorward, leading to a modified system of thermospheric winds moving equatorward and deflected westward by the Coriolis effect, causing the "disturbance dynamo," which generates an altered pattern of ionospheric currents (e.g., Blanc & Richmond, 1980; Fejer et al., 1983; Huang, 2013) [34, 82, 145]. Prompt penetration electric fields during geomagnetic disturbances can also directly modify electric fields in the equatorial ionosphere. These fields arise when sudden changes in magnetospheric convection reduce the ability of the plasma sheet to shield the inner magnetosphere and ionosphere from high-altitude electric fields (e.g., Spiro et al., 1988; Fejer, 2002) [328, 81]. Considering these effects will be important when disentangling the impacts of the Tonga eruption and

[15]EPBs were first observed by Booker and Wells (1938) [35], who detected them as a spread in the range of radio waves scattered off of the F Region. As a result, these bubbles are often referred to as "spread-F" in the literature.

the moderate geomagnetic storm that occurred the day prior, as discussed in Chapter 3.

The Auroral Ionosphere

In the high-latitude ionosphere, the magnetic field configuration differs significantly from that at the equator, leading to distinct phenomena. Unlike the predominantly north/south horizontal magnetic field lines at the equator, high-latitude magnetic field lines are nearly vertical in the ionosphere and extend deep into the magnetosphere or connect to the interplanetary magnetic field, which is subject to solar wind forcing (e.g., Tsyganenko, 1995) [344]. Consequently, charged particles energized thousands of kilometers away from the polar ionosphere can stream along magnetic field lines, colliding with Earth's upper atmosphere and producing captivating auroral displays.

The aurora is perhaps the most striking visual manifestation of plasma physics. The *auroral oval*, which encircles both magnetic poles between approximately 60° to 75° latitude, represents the region with the highest occurrence of auroras (Vallance Jones, 1974) [353]. While this dissertation does not directly delve into auroral physics, the green streaks of the subauroral picket fence phenomenon investigated in Chapter 5 is visually similar to other auroral forms, and there remains controversy in the community over whether it is generated through similar processes (Nishimura et al., 2023) [249]. Gasque et al. (2023) [107] (presented in Chapter 5) demonstrates a mechanism to generate picket fence emissions which is distinct from the particle precipitation which generates regular auroral emissions. To better put those results in perspective, this section describes the generation and characterization of regular auroral forms.

Auroral emissions result from the precipitation of energetic charged particles into the neutral atmosphere. Through collisions, these charged particles transfer energy to the neutrals, ionizing them or exciting them to higher energy states. Once excited, particles may undergo radiative relaxation to lower energy states, emitting photons. In some instances, additional collisions may occur before photon release, leading to quenching of some emissions or transfer of energy to other neutral species, which then emit photons. The observable aurora is composed of these released photons. The wavelength (color) of the observed light is determined by the energy difference between the upper and lower states in the relaxation process. For a more detailed understanding of the chemistry involved in these processes and an extensive survey of common auroral emission features, refer to Vallance Jones (1974) [353].

While a diverse range of auroral forms have been documented (e.g., Paschmann et al., 2003) [259], they all arise from the precipitation of particles accelerated hundreds or thousands of kilometers above Earth's upper atmosphere. There are three known ways for these particles to be accelerated: (1) large potential drops parallel to the magnetic field line in the magnetospheric *auroral acceleration region*, approximately 2,000 to 20,000 km above Earth's surface (e.g., Evans, 1974; Mozer et al., 1980; Carlson et al. 1998; Paschmann et al. 2003; Pfaff, 2012) [76, 241, 38, 259, 264]; (2) dispersive Alfvén waves which resonate in the cavity between the ionosphere and the location of peak Alfvén speed at ∼6,000 km (e.g., Lotko,

1986; Chaston et al., 2004; Chaston et al., 2007) [203, 43, 44]; and (3) scattering of plasma-sheet particles by whistler-mode chorus waves tens of thousands of kilometers above Earth's surface near the magnetic equator (e.g., Johnstone, 1983; Davidson, 1990; Nishimura et al., 2010; Thorne et al., 2010) [162, 58, 247, 341].

Each of these accelerations mechanisms produce auroras with different characteristics. Parallel potential drops generate a monoenergetic precipitating electron population, with a single peak in the electron energy, and form *discrete auroral arcs,* appearing as undulating curtains of light in the polar sky (e.g., Evans, 1974; Mozer et al., 1980) [76, 241]. In contrast, dispersive Alfvén waves result in a more broad-band electron energy spectrum (e.g., Chaston et al., 2004; Chaston et al., 2007) [203, 43, 44]. Finally, particles accelerated by whistler-mode chorus waves form *diffuse aurora*, which are fainter and less structured, although they sometimes pulsate, flashing on and off with periods of several seconds (e.g., Johnstone, 1978; Johnstone, 1983; Thorne et al., 2010) [161, 162, 341]. All three types of aurora contribute meaningfully to the deposition of energy into the auroral I-T system. In a modeling study examining the incident energy flux contributed by each type of aurora, Newell et al. (2009) [245] found that diffuse aurora contribute ∼71%, monoenegetic aurora contribute ∼ 15%, and broad band aurora contribute ∼13% of the energy flux conveyed by particle precipitation under geomagnetically active conditions.

It is crucial to highlight that each of the known auroral acceleration mechanisms involves particle acceleration taking place hundreds or thousands of kilometers away from where the auroral light is actually produced.[16] In Chapter 5, we investigate a local parallel electric field mechanism for generating picket fence emissions in the subauroral region. This mechanism is distinct from these auroral acceleration mechanisms because, for the local parallel electric field mechanism, the particle energization occurs precisely where the light is observed, within the ionosphere itself. For precipitating particles to reach those altitudes requires high energies which would produce a spectrum different from that which is observed in the picket fence (see Appendix D.2 for more details). In that chapter, we also note that certain features in the aurora itself, including enhanced aurora (Hallinan et al., 1985; Hallinan et al., 1997; Karlsson et al., 2005) [121, 122, 168] and fragmented aurora-like emissions (Dreyer et al., 2021) [63] may also be produced in situ. This raises the possibility of a re-evaluation of the auroral energy budget to determine whether direct electric field heating is a significant energy source, comparable to precipitation. This mechanism is currently not included in any models of magnetosphere-ionosphere coupling.

The Subauroral Ionosphere

The *subauroral region*, located just equatorward of the auroral oval (typically near 60° magnetic latitude), marks the transition between the approximate dipole magnetic field near the equator and the stretched magnetic tail connected to the auroral ionosphere (e.g., Gallardo-

[16] Auroral emissions typically come from 80 - 400 km altitude, with most emissions concentrated between 95 and 120 km.

Lacourt et al., 2021) [97]. Under disturbed geomagnetic conditions, this region hosts extremely rapid plasma flows, as well as STEVE and the picket fence, the mysterious optical phenomena which will be the subject of Chapter 5.

The nighttime subauroral ionosphere is often collocated with the *mid-latitude trough*, a narrow region (spanning only a few degrees latitude) with decreased F Region plasma densities compared to the neighboring auroral and mid-latitude zones (e.g., Sharp, 1966; Rodger, 2008) [308, 299]. Under geomagnetically quiet conditions, the sharp density gradient on the poleward side of the trough is created by particle precipitation and plasma transport in the auroral region, while the equatorward side, which has a shallower density gradient, forms via the usual ionospheric density decay following sunset (Rodger et al., 1986) [300].

Under geomagnetically active conditions, altered ionospheric current systems can result in relatively strong (>50 mV/m) poleward electric fields and fast (>500 m/s) plasma flows in the subauroral region, increasing plasma recombination rates and causing the mid-latitude trough to narrow and intensify (Rodger, 2008) [299]. Fast ion flows known as *subauroral polarization streams (SAPS)* are typically $3-5^\circ$ degrees wide in latitude, with flow velocities exceeding 1 km/s (e.g., Foster & Burke, 2002) [92]. Within SAPS are sometimes embedded narrow and intense *subauroral ion drifts (SAIDs)*, which are typically only $1-2^\circ$ degrees wide latitudinally and exhibit ion flow velocities of several km/s (e.g., Spiro et al., 1979; Anderson et al., 1991; Mishin, 2013) [327, 8, 237].

Several optical phenomena occasionally illuminate the subauroral sky. The most well-studied of these are bands of (typically sub-visual) red light known as *stable auroral red arcs (SAR arcs)* (e.g., Roach & Roach, 1963; Kozyra et al., 1997) [296, 177]. Occurring at altitudes near 400 km, SAR arcs are generally composed of spectrally-pure 630 nm emissions, produced by the relaxation of atomic oxygen excited to the $O(^1D)$ state by collisions with energetic electrons. The electrons responsible for these emissions are thought to be energized through heat conduction from the plasmaspheric ring current (e.g., Rees and Roble 1975; Baumgardner et al., 2007) [280, 17].

In 2018, the subauroral optical phenomenon known as *STEVE (Strong Thermal Emission Velocity Enhancement)* and the associated green streaks called the *picket fence* (Figure 1.6) were introduced to the scientific community (MacDonald et al., 2018) [210]. The story of STEVE's discovery, as recounted by Gallardo-Lacourt et al. (2019) [98], highlights the substantial contributions of citizen scientists. Located between 130 km and 270 km in altitude, STEVE is a narrow (tens of km in latitude) purpleish-white arc that stretches thousands of km east-west across the subauroral sky (Archer et al., 2019b) [11]. Typically occurring approximately 1 hour after the onset of a substorm (Gallardo-Lacourt et al., 2018b) [100], it is collocated with extreme SAIDs, with ion flow velocities typically exceeding 5 km/s and elevated electron temperatures above 6,000 K (Archer et al., 2019a) [10].

Satellite overflights of STEVE events have revealed a notable absence of aurora-like particle precipitation, suggesting that STEVE emissions likely have a different origin (Gallardo-Lacourt et al., 2018a; Nishimura et al., 2019) [99, 248]. The optical spectrum of STEVE, observed by Gillies et al. (2019) [110], differs significantly from any previously observed auroral spectrum. While traditional auroral spectra exhibit distinct spectral lines and bands gen-

erated via relaxation of various excited states of atmospheric atomic and molecular species, STEVE emissions are uniformly elevated across all optical wavelengths, forming a continuum of emissions. Although the photochemical origin of this continuum emission is still not conclusively determined, Harding et al. (2020) [126] proposed that the continuum might result from the collision of ions in fast SAID flows with N_2, vibrationally exciting it and inducing a chemical cascade that generates NO_2 and spectrally broad light. Recently, several papers have reported observations of a SAR arc transitioning into STEVE, a connection between two subauroral optical phenomena that current models are unable to replicate (Martinis et al., 2022; Gillies et al., 2023) [215, 111].

The *picket fence*, a series of vibrant green streaks occurring between 95 and 150 km, often accompanies STEVE, and is thought to occur on the same magnetic field lines (Archer et al., 2019b) [11]. Initially, it was believed that these streaks were generated by particle precipitation, similarly to typical green auroral forms (MacDonald et al., 2018; Chu et al., 2019; Nishimura et al., 2019) [210, 48, 248]. Nishimura et al. (2019) [248] detected > 1 keV electron precipitation magnetically conjugate to the picket fence, and Bennett and Bourassa (2021) [27] showed that the altitude profile of the picket fence's O(^{1}S) 557.7 nm green-line emissions could be replicated with an auroral electron precipitation model.

However, observations of the picket fence's optical spectrum (Gillies et al., 2019) [110] are not consistent with spectra of aurora created by particle precipitation (Mende et al., 2019) [228]. Instead, several recent modeling studies suggest that the emissions may be generated by local thermal electrons energized by local parallel electric fields in the ionosphere, although they did not conclusively demonstrate such electrons could quantitatively reproduce the observed spectrum (Lynch et al., 2022; Mishin & Streltsov, 2022) [208, 235]. This dissertation addresses the question of the origin of picket fence emissions in Chapter 5 (published in Gasque et al. (2023) [107]), presenting spectral observations in conjunction with the results of a kinetic model to show that parallel electric fields can quantitatively explain the picket fence's unique emission spectrum. Understanding plasma and neutral dynamics in the subauroral region remains an ongoing area of research, and open questions in this field will be summarized in Chapter 6.

2.5 Summary: Plasma/Neutral Interactions in the Coupled Ionosphere/Thermosphere System

This chapter provided an overview of the ionosphere/thermosphere system and the various mechanisms of plasma/neutral interactions that couple the systems together. It began with an overview of the formation and structure of both the neutral and ionized portions of Earth's atmosphere. It then explored neutral and plasma wave phenomena in the upper atmosphere and ionosphere. Following that, it delved into plasma/neutral coupling mechanisms by examining the ion continuity equation, demonstrating how the local ion density can be altered by changes in plasma production rates, recombination rates, and transport along and

perpendicular to the background magnetic field. Lastly, it discussed the structure of Earth's magnetic field and how it effectively divides the ionosphere into equatorial, subauroral, and auroral sectors. For each sector, it highlighted some of the main processes and phenomena. The following chapters will begin investigating the effects of different energy drivers on the I-T system.

Chapter 3 explores the ionospheric impact of the Tonga volcanic eruption in the near-field (within 5,000 km of the volcano). This chapter will refer to the ionospheric and thermospheric structure, gravity waves, Alfvén waves, ion continuity (covering production, loss, and transport), and equatorial ionospheric dynamics including the fountain effect and wind-driven dynamo, discussed above.

Chapter 4 investigates the influence of changing solar inputs on the thermosphere, reporting observations of evening thermospheric solar terminator waves. Relevant to this chapter are discussions on thermospheric structure, solar thermal tides, gravity waves, and equatorial processes.

Finally, Chapter 5 investigates the picket fence, a subauroral optical phenomenon associated with fast-flowing ionospheric plasma. Topics relevant to this chapter include the structure of the E Region ionosphere and lower thermosphere, charged particle gyromotion, plasma production and loss chemistry, and phenomena in the auroral and subauroral regions, including auroral acceleration processes, SAIDs, and STEVE.

Chapter 3

Rapid Volcanic Modification of the E Region Dynamo: ICON's First Glimpse of the Tonga Eruption [108]

This chapter begins our exploration into how various energy inputs affect plasma/neutral coupling in the I-T system, building on the background information presented in the previous chapter. This work considers the effects of explosive events in the lower atmosphere, focusing on the 2022 eruption of the Hunga Tonga-Hunga Ha'apai volcano. The majority of this chapter presents the peer-reviewed publication Gasque et al. (2022) [108], which was published in Geophysical Research Letters in September 2022, approximately seven months after the eruption of the Hunga Tonga-Hunga Ha'apai volcano disrupted the Pacific Ocean and the global ionosphere. The full author list for this publication is L. Claire Gasque, Yen-Jung Wu, Brian J. Harding, Thomas J. Immel, and Colin C. Triplett.

In particular, this study examines plasma drifts observed by the Ion Velocity Meter (IVM) on board NASA's Ionospheric Connection Explorer (ICON) satellite within 4,000 km of the volcano less than an hour after the eruption. Further details about ICON and the IVM are provided in Appendix B.1. This work shows that ICON observes extreme (compared to a representative climatology) plasma drifts perpendicular to the local magnetic field shortly after the eruption, but well before the arrival of any known neutral atmospheric wave emanating from the eruption. Instead, this chapter shows that these drifts result the alteration in the ionospheric E Region dynamo (introduced in Section 2.3) generated by rapid horizontal thermospheric winds near the volcano. It is argued that these winds generate electric fields which are then transmitted along the magnetic field to the conjugate hemisphere via Alfvén waves to produce the observed drifts.

Appendix B.2 presents the details of the E Region dynamo calculation, demonstrating the likely connection between the winds and plasma drifts and also allowing the prediction of the winds produced by the eruption shortly after it occurred. Although there were no thermospheric wind instruments in the vicinity of the volcano shortly after the eruption, the predicted winds have since been shown to be consistent with the results of whole atmosphere

models, such as the one presented in Vadas et al. (2023) [352], as detailed in Appendix B.2.

This work is one of few studies which investigate the plasma-neutral coupling in the near-field (within ∼5,000 km) of a volcanic eruption, and therefore provides important observational constraints for future models of these events.

Abstract

The 15 January 2022 Hunga Tonga-Hunga Ha'apai volcano eruption drove global atmospheric waves that propagated into space and impacted the ionosphere. Here we show immediate large-scale electrodynamic effects of the eruption using observations from NASA's Ionospheric Connection Explorer. We report extreme zonal and vertical $\vec{E} \times \vec{B}$ ion drifts thousands of kilometers away from Tonga within an hour of the eruption, before the arrival of any atmospheric wave. The measured drifts were magnetically conjugate to the ionospheric E Region just 400 km from Tonga, suggesting that the expanding wavefront created strong electric potentials which were transmitted along Earth's magnetic field. A simple theoretical model suggests that the observed drifts are consistent with an expanding wave with a large (>200 m/s) neutral wind amplitude. These observations are the first direct detection in space of the immediate electrodynamic effects of a volcanic eruption and will help constrain future models of impulsive lower atmospheric events.

Plain Language Summary

The Hunga Tonga-Hunga Ha'apai volcano eruption on 15 Jan 2022 sent seismic waves rippling through the Earth, launched tsunamis across the Pacific, and drove waves globally through the atmosphere. The atmospheric waves travelled into space, where they impacted the ionosphere, which extends from ∼80 to 1,000 km above Earth's surface and is composed of ionized gas. Using observations from NASA's Ionospheric Connection Explorer, we show that the eruption dramatically modified charged particle motion in the ionosphere thousands of kilometers away from Tonga well before any atmospheric waves arrived. These changes are likely driven by strong electric fields generated near the volcano and transmitted along the Earth's magnetic field. A simple model suggests that the electric fields are generated by a fast neutral wind wavefront expanding away from the volcano. These observations are the first in-situ measurements of the immediate ionospheric electrodynamic effects of a volcanic eruption, and will help calibrate models of the event, improving our understanding of how energy moves between the lower atmosphere and space.

3.1 Introduction

When it erupted on 15 Jan 2022, the submarine Hunga Tonga-Hunga Ha'apai volcano (subsequently called 'Tonga') released an immense amount of energy, with estimates ranging from 4 to 200 Megatons of TNT equivalent (Astafyeva et al., 2022; Garvin, 2022; Kulichkov

et al., 2022; Vergoz et al., 2022) [13, 103, 179, 355]. These energies are comparable to the energy released by the largest nuclear bombs, and rank the Tonga volcanic eruption as the strongest in the last 30 years (Duncombe, 2022) [65]. After the eruption, energy propagated outward via seismic waves traveling through the Earth (Poli & Shapiro, 2022) [269], tsunamis moving across the ocean (Carvajal et al., 2022) [41], and various acoustic and gravity wave modes propagating in the atmosphere, which were subsequently able to reach space and affect the ionosphere (Wright et al., 2022) [371]. Here, we will investigate the eruption's immediate ionospheric effect, examining how atmospheric waves emanating from the eruption rapidly modified the ionospheric dynamo, dramatically changing plasma behavior thousands of kilometers away.

The United States Geological Survey (USGS) used seismic data to estimate that the main volcanic blast occurred at 4:14:45 UT on 15 Jan 2022 (USGS, 2022) [345]. However, it took additional time for the effects of the blast to set up an atmospheric disturbance. The eruption vaporized the surrounding seawater, lofting more than 100 million tons of water vapor tens of kilometers into the stratosphere (Millan et al., 2022) [233]. There, the vapor again condensed and released its latent heat, transferring energy into the atmosphere and generating outward propagating waves (Wright et al., 2022) [371]. Maletckii and Astafyeva (2022) [211] estimated that it would take approximately 11 minutes for energy to propagate vertically from the volcano to the ionosphere assuming acoustic speeds. By backpropagating the observed pressure waves, Wright et al. (2022) [371] found an atmospheric origin time of 4:28±2 UT, which we adopt for our analysis.

Once the waves were generated in the atmosphere, wave signatures were observed propagating horizontally around the globe. The most persistent of these had properties consistent with a Lamb wave, a non-dispersive pressure wave which propagated globally at speeds estimated between 300 and 390 m/s (with most estimates around 310 m/s), and whose signature was clearly distinguishable in total electron content (TEC) data taken by the Global Navigation Satellite System (GNSS) (Aa et al., 2022; Amores et al., 2022; Hong et al., 2022; Kataoka et al., 2022; Kulichkov et al., 2022; Lin et al., 2022; Otsuka, 2022; Wright et al., 2022; Zhang et al., 2022) [2, 7, 144, 169, 179, 192, 253, 371, 383]. Zhang et al. (2022) [383] detected a TEC signature consistent with a propagating Lamb wave up to 100 hours after the eruption, after the wave had circled the globe at least three times.

Observations of previous volcanic eruptions, such as the 2015 Calbuco volcano, have also shown signatures of fast-moving wave modes (>500 m/s), which are mainly confined to within a few thousand kilometers of the source (Shults et al., 2015) [315]. For the Tonga eruption, close to the eruption site, TEC observations reported by Zhang et al. (2022) [383] showed an initial supersonic infrasound wave traveling at ∼1 km/s for approximately 20 minutes, which, following Astafyeva (2019) [12], they identified as consistent with a Rayleigh wave. Zhang et al. (2022) [383] also deduced two shocks with initial radial propagation of ∼700 m/s which they observed slow to ∼450 m/s and which were confined to within 5,000 km of the volcano. Similarly, Themens et al. (2022) [338] reported a large scale TID radially propagating at 950±170 m/s and a second TID propagating at 555±45 m/s. Within 3,000 km, both of these waves reportedly slowed down to 550 ± 15 m/s and 390 ± 15 m/s, respectively. Astafyeva

et al. (2022) [13] used surface pressure data recorded only 64 km from Tonga, and found a likely propagation speed of $\sim$ 620 m/s for the ionospheric disturbance produced by the main eruption, which they posited to be due to a shock-acoustic wave mode due to its appearance as a sharp TEC increase. Additionally, Aa et al. (2022) [2] reported observations of fast acoustic modes of 1,050 m/s and 760 m/s from TEC data.

While many prior studies have investigated wave modes produced from volcanic eruptions (primarily using TEC data), only a few works have investigated the eruptions' impact on the ionospheric dynamo. TEC disturbances can result from a variety of mechanisms, including field-aligned drag, dynamo electric fields, and composition changes, but studies using TEC data alone are often unable to distinguish between these mechanisms. Yamazaki et al. (2022) [377] and Iyemori et al. (2022) [160] reported surface geomagnetic field variations shortly after the eruption both at a site $\sim$835 km from Tonga, and in Honolulu, Hawaii, which is near Tonga's geomagnetic conjugate point. Based on numerical modeling results by Zettergren and Snively (2019) [380], Yamazaki et al. (2022) [377] suggested that the observed geomagnetic field variations were signatures of ionospheric dynamo currents driven by neutral wind variations caused by the volcano. Using Super Dual Auroral Radar Network (SuperDARN) radar observations, Shinbori et al. (2022) [314] reported meridional plasma drift variations with $\sim$100 m/s amplitude in the conjugate hemisphere shortly after the Tonga eruption. They similarly suggested that these variations resulted from an E Region dynamo driven by atmospheric neutral wind variations associated with the eruption.

In another study which looked more closely at the dynamo mechanisms, Harding et al. (2022) [127] investigated the Tonga eruption using data from the National Aeronautics and Space Administration's (NASA's) Ionospheric Connection Explorer (ICON) and the European Space Agency's (ESA's) Swarm satellites to observe extreme disruptions in the equatorial electrojet (EEJ) once the Lamb wave entered the dayside about 10 hours after the eruption. In particular, they reported that the EEJ disruption coincided with extreme ($\sim$200 m/s) zonal winds in the dynamo region of the ionosphere ($\sim$100-150 km). As noted by Harding et al. (2022) [127], these winds are larger than 99.9% of winds observed for the entire ICON mission to date.

Here, we investigate in-situ measurements of the immediate effects of the eruption on the E Region dynamo. Within an hour of the eruption, the ICON satellite sampled in-situ ion drifts and densities on magnetic field lines with footpoints within 400 km from Tonga. We report observations of extreme ion drifts consistent with extreme winds directed away from the eruption site, evidence of the volcano's influence on the ionospheric dynamo. In Section 3.2, we describe the data products and methods used to infer the volcanic effects. In Section 3.3, we present the observations and propose a theoretical model to interpret them. Finally, in Section 3.4 we conclude and suggest directions for future work.

3.2 Data and Methods

NASA's ICON mission was designed to explore energy and momentum transfer into the ionosphere from both solar and lower atmospheric sources (Immel et al., 2018) [156]. As a result, it is well-suited to study the effects of a volcanic eruption, a large impulsive lower atmospheric energy source. This study uses data from ICON's Ion Velocity Meter (IVM), which employs a Retarding Potential Analyzer (RPA) and Ion Drift Meter (IDM) to make in-situ measurements of ion drifts and densities (Heelis et al., 2017) [134]. More details about ICON and the IVM are provided in Appendix B.1.

The ICON observatory travels in a near-circular, 27° inclination orbit at roughly 575 km altitude, with an orbital period of ∼97 minutes. The observatory passed within 4,000 km of the Tonga eruption site at around 4:54 UT, less than an hour after the eruption. Figure 3.1(a) depicts ICON's trajectory for its first orbit following the eruption. The observatory's path is shown in black. For reference, the locations of several nominal wavefronts with phase speeds of 310 m/s (yellow), 600 m/s (purple), and 900 m/s (green) are shown, roughly identifying the regions affected by waves reported by previous studies (see Section **??**). We assume each of these waves propagates isotropically and at constant velocity from the eruption site with an origin time of 4:28 UT. The wavefronts are calculated at each longitude based on the time ICON's south magnetic footpoint (described further below) reaches that longitude, explaining why the wavefronts are slightly distorted. We neglect any potential influence from global wind patterns which may cause asymmetric propagation, despite some evidence that the waves did not propagate evenly in all directions and that some of the phase fronts slowed significantly in the near-field (Astafyeva et al., 2022; Themens et al., 2022; Zhang et al., 2022) [13, 338, 383]. As we are mainly using these regions as a tool to qualitatively reveal where it might be possible to observe the effects of the volcano, these considerations do not affect our interpretation.

While the path of the observatory itself does not pass through the region affected by the volcano during this initial pass, the IVM's south magnetic footpoint passes within 500 km of Tonga. The south magnetic footpoint is identified in Figure 3.1(b) as the point in the ionospheric E Region (at 120 km) connected to the same magnetic field line as the observatory, which is calculated using quasi-dipole coordinates (Emmert et al., 2010) [72]. Although the IVM makes measurements in situ at the observatory, ion drifts are driven by electric fields which are rapidly transmitted along magnetic field lines via Alfvén waves. The electric fields are therefore the same at all points along a single magnetic field line, assuming the field lines are equipotentials (Heelis et al., 2017) [134]. Daytime electric fields are typically dominated by forcing in the E Region where the Hall and Pedersen conductivities are highest. Therefore, the ion drifts ICON measures during this pass are likely to be affected by the eruption.

To distinguish differences in the observed drifts from what would be expected at these solar local times (SLTs), we established a background climatology using ion drift data from 8 - 13 Jan, 2022, during which magnetic conditions were relatively quiet. We excluded data from 14 Jan 2022 (the day before the eruption) to avoid contamination from a moderate

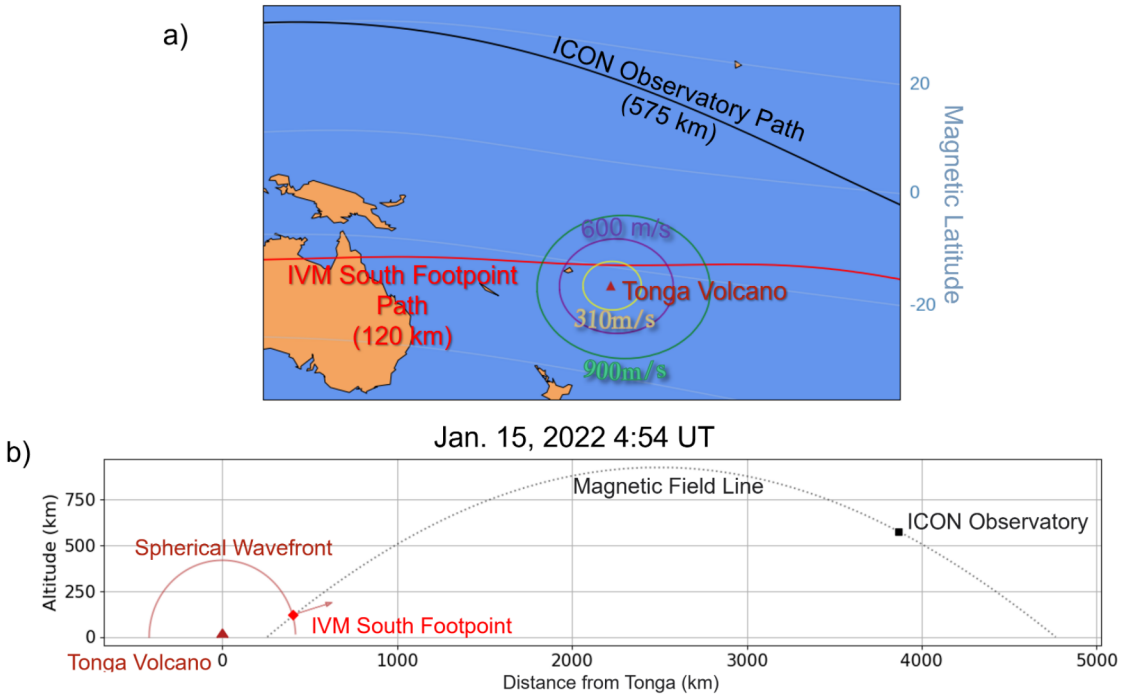

Figure 3.1: (a) ICON's geographic and south magnetic footpoint positions relative to the Tonga volcano. Also shown are wavefronts for disturbances traveling from the eruption site at 310 m/s (yellow), 600 m/s (purple) and 900 m/s (green). The wavefronts are assumed to propagate isotropically at constant velocity, and are shown at the moment that the IVM south footpoint is at the same longitude as the wavefront. (b) The magnetic field line connected to ICON at its closest approach to Tonga, showing the IVM south magnetic footpoint. A simple spherical wavefront model shows that when the IVM south magnetic footpoint is north of the volcano, the normal to it points mostly northward.

geomagnetic storm which occurred on that day. The climatology was performed by sorting the data on a 6-minute SLT grid and finding the median as well as the 90th, 75th, 25th, and 10th quantiles.

3.3 Results and Discussion

Figure 3.2 presents ICON IVM ion density and drift measurements for the first orbit following the Tonga eruption. The green, purple, and yellow highlighted regions correspond to the nominal wavefronts shown in Figure 3.1(a), representing wavefronts traveling at 900 m/s, 600 m/s, and 310 m/s, respectively. The SLT climatology is shown in gray, with the dark gray line representing the median of the measurements, the dark gray region bounding the 25th to 75th quantiles, and the light gray region bounding the 10th to 90th quantiles. In particular, note the extreme vertical and zonal ion drifts observed within the region affected by the volcano, peaking at 6.9σ and 8.8σ respectively with respect to the quiet-time climatology.

During the same period, we observe a modest increase in the ion density, and little change in the field-aligned ion drift. The ion density enhancement occurs at the same time as the largest observed vertical ion drifts, suggesting that the enhancement results from local ions lifted up to the site of the observatory via $\vec{E} \times \vec{B}$ drift. However, this signature is small compared to background variability.

These observations occur during the recovery phase of the 14 Jan geomagnetic storm. We argue that the observed extreme ion drifts are dominated by volcanic forcing, not geomagnetic influences. If present, storm-induced penetration electric fields could theoretically influence ion drifts, although the effects would be largely independent of longitude. The extreme variation in the vertical and zonal ion drifts ICON observes are confined to only the longitudes already under the influence of the disturbances propagating away from the volcano, suggesting they are directly related to the effects of the eruption. Furthermore, as Harding et al. (2022) [127] showed, there is no evidence of large penetration electric fields due to the storm. One likely effect is a storm-related deviation of the zonal ion drifts from the climatology prior to and following the region affected by the volcano. This deviation in the background zonal drifts begins around 19 UT on 14 Jan 2022, near the onset of the storm, and is also seen during previous and future orbits on this day (not shown). The feature beginning at around 5:05 UT is equatorial spread-F, which occurs shortly after the observatory crosses the solar terminator, and is unrelated to the eruption.

ICON first observes the volcanically-driven ion drifts at ∼4:51:40 UT, determined using the time of the abrupt change in slope in the vertical ion drift in Figure 3.2. Similarly, ICON no longer observed the volcanically-driven ion drift perturbation at 4:56:30 UT. Given the observatory's location >4,000 km from Tonga, the wavefront would have had to propagate at 3000±250 m/s to reach the observatory at the observed time, which is far faster than any known ionospheric wave mode. In order to reach ICON's south magnetic footpoint in the same time, the wavefront would need to propagate at 600±50 m/s. This observation is in line with wavefront velocities inferred by Zhang et al. (2022) [383], Themens et al.

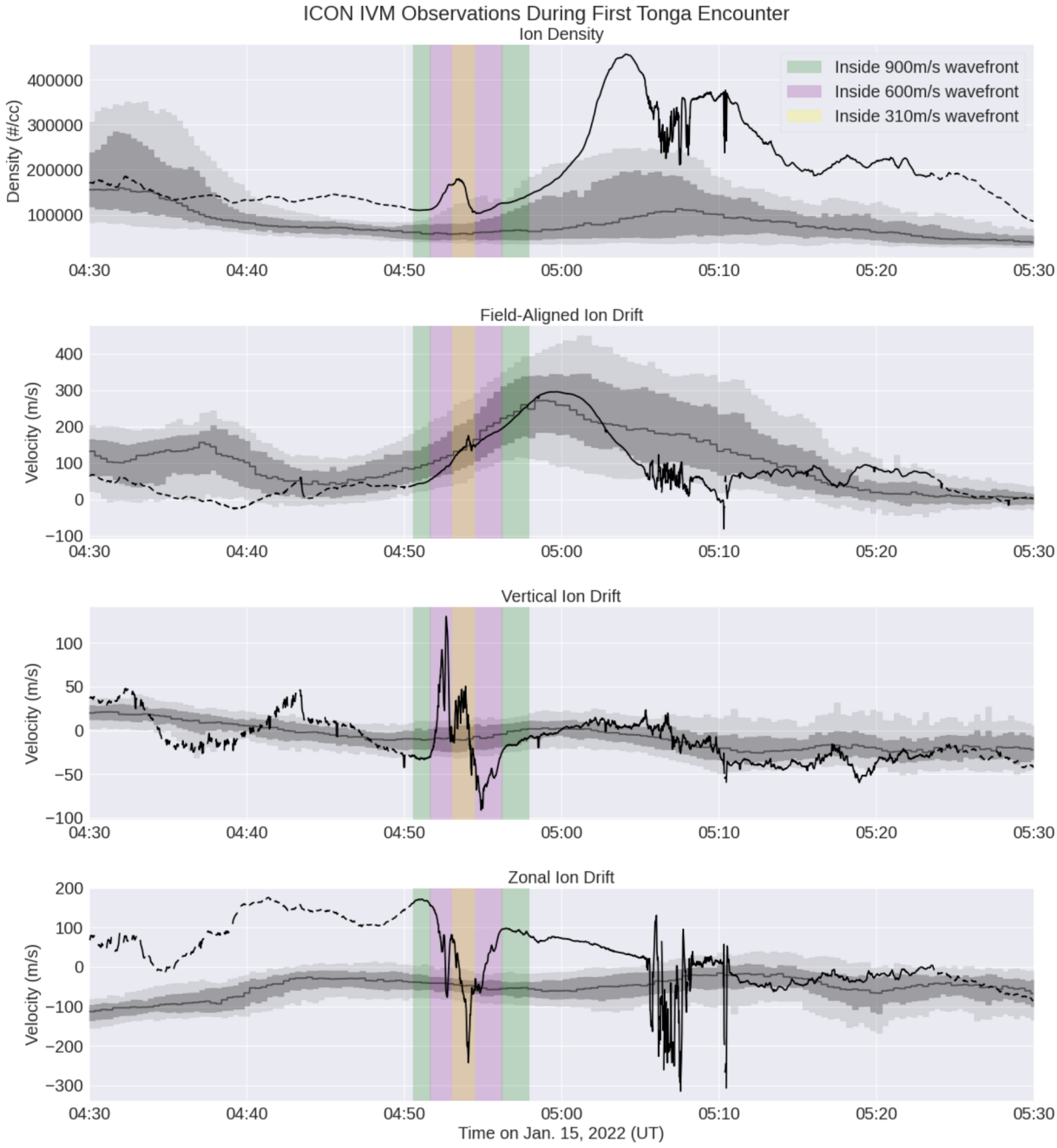

Figure 3.2: IVM ion density and drift measurements during ICON's orbit following the Tonga eruption. The data taken when the south footpoint was within nominal wavefronts moving at 900 m/s, 600 m/s, and 310 m/s are highlighted in green, purple, and yellow, respectively. The SLT climatologies are shown in gray, with light gray bounding the 10th to 90th quantiles, dark gray bounding the 25th to 75th quantiles, and the median shown as the darker gray line. Note the extreme vertical and zonal ion drifts in the region affected by the volcano.

(2022) [338], and Astafyeva et al. (2022) [13]. Therefore, the extreme vertical and zonal ion drifts are likely $\vec{E} \times \vec{B}$ ion drifts resulting from polarization electric fields (PEFs) caused by the ion drag established by the eruption's forcing of the neutral atmosphere. The PEFs are transmitted almost instantaneously along the magnetic field line to the observatory's location via Alfvén waves (Kikuchi & Araki, 1979) [174]. These observations are direct evidence that the electrodynamic effects of the volcano were rapidly transmitted to the conjugate hemisphere.

To investigate the origin of the observed ion drifts, we consider a simple theoretical model of how the neutral winds driven by the volcano might drive the ionospheric dynamo.[1] First, we assume that neutral wind perturbations due to the eruption are large compared to background neutral winds, implying that the perturbation wind will be the main driver of local changes in the ionospheric dynamo. This is consistent with Harding et al. (2022)'s [127] report of unusually large (>99.9th percentile) neutral winds in the ionospheric dynamo region following the Tonga eruption.

While the phase fronts of waves driven by the volcano propagate outward from the eruption site, there is less certainty about the direction of the neutral wind velocity along the phase fronts. As an initial estimate, we assume that the neutral wind velocities align with the phase fronts, expanding spherically away from the eruption site as illustrated in Figure 3.1(b). As the IVM south magnetic footpoint transits the affected region (Figure 3.3(a)), this simple model suggests it would encounter first a primarily westward, then northward, then eastward wind. We will determine the expected electric fields and ion drifts driven by this neutral wind, and compare the expected ion drifts with ICON's observations to assess the validity of our assumed neutral wind model.

In order to determine the PEFs and resulting $\vec{E} \times \vec{B}$ ion drifts generated by this wind model, we use a theoretical slab model of the ionosphere following Kelley (2009) [172]. In this model, currents in the Hall region (∼100-120 km altitude) drive the electric fields along the slab of the ionosphere surrounding a single magnetic field line. Hall currents flow in the $\hat{b} \times (\vec{U} \times \vec{B})$ direction, where $\hat{b}$ is a unit vector in the magnetic field direction, $\vec{U}$ is the neutral wind, and $\vec{B}$ is the magnetic field. The wind-driven current causes a separation of charges, which sets up an opposing PEF in the $-\hat{b} \times (\vec{U} \times \vec{B})$ direction. This, in turn, will cause an $\vec{E} \times \vec{B}$ ion drift in the $(-\hat{b} \times (\vec{U} \times \vec{B})) \times \vec{B}$ direction, which is the same as the $\hat{b} \times \vec{U}$ direction.

Figure 3.3(b) uses this theoretical model to predict the direction of the observed drifts given the neutral wind input. Adopting a coordinate system where the magnetic field points into the page, the east and west point right and left, respectively, and the component of the northward neutral wind perpendicular to the magnetic field line will point down. Assuming the IVM south footpoint encounters first a westward, then northward, then eastward neutral wind, the Hall-region slab model predicts we will observe first upward, then westward, then downward ion drifts. Figure 3.3(c) shows perturbations in IVM ion drift observations from the background during the same time period. A linear trend between 4:51 and 4:57 UT (immediately before and after we observe the volcanogenic drift perturbations) has been

[1] Additional details about this calculation and the assumptions that are made are given in Appendix B.2.

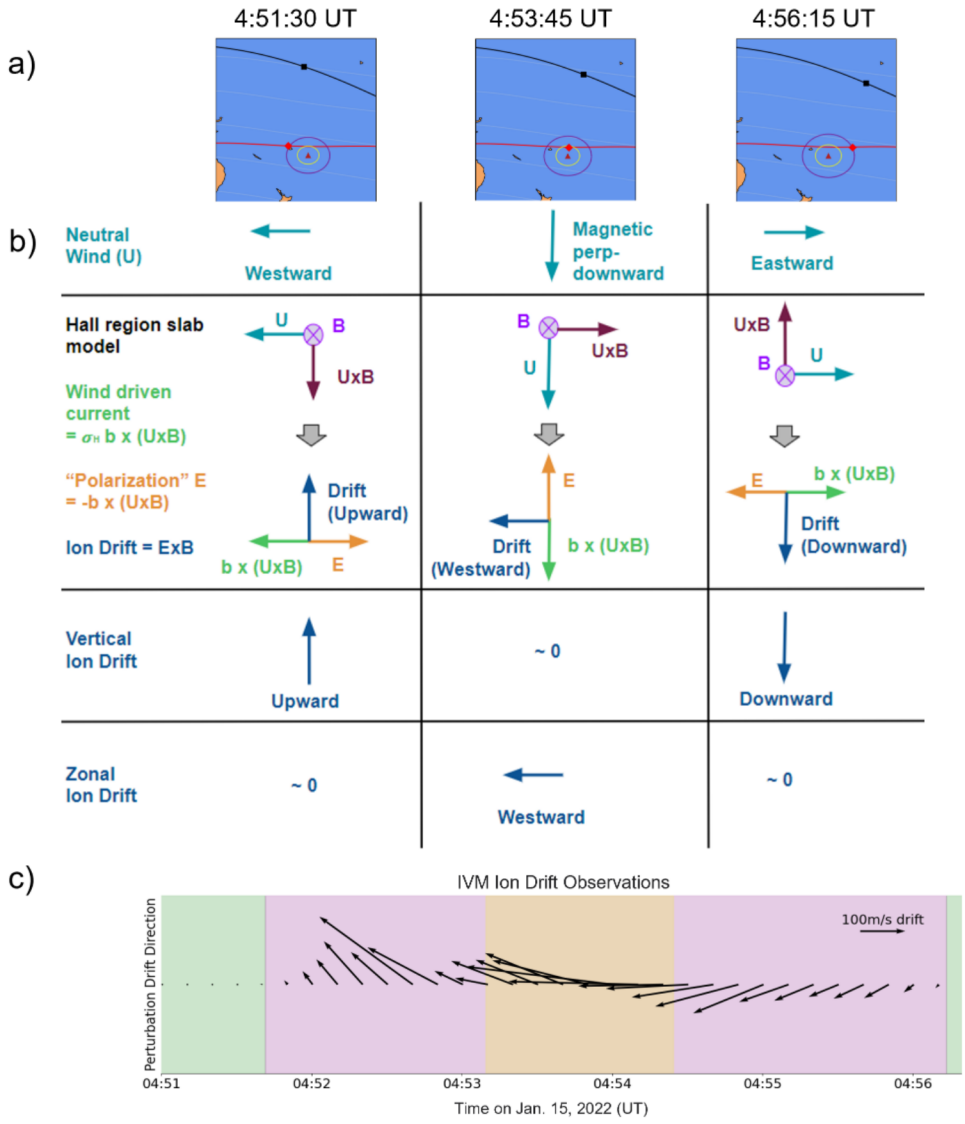

Figure 3.3: Predictions from a simplified slab model of Hall region currents driving the ionospheric dynamo (see text for details). (a) The locations of the ICON observatory and IVM south footpoint with respect to the expanding 600 m/s (purple) and 310 m/s (yellow) wavefronts at times which correspond to the westward, northward, and eastward neutral winds. (b) A chart showing predicted ion drifts given the assumed neutral wind input. The top row shows the neutral wind input, the middle shows the determination of the ion drift direction from PEF established by the Hall region current. The bottom two rows show the theoretically predicted vertical and zonal ion drifts. (c) The IVM drift data with a linear trend removed aligned with the columns of the chart above. Upward pointing arrows represent upward perturbation drifts and rightward pointing arrows represent eastward perturbation drifts. These observations show good agreement with the theoretical results.

subtracted from the drift data to better distinguish the perturbation due to the volcano from the background variation. The theoretical model succeeds at explaining the large-scale structure in the observed drifts; we first observe a predominantly upward, then westward, then downward ion drift, as predicted.

The theory does not perfectly match the observations, likely because of the model's simplicity. Even when the drifts are predominantly vertical, they still have a considerable westward component. This is partially due to the fact that, since the IVM south footpoint passes equator-ward of Tonga, there will be a northward wind component even when the neutral wind is predominantly zonal. Thus, we should expect to see a westward zonal drift component throughout the pass. The model also neglects Pedersen currents, which would add a component to the wind-driven current in the $\vec{U} \times \vec{B}$ direction, altering the direction of the PEF and resulting $\vec{E} \times \vec{B}$ ion drift. While both Hall and Pedersen region currents contribute to the $\vec{E} \times \vec{B}$ drifts in the evening at low latitudes (Maute et al., 2012) [216], our model with the Hall currents alone reproduces the large scale ion drift features. A full theoretical treatment would necessarily include Pedersen currents as well as non-local effects.

This theoretical model also predicts that the magnitude of the ion drifts will be the same as the magnitude of the driving neutral wind. The IVM observed a maximum perturbation drift speed of 330 m/s, suggesting that the volcano drove neutral winds in the ionosphere at comparable speeds. While we do not have measurements of the neutral winds at the same times as these drift observations since the field-of-view of the neutral wind measurement is looking further north, Harding et al. (2022) [127] reported Hall-region winds exceeding 200 m/s several hours following the Tonga eruption, suggesting that the inferred speeds are reasonable. The simplified model assumes perfect dynamo driving efficiency, which is unlikely given the simplifications above, as well as the influence of the northern footpoint winds. Thus, it is likely that the volcanogenic winds would need to be larger than 330 m/s to explain the observed drift perturbations.

3.4 Conclusion

In this work, we reported ICON IVM ion drift measurements for the first orbit following the 15 Jan 2022 Tonga volcanic eruption. Although the ICON observatory passed ∼4,000 km away from the site of the eruption, it was magnetically connected to the ionospheric E Region just 400 km from Tonga, allowing the IVM to remotely sample the dynamo region close to Tonga within an hour of the main eruption.

We observed extreme vertical and zonal ion drifts, with maximum drift velocity perturbations exceeding 300 m/s. We find that the observed ion drifts appear too soon to be forced by a wave with a 310 m/s group velocity. An effective propagation velocity of 600±50 m/s is needed to explain the arrival of the ion drift signature given the 4:28±0:02 UT origination time found by Wright et al. (2022) [371]. A simple theoretical model revealed that the changing direction of the drifts as ICON's IVM south magnetic footpoint transited the region affected by the volcano was largely consistent with the electrodynamic effects of a

high amplitude (>300 m/s) neutral wind wavefront expanding away from the eruption site. These observations are also clear evidence of a conjugate effect: electric fields established by wind-driven currents in the vicinity of the volcano were transported to the observatory's location via Alfvén waves, and arrived much sooner than any reported atmospheric waves. This observation and interpretation supports previous reports of conjugate effects due to this event (Iyemori et al., 2022; Lin et al., 2022; Shinbori et al., 2022; Yamazaki et al., 2022) [160, 192, 314, 377].

Here, we focused only on ICON's IVM data from its first pass following the eruption. In addition to the IVM, ICON carries remote sensing instruments capable of measuring neutral winds, temperatures, and ion density profiles (Englert et al., 2017; Kamalabadi et al., 2018; Mende et al., 2017; Sirk et al., 2017; Stephan et al., 2017, 2018) [75, 165, 230, 317, 329, 330]. During this orbit, the fields-of-view of ICON's remote sensing instruments were north of the observatory's path, outside of the region already influenced by the volcano, and so were unable to observe any volcanic effects. During later orbits, however, multiple ICON instruments can simultaneously observe the affected region. Although for this orbit we had to assume a neutral wind profile to predict the observed ion drift dynamics, future work will use observed neutral winds and drifts to investigate multiple aspects of the thermosphere/ionosphere effects of the eruption, applying methods described in Immel et al. (2021) [155]. Later orbits will likely be additionally complicated by a combination of dynamo forcing and direct drag acting on the ionosphere, as well as interactions between different direct and conjugate wavefronts.

The observations reported here are the first direct detection in space of the near-immediate dynamo effects of a volcanic eruption, and will prove iconic for constraining ionospheric models of this and other impulsive lower atmospheric events.

Chapter 4

Evening Solar Terminator Waves: Neutral Wind Signatures Observed by ICON-MIGHTI [106]

This chapter continues our exploration into how various energy inputs affect plasma/neutral coupling in the I-T system by tackling our next case study: the thermospheric effects of the setting sun. Below is presented the peer-reviewed publication Gasque et al. (2024) [106], which was published in the Journal of Geophysical Research: Space Physics in February, 2024. The full author list for this publication is L. Claire Gasque, Brian J. Harding, Thomas J. Immel, Yen-Jung Wu, Colin C. Triplett, Sharon L. Vadas, Erich Becker, and Astrid Maute.

Although the sunset represents a predictable, regular change in the energy input into the atmosphere, few observational studies have documented its thermospheric consequences. The study presented here presents data from the ICON Observatory's Michelson Interferometer for Global High-resolution Thermospheric Imaging (MIGHTI), showing the local time, latitude, and altitude dependence of the horizontal neutral winds near the equator. Further details about MIGHTI's operational principles can be found in Appendix C.1. The calculation to determine the location of the solar terminator as a function of altitude comes primarily from Colonna and Tramutoli (2021) [49] and is presented in Appendix C.2.

We present the first measurements of the northward neutral wind component and altitudinal wind profiles of thermospheric solar terminator waves. We compare our findings to simulation results from several whole-atmosphere models, determining that some models reproduce the observed features more successfully than others. By comparing the model capabilities, we conclude that these waves are likely generated in the lower atmosphere, with gravity waves potentially playing a significant role in their generation. Simulations from one of the primary whole atmosphere models used for comparison are only available for a 1.5 year subset of the ICON mission. Therefore, to ensure consistent comparisons, the MIGHTI observations presented are for the same window of time. Results for the whole mission are included in Appendix C.3, which was published as supplemental information in Gasque et al. (2024) [106].

This study highlights several open questions related to solar terminator waves and their generation, which are discussed in Section 4.4 and revisited in Chapter 6.

Abstract

The moving solar terminator (ST) generates atmospheric disturbances, broadly termed solar terminator waves (STWs). Despite theoretically recurring daily, STWs remain poorly understood, partially due to measurement challenges near the ST. Analyzing Michelson Interferometer for Global High-resolution Thermospheric Imaging (MIGHTI) data from NASA's Ionospheric Connection Explorer (ICON) observatory, we present observations of STW signatures in thermospheric neutral winds, including the first observed meridional wind signatures. Seasonal analysis reveals STWs are most prominent during solstices, when they intersect the ST about $\sim 20^\circ$ latitude from the equator in the winter hemisphere and have phase fronts inclined at a $\sim 40^\circ$ angle to the ST. We also provide the first observed STW altitude profiles, revealing large vertical wavelengths above 200 km. Comparing these observations to four different models suggests the STWs likely originate directly or indirectly from waves from below 97 km. STWs may play an under-recognized role in the daily variability of the thermosphere-ionosphere system, warranting further study.

Plain Language Summary

Every evening, the sunset removes the primary energy input to the upper atmosphere, causing rapid atmospheric cooling and generating disturbances called solar terminator waves (STWs). Although they theoretically occur every night, STWs remain poorly understood, partially because the rapidly changing atmospheric conditions near sunset make measurements challenging. This study examines neutral wind measurements from the Michelson Interferometer for Global High-resolution Thermospheric Imaging (MIGHTI) on board NASA's Ionospheric Connection Explorer (ICON) observatory to uncover signatures of STWs. We report the north-south wind signatures of STWs and their altitude profile from 200-300 km, both of which have never been previously reported. We show that STWs are some of the largest amplitude dynamical features above 200 km near solstices, but are much weaker near equinoxes. By comparing our observations with the outputs of four different models, we find that STWs are likely generated directly or indirectly (from wave propagation) below 97 km. Future work is necessary to better understand how STWs are generated, how they vary on a daily basis, and the extent of their impacts on Earth's upper atmosphere.

4.1 Introduction: Solar Terminator Waves in the Terrestrial Thermosphere

Every night, the evening solar terminator (ST) sweeps across Earth, dividing daylight from shadow and interrupting the solar radiation which plays a key role in atmospheric heating and ionospheric plasma production. This generates abrupt gradients in atmospheric temperature and pressure, which can launch disturbances in the mesosphere and thermosphere (Somsikov, 2011) [323]. Broadly termed solar terminator waves (STWs), these disturbances form near and propagate with the advancing ST (Miyoshi et al., 2009) [239]. Although they theoretically recur every night, STWs' morphology and occurrence patterns remain poorly characterized, and their specific generation mechanisms are still debated.

STW generation theory first emerged when, inspired by Chimonas and Hines (1970)'s [46] anticipation of gravity waves excited by time-variable heating during solar eclipses, Beer (1973) [25] proposed a similar effect from the daily motion of the ST. Subsequent research delved deeper into the theoretical underpinnings of STWs, generally confirming that the moving ST can generate gravity waves, but the scarcity of observations hampered further advancement of this work (Beer, 1978; Cot & Teitelbaum, 1980; Somsikov, 1987; Somsikov & Ganguly, 1995) [26, 53, 322, 324].

Only three studies have reported observations of STWs in the thermosphere. Using the CHAMP satellite's tri-axial accelerometer, Forbes et al. (2008) [89] identified an STW in thermospheric neutral densities. These had a $\sim$3000 km horizontal wavelength, had phase fronts inclined $\sim$30° with respect to the ST, and were more pronounced during solstices than equinoxes. Subsequently, Liu et al. (2009) [199] confirmed the density STW and also detected an STW in CHAMP's thermospheric cross-track (i.e. mainly zonal) winds. The zonal wind STW had comparable wavelength and inclination to the ST as the density STW, with zonal wind magnitudes ranging from 5-15 m/s, constituting 5-20% of the mean zonal wind velocity at those local times. Both studies concluded that the STW was more prominent at dusk than at dawn, with most wave structures appearing on the nightside, only extending into the sunlit region around solstices. These results correlated well with General Circulation Model (GCM) simulations conducted by Forbes et al. (2008) [89] and Miyoshi et al. (2009) [239]. In a third study, Bespalova et al. (2016) [30] examined in-situ neutral density perturbations detected by the Atmospheric Explorer-E satellite, finding density perturbations with amplitudes of 2-4% associated with the ST passage.

Recent modeling by Chou et al. (2022) [47] and Vadas et al. (2023) [352] suggests that STWs in neutral winds could have a more significant impact on equatorial thermospheric dynamics than previously considered. Using a Specified Dynamics Whole Atmosphere Community Climate Model with thermosphere-ionosphere eXtension (SD-WACCM-X) simulation from October 2020, Chou et al. (2022) [47] identified a large-amplitude evening STW with phase fronts aligned from northwest to southeast, the same orientation as winter solstice STWs observed with CHAMP (Forbes et al., 2008; Liu et al., 2009) [89, 199]. Chou et al. (2022) [47] proposed that evening STWs play an underrecognized role in driving equatorial

electrodynamic phenomena such as equatorial plasma bubbles (EPBs). Additionally, Vadas et al. (2023) [352] identified STWs with horizontal wind magnitudes of 50-100 m/s in a HIgh Altitude Mechanistic general Circulation Model (HIAMCM) simulation of 15 January 2022. Although their primary focus was simulating the primary and secondary gravity waves triggered by the Hunga Tonga-Hunga Ha'apai volcanic eruption, the STW was surprisingly prominent in the simulation results and interacted non-linearly with the eruption-induced gravity waves. While both studies report STWs with significant neutral wind amplitudes and emphasize their potential influence on thermospheric and ionospheric dynamics, these conclusions remain to be confirmed with observational evidence.

This study presents the first remotely-sensed measurements of evening STWs in thermospheric neutral winds, including the first STW meridional wind observations. By analyzing $\sim$ 1.5 years of data from NASA's Ionospheric Connection Explorer (ICON) satellite, we investigate seasonal variation in STWs, and compare these findings to simulations from several models. We also present the first observed altitude profiles of thermospheric evening STWs, comparing our observations with HIAMCM simulation results. This work confirms that STWs are prominent features in the terrestrial thermosphere, suggesting the necessity of future modeling and observational studies which will further enhance our understanding of STW drivers and effects.

4.2 Methods: Observations and Modeling

ICON/MIGHTI Neutral Wind Observations

In this study, we examine evening STW signatures in neutral wind measurements from ICON's Michelson Interferometer for Global High-Resolution Thermospheric Imaging (MIGHTI). ICON follows a nearly circular orbit with 27° inclination at $\sim$600 km and achieves complete local time coverage across sampled latitudes every $\sim$48 days (Immel et al., 2018) [156]. Further details about ICON's design and objectives can be found in Immel et al. (2018) [156], and the significant findings from its prime mission period are outlined in Immel et al. (2023) [157].

MIGHTI measures Doppler shifts in oxygen red-line (630.0 nm) and green-line (557.7 nm) airglow emissions to determine horizontal neutral wind profiles between $-12°$ and $+42°$ latitude (Englert et al., 2017) [75]. Unlike CHAMP, which made in situ measurements, ICON remotely measures neutral wind altitudinal profiles, enabling observations of the vertical structure of STWs. MIGHTI captures daytime wind profiles every 30 seconds between 90 and 300 km. Nighttime winds are sampled every 60 seconds at the same altitudes, except for a gap spanning $\sim$109 to 210 km where the airglow brightness is insufficient to take reliable measurements (Harlander et al., 2017; Harding et al., 2021) [130, 129].

Here, we use MIGHTI Level 2.2 Version 5 data, which provides meridional and zonal neutral wind measurements. Near the ST, there is a brief (typically $<$5 minute) data gap when MIGHTI switches from day to night mode (Englert et al., 2023) [74]. Additionally, the

MIGHTI wind retrieval algorithm assumes that the atmosphere is spherically symmetric, but this assumption is violated by the rapidly changing conditions near the ST (Harding et al., 2017) [128]. While the resulting asymmetry-associated errors can surpass 10 m/s near 150 km, above 200 km these errors are expected to be less than 1 m/s and therefore should not affect our analysis (Wu et al., 2020) [374]. Furthermore, Version 5 incorporates three updates important for improving the wind data quality near the ST: an independent, higher accuracy zero-wind calibration, an updated thermal drift correction, and a correction for the "anomalous low-signal phase shift" (Englert et al., 2023) [74]. Additional details about the MIGHTI instrument design and data processing can be found in Englert et al. (2017) [75], Harding et al. (2017) [128], and Harlander et al. (2017) [130], while the updated Version 5 processing is detailed in Englert et al. (2023) [74].

Due to the significant variations in STW morphology between seasons (Forbes et al., 2008; Liu et al., 2009) [89, 199], we divide the data into three seasons for analysis: northern hemisphere (NH) winter, combined equinox, and NH summer. Spring and autumn are combined as they exhibit minimal differences in our analysis. For each season, we include data captured in the period from 45 days before to 45 days after the corresponding solstice or equinox, encompassing 90 days total or nearly 2 full precession cycles. While MIGHTI data is available almost continuously from December 2019 to November 2022, the SD-WACCM-X simulations used for comparison (see Section 4.2) only extend until March 27, 2021. Consequently, we limit our analysis to this period (December 2019 - March 2021), covering 2 NH winters, nearly 3 equinoxes, and 1 NH summer. Extending our analysis to the end of the mission does not alter our observational conclusions (refer to Appendix C.3 for the results for the full ICON mission). With the exception of some moderate solar activity in November 2020, all of the data surveyed here is for solar quiet (F10.7 < 80) conditions (Wu et al., 2023) [373]. This period also encompasses a small geomagnetic storm, described in McGinness et al. (2023) [223].

We bin the meridional and zonal winds for each season into 30-minute solar local time (SLT) intervals and 1° latitude bins, taking the median value in each bin. We take the median to minimize the influence of outliers arising from artifacts near the terminator. By averaging over all longitudes, we selectively retain features traveling with Earth's rotation, filtering out non-migrating components (Miyoshi et al., 2009) [239]. MIGHTI's horizontal resolution is affected by its integration time, horizontal field of view, line-of-sight averaging, and the spacecraft velocity, as detailed in Harding et al. (2021)'s [129] Appendix. We reproduced Harding et al. (2021)'s [129] analysis for the MIGHTI red-line measurements, finding that near 280 km, where we report STW amplitudes and scale sizes in this work, these combined effects generate a horizontal averaging kernel of ∼700 km. Our 30-minute SLT bins are equivalent to roughly 850 km resolution. Given an expected evening STW scale size of ∼3,000 km (Forbes et al., 2008) [89], the resolution is sufficient for capturing these features. Although data sampled within ∼ 500 km of the ST carries a 'caution' label in MIGHTI's data quality flags, we nonetheless include this data in our analysis. Despite binning and averaging the data, some artifacts near the ST persist, especially in NH summer where we incorporate only a single season of data. However, since any data artifacts have

a much smaller scale than the evening STWs, and are oriented exactly parallel to the ST, they are not expected to affect our conclusions.

In the cases where we find the largest evening STW amplitudes, we further characterize the STW's morphology. First, we remove diurnal variations as a function of SLT at each latitude by fitting and subtracting a 24-hour period sinusoid (representing the diurnal tide). Then, we perform a least-squares fit of a Gaussian near the evening ST at each latitude, determining the amplitude and defining the scale size as the full-width at half-maximum (FWHM). The reported amplitudes and scale sizes in Section 4.3 represent averages across all latitudes observed by MIGHTI. By fitting a line to the STW as a function of latitude and SLT and intersecting it with the ST's position, computed using the method described in Colonna and Tramutoli (2021) [49] (see Appendix C.2), we determine the latitude of intersection and the STW's angle relative to the ST.

Simulations

To determine whether current global models capture the physics necessary to reproduce STW signatures observed by MIGHTI, we compare the observations to simulations from three different models: the Thermosphere-Ionosphere-Electrodynamics General Circulation Model for the Ionospheric Connection Explorer (TIEGCM-ICON) (Maute, 2017) [217], SD-WACCM-X 2.0 (Liu et al., 2018; Maute & HAO WACCM team, 2022)[198, 218], and the HIAMCM (Becker & Vadas, 2020; Becker, Vadas, et al., 2022; Becker, Goncharenko, et al., 2022; Becker & Vadas, 2022) [20, 23, 24, 21].

The TIEGCM describes thermospheric and ionospheric dynamics, energetics, and chemistry, coupled with ionospheric electrodynamics (Richmond, 1995; Qian et al., 2014) [282, 274]. In this study, we used TIEGCM-ICON, ICON's Level 4 data product (Maute, 2017; Maute & ICON Team, 2022; Maute et al., 2023) [217, 219, 221], which includes two runs of the TIEGCM: a simulation which incorporates data-driven 42-day averages of diurnal and semidiurnal tidal forcing at the 97 km lower boundary via the Hough Mode Extension (HME) from MIGHTI horizontal winds and temperatures (Forbes et al., 2017; Cullens et al., 2020) [90, 55], and one without such a tidal specification. The background at the lower boundary is obtained from global averages of horizontal winds (Drob et al., 2008) [64] and neutral temperatures and densities (Picone et al., 2002) [267]. The model resolution is 2.5° by 2.5° in geographic latitude and longitude and the numerical damping suppresses features with wavelengths below $\sim$ 2500 km. This model does not include gravity waves generated below its lower boundary, although it implicitly incorporates some effects of turbulent mixing due to gravity wave breaking by specifying the eddy diffusivity at the lower boundary (Qian et al., 2014) [274]. This method does not, however, account for the spatial distribution of lower/middle atmosphere gravity wave sources.

Unlike the TIEGCM, SD-WACCM-X 2.0 includes lower atmospheric dynamics to capture large-scale day-to-day variations (Liu et al., 2018) [198]. We use the run performed by England et al. (2022) [73], which is nudged to GEOS-5 (Maute & HAO WACCM team, 2022) [218]. The detailed lower atmospheric physics, including tropospheric weather, deep

convection, and ozone variability, are described by Marsh et al. (2013) [214] and Neale et al. (2013) [244]. The SD-WACCM-X simulations we use have 0.9° by 1.25° resolution in latitude and longitude, respectively, capable of resolving features with wavelengths larger than ∼500 km. To account for small-scale gravity wave momentum deposition, SD-WACCM-X includes a gravity wave parametrization, detailed by Richter et al. (2010) [286] and Garcia et al. (2017) [102], which identifies gravity wave sources (e.g., convection, fronts, orographic features) and incorporates resulting wave dissipation effects into the simulations.

The TIEGCM (with and without HMEs) and SD-WACCM-X simulations in this analysis cover the period from ICON mission's start until spring 2021. We sampled model outputs at the same times and locations as MIGHTI data, and processed this "synthetic data" in the same manner as the MIGHTI data (described in Section 4.2).

We also compare NH winter STW results from the HIAMCM, a high-resolution global whole-atmosphere model for neutral dynamics. The HIAMCM's horizontal grid spacing is ∼ 52 km (∼0.45°), enabling it to effectively resolve waves with horizontal scales above ∼200 km, smaller than the TIEGCM and SD-WACCM-X simulations examined here (Becker, Vadas, et al., 2022) [23]. This model also incorporates lower atmospheric processes, detailed in Becker and Vadas (2020) [20], with large scales nudged to Modern-Era Retrospective analysis for Research and Applications, Version 2 (MERRA-2) reanalysis up to ∼ 70 km. Unlike the other models, the HIAMCM explicitly resolves gravity waves, including both primary gravity waves and the secondary gravity waves which arise from dissipation of the primaries (Becker & Vadas, 2020; Becker, Goncharenko, et al., 2022) [20, 24]. Resolved gravity wave packets that become dynamically unstable are damped by physics-based subgrid-scale turbulent diffusion, simulating wave-mean flow interactions caused by wave instability and subsequent dissipation (Lindzen, 1981) [193]. The HIAMCM neglects non-local momentum and energy transfer caused by non-resolved gravity waves.

This study uses the HIAMCM 'background' run from 15 January 2022, which excludes the effects of the Tonga volcano eruption on that day and the geomagnetic storm on the day prior (Vadas et al., 2023; Becker & Vadas, 2022) [352, 21]. To facilitate comparisons, we bin and average the data from every time step of the simulation as functions of the same latitude and SLT bins used for MIGHTI and extract the STW features in the same manner.

4.3 Results

Figure 4.1(a) presents NH winter MIGHTI meridional winds at ∼283 km, binned and averaged as a function of latitude and SLT. This altitude was chosen to minimize terminator-related data artifacts. Gray shading marks nighttime regions (for which the sun is below the horizon) at this altitude. Note that, although none of the tides have been removed in Figure 4.1(a), the evening STW is a prominent feature in the meridional winds, appearing as a northward wind enhancement near the evening ST (the transition between illumination and shadow near 20 SLT). At most MIGHTI-sampled latitudes, the STW-related enhancement corresponds to the largest total meridional wind amplitude with respect to SLT, suggesting

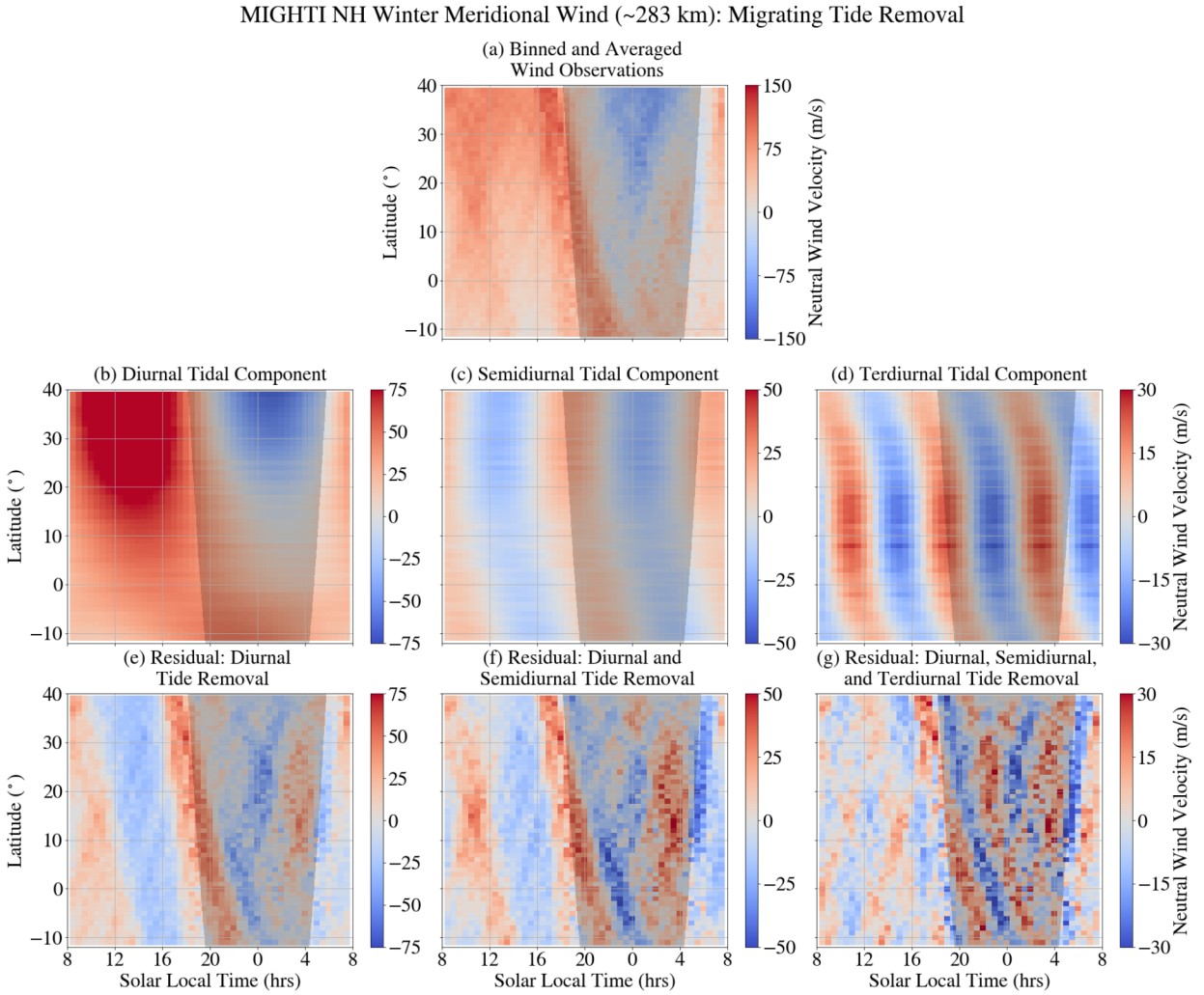

Figure 4.1: Meridional winds during NH winter as observed by MIGHTI, presented as a function of latitude and SLT. In the first row, (a) shows the binned and averaged data prior to the removal of tidal components. The second row displays the fits for the (b) diurnal, (c) semidiurnal, and (d) terdiurnal tidal components. The final row shows the data residuals after successively removing the (e) diurnal, (f) semidiurnal, and (g) terdiurnal tides. Note that the colorbar amplitude varies between subfigures.

its potentially significant role in thermospheric and ionospheric dynamics, including field-aligned ion drag and interhemispheric transport (Heelis et al., 2022) [136].

The second row of Figure 4.1 shows the tidal decomposition of Figure 4.1(a) into its diurnal (Figure 4.1(b)), semidiurnal (Figure 4.1(c)), and terdiurnal (Figure 4.1(d)) components. These components were obtained by fitting sinusoids with 24-hour, 12-hour, and

8-hour periods, respectively, as a function of SLT at each latitude. The amplitude of the colorbar is reduced for each successive tidal component, reflecting the diminishing power in each subsequent component. The final row (Figures 4.1(e), 4.1(f), and 4.1(g)) displays the residuals in the data after removing each successive tidal component.

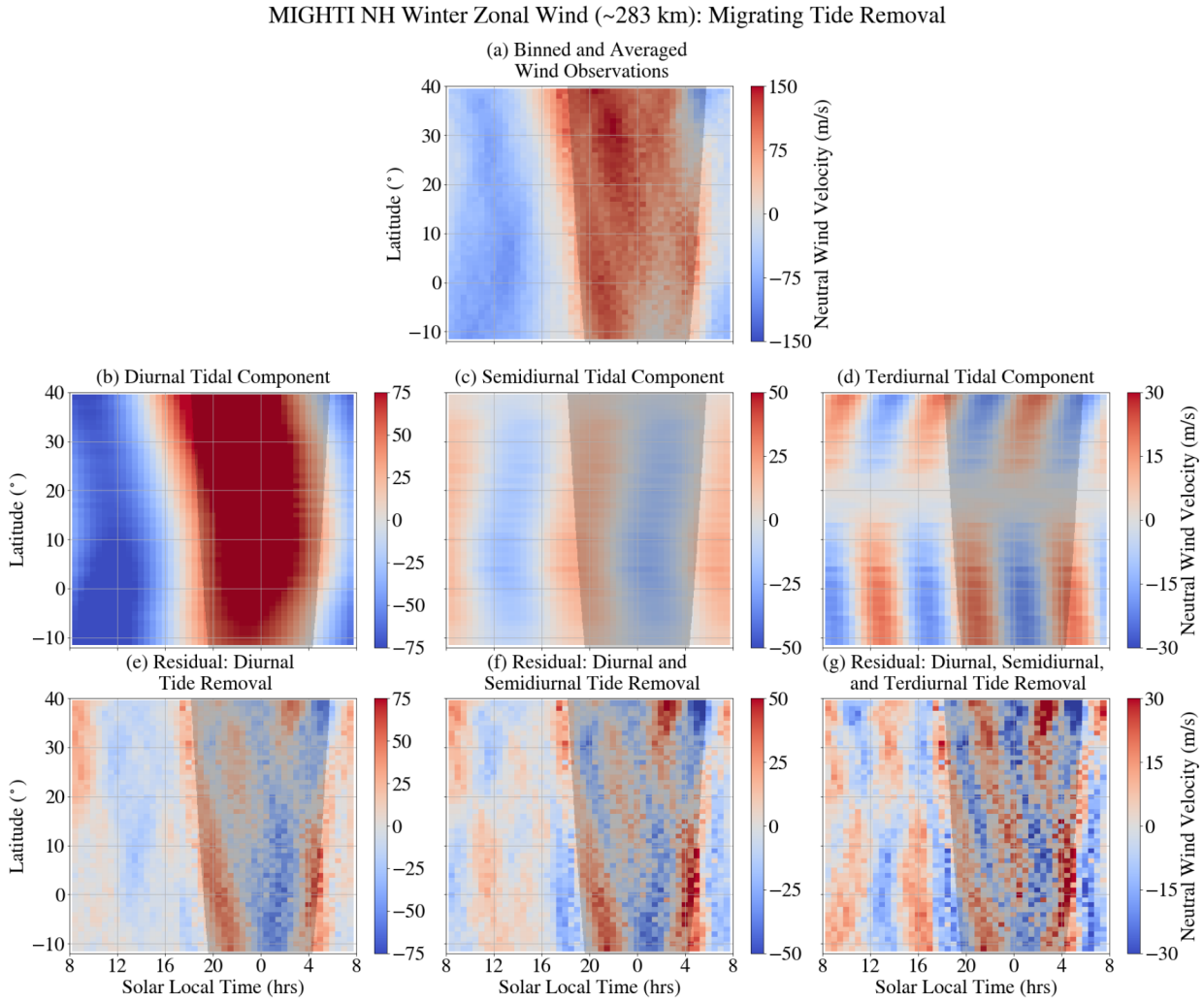

Figure 4.2: Same as Figure 4.1, but for the observed zonal wind component.

Figure 4.2 shows the corresponding tidal decomposition of the observed zonal winds. In this case, the diurnal tide is more dominant than in the meridional winds, with the binned wind measurements in Figure 4.2(a) showing a clear pattern of westward winds during the day and eastward winds at night. However, with the removal of the diurnal tidal component (Figure 4.2(e)), an enhanced eastward wind feature emerges which has a similar amplitude and proximity to the evening ST as the northward meridional wind enhancement.

With the successive removal of the migrating diurnal, semidiurnal, and terdiurnal tidal components, the STW amplitude is reduced, although a distinct signature persists. This suggests the STW has power in multiple tidal components and is not attributable to any individual tide. Therefore, in the subsequent analysis, we characterize the STW after removing only the migrating diurnal tidal component.

Figure 4.3 displays binned MIGHTI meridional and zonal winds at ∼283 km for NH winter, combined equinox, and NH summer after removing the migrating diurnal tide. Black dotted lines identify the STW feature in the solstice cases. The NH winter STW is characterized by ∼50 m/s northward winds (Figure 4.3(a)) and ∼50 m/s eastward winds on the nightside, although the zonal wind component diminishes on the dayside (Figure 4.3(b)). In both meridional and zonal wind components, it has a ∼3,400 km scale size (calculated as described in Section 4.2), intersecting the ST between ∼15° to 20° latitude (∼18.8 SLT) with a ∼31° phase front inclination compared to the ST.

For the NH summer case, MIGHTI's latitude sampling does not reach father south than −12°, where we might expect the NH summer STW to intersect the evening ST. However, we observe a ∼40 m/s southward wind enhancement (Figure 4.3(e)) and a ∼ 25 m/s eastward wind enhancement (Figure 4.3(f)), whose phase fronts, when extrapolated down to lower latitudes, intersect the evening ST between ∼-20° to -25° latitude (∼18.6 SLT). The scale size of this feature is ∼2,700 km, comparable to the NH winter STW, and its phase front is inclined ∼ 41° relative to the ST at the intersection point. Although there is also a strong northward wind component close to the evening ST and therefore associated with the evening STW during NH summer, a data artifact near the ST prevents us from characterizing it fully.

In combined equinox, the STW is less evident, even after removing diurnal tides (Figures 4.3(c) and 4.3(d)), consistent with Forbes et al. (2008)'s [89] findings of seasonal asymmetry.

The NH winter and NH summer STWs mirror each other. The NH winter STW wavefront stretches from northwest to southeast with winds blowing northeast, while the NH summer STW wavefront extends from northeast to southwest with winds blowing southeast. Both have phase fronts inclined relative to the ST and intersect it ∼20° off the equator in the winter hemisphere, near 18.7 SLT. The persistent presence of the STW in solstice winds, even with long-term averaging, shows that it is a robust feature. While there is likely day-to-day variability, the large average magnitude of the STW implies that it is a dominant feature in thermospheric winds, at least under solstice solar quiet conditions.

While it is tempting to quantitatively compare our estimated amplitudes to previous studies, each study used a different filtering method, so it is necessary to use caution. Miyoshi et al. (2009) [239] removed diurnal, semidiurnal, and terdiurnal tidal components from their simulation results, Forbes et al. (2008) [89] applied high-pass filtering with a 4800 km wavelength cutoff to CHAMP neutral density data, and Liu et al. (2009) [199] subtracted a 3rd order polynomial from CHAMP densities and zonal winds along each satellite track. This makes an analogous ICON analysis impossible due to the difference in orbital inclinations. Both Vadas et al. (2023) [352] and Chou et al. (2022) [47] presented unfiltered simulation results. The figures we show are binned and averaged to remove the non-migrating tidal features, and we report STW amplitudes after having removed the diurnal tide.

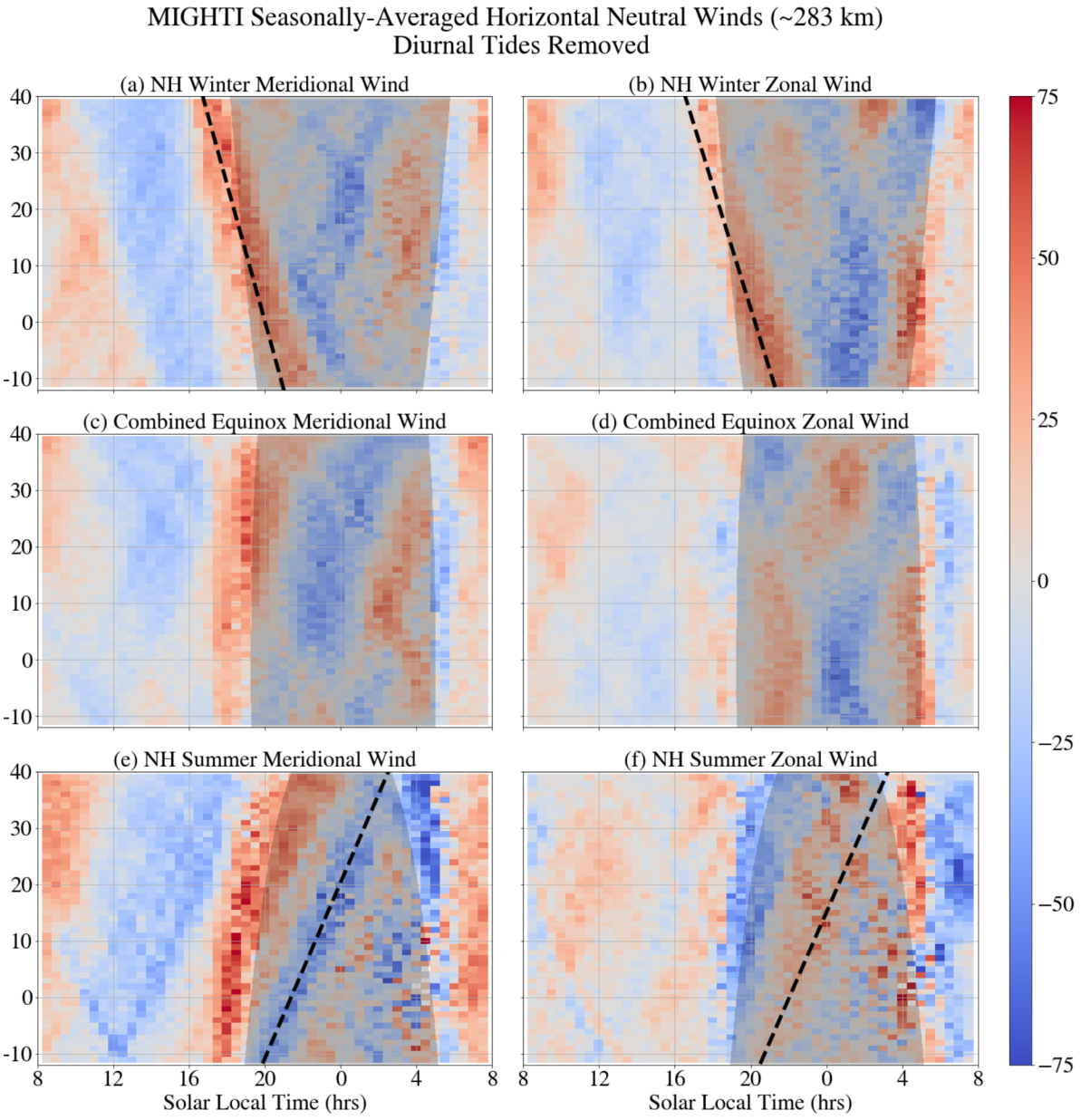

Figure 4.3: Binned and averaged MIGHTI meridional (left column) and zonal (right column) neutral winds for NH winter (top row), combined equinox (middle row), and NH summer (bottom row). Diurnal tides have been removed. Northward and eastward winds are positive. The gray shading shows the portion of the latitude/SLT space that is in darkness for each season. Clear STW features are marked by a black dotted line for the solstice cases ((a), (b), (e), and (f)).

Analyzing simulation outputs alongside MIGHTI observations provides insight into the origins of STWs. Figure 4.4 displays NH winter meridional winds simulated by four different models, all with diurnal tides removed. In the TIEGCM run without HMEs (Figure 4.4(a)), there is no clear STW signature, though a weak ($\sim$25 m/s) signature appears when HMEs are included (Figure 4.4(b)). In contrast, both SD-WACCM-X (Figure 4.4(c)) and HIAMCM simulations (Figure 4.4(d)) exhibit a distinct STW signature. Both models overestimate the STW amplitude relative to observations, with SD-WACCM-X producing $\sim$ 60 m/s northward winds and HIAMCM producing $\sim$ 100 m/s northward winds. It is important to be cautious when interpreting the HIAMCM's STW amplitude, however, as it is based on a single day and is not averaged like the other models and observations. It is possible that the amplitude is high in this case simply because the STW was particularly strong on this day and that an average, considering more daily variability, would reduce the amplitude. The slight amplitude overestimation in SD-WACCM-X is real since the SD-WACCM-X simulations are sampled identically to MIGHTI. Both models generally capture the STW's scale size and phase front inclination with respect to the ST.

The same figure, but showing the modeled zonal winds, is presented in Figure 4.5. Again, the TIEGCM run without HMEs (Figure 4.5(a)) shows little evidence of an evening STW. The case with HMEs does show an eastward wind enhancement near the evening ST, but the phase front is not comparably inclined with respect to the ST as the observed STW and does not intersect the ST at the sampled latitudes. Therefore, even with HMEs driving the lower boundary, the TIEGCM does not appear to accurately reproduce the observed evening STW. Both the SD-WACCM-X and HIAMCM simulations capture the STW signature in the zonal winds, although the signal does not diminish on the dayside as much as it does in the observations. Further discussion on the implications of STW appearance or absence in the various models is found in Section 4.4.

Figures 4.6(a) and 4.6(b) display the altitude structure of the NH winter STW in MIGHTI meridional winds and zonal winds, respectively. The data have been averaged data between 10° and 20° latitude, where the STW intersects the ST, and diurnal tides have been removed. Although MIGHTI data is available between 109 and 200 km during the day, the nighttime gap precluded the removal of diurnal tides at these altitudes, so we do not report any data in this altitude range.

Above 200 km, where nighttime MIGHTI data is available, the STW has a vertical wavelength greater than 200 kilometers. Below 115 km, the STW is not distinguishable, although it may be masked by the large-amplitude tides at these altitudes. The SD-WACCM-X (Figure 4.6(c) and 4.6(d)) and HIAMCM (Figure 4.6(e) and 4.6(f)) simulations similarly suggest a nearly constant phase with altitude above 200 km. In their simulations, Miyoshi et al. (2009) [239] similarly reported a nearly constant phase line with altitude above 250 km, descending with local time below. Below 200 km, both simulations show a descent of the phase line with local time, possibly indicating upward wave propagation. The variation with altitude for the NH summer case for MIGHTI observations and SD-WACCM-X simulations are presented in Figure 4.7.

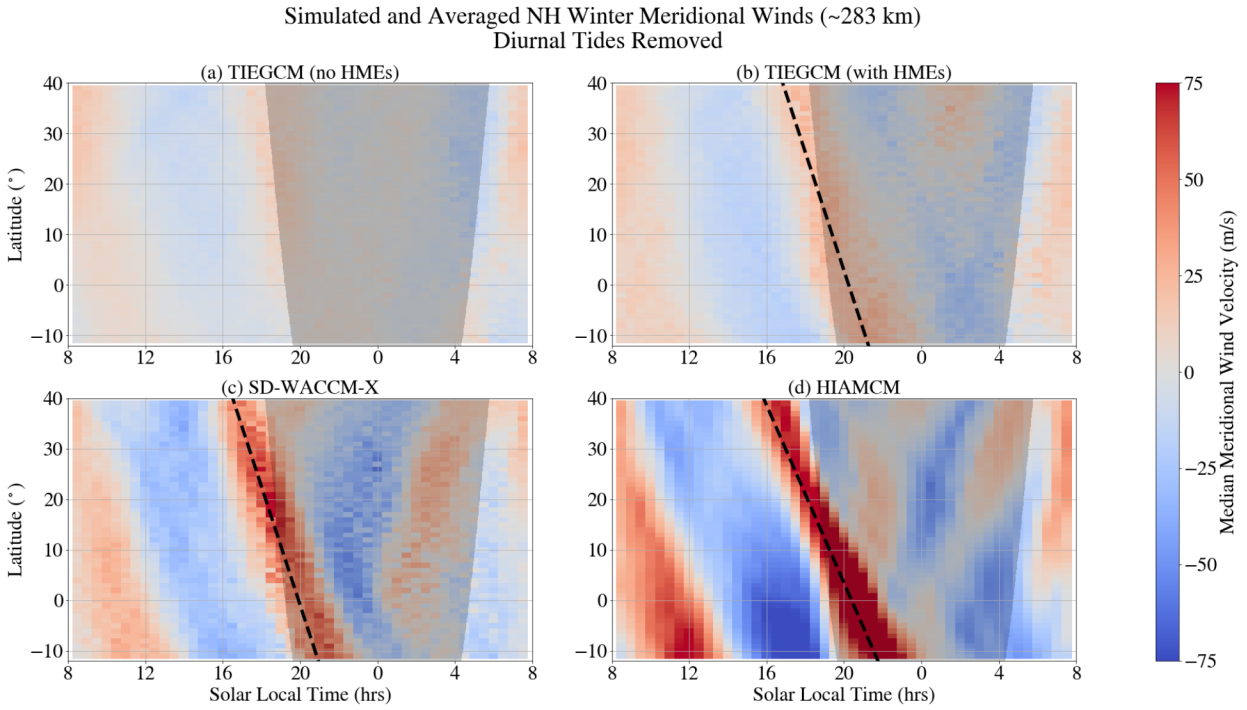

Figure 4.4: Each panel shows NH winter meridional winds binned by latitude and SLT with diurnal tides removed (the same as Figure 4.3(a)), but for (a) TIEGCM simulations without HME inputs, (b) TIEGCM simulations with HMEs derived from MIGHTI observations, (c) SD-WACCM-X simulations, and (d) HIAMCM simulations. The first three simulation results incorporate winter 2019 and 2020, while the HIAMCM result is for 15 January 2022.

4.4 Discussion

While STWs are believed to arise from traveling atmospheric pressure and temperature gradients, precisely where they originate in the atmosphere remains uncertain. Bespalova et al. (2016) [30] suggested that neutral density perturbations observed following the ST might result from gravity waves generated in situ in the thermosphere by solar extreme ultra violet (EUV) heating gradients. In contrast, based on modeling results with and without lower atmospheric effects, Miyoshi et al. (2009) [239] suggested that STWs may propagate up from the lower atmosphere, possibly in line with Chimonas and Hines (1970)'s [46] initial proposal of STW generation initiated by heating due to UV absorption by middle atmospheric ozone.

Our analysis reveals a significant STW signature in solstice neutral wind observations. Both SD-WACCM-X and HIAMCM simulations capture the STW scale size and inclination relative to the ST, although the simulated STWs exceed the observed STW amplitudes. In contrast, TIEGCM simulations lack the STW signature, although introducing HMEs at the

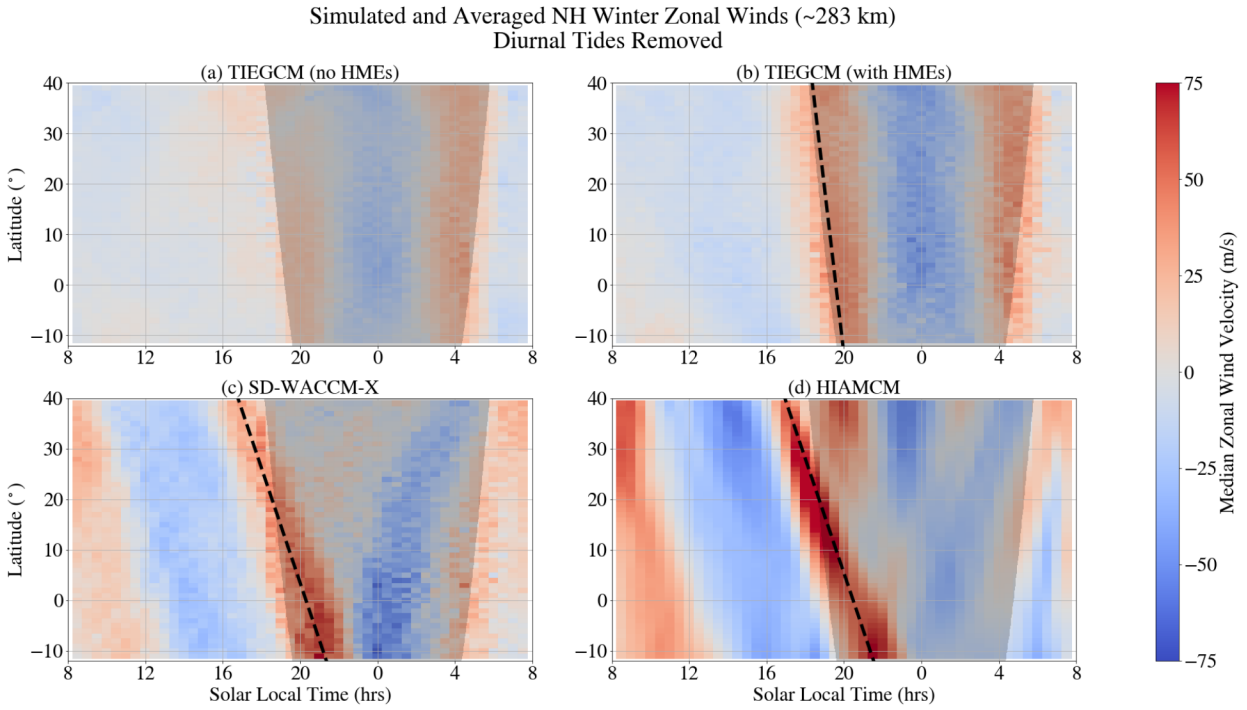

Figure 4.5: Same as Figure 4.4, but for the modeled zonal wind component.

lower boundary leads to the emergence of a weak (∼25 m/s) signature in the meridional wind component.

Both SD-WACCM-X and HIAMCM simulate the atmosphere down to Earth's surface (Liu et al., 2018; Becker & Vadas, 2020) [198, 20], whereas the TIEGCM cannot self-consistently resolve atmospheric processes below its 97 km lower boundary (Qian et al., 2014) [274]. Including ICON HMEs into the TIEGCM partially accounts for lower atmospheric effects by including data-informed diurnal and semidirunal tidal propagation up from the lower atmosphere (Maute et al., 2023) [221], suggesting that global-scale waves from the lower atmosphere may play a role in STW generation. The presence of STW signatures in models with the lower atmosphere but their absence in those without suggests that the lower atmosphere plays an important role in STW generation. This aligns with Miyoshi et al. (2009) [239], who found that excluding atmospheric dynamics below 80 km in their simulations resulted in the disappearance of STW signatures. Further, the weak STW signature in the TIEGCM simulations with ICON HMEs implies that diurnal and semidiurnal tides from the lower and middle atmosphere contribute to, but cannot fully explain, the STW. Although Miyoshi et al. (2009) [239] found that upward propagating migrating tides contributed to STW formation, they suggested that STWs mainly arise from a superposition of these tides with zonal wavenumbers 4 to 6, while our results suggest that lower-order tides

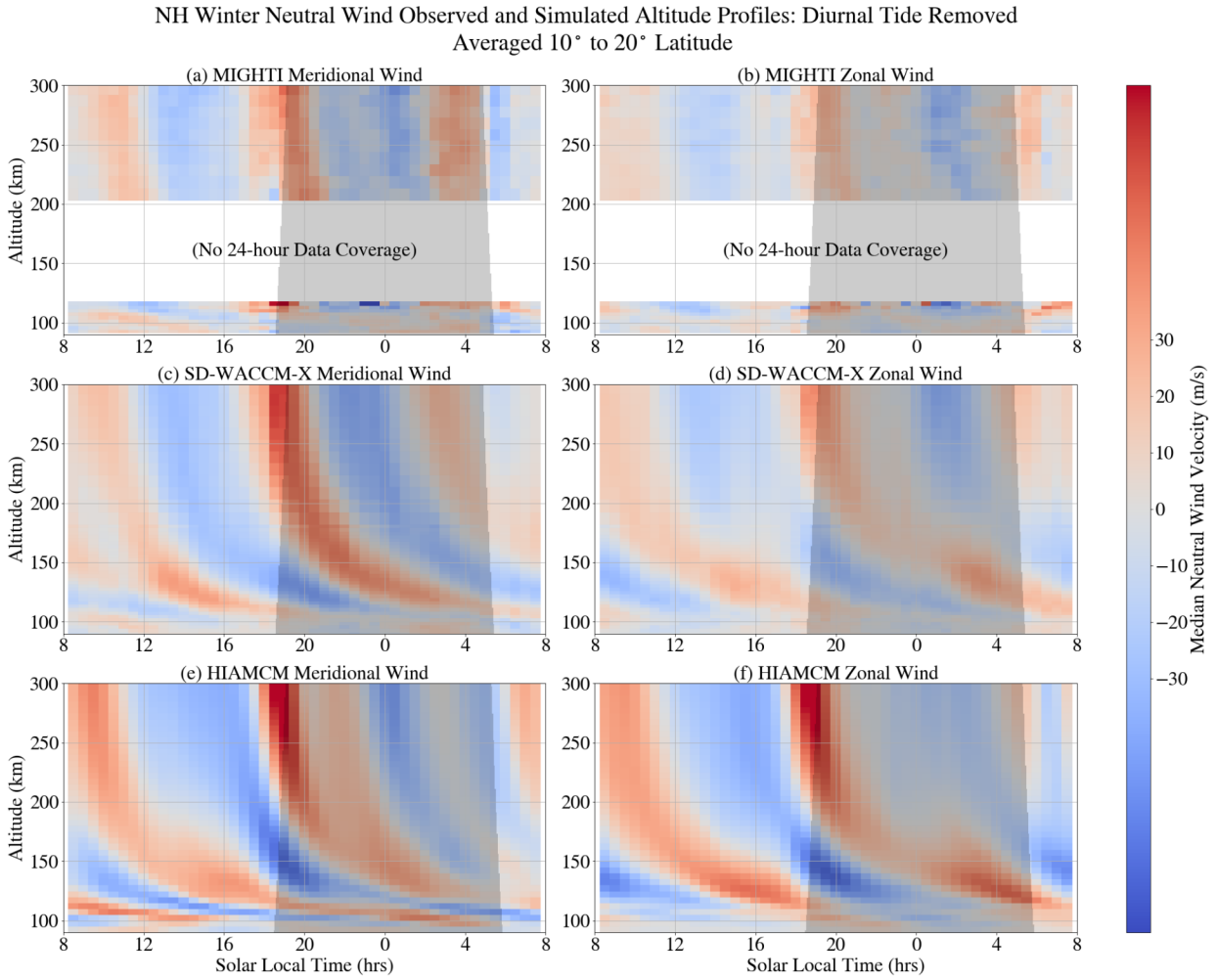

Figure 4.6: NH winter meridional (left) and zonal (right) winds averaged between 10° and 20° latitude as a function of altitude and SLT for (top) MIGHTI data (winter 2019 and 2020), (middle) SD-WACCM-X simulations (winter 2019 and 2020), and (bottom) HIAMCM simulations (15 January 2022). Diurnal tides have been removed. The gray shading shows the portion of the altitude/SLT space that is in darkness. Northward and eastward winds are defined to be positive.

also play an important role.

Differences in how the models account for gravity wave effects may also affect their ability to reproduce STWs. STWs could be generated in part by large-scale gravity waves which either propagate directly from the lower/middle atmosphere to the thermosphere, or which are indirectly generated in the thermosphere through the dissipation of upward-propagating gravity waves (Vadas, 2007; Lund & Fritts, 2012; Heale et al., 2014) [347,

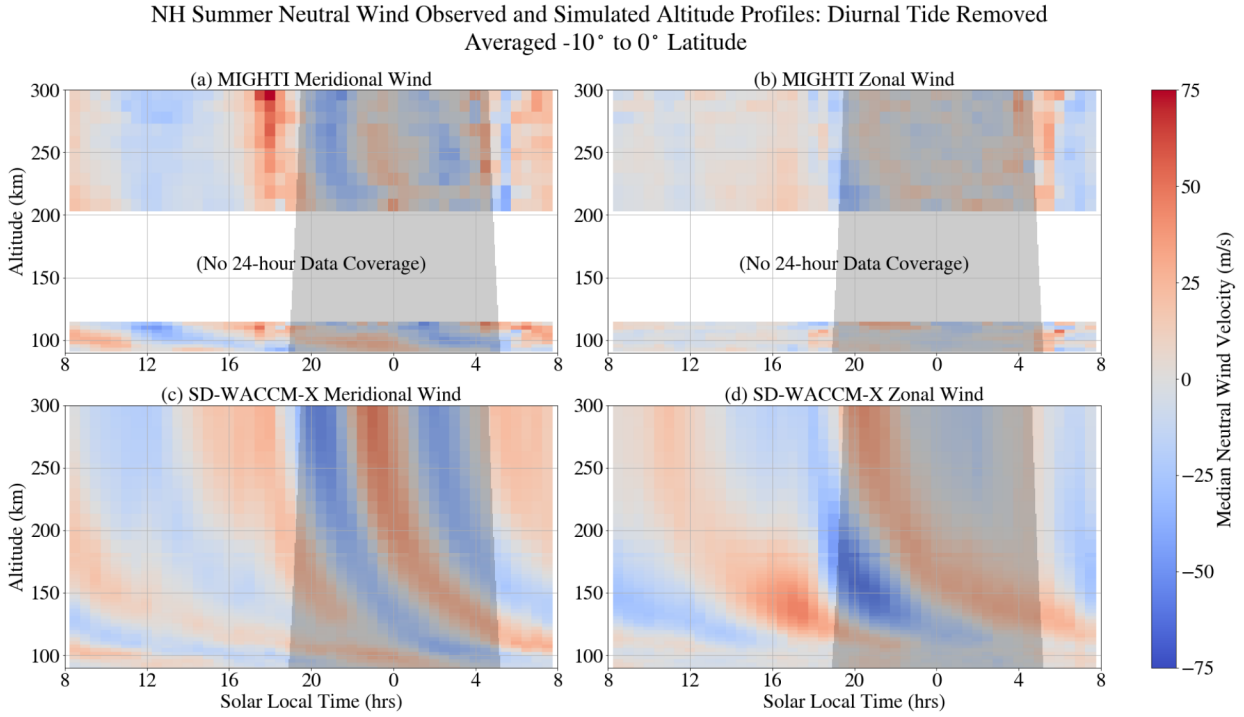

Figure 4.7: NH summer meridional (left) and zonal (right) winds averaged between -10° and 0° latitude as a function of altitude and SLT for (top) MIGHTI data (winter 2019 and 2020), (bottom) SD-WACCM-X simulations (winter 2019 and 2020). Diurnal tides have been removed. The gray shading shows the portion of the altitude/SLT space that is in darkness. Northward and eastward winds are defined to be positive.

207, 131]. This latter 'indirect' mechanism would arise because gravity wave dissipation by molecular viscosity depends critically on the background temperature, resulting in larger amplitude force/heating at lower altitudes on the nightside of the ST (Vadas, 2007) [347]. The resulting 'jump' in the force/heating across the ST from gravity wave dissipation could then generate large-scale secondary gravity waves (Vadas, 2013) [346].

Large-scale gravity waves arising from the ST passage would be captured by SD-WACCM-X and the HIAMCM, which resolve gravity waves from below, but not by the TIEGCM. Although direct EUV heating can also generate gravity waves (Chimonas & Hines, 1970; Vadas, 2013) [46, 346], the absence of STWs in the TIEGCM simulations suggests this mechanism is less significant. Notably, the amplitudes of stratospheric gravity waves have been found to be larger during solstice than equinox (Figure 6 of Hoffmann et al., 2013; Cullens et al., 2022) [142, 54], consistent with our finding of larger STW amplitudes during solstices, further supporting their potential connection to gravity waves. Furthermore, previous modeling and observations indicate that large (hundreds of kilometers) vertical wavelengths, like

those we have observed for STWs, are consistent with a spectrum of gravity waves (Vadas, 2007; Vadas & Nicolls, 2009; Nicolls et al., 2014) [347, 351, 246].

Future modeling studies will investigate these mechanisms, as well as possible non-linear tidal interactions, as the source of the STWs. Furthermore, the reason for the evening STW's inclination with respect to the ST remains an open question which future modeling should address.

Although we reported significant evening STWs, we do not observe any comparable signature near the morning ST. Both Forbes et al. (2008) [89] and Liu et al. (2009) [199] also noted this asymmetry, finding morning STWs to be less well-defined than their evening counterparts. Liu et al. (2009) [199] postulated that larger neutral temperature gradients near the evening ST, as suggested by modeled neutral temperatures at 400 km, may make wave generation more efficient in the evening. Some authors suggested the opposite, claiming that the morning heating process is more efficient than evening cooling, resulting in a sharper sunrise gradient which produces smaller scale STWs (Somsikov & Ganguly, 1995) [324].

Indeed, both Chou et al. (2022) [47] and Vadas et al. (2023) [352] report a smaller scale, weaker amplitude morning STW in their simulation results. Ionospheric studies have also shown evidence of morning STWs (Galushko et al., 1998; Afraimovich, 2008; Song et al., 2013; Ding et al., 2014) [101, 3, 325, 61]. For example, Zhang et al. (2021) [384] measured post-sunrise electron density perturbations using the Millstone Hill Incoherent Scatter Radar (ISR), identifying traveling ionospheric disturbances (TIDs) with zonal wavelengths of ∼445 km. If similarly-sized thermospheric disturbances accompany these TIDs, it is unlikely that MIGHTI would be able to resolve them due to its horizontal resolution.

The thermospheric evening STW may play a currently under-recognized role in driving ionospheric dynamics. The large-amplitude winds reported in this study could influence ionospheric circulation through ion drag or dynamo effects. The meridional STW winds can push plasma along magnetic field lines, contributing to the summer to winter hemisphere redistribution of plasma (Heelis et al., 2022) [136] and affecting the plasma density altitude distribution. Additionally, the F-Region zonal STW winds, when blowing across the westward conductivity gradient caused by changing solar input, may influence the upward plasma drifts of the prereversal enhancement (PRE) (Richmond et al., 2015; Eccles et al., 2015; Liu, 2020) [283, 69, 197]. Variability in STWs may thus affect the PRE, which, in turn, is closely linked to equatorial plasma bubble (EPB) variability (Fejer et al., 1999) [83].

4.5 Conclusion

Leveraging ∼1.5 years of MIGHTI data, this study reported the first remotely-sensed observations of evening STWs, revealing them as one of the most prominent recurring features in the neutral winds above 200 km during solstices. The STW meridional wind component, reported for the first time, has a similar (and sometimes larger) magnitude compared to the zonal component, indicating that STW winds blow predominantly northeastward during NH winter and southeastward during NH summer. Furthermore, we provided the first observa-

tional altitude profile of a STW, revealing vertical wavelengths longer than several hundred kilometers above 200 km. Model comparisons suggested that STW generation is strongly influenced by the lower atmosphere and may result from large-scale gravity waves or their interactions with atmospheric tides.

Given their substantial and persistent presence, STWs hold intrinsic scientific significance, potentially serving as key drivers of thermospheric and ionospheric processes. Future research endeavors, including modeling and observations, are crucial for unraveling the origins and daily variability of these waves, fostering a deeper understanding of their impact on Earth's upper atmosphere.

Chapter 5

It's Not Easy Being Green: Kinetic Modeling of the Emission Spectrum Observed in STEVE's Picket Fence [107]

This chapter shifts the focus poleward to the subauroral latitudes and considers the last ionospheric energy input: the extremely fast subauroral ion drifts (SAIDs) which are associated with unusual optical phenomena. This study investigates the picket fence, one of these optical phenomena, and shows that its unique spectrum can be recreated by a kinetic model driven only by local parallel electric fields. Below is presented the peer-reviewed publication Gasque et al. (2023) [107], which was published in Geophysical Research Letters in November 2023. The full author list for this publication is L. Claire Gasque, Reza Janalizadeh, Brian J. Harding, Justin D. Yonker, and D. Megan Gillies.

This chapter's methodology demonstrates the synergistic use of optical data and first principles modeling to draw quantitative inferences which would not have been possible using data or models alone. First, this study presents and analyzes optical spectra of the picket fence captured by a spectrograph at the University of Calgary in Saskatchewan, Canada. Multiple spectra from picket fence observations throughout a single night reveal a linear relationship between the brightness of two observed spectral features. Subsequently, kinetic modeling is used to evaluate whether it is possible to reproduce this linear relationship in the modeled spectral brightness within a realistic ionosphere influenced by parallel electric fields of varying magnitudes. This analysis also enables the constraint of the expected magnitudes of the parallel electric fields responsible for generating the observed emissions.

Several appendices follow this chapter, providing additional details on the instrumentation, modeling, and underlying physics presented here. Appendix D.1 gives additional details about the TREx spectrograph, which was used to capture the observations presented in this work. Appendix D.2 uses a model of auroral precipitation and emissions to demonstrate

that precipitation is not a viable means of producing the emissions observed in the picket fence. Appendix D.3 walks through the method to calculate the electron impact excitation rate given the electron energy distribution function and excitation cross section for a given electron impact excitation reaction. Following, Appendix D.4 presents the details of the additional kinetic modeling used to obtain the volume emission rates for the relevant emissions, including tables with all relevant reactions and rate constants used. Appendix D.5 compares the results of the steady-state modeling used in this study with those obtained in the model presented by Yonker and Bailey (2020) [379]. Finally, Appendix D.6 extends the steady-state model to consider the ultra-violet emissions that would be expected to be associated with the picket fence.

This research has uncovered various unanswered questions and potential avenues for further exploration, as discussed in Chapter 6. It marks progress for the community investigating STEVE, the picket fence, and subauroral processes as we try to understand how the extreme conditions which sometimes arise in the subauroral region affect the I-T system more broadly and what we can learn from them from a fundamental physics perspective.

Abstract

Recent studies suggest that, despite its aurora-like appearance, the picket fence may not be driven by magnetospheric particle precipitation but instead by local electric fields parallel to Earth's magnetic field. Here, we evaluate the parallel electric fields hypothesis by quantitatively comparing picket fence spectra with the emissions generated in a kinetic model driven by local parallel electric fields energizing ambient electrons in a realistic neutral atmosphere. We find that, at a typical picket fence altitude of 110 km, parallel electric fields between 40 and 70 Td (∼80 to 150 mV/m at 110 km) energize ambient electrons sufficiently so that, when they collide with neutrals, they reproduce the observed ratio of N_2 first positive to atomic oxygen green line emissions, without producing N_2^+ first negative emissions. These findings establish a quantitative connection between ionospheric electrodynamics and observable picket fence emissions, offering verifiable targets for future models and experiments.

Plain Language Summary

The 'picket fence' is a captivating visual phenomenon featuring vibrant green streaks often observed with and at lower altitudes than the rare purpleish-white arc called STEVE. It occurs in the subauroral sky, at lower latitudes than the auroral oval, raising questions about whether it is a type of aurora or a separate phenomenon. A recent hypothesis proposes that electric fields aligned with Earth's magnetic field in the dense part of the atmosphere where the picket fence forms might energize local electrons, which collide with the neutral atmosphere to create picket fence emissions. This distinguishes the picket fence from traditional auroras caused by energetic particles accelerated higher up in space which stream

down and collide with the upper atmosphere. In this study, we compare optical observations of the picket fence to a detailed calculation of the emissions produced by ambient electrons energized by parallel electric fields in the upper atmosphere. The results show that large parallel electric fields can indeed replicate the observed picket fence phenomenon. These findings offer important targets for future picket fence models and experiments. This research demonstrates that the picket fence serves as a valuable testing ground for understanding the chemistry and electrodynamics of Earth's upper atmosphere.

5.1 Introduction: Debate Over the Picket Fence's Origin

STEVE (Strong Thermal Emission Velocity Enhancement) is a rare ionospheric optical phenomenon characterized by a narrow mauve arc extending thousands of kilometers east/west across the subauroral sky (MacDonald et al., 2018) [210]. Concurrently with STEVE, vibrant green streaks known as the "picket fence" often appear at lower altitudes after the mauve arc develops and occasionally persist after it fades (Yadav et al., 2021; Martinis et al., 2022; Nishimura et al., 2023) [375, 215, 249]. STEVEs are associated with strong sub-auroral ion drifts (SAIDs) (Archer et al., 2019a) [10], but the mechanism behind the optical emissions is still debated (Harding et al., 2020) [126].

Early studies proposed that picket fence emissions, like auroras, are generated by magnetospheric particle precipitation (MacDonald et al., 2018; Chu et al., 2019; Nishimura et al., 2019; Bennett & Bourassa, 2021) [210, 48, 248, 27]. Like green aurora, the picket fence primarily consists of 557.7 nm green line (GL) emissions (Gillies et al., 2019) [110]. However, the picket fence spectrum published by Gillies et al. (2019) [110] and reanalyzed by Mende et al. (2019) [228] lacks 427.8 nm N_2^+ first negative (N_2^+ 1N) emissions, which are ubiquitous and prominent in auroral spectra (see Appendix D.2). The absence cannot be explained by a local N_2 depletion, as Mende et al. (2019) [228] also detect N_2 first positive (N_2 1P) emissions. Instead, Mende et al. (2019) [228] proposed that a local electron population with energies above 7.35 eV but below 18.75 eV, could, via collisions with the neutral atmosphere, generate the picket fence emission spectrum (sufficient for N_2^+ 1N emissions). However, they did not quantify how electrons might be locally energized to this energy range.

Recent studies by Lynch et al. (2022) [208] and Mishin and Streltsov (2022) [235] proposed that picket fence emissions arise when low-altitude electric fields parallel to Earth's magnetic field energize local electrons. Lynch et al. (2022) [208] demonstrate that ionospheric conductance gradients created by SAIDs create large field-aligned currents, potentially triggering tearing-mode instabilities similar to those observed in rayed auroral arcs. Mishin and Streltsov (2022) [235] simulated the ionospheric feedback instability (IFI) under SAID conditions. Their approximate solution of the Boltzmann equation indicated that parallel electric fields generated by the IFI might be sufficient to produce the suprathermal electron population responsible for the picket fence emissions. However, neither study con-

clusively demonstrated whether the electron population energized via their proposed method quantitatively reproduces the observed picket fence spectral features.

In this study, we conduct kinetic calculations to analyze the electron population energized by a parallel electric field in a realistic neutral atmosphere from 100 to 180 km, considering all relevant electron-neutral collisions. Additionally, we compare our calculated spectral features with those in ground-based picket fence observations. Our findings demonstrate that low-altitude parallel electric fields can accelerate local thermal electrons which quantitatively replicate observed picket fence spectra without requiring particle precipitation. Estimating the magnitude of these fields provides a benchmark for future models and observations. This work enables a quantitative comparison between ionospheric electrodynamic models and observable optical emissions, which previous studies have not achieved.

5.2 Picket Fence Spectral Observations

The Transition Region Explorer (TREx) Spectrograph in Lucky Lake, Saskatchewan captures visible (385-801 nm) spectral data for a narrow ($\sim$2.1° wide) North/South latitudinal slice of the sky. For additional details about TREx's operation and calibration, see Appendix D.1 and refer to Gillies et al. (2019) [110]. On April 10, 2018, the same night as the observations presented by Gillies et al. (2019) [110], TREx observed the picket fence several times between 6:28 and 8:00 UT. Figure 5.1(a) presents a keogram of the observations, showing the total observed luminosity as a function of elevation angle and time. A full spectrum (385-801 nm) is available at every point. Thin horizontal features brighter than the background are stellar contamination.

Figure 5.1(b) displays a keogram of the GL portion of the spectrum (555.2-560.7 nm). Picket fence spectra are identified following the method in Gillies et al. (2019) [110] and Mende et al. (2019) [228]. We fit a Gaussian function to the GL luminosity with respect to elevation angle at each time step, determining the elevation angle at the peak brightness μ and the standard deviation σ. For luminosity curves with a defined peak at least 200 R above background luminosity, the picket fence spectrum is selected at the elevation bin μ, while background spectra are selected at elevation bins $\pm 3\sigma$ away from μ. Picket fence spectra with stellar contamination are discarded, and contaminated background spectra are replaced by neighboring uncontaminated pixels. Figure 5.1(c) displays the extracted picket fence spectra (black dots) and the selected poleward (blue triangles pointing up) and equatorward (red triangles pointing down) backgrounds between 6:49 and 7:00 UT.

The picket fence is expected to lie between 97 and 150 km and be approximately aligned with the magnetic field (Archer et al., 2019b; Semeter et al., 2020) [11, 307]. The black dotted line in Figure 5.1(d) represents the look direction up the magnetic field, calculated using the International Geomagnetic Reference Field, Version 13 (IGRF13) (Wardinski et al., 2020; Michael, 2021) [364, 231]. Our kinetic model described in Section 5.3 assumes emissions originate from a uniform source at a single altitude, avoiding assumptions about the vertical parallel electric field profile. Consequently, we select picket fence spectra closer

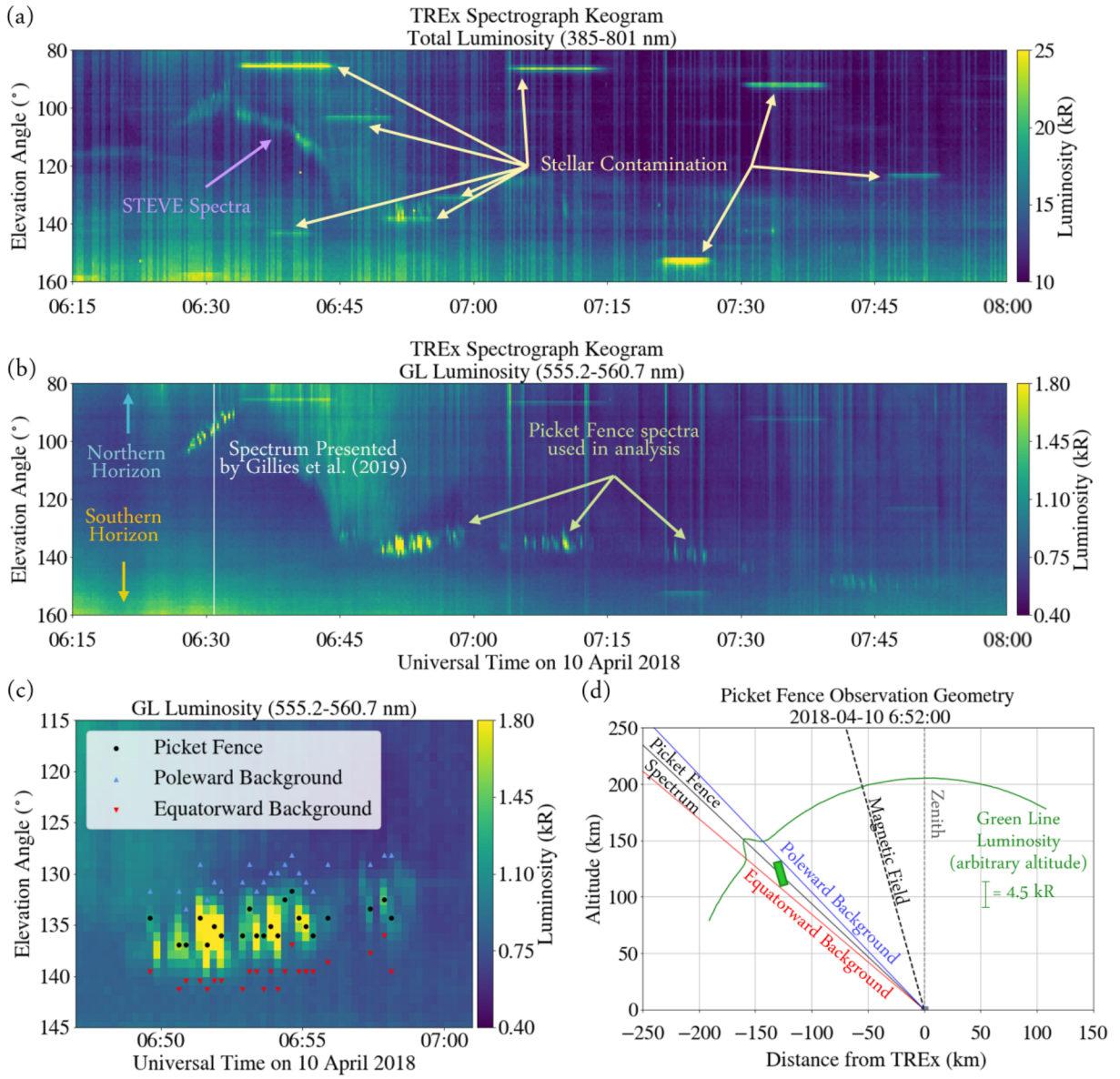

Figure 5.1: (a) Keogram of total TREx luminosity between 6:15 and 8:00 UT on April 10, 2018, showing STEVE emissions and stellar contamination. A full spectrum (385-801 nm) is available at every point. (b) Keogram of TREx GL observations (555.2-560.7 nm) during the same period, highlighting the picket fence observations. (c) Picket fence and background spectra extracted between 6:49 and 7:00 UT. Some spectra were removed due to stellar contamination. See text for details of selection process. (d) Approximate observation geometry for picket fence observed at 6:52 UT. The sample picket shown is only a representation as the altitude of the emissions is unknown.

to the horizon, away from the magnetic field look direction, to reduce the vertical profile intersected by the line-of-sight. Specifically, we use 45 uncontaminated picket fence spectra observed between 6:45 and 7:30 UT, all with elevation angles between 131° and 142°. Figure 5.1(d) depicts the picket fence observation geometry at 6:52 UT. The observed GL luminosity is projected onto an arc (shown as a green line arbitrarily depicted at 200 km for illustration purposes), and the equatorward and poleward picket fence boundaries are marked by solid red and blue lines, respectively. The observed picket must lie within the wedge formed by these boundaries, as illustrated by the green rectangle in Figure 5.1(d). Assuming that the picket fences are 5-25 km wide latitudinally (Liang et al., 2021a) [190], we estimate that the line-of-sight cuts through no more than 25 km of the altitudinal profile for the selected observations, with most examples cutting through no more than 15 km. Due to these observational constraints, our quantitative results in Section **??** represent vertical averages over a maximum of 25 km.

We isolate individual picket fence spectra by subtracting the average of their poleward and equatorward background spectra. The error in each spectrum is determined by propagating the standard deviation variations in the background spectra at each wavelength through the background subtraction. We compute median luminosities from the 45 picket fence spectra at each wavelength (Figure 5.2(a)), repeating the procedure for the background-subtracted spectra (Figure 5.2(b)). The dominant features are the 557.7 nm GL and the N_2 1P band system, while the 427.8 nm N_2^+ 1N emissions observed in the background spectra are absent in the picket fence spectrum, consistent with the findings of Mende et al. (2019) [228].

Instead of directly comparing the absolute observed brightness to our model results, which requires assuming the picket fence's latitudinal width and the local electron density, we focus on comparing the ratio of N_2 1P and GL luminosities. For the GL, we calculate the luminosity between 555.2-560.7 nm, accounting for the GL's spectral width. For N_2 1P, we calculate the luminosity between 642 and 700 nm. Although N_2 1P emissions extend to infrared (IR) wavelengths and TREx's range extends to 800 nm, we only consider this part of the spectrum to avoid larger errors near the edge of TREx's observational band and complications from O_2 atmospheric absorption above 700 nm.

To quantitatively compare the in situ ratio of N_2 1P to GL emissions, we must consider atmospheric transmission between the emission source and TREx. We apply an atmospheric transmission profile from Figure 1(a) of Morrill et al. (1998) [240], which corresponds to a source at 65 km observed from the ground at an elevation angle of 40°, similar to our observations. While the picket fence occurs at higher altitudes, most atmospheric scattering and absorption occur in the lower atmosphere, so this difference is assumed to be negligible (Meier, 1991) [227]. According to Morrill et al. (1998) [240], the transmittance at 557.7 nm for GL is 0.42, and the average transmittance for N_2 1P between 642 and 700 nm is 0.53. This results in a transmittance ratio of $\sim$1.26 between the two features.

We perform linear regression on the data using the model $y = \alpha x + \beta$, where y represents the N_2 1P luminosities, x represents the GL luminosities, α represents the luminosity ratio, and β represents the intercept. We estimate the best fit parameters and their errors following the method described by Gull (1989) [117], applying Bayesian statistics to linear regression

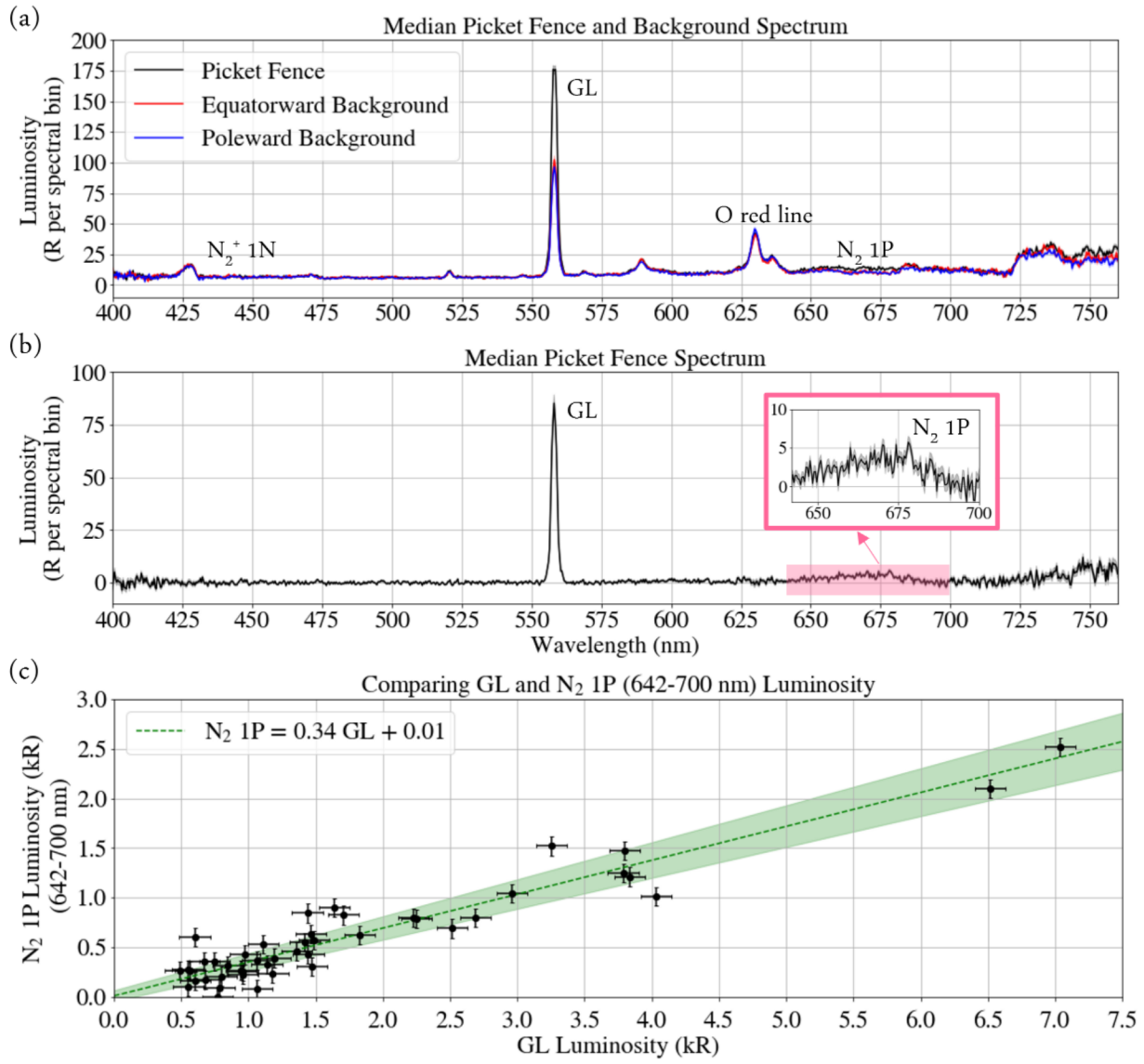

Figure 5.2: (a) Median picket fence spectrum (black) and poleward (blue) and equatorward (red) background spectra. (b) Median picket fence spectrum after background subtraction. Inset: N_2 1P spectrum (642-700 nm). (c) Ratio of N_2 1P (642-700 nm) to GL luminosity from the TREx observations, scaled to account for atmospheric transmission.

with errors in both variables. Our analysis yields $\alpha = 0.34 \pm 0.03$ and $\beta = 9.4 \pm 56.9$ R. These results are displayed in Figure 5.2(c). Mende et al. (2019) [228] conducted a similar analysis without considering transmission effects and found an N_2 1P to GL ratio of 0.39. If we neglect transmission effects, our ratio is $\alpha = 0.43 \pm 0.04$, which is consistent with Mende et al. (2019)'s [228] findings. We emphasize that the ratio for green aurora is 0.72 (Vallance Jones, 1974) [353], significantly different from our picket fence results. This observation reinforces that the picket fence and green aurora are likely generated by different mechanisms.

5.3 Kinetic Modeling of Emissions Driven by Parallel Electric Fields

Successful models of mechanisms generating the picket fence must be able to achieve the observed ratio of 0.34 between N_2 1P (642-700 nm) and GL emissions while keeping N_2^+ 1N emissions undetectable. Here, we explore whether a kinetic model driven solely by parallel electric fields can replicate these features. The following subsections outline the modeling process, including determining the atmospheric and ionospheric inputs, analyzing the effect of a parallel electric field on the local electron energy distribution function (EEDF), and employing steady-state kinetic modeling to calculate volume emission rates (VERs) of excited atomic and molecular states. Figure 5.3 summarizes the modeling process.

Model Inputs: Atmospheric and Ionospheric Conditions

We use established models to characterize atmospheric, ionospheric, and magnetic field conditions for the time, location, and geomagnetic conditions of the TREx observations described in Section 5.2. The Naval Research Laboratory's Mass Spectrometer Incoherent Scatter Radar (MSIS) model version 2.1 provided profiles of neutral temperature and densities for eight neutral species (Picone et al., 2002; Emmert et al., 2021, 2022; Lucas et al., 2023) [266, 70, 71, 205]. Ionospheric electron density and temperature profiles were taken from the International Reference Ionosphere 2016 (IRI16) (Bilitza et al., 2017; Ilma, 2017) [31, 153]. The magnitude of the magnetic field was obtained from IGRF13 (Wardinski et al., 2020; Michael, 2021) [364, 231]. The resulting profiles are shown in Figure D.2 in Appendix D.4.

Using these profiles assumes that picket fence conditions are similar to climatological conditions. However, STEVE and the picket fence are associated with intense SAIDs (MacDonald et al., 2018; Archer et al., 2019a) [210, 10], rare events characterized by narrow channels of hot, fast-flowing, and depleted plasma (Liang et al., 2021b) [188]. Although IRI does not replicate these conditions, the ratio between N_2 1P (642-700 nm) and GL emissions is independent of electron density, so this does not affect our results. Additionally, Mishin and Streltsov (2022) [235] suggested that SAID conditions may lead to neutral upwelling, which is not captured by MSIS and which may decrease the O/N_2 ratio at picket fence altitudes. Doubling the O/N_2 ratio input in our model introduces changes on the order of

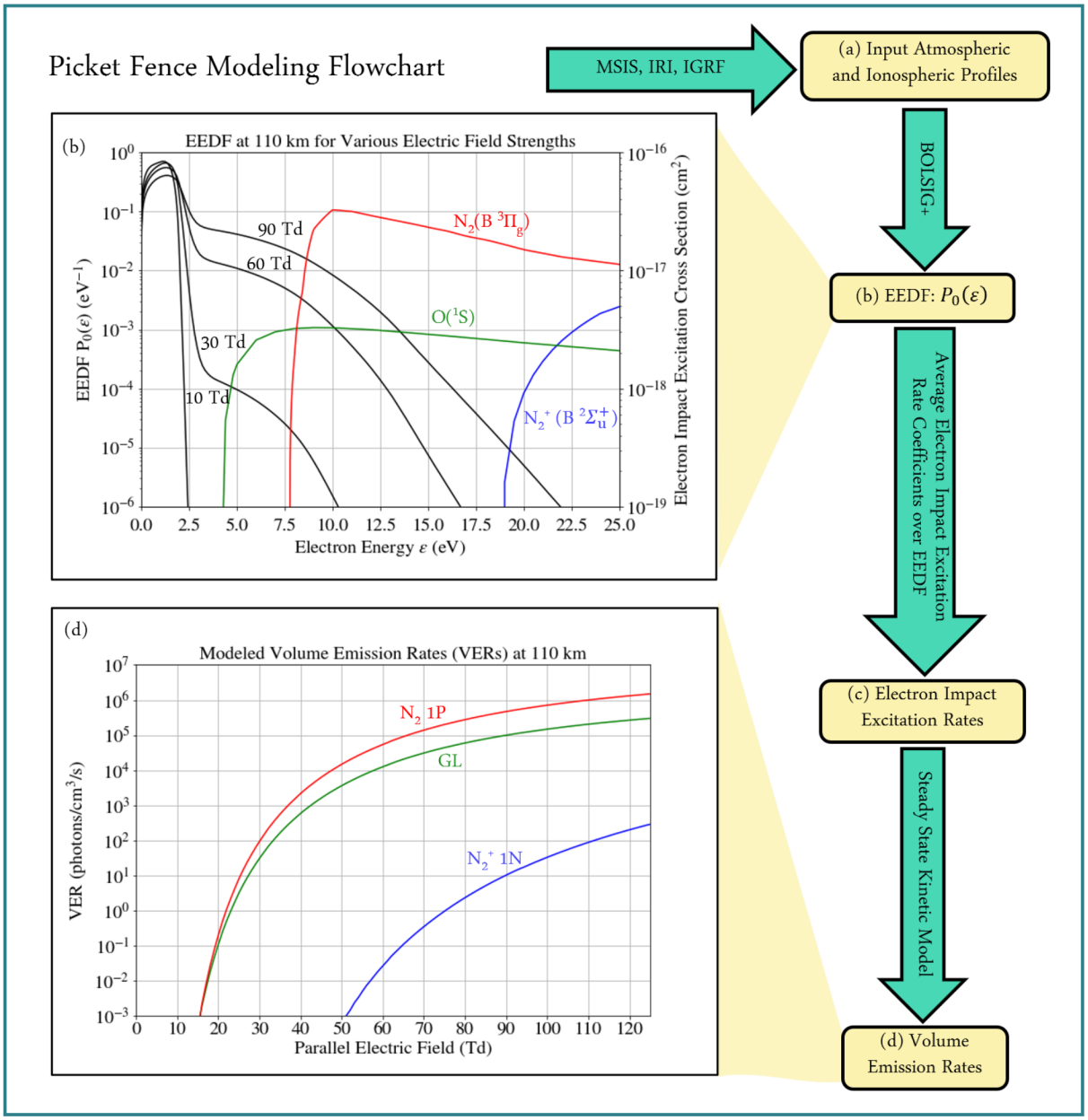

Figure 5.3: Modeling process flowchart of steps (a) - (d), with subfigures to further elucidate steps (b) and (d). (b) EEDFs at 110 km for different parallel electric field strengths, overlaid with electron impact excitation cross sections for $O(^1S)$, $N_2\,(B^3\Pi_g)$, and $N_2^+\,(B^2\Sigma_u^+)$. (d) VERs at 110 km for GL, N_2 1P, and N_2^+ 1N calculated with the steady state kinetic model.

25% to our electric field magnitude predictions which, while significant, do not alter our qualitative findings.

Calculating EEDFs and Electron Impact Excitation Rates

We used BOLSIG+ (version 12/2019) (Hagelaar & Pitchford, 2005) [120] to solve the Boltzmann equation, quantifying changes in the EEDF with altitude and parallel electric field strength. BOLSIG+ calculates a steady-state solution under a uniform electric field, accounting for the effects of electron-neutral collisions in a user-defined atmosphere. Time-dynamics, non-local electron transport, and electric field gradients are not considered, and we neglect the effect of Coulomb collisions (Gurevich, 1978) [118]. For additional details about BOLSIG+, see Hagelaar and Pitchford (2005) [120]. Fractional densities of N_2, O_2, and O were obtained from MSIS. Electron impact collisional cross sections of N_2, O_2, as packaged with the BOLSIG+ software, were obtained from the LXCat Database (Pancheshnyi et al., 2012) [258] based on data published by Phelps and Pitchford (1985) [265] and Lawton and Phelps (1978) [183], respectively. We added the O cross sections, obtained from Laher and Gilmore (1990) [181], to BOLSIG+. Appendix D.3 demonstrates the method used to calculate electron impact excitation rate coefficients using the EEDF and electron impact excitation cross sections.

We consider altitudes between 100 and 180 km, where the 180 km upper bound is well above the expected picket fence altitude (Archer et al., 2019b) [11]. The 100 km lower bound approximately marks the division between the atmospheric collisional regime, where collisions among excited states are important, and the radiational regime dominated by electron impact excitation (Yonker & Bailey, 2020) [379]. We considered reduced parallel electric fields ranging from $E/N = 0$ to 120 Townsend (Td) where E is the electric field in V/m, N is the neutral density in m^{-3}, and 1 Td = 10^{-21} V m^2. The upper limit corresponds to the breakdown field E_k in conventional air at low altitudes (Raizer, 1991, p. 137) [276].

Figure 5.3(b) displays EEDFs at 110 km for parallel electric fields of 10, 30, 60, and 90 Td (equivalent to 20, 60, 115, and 170 mV/m at 110 km, respectively). The figure highlights several electron impact collisional cross sections: $O(^1S)$ in green, $N_2\,(B^3\Pi_g)$ in red, and $N_2^+\,(B^2\Sigma_u^+)$ in blue. Stronger electric fields stretch the tail of the EEDF to higher energies, enhancing high-energy electron populations and increasing electron impact excitation rate coefficients.

Calculating Volume Emission Rates

To calculate theoretical VERs for N_2 1P, GL, and N_2^+ 1N emissions, we implement a steady-state kinetic model which accounts for additional production and loss processes for excited states of N_2 and O. For N_2 1P emissions, produced through relaxation of the $N_2\,(B^3\Pi_g)$ state to the $N_2\,(A^3\Sigma_u^+)$ state, we account for radiative cascade from higher N_2 triplet states (Meier, 1991) [227]. For GL emissions, produced via relaxation of the $O(^1S)$ state to the $O(^1D)$ state, we incorporate additional $O(^1S)$ production via O quenching of $N_2\,(A^3\Sigma_u^+)$. We also consider

additional quenching of $O(^1S)$ and N_2 $(A^3\Sigma_u^+)$ by O, O_2, and NO. N_2^+ 1N emissions occur via relaxation of N_2^+ $(B^2\Sigma_u^+)$ state to the ground state of N_2^+ following electron impact ionization (Shemansky & Liu, 2005) [311]. For more details about these calculations, see Appendix D.4.

We compared these calculated VERs to those obtained by inputting our electron impact excitation rates into Yonker and Bailey (2020)'s [379] model, which includes interactions between individual N_2 excited states and resolves the vibrational states of N_2. Between 105 and 150 km, the difference in the N_2 1P to GL emission ratio between our model and Yonker and Bailey (2020)'s [379] is below 15%, demonstrating excellent agreement. At lower altitudes, where the collisional regime dominates, the difference remains below 40%. This comparison is presented in more detail in Appendix D.5.

Figure 5.3(d) presents the modeled VERs for N_2 1P, GL, and N_2^+ 1N at 110 km as a function of parallel electric field strength. The VERs are directly proportional to electron density, which may be depleted under SAID conditions, so the actual VERs may be reduced if the picket fence lies within the depleted channel. However, the ratio between these VERs remains independent of the electron density.

5.4 Comparison with Observations

Figures 5.4(a) and 5.4(b) present calculated N_2 1P to GL VER ratios for parallel electric fields in units of Td and mV/m, respectively, where the N_2 1P spectrum has been truncated to only include the 642-700 nm portion. The IR picket fence N_2 1P spectrum has never been measured, so we use an estimated scaling factor of ∼8% determined from modeling of the N_2 1P spectrum in aurora, presented in Table 4.12 of Vallance Jones (1974) [353]. The observed ratio and its data-driven uncertainty are indicated in Figures 5.4(a) and 5.4(b) by the black dotted lines and shaded regions, respectively. At 110 km, the observed N_2 1P (642-700 nm) to GL ratio is reproduced for parallel electric field strengths between 40 and 70 Td (∼80 to 150 mV/m at 110 km). Assuming a picket fence width of ∼10 km, a uniform emission source, and electron densities given by IRI, this corresponds to GL luminosities between 0.5 and 31 kR, consistent with observations.

If the N_2 $(B^3\Pi_g)$ vibrational distribution differs between aurora and the picket fence, the shape of the N_2 1P spectrum may also differ. A test was performed in which our electron impact excitation rates were inputs to Yonker's vibrationally-resolved model; the results suggested the 642-700 nm portion may account for 12-14% of the total N_2 1P spectrum. Adopting this higher scale factor leads to a ∼50% reduction in our predicted parallel electric field strength at 110 km. Obtaining a picket fence N_2 1P spectrum extending into the IR would enhance confidence in our quantitative estimates of parallel electric field strength, although our qualitative findings remain unchanged.

The calculated N_2^+ 1N to GL VER ratios are presented in Figure 5.4(c). Even for large parallel electric field strengths, this ratio remains below 10^{-3} at picket fence altitudes, undetectable by the TREx spectrograph for even the brightest picket fence events. Thus, we

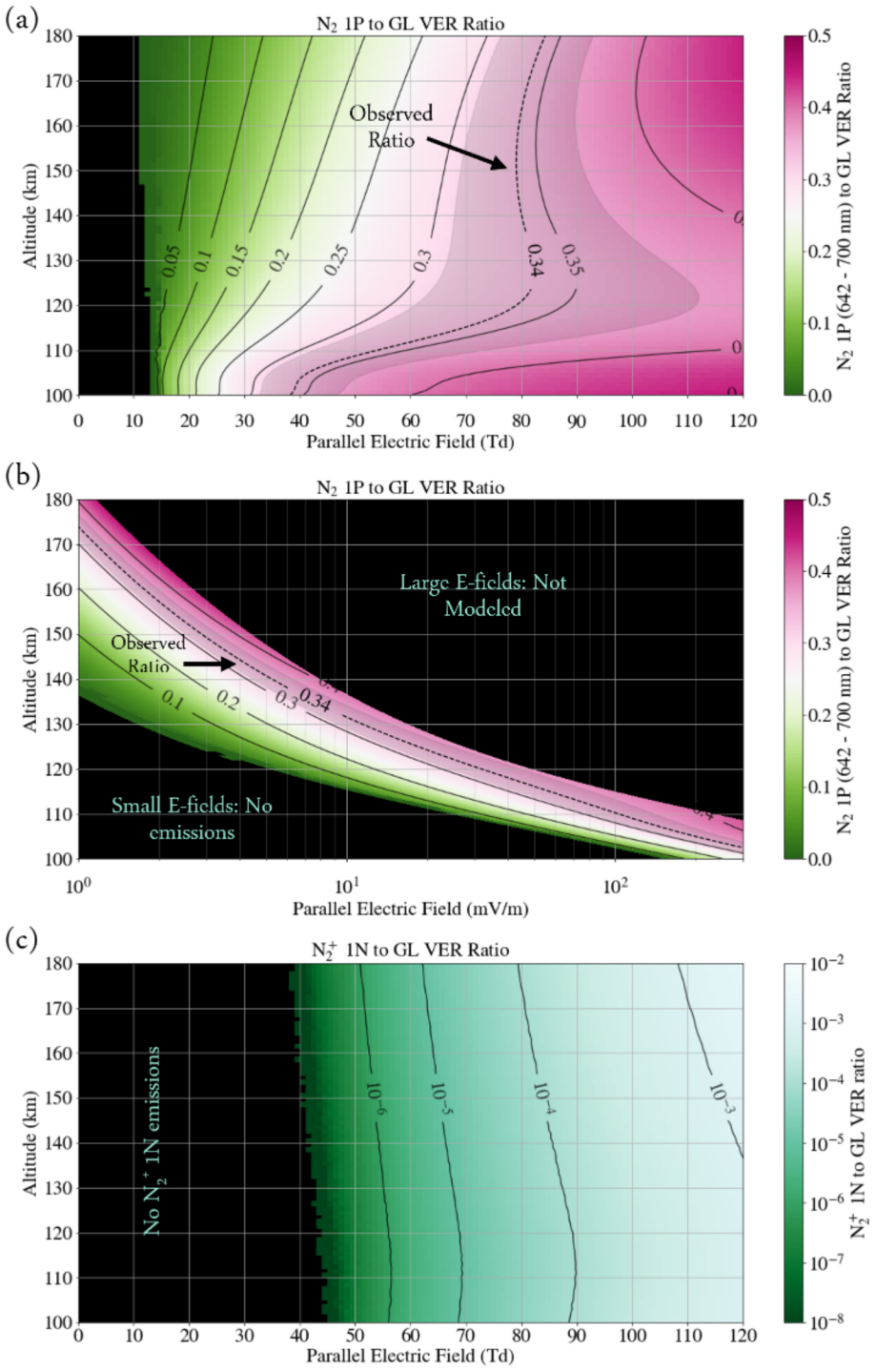

Figure 5.4: (a) Calculated N_2 1P (642-700 nm) to GL VER ratios. Observed luminosity ratios and margins of error are indicated by the black dotted line and shaded region, respectively. (b) The same as (a), but with parallel electric field strength in mV/m. (c) Calculated N_2^+ 1N (421-431 nm) to GL VER ratios.

find that parallel electric fields of realistic magnitudes will not produce observable N_2^+ 1N emissions.

These results demonstrate that a model driven by parallel electric fields can reproduce all of the key picket fence spectral features at picket fence altitudes, strongly supporting local parallel electric fields as a plausible driving mechanism for picket fence emissions.

5.5 Discussion and Conclusion

This study provides quantitative evidence that spectral features of picket fence emissions can be reproduced by a kinetic model driven solely by local parallel electric fields, offering a substantiated alternative to magnetospheric precipitation, which lacks supporting spectral evidence. As a reference point for future observations and modeling, we find that at 110 km 40-70 Td (∼80-150 mV/m at 110 km) parallel electric fields produce observationally-consistent picket fence spectra. The developed kinetic and chemical modeling tools could be used as post-processors or two-way coupled into global or regional magnetohydrodynamic models to simulate the picket fence or its potential connections to other subauroral phenomena such as SAIDs, STEVE, or stable auroral red (SAR) arcs (Harding et al., 2020; Gallardo-Lacourt et al., 2021; Liang et al., 2021b; Martinis et al., 2022; Gillies et al., 2023) [126, 97, 188, 215, 111].

While we have demonstrated the plausibility of parallel electric fields as a driving mechanism for the picket fence, further measurements are essential to validate or challenge this hypothesis. Our modeling demonstrates that parallel electric fields of magnitudes considered here would not generate observable N_2^+ 1N emissions. Therefore, any future observations of N_2^+ 1N emissions in a picket fence would prompt reassessment of this mechanism. Furthermore, Appendix D.6 describes an extension of our model to predict ultraviolet (UV) spectral features of the picket fence, which could be confirmed by space-based observations. For the brightest picket fence events, we find that N_2 Vegard-Kaplan (VK), Lyman-Birge-Hopfield (LBH), and N_2 Second Positive emissions could be promising observational targets. However, 1356 Å atomic oxygen emissions are unlikely to be observable, as shown in Figure D.7. Additionally, expanding this analysis to include more picket fence spectra would help capture the true extent of the variability in these spectra and further assess the consistency with the parallel electric field driving mechanism.

If parallel electric fields indeed drive picket fence emissions, the structure of the picket fence constrains the electric field's structure. Under the influence of a parallel electric field at picket fence altitudes, the EEDF equilibrates in between ∼0.1 and 50 ms, increasing with altitude (Gurevich, 1978) [118]. Given the ∼0.7 s radiative lifetime of $O(^1S)$ (Itikawa & Ichimura, 1990) [159], and the several microseconds radiative lifetime of $N_2\,(B^3\Pi_g)$ (Eyler & Pipkin, 1983) [77], visible emissions should emerge within 1 s of the parallel electric field onset, depending on the altitude. While electron transport or neutral winds may induce some blurring, the emissions should predominantly trace the parallel electric fields. As a result, the electric fields would exhibit similar structure to the picket fence itself: aligned

in a rayed east/west arc, confined between 97 and 150 km in altitude, and organized along the local magnetic field (Archer et al., 2019b) [11]. However, the non-field-aligned emission 'streaks' below the picket fence (103-108 km) may not trace parallel electric fields, as these are hypothesized to be a consequence of plasma turbulence (Semeter et al., 2020) [307].

While this study refrains from speculating on sources or resulting altitude profiles of parallel electric fields, Lynch et al. (2022) [208] and Mishin and Streltsov (2022) [235] suggest that parallel electric fields could be the consequence of different ionospheric instabilities driven by extreme SAIDs. Lynch et al. (2022) [208] suggest that wave electric fields parallel to the magnetic field, arising from a tearing-mode instability, could drive the picket fence. Although they do not model the magnitude or frequency of these waves, our study's results are applicable to wave electric fields which vary significantly slower than the EEDF equilibration timescale. Mishin and Stretlsov (2022)'s [235] simulation of the ionospheric feedback instability yielded maximum field strengths of ∼26 mV/m, occurring at 130-140 km. Our predictions achieved the observed N_2 1P to GL emissions ratio for ∼7 mV/m electric field strengths at 135 km, showing reasonable agreement with Mishin and Stretlsov (2022)'s [235] results.

Local parallel electric fields may play a significant role in the ionosphere beyond the picket fence. In the auroral region, certain optical features share spectral characteristics with the picket fence and cannot be explained by precipitation. Fragmented aurora-like emissions (FAE) are non-field aligned green patches showing GL and N_2 1P emissions but lacking N_2^+ 1N (Dreyer et al., 2021) [63]. Enhanced aurora (EA) consist of thin, bright layers within regular aurora, exhibiting increased N_2 1P relative to N_2^+ 1N (Hallinan et al., 1997) [122]. Similar to the picket fence, both FAE and EA are suggested to result from suprathermal electron populations locally generated by parallel electric fields or wave-particle interactions (Hallinan et al., 1997; Dreyer et al., 2021) [122, 63]. Karlsson and Marklund (2005) [168] simulated EA using a simple auroral current model, generating parallel electric fields with maximum strength of ∼30 mV/m peaking between 80-120 km. Collectively, this suggests that the picket fence might represent one example of a class of aurora-like emissions generated locally by parallel electric fields, not magnetospheric particle precipitation, although the sources of these fields may differ. These findings underscore the potential significance of local parallel electric fields. In particular, since visible and ultraviolet auroral observations are increasingly used to trace particle precipitation and infer magnetospheric activity, it is important to better understand and quantify other sources of emission beyond particle precipitation. Thus, investigating the prevalence and sources of these parallel electric fields warrants further attention from the broader scientific community.

The most definitive way to verify the existence of these parallel electric fields is with in situ measurements. While magnetospheric parallel electric fields have long been associated with auroral particle acceleration and precipitation (Marklund, 1993; Shelley, 1995; Paschmann et al., 2003)[212, 310, 259], static current closure models predict parallel electric fields from the ionospheric F-region to the E-region to be orders of magnitude weaker than perpendicular fields (μV/m rather than mV/m) (e.g., Farley Jr, 1959) [79]. Ionospheric electric field measurements routinely assume zero parallel electric field when deriving a full vector perpen-

dicular field from two-dimensional measurements (Pfaff et al., 2021) [263]. However, satellite measurements of enhanced downward currents and modeling of the ionospheric response suggest significant parallel fields in the collisional base of the D and E regions (Marklund et al., 1997; Karlsson & Marklund, 1998) [213, 167], but to our knowledge, no measurements have probed the existence of these fields. Confirming the existence of these fields is crucial for advancing our understanding of a wide variety of phenomena in the auroral and subauroral regions. Based on our study's results, we propose that attempting to measure these electric fields in situ should be a priority for the space physics community.

Chapter 6

Conclusion and Directions for Future Work

This dissertation presented three studies which examine ionospheric and thermospheric responses to three different energy drivers. This concluding chapter summarizes the findings pertaining to each considered driver, outlining the contributions that this dissertation has made to the scientific community and highlighting the remaining open questions and directions for future work.

6.1 Ionospheric Effects of the 2022 Tonga Volcanic Eruption

The first I-T system driver considered was an explosive, impulsive event originating in the lower atmosphere. In particular, this dissertation used data from NASA's ICON mission to investigate the near-field (within ∼5,000 km) ionospheric effects of the 2022 Tonga volcanic eruption.

Chapter 3 presented Gasque et al. (2022) [108], which focused on understanding the rapid ionospheric changes which occurred within an hour of the eruption. The study presented observations of extreme (up to several hundred m/s) zonal and vertical plasma drifts in the ionosphere conjugate to the ionosphere near the volcano only ∼45 minutes after the eruption. It was found that the extreme drifts were likely caused by a thermospheric wave impulse with neutral wind directed away from the eruption site with amplitudes exceeding 300 m/s and with an effective propagation velocity from the eruption site of 600±50 m/s. These winds, colliding with ions in the ionospheric dynamo region near the volcano, caused charge separation and therefore polarization electric fields, which were transmitted along the magnetic field to the ICON observatory's location via Alfvén waves, where they caused the extreme $\vec{E} \times \vec{B}$ ion drifts observed by ICON. The observations we presented are the first direct detection in space of the near-immediate dynamo effects of a volcanic eruption, and show evidence for rapid plasma redistribution in the near field shortly after the eruption.

Future work is planned which will expand upon the previous study to examine the near-field ionospheric effects of the eruption over a 24-hour period. Analysis of ion densities measured by the ICON observatory near the eruption site have revealed a significant top-side ionospheric depletion spanning approximately 2,000 km in radius, which persisted until sunrise about 14 hours later, when plasma production resumed. While similar depletions have been observed following earthquakes, this event stands out due to its larger spatial extent, greater depletion magnitude, and longer duration compared to previous ionospheric depletions associated with natural hazards.

The 2022 Tonga eruption was one of the largest volcanic eruptions of the satellite era, and therefore serves as a crucial test case for evaluating understanding of the ionospheric effects of such phenomena. Following the event, changes in thermospheric density changed the drag on low-Earth orbiting satellites (Li et al., 2023) [187], and satellite-based navigational systems (e.g., Ke et al., 2023) [170]. Current ionospheric models do not yet successfully replicate the observed plasma drifts or the subsequent ionospheric hole. The observations provided in this dissertation will provide important benchmarks for future modeling efforts seeking to accurately capture the near-field effects of this event. While this eruption had significant global consequences, not all impulsive events exhibit such far-reaching impacts. Therefore, focusing on studying the near field may be crucial for extrapolating the outcomes of this event to smaller-scale events in the future.

6.2 Solar Terminator Waves in the Terrestrial Thermosphere

The second energy driver examined in this dissertation was the abrupt change in solar heating associated with the passage of the solar terminator. Chapter 4 presented Gasque et al. (2024) [106], which provided the first remotely observed evidence of neutral wind signatures associated with solar terminator waves. Several years of neutral wind observations from ICON/MIGHTI were analyzed to generate average maps of the zonal and meridional thermospheric winds as a function of season, local time, and latitude near the equator. Consistent with previous studies (Forbes et al., 2008; Liu et al., 2009) [89, 199], it was observed that the thermospheric signatures of these waves are more pronounced near the evening terminator compared to the morning terminator and are more prominent under solstice conditions than equinox conditions. This study reported that, under solstice conditions, the average scale size of the terminator waves was around 3,000 km, and the wave's phase front is inclined $\sim 30^\circ$ to 40° with respect to the solar terminator. This study also reported the first altitude profile of these features, showing that they have a large vertical wavelength (exceeding 200 km) above 200 km altitude. By comparing the observations with the results of various whole-atmosphere simulations, it was determined that the lower atmosphere plays an important role in the generation of these waves, similar to the conclusions of Miyoshi et al., (2009) [239].

This investigation showed that, under solstice conditions, the solar terminator wave signature above 200 km is, on average, the largest feature in the meridional winds and a prominent feature after the removal of the migrating diurnal tide in the zonal winds. As such, it may play a currently under-recognized role in driving ionospheric dynamics. The effects of atmospheric tides on ionospheric processes, such as the ionospheric wind dynamo and momentum transfer due to ion-neutral collisions, have been investigated by many prior studies (e.g., Forbes & Lindzen, 1976; Richmond & Roble, 1987; Millward et al., 2001; Immel et al., 2006; Liu & Richmond, 2013) [88, 285, 234, 158, 195]. However, there has never been a comprehensive study of the effects of evening thermospheric solar terminator waves on the ionosphere. Studies of solar terminator waves in ionospheric total electron content have found that morning terminator waves are more prominent than evening waves in the ionosphere (e.g., Galushko et al., 1998; Afraimovich, 2008; Song et al., 2013; Ding et al., 2014) [101, 3, 325, 61], and the reason for the discrepancy is currently unknown. Furthermore, it is now understood that daily tidal variability contributes significantly to daily ionospheric variability (e.g., Liu, 2016) [194], but no studies to date have investigated the daily variability of solar terminator waves, either with models or observations.

This work has therefore revealed several open questions which could be addressed by future studies. These questions include:

- Why is the evening signature of thermospheric solar terminator waves more prominent than the morning signature? And why is the opposite effect observed in ionospheric data?
- Why is the thermospheric solar terminator wave phase front inclined with respect to the terminator?
- What is the specific physical mechanism that generates these wave signatures, and where does it occur in the atmosphere?
- How do these waves couple to the ionosphere, and what effect do they have on ionospheric dynamics?
- How variable are these waves, and how might their variability affect ionospheric variability?

Given that these features are already well-reproduced in several whole-atmosphere models, including WACCM-X and HIAMCM, further investigation into the mechanisms underlying these waves may be possible through targeted modeling studies. For example, one could explore whether gravity waves play a significant role in solar terminator wave generation by conducting simulation runs in which gravity wave generation is "turned off" and observing the resulting changes in solar terminator wave morphology. Such targeted modeling studies can provide valuable insights into the processes driving solar terminator wave dynamics. Although the ICON mission is no longer operational and cannot provide additional observations of thermospheric solar terminator waves, upcoming planned missions to study the I-T

system, such as the Geospace Dynamics Constellation (GDC) and Dynamic, hold promise for providing additional observations that will enable further study of these phenomena.

6.3 Picket Fence Optical Emissions

The final driver considered was fast ion flows in the subauroral region which are associated with unusual optical phenomena in the subauroral ionosphere. Chapter 5 presented Gasque et al. (2023) [107], which studied the physical mechanisms which produce emissions in the picket fence. Using a kinetic model of a realistic neutral atmosphere, it was possible to calculate the modifications in the local electron energy distribution function that results when electric fields parallel to Earth's magnetic field energize local electrons. The study showed that, at a typical picket fence altitude of 110 km, electric fields with magnitudes between 40 and 70 Td (∼80 - 150 mV/m at 110 km) energize local thermal electrons sufficiently such that, when the electrons collide with and excite neutral atoms and molecules, the observed picket fence spectrum can be reproduced. Specifically, the study demonstrated that a realistic neutral atmosphere and ionosphere influenced by these parallel electric fields will reproduce the observed ratio of N_2 first positive to atomic oxygen green line emissions without generating N_2^+ first negative emissions. Notably, this study quantitatively offered an alternative mechanism to produce picket fence observations that does not rely on magnetospheric particle precipitation, distinguishing the picket fence from typical aurora.

Following this study, numerous open questions about the picket fence and related subauroral and auroral optical phenomena remain, including:

- How do the parallel electric fields arise at picket fence altitudes? Are they driven though ionospheric instabilities such as the tearing mode instability (Lynch et al., 2022) [208] or the ionospheric feedback instability (Mishin & Streltsov, 2022) [235], or another mechanism? Are these mechanisms also responsible for the structure of the picket fence?

- How are STEVE and the picket fence related electrodynamically? Under what conditions can one appear without the other? Given the recent observations of SAR arcs evolving into STEVE (Martinis et al., 2022; Gillies et al., 2023) [215, 111], how are SAR arcs related? Also, what is the relation to the detached green 'streaks' that sometimes appear beneath the picket fence (Semeter et al., 2020) [307]?

- Given their spectral similarity to the picket fence, are auroral phenomena such as fragmented aurora-like emissions (FAE) (Dreyer et al., 2021) [63] and enhanced aurora (e.g., Hallinan et al., 1985; Karlsson et al., 2005) [121, 168], also driven by parallel electric fields?

This study contributes to a broader effort towards developing a unified model of subauroral optical phenomena. A successful model will integrate both large-scale electrodynamics

and the type of kinetic modeling demonstrated in this work to quantitatively reproduce the observed optical emissions. This aligns with a broader trend in the field, moving away from qualitative descriptions of optical forms and potential drivers towards more quantitative approaches (e.g., Solomon, 1991) [319]. Further observational follow-ups to the study, encompassing observations of picket fence spectra over multiple nights, would help evaluate the variability of the picket fence spectrum and consequently the variability of the predicted parallel electric fields. Additionally, while previous studies have proposed various ionospheric instabilities as potential mechanisms for generating the picket fence, additional modeling is necessary to confirm whether these instabilities can produce sufficiently large parallel electric fields to induce picket fence emissions.

The most definitive way to verify the existence of these parallel electric fields is with in-situ measurements, since electric fields cannot be measured remotely. Unfortunately, due to the high density of the neutral atmosphere at picket fence altitudes, a satellite placed in orbit at 100 km would decay into Earth's atmosphere in less than a day (e.g., Sebestyen et al., 2018) [306]. Additionally, the highest altitude achieved by a NASA balloon measurement has only been about 50 km.[1] The only space vehicles which routinely make measurements at picket fence altitudes are sounding rockets (e.g., Palmroth et al., 2020) [257]. Unfortunately, the picket fence is a rare optical phenomena, which would provide significant challenges for making in situ measurements during a standard two week launch window. However, it may be possible to measure parallel electric fields within other, more common, optical phenomena.

The discussion section of Gasque et al. (2023) [107] (Chapter 5.5 of this dissertation) highlighted the spectral similarity between the picket fence and other auroral optical phenomena, such as fragmented aurora-like emissions (FAE) (Dreyer et al., 2021) [63] and enhanced aurora (e.g., Hallinan et al., 1985; Karlsson et al., 2005) [121, 168]. Notably, all these phenomena exhibit more green line or N_2 first positive emissions relative to N_2^+ first negative emissions compared with typical aurora. Among these, the enhanced aurora, depicted in the right panel of Figure 6.1 alongside a "regular" aurora on the left, are perhaps the most common, occurring in as many as $\sim$50% of aurora (Hallinan et al., 1985) [121]. As shown in Figure 6.1, while the regular aurora has a smooth brightness profile with altitude, the enhanced aurora appears as a sharply defined layer of enhanced brightness embedded within the regular aurora which cannot be explained with traditional models of magnetospheric particle precipitation (Hallinan et al., 1997) [122]. Modeling by Karlsson et al. (2005) [168] suggested that the enhanced aurora may also be driven by parallel electric fields.

The work presented in Chapter 5 of this dissertation heavily influenced the development of a rocket proposal to attempt to make the first in-situ measurements of parallel electric fields in the collisional base of the ionosphere associated with enhanced aurora. The proposal was submitted to NASA's Low Cost Access to Space (LCAS) program in fall of 2023, and, as of the time of this writing, we have not yet received a funding decision. However, if selected, this mission will seek to determine whether the enhanced aurora are driven by local parallel electric fields, and, if so, whether these fields contribute significantly to auroral

[1] See, e.g., `https://www.nasa.gov/scientificballoons/faqs/`.

Figure 6.1: Images of two types of aurora, both captured by Vincent Ledvina (theauroraguy.com). (Left) A 'typical' aurora which has a smooth brightness profile with altitude. (Right) An 'enhanced' aurora, which shows a sharp discontinuity in the brightness profile with altitude that cannot be explained by traditional magnetospheric particle precipitation models.

emissions and energy deposition. It is hoped that this mission would serve as a pathfinder to a STEVE/picket fence rocket campaign.

6.4 Overarching Conclusions

This dissertation served as an exploration of I-T coupling and phenomena through the lens of three different drivers. The work used a combination of observational data, in particular from NASA's ICON observatory and the University of Calgary's TREx spectrograph, in concert with theoretical calculations, kinetic modeling, and whole-atmosphere simulations to improve our knowledge and understanding of various ionospheric and thermospheric phenomena. Furthermore, it has paved the way for multiple avenues of future research, providing benchmarks for future modeling studies and highlighting the need for new observations, as exemplified by the proposed rocket campaign. Ultimately, the findings presented in this dis-

sertation will advance our understanding of the I-T system and bolster our ability to forecast its behavior in response to diverse energy inputs, thereby aiding in mitigating the risk to human activities.

Bibliography

[1] Ercha Aa et al. "Pronounced suppression and X-pattern merging of equatorial ionization anomalies after the 2022 Tonga volcano eruption". In: *Journal of Geophysical Research: Space Physics* 127.6 (2022), e2022JA030527.

[2] Ercha Aa et al. "Significant equatorial plasma bubbles and global ionospheric disturbances after the 2022 Tonga volcano eruption". In: *Earth and Space Science Open Archive* (2022), p. 17. DOI: 10.1002/essoar.10510637.1. URL: https://doi.org/10.1002/essoar.10510637.1.

[3] EL Afraimovich. "First GPS-TEC evidence for the wave structure excited by the solar terminator". In: *Earth, planets and space* 60 (2008), pp. 895–900.

[4] VS Airapetian et al. "Impact of space weather on climate and habitability of terrestrial-type exoplanets". In: *International Journal of Astrobiology* 19.2 (2020), pp. 136–194.

[5] S-I Akasofu. "The development of the auroral substorm". In: *Planetary and Space Science* 12.4 (1964), pp. 273–282.

[6] Hannes Alfvén. "Existence of electromagnetic-hydrodynamic waves". In: *Nature* 150.3805 (1942), pp. 405–406.

[7] Angel Amores et al. "Numerical simulation of atmospheric Lamb waves generated by the 2022 Hunga-Tonga volcanic eruption". In: *Geophysical Research Letters* (2022), e2022GL098240.

[8] PC Anderson, RA Heelis, and WB Hanson. "The ionospheric signatures of rapid subauroral ion drifts". In: *Journal of Geophysical Research: Space Physics* 96.A4 (1991), pp. 5785–5792.

[9] Edward V Appleton. "Two anomalies in the ionosphere". In: *Nature* 157.3995 (1946), pp. 691–691.

[10] WE Archer et al. "Steve: The optical signature of intense subauroral ion drifts". In: *Geophys. Res. Lett.* 46.12 (2019), pp. 6279–6286.

[11] WE Archer et al. "The vertical distribution of the optical emissions of a Steve and Picket Fence event". In: *Geophys. Res. Lett.* 46.19 (2019), pp. 10719–10725.

[12] Elvira Astafyeva. "Ionospheric detection of natural hazards". In: *Reviews of Geophysics* 57.4 (2019), pp. 1265–1288.

[13] Elvira Astafyeva et al. "The 15 January 2022 Hunga Tonga eruption history as inferred from ionospheric observations". In: *Geophysical Research Letters* 49.10 (2022), e2022GL098827.

[14] N Balan and GJ Bailey. "Equatorial plasma fountain and its effects: Possibility of an additional layer". In: *Journal of Geophysical Research: Space Physics* 100.A11 (1995), pp. 21421–21432.

[15] Nanan Balan, LiBo Liu, and HuiJun Le. "A brief review of equatorial ionization anomaly and ionospheric irregularities". In: *Earth and Planetary Physics* 2.4 (2018), pp. 257–275.

[16] Peter M Banks and Gaston Kockarts. *Aeronomy*. Elsevier, 1973.

[17] J Baumgardner et al. "A very bright SAR arc: implications for extreme magnetosphere-ionosphere coupling". In: *Annales Geophysicae*. Vol. 25. 12. Copernicus Publications Göttingen, Germany. 2007, pp. 2593–2608.

[18] Wolfgang Baumjohann and Rudolf A Treumann. *Basic space plasma physics*. World Scientific, 2012.

[19] SB Bayram and MV Freamat. "Vibrational spectra of N2: An advanced undergraduate laboratory in atomic and molecular spectroscopy". In: *American Journal of Physics* 80.8 (2012), pp. 664–669.

[20] Erich Becker and Sharon L Vadas. "Explicit global simulation of gravity waves in the thermosphere". In: *Journal of Geophysical Research: Space Physics* 125.10 (2020), e2020JA028034.

[21] Erich Becker and Sharon L Vadas. *HIAMCM Background Run January 15, 2022 [dataset]*. 2022. URL: `https://www.cora.nwra.com/vadas/Vadas-etal-JGR-2023-TongaICON-files/HIAMCM_data_0-400km_5min/nomeso-0-400km_15JAN2022_00-23p9UT.hzti_zlev.dat`.

[22] Erich Becker and Sharon L Vadas. "Secondary gravity waves in the winter mesosphere: Results from a high-resolution global circulation model". In: *Journal of Geophysical Research: Atmospheres* 123.5 (2018), pp. 2605–2627.

[23] Erich Becker et al. "A high-resolution whole-atmosphere model with resolved gravity waves and specified large-scale dynamics in the troposphere and stratosphere". In: *Journal of Geophysical Research: Atmospheres* 127.2 (2022), e2021JD035018.

[24] Erich Becker et al. "Multi-step vertical coupling during the January 2017 sudden stratospheric warming". In: *Journal of Geophysical Research: Space Physics* 127.12 (2022), e2022JA030866.

[25] TOM Beer. "Supersonic generation of atmospheric waves". In: *Nature* 242.5392 (1973), pp. 34–34.

[26] Tom Beer. "On atmospheric wave generation by the terminator". In: *Planetary and Space Science* 26.2 (1978), pp. 185–188.

[27] Charles L Bennett and Notanee Bourassa. "Improved analysis of STEVE photographs". In: *J. Geophys. Res.: Space Phys.* 126.4 (2021), e2020JA027843.

[28] TE Berger et al. "The thermosphere is a drag: The 2022 Starlink incident and the threat of geomagnetic storms to low earth orbit space operations". In: *Space Weather* 21.3 (2023), e2022SW003330.

[29] PA Bernhardt et al. "Lifetime of a depression in the plasma density over Jicamarca produced by space shuttle exhaust in the ionosphere". In: *Radio Science* 36.5 (2001), pp. 1209–1220.

[30] AV Bespalova et al. "Satellite observations of wave disturbances caused by moving solar terminator". In: *Journal of Atmospheric and Solar-Terrestrial Physics* 140 (2016), pp. 79–85.

[31] Dieter Bilitza et al. "International Reference Ionosphere 2016: From ionospheric climate to real-time weather predictions". In: *Space Weather* 15.2 (2017), pp. 418–429.

[32] J Birn et al. "Particle acceleration in the magnetotail and aurora". In: *Space science reviews* 173 (2012), pp. 49–102.

[33] Elisabeth Blanc. "Observations in the upper atmosphere of infrasonic waves from natural or artificial sources: A summary". In: *Annales geophysicae*. Vol. 3. 1985, pp. 673–687.

[34] M Blanc and AD Richmond. "The ionospheric disturbance dynamo". In: *Journal of Geophysical Research: Space Physics* 85.A4 (1980), pp. 1669–1686.

[35] HG Booker and HW Wells. "Scattering of radio waves by the F-region of the ionosphere". In: *Terrestrial Magnetism and Atmospheric Electricity* 43.3 (1938), pp. 249–256.

[36] L. Campbell et al. "Role of electronic excited N_2 in vibrational excitation of the N_2 ground state at high latitudes". In: *J. Geophys. Res.: Space Phys.* 111.A9 (2006).

[37] Paul Cannon et al. *Extreme space weather: Impacts on engineered systems and infrastructure*. Royal Academy of Engineering, 2013.

[38] CW Carlson et al. "FAST observations in the downward auroral current region: Energetic upgoing electron beams, parallel potential drops, and ion heating". In: *Geophysical Research Letters* 25.12 (1998), pp. 2017–2020.

[39] Donald L Carpenter and CG Park. "On what ionospheric workers should know about the plasmapause-plasmasphere". In: *Reviews of Geophysics* 11.1 (1973), pp. 133–154.

[40] James L Carr et al. "Stereo plume height and motion retrievals for the record-setting Hunga Tonga-Hunga Ha'apai eruption of 15 January 2022". In: *Geophysical Research Letters* 49.9 (2022), e2022GL098131.

[41] Matıas Carvajal et al. "Worldwide Signature of the 2022 Tonga Volcanic Tsunami". In: *Geophysical Research Letters* (2022), e2022GL098153.

[42] Sydney Chapman and Richard S Lindzen. *Atmospheric tides: thermal and gravitational*. Springer Science & Business Media, 1970.

[43] CC Chaston et al. "Auroral ion acceleration in dispersive Alfvén waves". In: *Journal of Geophysical Research: Space Physics* 109.A4 (2004).

[44] CC Chaston et al. "How important are dispersive Alfvén waves for auroral particle acceleration?" In: *Geophysical Research Letters* 34.7 (2007).

[45] Francis F Chen. *Introduction to plasma physics and controlled fusion, 3rd edition*. Vol. 1. Springer, 2016.

[46] G. Chimonas and C. O. Hines. "Atmospheric gravity waves induced by a solar eclipse". In: *Journal of Geophysical Research (1896-1977)* 75.4 (1970), pp. 875–875. ISSN: 2156-2202. DOI: 10.1029/JA075i004p00875.

[47] Min-Yang Chou et al. "Modeling the Day-to-Day Variability of Midnight Equatorial Plasma Bubbles with SAMI3/SD-WACCM-X". In: *Journal of Geophysical Research: Space Physics* (2022), e2023JA031585.

[48] Xiangning Chu et al. "Identifying STEVE's magnetospheric driver using conjugate observations in the magnetosphere and on the ground". In: *Geophys. Res. Lett.* 46.22 (2019), pp. 12665–12674.

[49] Roberto Colonna and Valerio Tramutoli. "A New Model of Solar Illumination of Earth's Atmosphere during Night-Time". In: *Earth* 2.2 (2021), pp. 191–207.

[50] MG Conde et al. "Multiinstrument studies of thermospheric weather above Alaska". In: *Journal of Geophysical Research: Space Physics* 123.11 (2018), pp. 9836–9861.

[51] Russell B Cosgrove. "Does a localized plasma disturbance in the ionosphere evolve to electrostatic equilibrium? Evidence to the contrary". In: *Journal of Geophysical Research: Space Physics* 121.1 (2016), pp. 649–687.

[52] Anthea Coster and Attila Komjathy. "Space weather and the global positioning system". In: *Space Weather* 6.6 (2008).

[53] C Cot and H Teitelbaum. "Generation of gravity waves by inhomogeneous heating of the atmosphere". In: *Journal of Atmospheric and Terrestrial Physics* 42.9-10 (1980), pp. 877–883.

[54] Chihoko Y Cullens et al. "Seasonal Variations of Medium-Scale Waves Observed by ICON-MIGHTI". In: *Geophysical Research Letters* 49.17 (2022), e2022GL099383.

[55] Chihoko Y Cullens et al. "Sensitivity study for ICON tidal analysis". In: *Progress in Earth and Planetary Science* 7 (2020), pp. 1–13.

[56] Judith A Curry and Peter J Webster. *Thermodynamics of atmospheres and oceans*. Vol. 65. Academic press, 1999.

[57] Thomas Dautermann, Eric Calais, and Glen S Mattioli. "Global Positioning System detection and energy estimation of the ionospheric wave caused by the 13 July 2003 explosion of the Soufrière Hills Volcano, Montserrat". In: *Journal of Geophysical Research: Solid Earth* 114.B2 (2009).

[58] Gerald T Davidson. "Pitch-angle diffusion and the origin of temporal and spatial structures in morningside aurorae". In: *Space Science Reviews* 53.1-2 (1990), pp. 45–82.

[59] VV Demyanov and Yu V Yasyukevich. "Space weather: Risk factors for global navigation satellite systems". In: *Solar-Terrestrial Physics* 7.2 (2021), pp. 28–47.

[60] Walter Dieminger and Harry Kohl. "Effects of nuclear explosions on the ionosphere". In: *Nature* 193.4819 (1962), pp. 963–964.

[61] Feng Ding et al. "Comparative climatological study of large-scale traveling ionospheric disturbances over North America and China in 2011–2012". In: *Journal of Geophysical Research: Space Physics* 119.1 (2014), pp. 519–529.

[62] TM Donahue. "Ionospheric Composition and Reactions". In: *Science* 159.3814 (1968), pp. 489–498.

[63] Joshua Dreyer et al. "Characteristics of fragmented aurora-like emissions (FAEs) observed on Svalbard". In: *Annales Geophysicae*. Vol. 39. 2. Copernicus GmbH. 2021, pp. 277–288.

[64] DP Drob et al. "An empirical model of the Earth's horizontal wind fields: HWM07". In: *Journal of Geophysical Research: Space Physics* 113.A12 (2008).

[65] J Duncombe. "The surprising reach of Tonga's giant atmospheric waves". In: *Eos* 103 (2022).

[66] Richard W Eastes. "Modeling the N_2 Lyman-Birge-Hopfield bands in the dayglow: Including radiative and collisional cascading between the singlet states". In: *J. Geophys. Res.: Space Phys.* 105.A8 (2000), pp. 18557–18573.

[67] JP Eastwood et al. "The economic impact of space weather: Where do we stand?" In: *Risk analysis* 37.2 (2017), pp. 206–218.

[68] J Vincent Eccles. "Modeling investigation of the evening prereversal enhancement of the zonal electric field in the equatorial ionosphere". In: *Journal of Geophysical Research: Space Physics* 103.A11 (1998), pp. 26709–26719.

[69] JV Eccles, JP St. Maurice, and Robert W Schunk. "Mechanisms underlying the prereversal enhancement of the vertical plasma drift in the low-latitude ionosphere". In: *Journal of Geophysical Research: Space Physics* 120.6 (2015), pp. 4950–4970.

[70] John T Emmert et al. "NRLMSIS 2.0: A whole-atmosphere empirical model of temperature and neutral species densities". In: *Earth Space Sci.* 8.3 (2021), e2020EA001321.

[71] John T Emmert et al. "NRLMSIS 2.1: An empirical model of nitric oxide incorporated into MSIS". In: *J. Geophys. Res.: Space Phys.* 127.10 (2022), e2022JA030896.

[72] JT Emmert, AD Richmond, and DP Drob. "A computationally compact representation of Magnetic-Apex and Quasi-Dipole coordinates with smooth base vectors". In: *Journal of Geophysical Research: Space Physics* 115.A8 (2010).

[73] Scott L England et al. "Vertical shears of horizontal winds in the lower thermosphere observed by ICON". In: *Geophysical Research Letters* 49.11 (2022), e2022GL098337.

[74] Christoph R Englert et al. "Michelson Interferometer for Global High-resolution Thermospheric Imaging (MIGHTI) on-orbit wind observations: Data analysis and instrument performance". In: *Space Science Reviews* 219.3 (2023), p. 27.

[75] Christoph R Englert et al. "Michelson interferometer for global high-resolution thermospheric imaging (MIGHTI): instrument design and calibration". In: *Space science reviews* 212.1 (2017), pp. 553–584.

[76] David S Evans. "Precipitating electron fluxes formed by a magnetic field aligned potential difference". In: *Journal of Geophysical Research* 79.19 (1974), pp. 2853–2858.

[77] EE Eyler and FM Pipkin. "Lifetime measurements of the $B^3\Pi_g$ state of N_2 using laser excitation". In: *J. Chem. Phys.* 79.8 (1983), pp. 3654–3659.

[78] Tzu-Wei Fang et al. "Space weather environment during the SpaceX Starlink satellite loss in February 2022". In: *Space weather* 20.11 (2022), e2022SW003193.

[79] DT Farley Jr. "A theory of electrostatic fields in a horizontally stratified ionosphere subject to a vertical magnetic field". In: *J. Geophys. Res.* 64.9 (1959), pp. 1225–1233.

[80] David Farmer and Laurence Armi. "Stratified flow over topography: The role of small-scale entrainment and mixing in flow establishment". In: *Proceedings of the Royal Society of London. Series A: Mathematical, Physical and Engineering Sciences* 455.1989 (1999), pp. 3221–3258.

[81] Bela G Fejer. "Low latitude storm time ionospheric electrodynamics". In: *Journal of atmospheric and solar-terrestrial physics* 64.12-14 (2002), pp. 1401–1408.

[82] Bela G Fejer, MF Larsen, and DT Farley. "Equatorial disturbance dynamo electric fields". In: *Geophysical Research Letters* 10.7 (1983), pp. 537–540.

[83] Bela G Fejer, L Scherliess, and ER De Paula. "Effects of the vertical plasma drift velocity on the generation and evolution of equatorial spread F". In: *Journal of Geophysical Research: Space Physics* 104.A9 (1999), pp. 19859–19869.

[84] Christopher Charles Finlay et al. "International geomagnetic reference field: The eleventh generation". In: *Geophysical Journal International* 183.3 (2010), pp. 1216–1230.

[85] Jeffrey M Forbes. "Tidal and planetary waves". In: *The upper mesosphere and lower thermosphere: A review of experiment and theory* 87 (1995), pp. 67–87.

[86] Jeffrey M Forbes, Scott E Palo, and Xiaoli Zhang. "Variability of the ionosphere". In: *Journal of Atmospheric and Solar-Terrestrial Physics* 62.8 (2000), pp. 685–693.

[87] Jeffrey M Forbes et al. "Surface-exosphere coupling due to thermal tides". In: *Geophysical Research Letters* 36.15 (2009).

[88] JM Forbes and RS Lindzen. "Atmospheric solar tides and their electrodynamic effects—I. The global Sq current system". In: *Journal of Atmospheric and Terrestrial Physics* 38.9-10 (1976), pp. 897–910.

[89] JM Forbes et al. "A solar terminator wave in thermosphere neutral densities measured by the CHAMP satellite". In: *Geophysical Research Letters* 35.14 (2008).

[90] JM Forbes et al. "On the specification of upward-propagating tides for ICON science investigations". In: *Space Science Reviews* 212 (2017), pp. 697–713.

[91] C Forsyth et al. "Physical processes of meso-scale, dynamic auroral forms". In: *Space Science Reviews* 216 (2020), pp. 1–45.

[92] JC Foster and WJ Burke. "SAPS: A new categorization for sub-auroral electric fields". In: *Eos, Transactions American Geophysical Union* 83.36 (2002), pp. 393–394.

[93] David C Fritts and M Joan Alexander. "Gravity wave dynamics and effects in the middle atmosphere". In: *Reviews of geophysics* 41.1 (2003).

[94] David C Fritts, Sharon L Vadas, and Yoshinori Yamada. "An estimate of strong local body forcing and gravity wave radiation based on OH airglow and meteor radar observations". In: *Geophysical Research Letters* 29.10 (2002), pp. 71–1.

[95] David C Fritts et al. "Mean and variable forcing of the middle atmosphere by gravity waves". In: *Journal of Atmospheric and Solar-Terrestrial Physics* 68.3-5 (2006), pp. 247–265.

[96] TJ Fuller-Rowell, MC Codrescu, and P Wilkinson. "Quantitative modeling of the ionospheric response to geomagnetic activity". In: *Annales Geophysicae*. Vol. 18. 7. Springer Verlag Göttingen, Germany. 2000, pp. 766–781.

[97] B Gallardo-Lacourt, HU Frey, and C Martinis. "Proton aurora and optical emissions in the subauroral region". In: *Space Sci. Rev.* 217 (2021), pp. 1–36.

[98] B Gallardo-Lacourt et al. "How did we miss this? An upper atmospheric discovery named STEVE". In: *Eos* 100 (2019).

[99] B Gallardo-Lacourt et al. "On the origin of STEVE: Particle precipitation or ionospheric skyglow?" In: *Geophys. Res. Lett.* 45.16 (2018), pp. 7968–7973.

[100] Bea Gallardo-Lacourt et al. "A statistical analysis of STEVE". In: *J. Geophys. Res.: Space Phys.* 123.11 (2018), pp. 9893–9905.

[101] VG Galushko et al. "Incoherent scatter radar observations of AGW/TID events generated by the moving solar terminator". In: *Annales Geophysicae*. Vol. 16. 7. Springer Verlag Göttingen, Germany. 1998, pp. 821–827.

[102] Rolando R Garcia et al. "Modification of the gravity wave parameterization in the Whole Atmosphere Community Climate Model: Motivation and results". In: *Journal of the Atmospheric Sciences* 74.1 (2017), pp. 275–291.

[103] Jim Garvin. *Dramatic Changes at Hunga Tonga-Hunga Ha'apai*. Publisher: NASA Earth Observatory. Jan. 21, 2022. URL: `https://earthobservatory.nasa.gov/images/149367/dramatic-changes-at-hunga-tonga-hunga-haapai` (visited on 07/19/2022).

[104] Federico Gasperini et al. "Vertical wave coupling in the low-latitude Ionosphere-Thermosphere as revealed by concurrent ICON and COSMIC-2 Observations". In: *Space Science Reviews* 218.7 (2022), p. 55.

[105] Federico Gasperini et al. "Wave coupling between the lower and middle thermosphere as viewed from TIMED and GOCE". In: *Journal of Geophysical Research: Space Physics* 120.7 (2015), pp. 5788–5804.

[106] L Claire Gasque et al. "Evening solar terminator waves in Earth's thermosphere: Neutral wind signatures observed by ICON-MIGHTI". In: *Journal of Geophysical Research: Space Physics* 129.2 (2024), e2023JA032274.

[107] L Claire Gasque et al. "It's not easy being green: Kinetic modeling of the emission spectrum observed in STEVE's picket fence". In: *Geophysical Research Letters* 50.21 (2023), e2023GL106073.

[108] L Claire Gasque et al. "Rapid Volcanic Modification of the E-Region Dynamo: ICON's First Glimpse of the Tonga Eruption". In: *Geophysical Research Letters* 49.18 (2022), e2022GL100825.

[109] Jessica N Ghent and Brendan W Crowell. "Spectral characteristics of ionospheric disturbances over the southwestern Pacific from the 15 January 2022 Tonga eruption and tsunami". In: *Geophysical Research Letters* 49.20 (2022), e2022GL100145.

[110] D Megan Gillies et al. "First observations from the TREx spectrograph: The optical spectrum of STEVE and the picket fence phenomena". In: *Geophys. Res. Lett.* 46.13 (2019), pp. 7207–7213.

[111] D Megan Gillies et al. "New insight into the transition from a SAR arc to STEVE". In: *Geophys. Res. Lett.* 50.6 (2023), e2022GL101205.

[112] LP Goncharenko et al. "Unexpected connections between the stratosphere and ionosphere". In: *Geophysical Research Letters* 37.10 (2010).

[113] Nat Gopalswamy et al. "The Solar Cause of the 2022 February 3 Geomagnetic Storm that Led to the Demise of the Starlink Satellites". In: *arXiv preprint arXiv:2303.02330* (2023).

[114] Katelynn R Greer. "Wave Driven Disturbances of the Thermal Structure in the Polar Winter Upper Stratosphere and Lower Mesosphere". PhD thesis. University of Colorado at Boulder, 2013.

[115] David J Griffiths. *Introduction to electrodynamics, fourth edition*. Pearson Education, Inc., 2013.

[116] Guy Grubbs et al. "A comparative study of spectral auroral intensity predictions from multiple electron transport models". In: *J. Geophys. Res.: Space Phys.* 123.1 (2018), pp. 993–1005.

[117] Stephen F Gull. "Bayesian data analysis: Straight-line fitting". In: *Maximum Entropy and Bayesian Methods: Cambridge, England, 1988*. Springer, 1989, pp. 511–518.

[118] Aleksandr V Gurevich. *Nonlinear Phenomena in the Ionosphere*. New York, NY: Springer-Verlag, 1978.

[119] ME Hagan and JM Forbes. "Migrating and nonmigrating diurnal tides in the middle and upper atmosphere excited by tropospheric latent heat release". In: *Journal of Geophysical Research: Atmospheres* 107.D24 (2002), ACL–6.

[120] GJM Hagelaar and L C Pitchford. "Solving the Boltzmann equation to obtain electron transport coefficients and rate coefficients for fluid models". In: *Plasma Sources Sci. Technol.* 14.4 (2005), p. 722.

[121] TJ Hallinan, HC Stenbaek-Nielsen, and CS Deehr. "Enhanced aurora". In: *Journal of Geophysical Research: Space Physics* 90.A9 (1985), pp. 8461–8475.

[122] TJ Hallinan et al. "Spectroscopic evidence for suprathermal electrons in enhanced auroras". In: *J. Geophys. Res.: Space Phys.* 102.A4 (1997), pp. 7501–7508.

[123] Duane W Hamacher. "Aurorae in Australian aboriginal traditions". In: *arXiv preprint arXiv:1309.3367* (2013).

[124] Mike Hapgood, Huixin Liu, and Noé Lugaz. *SpaceX—Sailing close to the space weather?* 2022.

[125] Brian J Harding. "Midlatitude thermospheric wind and temperature: Networked Fabry-Perot interferometer observations and radiative transfer modeling". In: (2017).

[126] Brian J Harding et al. "A mechanism for the STEVE continuum emission". In: *Geophys. Res. Lett.* 47.7 (2020), e2020GL087102.

[127] Brian J Harding et al. "Impacts of the January 2022 Tonga volcanic eruption on the ionospheric dynamo: ICON-MIGHTI and Swarm observations of extreme neutral winds and currents". In: (2022).

[128] Brian J Harding et al. "The MIGHTI wind retrieval algorithm: Description and verification". In: *Space science reviews* 212.1 (2017), pp. 585–600.

[129] Brian J Harding et al. "Validation of ICON-MIGHTI thermospheric wind observations: 2. Green-line comparisons to specular meteor radars". In: *Journal of Geophysical Research: Space Physics* 126.3 (2021), e2020JA028947.

[130] John M Harlander et al. "Michelson interferometer for global high-resolution thermospheric imaging (MIGHTI): monolithic interferometer design and test". In: *Space science reviews* 212 (2017), pp. 601–613.

[131] CJ Heale et al. "Thermospheric dissipation of upward propagating gravity wave packets". In: *Journal of Geophysical Research: Space Physics* 119.5 (2014), pp. 3857–3872.

[132] RA Heelis. "Electrodynamics in the low and middle latitude ionosphere: A tutorial". In: *Journal of Atmospheric and Solar-Terrestrial Physics* 66.10 (2004), pp. 825–838.

[133] RA Heelis and A Maute. "Challenges to understanding the Earth's ionosphere and thermosphere". In: *Journal of Geophysical Research: Space Physics* 125.7 (2020), e2019JA027497.

[134] RA Heelis et al. "Ion velocity measurements for the ionospheric connections explorer". In: *Space science reviews* 212.1 (2017), pp. 615–629.

[135] RA Heelis et al. "Ionospheric Connections (ICON) Ion Velocity Meter (IVM) observations of the equatorial ionosphere at solar minimum". In: *Space Science Reviews* 218.8 (2022), p. 68.

[136] RA Heelis et al. "Topside Plasma Flows in the Equatorial Ionosphere and Their Relationships to F-Region Winds Near 250 km". In: *Journal of Geophysical Research: Space Physics* 127.5 (2022), e2022JA030415.

[137] Kosuke Heki. "Explosion energy of the 2004 eruption of the Asama Volcano, central Japan, inferred from ionospheric disturbances". In: *Geophysical Research Letters* 33.14 (2006).

[138] Michael P Hickey, G Schubert, and RL Walterscheid. "Acoustic wave heating of the thermosphere". In: *Journal of Geophysical Research: Space Physics* 106.A10 (2001), pp. 21543–21548.

[139] Michael P Hickey, G Schubert, and RL Walterscheid. "Propagation of tsunami-driven gravity waves into the thermosphere and ionosphere". In: *Journal of Geophysical Research: Space Physics* 114.A8 (2009).

[140] Colin O Hines. "Internal atmospheric gravity waves at ionospheric heights". In: *Canadian Journal of Physics* 38.11 (1960), pp. 1441–1481.

[141] K Hocke and K Schlegel. "A review of atmospheric gravity waves and travelling ionospheric disturbances: 1982–1995". In: *Annales geophysicae*. Vol. 14. 9. 1996, p. 917.

[142] L Hoffmann, X Xue, and MJ Alexander. "A global view of stratospheric gravity wave hotspots located with Atmospheric Infrared Sounder observations". In: *Journal of Geophysical Research: Atmospheres* 118.2 (2013), pp. 416–434.

[143] James R Holton. "An introduction to dynamic meteorology". In: *American Journal of Physics* 41.5 (1973), pp. 752–754.

[144] Junseok Hong et al. "Detection of Different Properties of Ionospheric Perturbations in the Vicinity of the Korean Peninsula After the Hunga-Tonga Volcanic Eruption on 15 January 2022". In: *Geophysical Research Letters* 49.14 (2022), e2022GL099163.

[145] CM Huang. "Disturbance dynamo electric fields in response to geomagnetic storms occurring at different universal times". In: *Journal of Geophysical Research: Space Physics* 118.1 (2013), pp. 496–501.

[146] JD Huba, E Becker, and SL Vadas. "Simulation study of the 15 January 2022 Tonga event: Development of super equatorial plasma bubbles". In: *Geophysical Research Letters* 50.1 (2023), e2022GL101185.

[147] JD Huba and H-L Liu. "Global modeling of equatorial spread F with SAMI3/WACCM-X". In: *Geophysical Research Letters* 47.14 (2020), e2020GL088258.

[148] RJ Hung, T Phan, and RE Smith. "Observation of gravity waves during the extreme tornado outbreak of 3 April 1974". In: *Journal of Atmospheric and Terrestrial Physics* 40.7 (1978), pp. 831–843.

[149] Michael Hunnekuhl. *Historical STEVE candidates*. 2019. DOI: `http://doi.org/10.17605/OSF.IO/WJGDS`.

[150] Michael Hunnekuhl and Elizabeth MacDonald. "Early ground-based work by auroral pioneer Carl Størmer on the high-altitude detached subauroral arcs now known as "STEVE"". In: *Space weather* 18.3 (2020), e2019SW002384.

[151] Robert D Hunsucker. "Atmospheric gravity waves generated in the high-latitude ionosphere: A review". In: *Reviews of Geophysics* 20.2 (1982), pp. 293–315.

[152] DL Hysell and E Kudeki. "Collisional shear instability in the equatorial F region ionosphere". In: *Journal of Geophysical Research: Space Physics* 109.A11 (2004).

[153] Ronald Ilma. "rilma/pyIRI2016: Official release of the IRI2016 wrapper in Python". In: (Jan. 2017). DOI: `10.5281/zenodo.240895`.

[154] Thomas J Immel et al. "Dayside enhancements of thermospheric O/N2 following magnetic storm onset". In: *Journal of Geophysical Research: Space Physics* 106.A8 (2001), pp. 15471–15488.

[155] Thomas J Immel et al. "Regulation of ionospheric plasma velocities by thermospheric winds". In: *Nature geoscience* 14.12 (2021), pp. 893–898.

[156] Thomas J Immel et al. "The ionospheric connection explorer mission: mission goals and design". In: *Space Science Reviews* 214.1 (2018), pp. 1–36.

[157] Thomas J Immel et al. "The Ionospheric Connection Explorer-Prime Mission Review". In: *Space Science Reviews* 219.5 (2023), p. 41.

[158] TJ Immel et al. "Control of equatorial ionospheric morphology by atmospheric tides". In: *Geophysical Research Letters* 33.15 (2006).

[159] Y Itikawa and A Ichimura. "Cross sections for collisions of electrons and photons with atomic oxygen". In: *J. Phys. Chem. Ref. Data* 19.3 (1990), pp. 637–651.

[160] Toshihiko Iyemori et al. "A confirmation of vertical acoustic resonance and field-aligned current generation just after the 2022 Hunga Tonga Hunga Ha'apai volcanic eruption". In: *Earth, Planets and Space* 74.1 (2022), pp. 1–15.

[161] AD Johnstone. "Pulsating aurora". In: *Nature* 274.5667 (1978), pp. 119–126.

[162] AD Johnstone. "The mechanism of pulsating aurora." In: *Annales Geophysicae*. Vol. 1. 1983, pp. 397–410.

[163] Olusegun Folarin Jonah et al. "TID observations and source analysis during the 2017 Memorial Day weekend geomagnetic storm over North America". In: *Journal of Geophysical Research: Space Physics* 123.10 (2018), pp. 8749–8765.

[164] McArthur Jones Jr. "Non-linear Tidal Interactions and Their Role in Determining the Mean State and Variability of the Ionosphere-Thermosphere (IT) System". PhD thesis. University of Colorado at Boulder, 2015.

[165] Farzad Kamalabadi et al. "Inferring nighttime ionospheric parameters with the far ultraviolet imager onboard the ionospheric connection explorer". In: *Space science reviews* 214.4 (2018), pp. 1–14.

[166] John G Kappenman. "An Introduction to Power Grid Impacts and Vulnerabilities from Space Weather: A review of geomagnetic storms, impacts to ground-based technology sytems, and the role of forecasting in risk management of critical systems". In: *Space Storms and Space Weather Hazards* (2001), pp. 335–361.

[167] Tomas Karlsson and Göran Marklund. "Simulations of effects of small-scale auroral current closure in the return current region". In: *Physics of Space Plasmas* 15 (1998), p. 401.

[168] Tomas Karlsson et al. "On enhanced aurora and low-altitude parallel electric fields". In: *Physica Scripta* 72.5 (2005), p. 419.

[169] Ryuho Kataoka, Stephen D Winn, and Emile Touber. "Meteotsunamis in Japan associated with the Tonga Eruption in January 2022". In: *SOLA* (2022).

[170] Fuyang Ke et al. "Ionospheric response and the impact on GPS positioning accuracy during the Tonga volcano eruption on 15 January 2022". In: *Advances in Space Research* (2023).

[171] Michael C Kelley. "In situ ionospheric observations of severe weather-related gravity waves and associated small-scale plasma structure". In: *Journal of Geophysical Research: Space Physics* 102.A1 (1997), pp. 329–335.

[172] Michael C Kelley. *The Earth's ionosphere: Plasma physics and electrodynamics*. Academic press, 2009.

[173] V Kharchenko, A Dalgarno, and Jane L Fox. "Thermospheric distribution of fast O (1D) atoms". In: *Journal of Geophysical Research: Space Physics* 110.A12 (2005).

[174] Takashi Kikuchi and Tohru Araki. "Horizontal transmission of the polar electric field to the equator". In: *Journal of Atmospheric and Terrestrial Physics* 41.9 (1979), pp. 927–936.

[175] Hyosub Kil. "The morphology of equatorial plasma bubbles: A review". In: *Journal of Astronomy and Space Sciences* 32.1 (2015), pp. 13–19.

[176] Timothy L Killeen et al. "Neutral winds in the polar thermosphere as measured from Dynamics Explorer". In: *Geophysical Research Letters* 9.9 (1982), pp. 957–960.

[177] JU Kozyra, AF Nagy, and DW Slater. "High-altitude energy source(s) for stable auroral red arcs". In: *Reviews of Geophysics* 35.2 (1997), pp. 155–190.

[178] Erhan Kudeki et al. "Equatorial spread-F initiation: Post-sunset vortex, thermospheric winds, gravity waves". In: *Journal of Atmospheric and Solar-Terrestrial Physics* 69.17-18 (2007), pp. 2416–2427.

[179] SN Kulichkov et al. "Acoustic-Gravity Lamb Waves from the Eruption of the Hunga-Tonga-Hunga-Hapai Volcano, Its Energy Release and Impact on Aerosol Concentrations and Tsunami". In: *Pure and Applied Geophysics* (2022), pp. 1–16.

[180] I Kutiev, S Stankov, and P Marinov. "Analytical expression of O+/H+ ion transition surface for use in IRI". In: *Advances in Space Research* 14.12 (1994), pp. 135–138.

[181] Russ R Laher and Forrest R Gilmore. "Updated excitation and ionization cross sections for electron impact on atomic oxygen". In: *J. Phys. Chem. Ref. Data* 19.1 (1990), pp. 277–305.

[182] Roberto Lanza and Antonio Meloni. *The Earth's Magnetic Field*. Springer, 2006.

[183] SA Lawton and AV Phelps. "Excitation of the $b^1\Sigma_g^+$ state of O_2 by low energy electrons". In: *J. Chem. Phys.* 69.3 (1978), pp. 1055–1068.

[184] Jiuhou Lei et al. "Observations and simulations of the ionospheric and thermospheric response to the December 2006 geomagnetic storm: Initial phase". In: *Journal of Geophysical Research: Space Physics* 113.A1 (2008).

[185] JM Leonard, Jeffrey M Forbes, and George H Born. "Impact of tidal density variability on orbital and reentry predictions". In: *Space Weather* 10.12 (2012).

[186] Robert S Leonard and RA Barnes Jr. "Observation of ionospheric disturbances following the Alaska earthquake". In: *Journal of Geophysical Research* 70.5 (1965), pp. 1250–1253.

[187] Ruoxi Li et al. "Large-Scale Disturbances in the Upper Thermosphere Induced by the 2022 Tonga Volcanic Eruption". In: *Geophysical Research Letters* 50.3 (2023), e2022GL102265.

[188] Jun Liang, JP St-Maurice, and E Donovan. "A time-dependent two-dimensional model simulation of lower ionospheric variations under intense SAID". In: *J. Geophys. Res.: Space Phys.* 126.12 (2021), e2021JA029756.

[189] Jun Liang et al. "Converting TREx-RGB green-channel data to 557.7 nm auroral intensity: Methodology and initial results". In: *Earth and Planetary Physics* 8.1 (2023), pp. 258–274.

[190] Jun Liang et al. "Neutral wind dynamics preceding the STEVE occurrence and their possible preconditioning role in STEVE formation". In: *J. Geophys. Res.: Space Phys.* 126.3 (2021), e2020JA028505.

[191] RS Lieberman et al. "Global observations and modeling of nonmigrating diurnal tides generated by tide-planetary wave interactions". In: *Journal of Geophysical Research: Atmospheres* 120.22 (2015), pp. 11–419.

[192] Jia-Ting Lin et al. "Rapid Conjugate Appearance of the Giant Ionospheric Lamb Wave in the Northern Hemisphere After Hunga-Tonga Volcano Eruptions". In: (2022).

[193] Richard S Lindzen. "Turbulence and stress owing to gravity wave and tidal breakdown". In: *Journal of Geophysical Research* 68.C10 (1981), pp. 9707–9714.

[194] H-L Liu. "Variability and predictability of the space environment as related to lower atmosphere forcing". In: *Space weather* 14.9 (2016), pp. 634–658.

[195] H-L Liu and AD Richmond. "Attribution of ionospheric vertical plasma drift perturbations to large-scale waves and the dependence on solar activity". In: *Journal of Geophysical Research: Space Physics* 118.5 (2013), pp. 2452–2465.

[196] H-L Liu et al. "Atmospheric and Ionospheric Responses to Hunga-Tonga Volcano Eruption Simulated by WACCM-X". In: *Geophysical Research Letters* 50.10 (2023), e2023GL103682.

[197] Han-Li Liu. "Day-to-day variability of prereversal enhancement in the vertical ion drift in response to large-scale forcing from the lower atmosphere". In: *Space Weather* 18.4 (2020), e2019SW002334.

[198] Han-Li Liu et al. "Development and validation of the Whole Atmosphere Community Climate Model with thermosphere and ionosphere extension (WACCM-X 2.0)". In: *Journal of Advances in Modeling Earth Systems* 10.2 (2018), pp. 381–402.

[199] Huixin Liu, Hermann Lühr, and Shigeto Watanabe. "A solar terminator wave in thermospheric wind and density simultaneously observed by CHAMP". In: *Geophysical Research Letters* 36.10 (2009).

[200] Ningyu Liu and Victor P Pasko. "Molecular nitrogen LBH band system far-UV emissions of sprite streamers". In: *Geophysical Research Letters* 32.5 (2005).

[201] Xin Liu et al. "Atmospheric-ionospheric disturbances following the April 2015 Calbuco volcano from GPS and OMI observations". In: *Advances in Space Research* 60.12 (2017), pp. 2836–2846.

[202] Robert R Long. "Some aspects of the flow of stratified fluids: III. Continuous density gradients". In: *Tellus* 7.3 (1955), pp. 341–357.

[203] William Lotko. "Diffusive acceleration of auroral primaries". In: *Journal of Geophysical Research: Space Physics* 91.A1 (1986), pp. 191–203.

[204] Gang Lu et al. "High-latitude energy input and its impact on the thermosphere". In: *Journal of Geophysical Research: Space Physics* 121.7 (2016), pp. 7108–7124.

[205] Greg Lucas. "pymsis". In: (Jan. 2023). DOI: 10.5281/zenodo.7581692.

[206] Hermann Lühr, S Maus, and Martin Rother. "Noon-time equatorial electrojet: Its spatial features as determined by the CHAMP satellite". In: *Journal of Geophysical Research: Space Physics* 109.A1 (2004).

[207] Thomas S Lund and David C Fritts. "Numerical simulation of gravity wave breaking in the lower thermosphere". In: *Journal of Geophysical Research: Atmospheres* 117.D21 (2012).

[208] Kristina A Lynch et al. "An ionospheric conductance gradient driver for subauroral picket fence visible signatures near STEVE events". In: *J. Geophys. Res.: Space Phys.* 127.12 (2022), e2022JA030863.

[209] Larry R Lyons et al. "Identification of auroral zone activity driving large-scale traveling ionospheric disturbances". In: *Journal of Geophysical Research: Space Physics* 124.1 (2019), pp. 700–714.

[210] Elizabeth A MacDonald et al. "New science in plain sight: Citizen scientists lead to the discovery of optical structure in the upper atmosphere". In: *Sci. Adv.* 4.3 (2018), eaaq0030.

[211] Boris Maletckii and Elvira Astafyeva. "Near-Real-Time analysis of the ionospheric response to the 15 January 2022 Hunga Tonga-Hunga Ha'apai volcanic eruption". In: (2022).

[212] Göran Marklund. "Viking investigations of auroral electrodynamical processes". In: *J. Geophys. Res.: Space Phys.* 98.A2 (1993), pp. 1691–1704.

[213] Göran Marklund, Tomas Karlsson, and James Clemmons. "On low-altitude particle acceleration and intense electric fields and their relationship to black aurora". In: *J. Geophys. Res.: Space Phys.* 102.A8 (1997), pp. 17509–17522.

[214] Daniel R Marsh et al. "Climate change from 1850 to 2005 simulated in CESM1 (WACCM)". In: *Journal of climate* 26.19 (2013), pp. 7372–7391.

[215] C Martinis et al. "Rainbow of the Night: First Direct Observation of a SAR arc evolving into STEVE". In: *Geophys. Res. Lett.* 49.11 (2022), e2022GL098511.

[216] A Maute, AD Richmond, and RG Roble. "Sources of low-latitude ionospheric E× B drifts and their variability". In: *Journal of Geophysical Research: Space Physics* 117.A6 (2012).

[217] Astrid Maute. "Thermosphere-ionosphere-electrodynamics general circulation model for the ionospheric connection explorer: TIEGCM-ICON". In: *Space Science Reviews* 212.1-2 (2017), pp. 523–551.

[218] Astrid Maute and HAO WACCM team. *WACCMX-SD V2 [Dataset]*. 2022. DOI: `https://doi.org/10.5065/RJGT-G951`.

[219] Astrid Maute and ICON Team. *TIEGCM-ICON [Dataset]*. 2022. URL: `https://cdaweb.gsfc.nasa.gov/pub/data/icon/l4/`.

[220] Astrid Maute and Arthur D Richmond. "F-region dynamo simulations at low and mid-latitude". In: *Space Science Reviews* 206.1 (2017), pp. 471–493.

[221] Astrid Maute et al. "Delineating the effect of upward propagating migrating solar tides with the TIEGCM-ICON". In: *Frontiers in Astronomy and Space Sciences* 10 (2023), p. 1147571.

[222] JP McClure, WB Hanson, and JH Hoffman. "Plasma bubbles and irregularities in the equatorial ionosphere". In: *Journal of Geophysical Research* 82.19 (1977), pp. 2650–2656.

[223] Emma C McGinness et al. "The Effects of a Small Geomagnetic Storm on Earth's Thermosphere and Ionosphere: ICON Observations of the 25 January 2021 Disturbance". In: *Journal of Geophysical Research: Space Physics* 128.7 (2023), e2022JA031207.

[224] Charles McLandress. "The seasonal variation of the propagating diurnal tide in the mesosphere and lower thermosphere. Part I: The role of gravity waves and planetary waves". In: *Journal of the Atmospheric Sciences* 59.5 (2002), pp. 893–906.

[225] Charles McLandress and WE Ward. "Tidal/gravity wave interactions and their influence on the large-scale dynamics of the middle atmosphere: Model results". In: *Journal of Geophysical Research: Atmospheres* 99.D4 (1994), pp. 8139–8155.

[226] Jean H Meeus. *Astronomical algorithms, 2nd edition*. Willmann-Bell, Incorporated, 1998.

[227] RR Meier. "Ultraviolet spectroscopy and remote sensing of the upper atmosphere". In: *Space Sci. Rev.* 58.1 (1991), pp. 1–185.

[228] SB Mende, BJ Harding, and C Turner. "Subauroral green STEVE arcs: Evidence for low-energy excitation". In: *Geophys. Res. Lett.* 46.24 (2019), pp. 14256–14262.

[229] SB Mende and C Turner. "Color ratios of subauroral (STEVE) arcs". In: *Journal of Geophysical Research: Space Physics* 124.7 (2019), pp. 5945–5955.

[230] SB Mende et al. "The far ultra-violet imager on the ICON mission". In: *Space Science Reviews* 212.1 (2017), pp. 655–696.

[231] Michael. "space-physics/igrf: Robust build, matlab unit test". In: (Oct. 2021). DOI: 10.5281/zenodo.5560949.

[232] Takeshi Mikumo and Shingo Watada. "Acoustic-gravity waves from earthquake sources". In: *Infrasound monitoring for atmospheric studies* (2009), pp. 263–279.

[233] Luis Millan et al. "The Hunga Tonga-Hunga Ha'apai Hydration of the Stratosphere". In: (2022).

[234] GH Millward et al. "An investigation into the influence of tidal forcing on F region equatorial vertical ion drift using a global ionosphere-thermosphere model with coupled electrodynamics". In: *Journal of Geophysical Research: Space Physics* 106.A11 (2001), pp. 24733–24744.

[235] Evgeny Mishin and Anatoly Streltsov. "On the Kinetic Theory of Subauroral Arcs". In: *J. Geophys. Res.: Space Phys.* 127.8 (2022), e2022JA030667.

[236] Evgeny Mishin and Anatoly Streltsov. "STEVE and the Picket Fence: Evidence of Feedback-Unstable Magnetosphere-Ionosphere Interaction". In: *Geophysical Research Letters* 46.24 (Dec. 2019), pp. 14247–14255. ISSN: 0094-8276. DOI: 10.1029/2019GL085446. URL: https://onlinelibrary.wiley.com/doi/10.1029/2019GL085446%20https://agupubs.onlinelibrary.wiley.com/doi/10.1029/2019GL085446.

[237] Evgeny V Mishin. "Interaction of substorm injections with the subauroral geospace: 1. Multispacecraft observations of SAID". In: *Journal of Geophysical Research: Space Physics* 118.9 (2013), pp. 5782–5796.

[238] S Miyahara and Yasunobu Miyoshi. "Migrating and non-migrating atmospheric tides simulated by a middle atmosphere general circulation model". In: *Advances in Space Research* 20.6 (1997), pp. 1201–1207.

[239] Yasunobu Miyoshi et al. "Solar terminator wave and its relation to the atmospheric tide". In: *Journal of Geophysical Research: Space Physics* 114.A7 (2009).

[240] JS Morrill et al. "Time resolved N_2 triplet state vibrational populations and emissions associated with red sprites". In: *J. Atmos. Sol. Terr. Phys.* 60.7-9 (1998), pp. 811–829.

[241] Fo S Mozer et al. "Satellite measurements and theories of low altitude auroral particle acceleration". In: *Space Science Reviews* 27 (1980), pp. 155–213.

[242] Yuki Nakashima et al. "Atmospheric resonant oscillations by the 2014 eruption of the Kelud volcano, Indonesia, observed with the ionospheric total electron contents and seismic signals". In: *Earth and Planetary Science Letters* 434 (2016), pp. 112–116.

[243] Gregory D Nastrom and David C Fritts. "Sources of mesoscale variability of gravity waves. Part I: Topographic excitation". In: *Journal of Atmospheric Sciences* 49.2 (1992), pp. 101–110.

[244] Richard B Neale et al. "The mean climate of the Community Atmosphere Model (CAM4) in forced SST and fully coupled experiments". In: *Journal of Climate* 26.14 (2013), pp. 5150–5168.

[245] PT Newell, T Sotirelis, and S Wing. "Diffuse, monoenergetic, and broadband aurora: The global precipitation budget". In: *Journal of Geophysical Research: Space Physics* 114.A9 (2009).

[246] Michael J Nicolls et al. "Horizontal parameters of daytime thermospheric gravity waves and E region neutral winds over Puerto Rico". In: *Journal of Geophysical Research: Space Physics* 119.1 (2014), pp. 575–600.

[247] Y Nishimura et al. "Identifying the driver of pulsating aurora". In: *Science* 330.6000 (2010), pp. 81–84.

[248] Y Nishimura et al. "Magnetospheric signatures of STEVE: Implications for the magnetospheric energy source and interhemispheric conjugacy". In: *Geophys. Res. Lett.* 46.11 (2019), pp. 5637–5644.

[249] Yukitoshi Nishimura et al. "Unsolved Problems in Strong Thermal Emission Velocity Enhancement (STEVE) and Picket Fence". In: *Front. Astron. Space Sci.* 10 (2023), p. 3.

[250] Kjellmar Oksavik et al. "Scintillation and loss of signal lock from poleward moving auroral forms in the cusp ionosphere". In: *Journal of Geophysical Research: Space Physics* 120.10 (2015), pp. 9161–9175.

[251] Denny M Oliveira and Eftyhia Zesta. "Satellite orbital drag during magnetic storms". In: *Space Weather* 17.11 (2019), pp. 1510–1533.

[252] Denny M Oliveira et al. "The current state and future directions of modeling thermosphere density enhancements during extreme magnetic storms". In: *Frontiers in Astronomy and Space Sciences* 8 (2021), p. 764144.

[253] S Otsuka. "Visualizing Lamb Waves From a Volcanic Eruption Using Meteorological Satellite Himawari-8". In: *Geophysical Research Letters* 49.8 (2022), e2022GL098324.

[254] S Oyama and BJ Watkins. "Generation of atmospheric gravity waves in the polar thermosphere in response to auroral activity". In: *Space science reviews* 168 (2012), pp. 463–473.

[255] Masaru Ozeki and Kosuke Heki. "Ionospheric holes made by ballistic missiles from North Korea detected with a Japanese dense GPS array". In: *Journal of Geophysical Research: Space Physics* 115.A9 (2010).

[256] Kwanchai Pakoksung, Anawat Suppasri, and Fumihiko Imamura. "The near-field tsunami generated by the 15 January 2022 eruption of the Hunga Tonga-Hunga Ha'apai volcano and its impact on Tongatapu, Tonga". In: *Scientific reports* 12.1 (2022), p. 15187.

[257] Minna Palmroth et al. "Lower thermosphere–ionosphere (LTI) quantities: Current status of measuring techniques and models". In: *Annales geophysicae discussions* 2020 (2020), pp. 1–73.

[258] Sergey Pancheshnyi et al. "The LXCat project: Electron scattering cross sections and swarm parameters for low temperature plasma modeling". In: *Chem. Phys.* 398 (2012), pp. 148–153.

[259] Götz Paschmann et al. *Auroral Plasma Physics*. Vol. 15. Springer Science & Business Media, 2003.

[260] AV Pavlov. "Photochemistry of ions at D-region altitudes of the ionosphere: A review". In: *Surveys in Geophysics* 35 (2014), pp. 259–334.

[261] Nicholas M Pedatella. "Response of the ionosphere-plasmasphere system to periodic forcing". PhD thesis. University of Colorado at Boulder, 2011.

[262] Nicholas M Pedatella and H-L Liu. "The influence of internal atmospheric variability on the ionosphere response to a geomagnetic storm". In: *Geophysical Research Letters* 45.10 (2018), pp. 4578–4585.

[263] Robert Pfaff et al. "The Vector Electric Field Investigation (VEFI) on the C/NOFS Satellite". In: *Space Sci. Rev.* 217 (2021), pp. 1–88.

[264] Robert F Pfaff. "The near-Earth plasma environment". In: *Space science reviews* 168 (2012), pp. 23–112.

[265] AV Phelps and LC Pitchford. "Anisotropic scattering of electrons by N_2 and its effect on electron transport". In: *Phys. Rev. A* 31.5 (1985), p. 2932.

[266] JM Picone et al. "NRLMSISE-00 empirical model of the atmosphere: Statistical comparisons and scientific issues". In: *J. Geophys. Res.: Space Phys.* 107.A12 (2002), SIA–15.

[267] JM Picone et al. "NRLMSISE-00 empirical model of the atmosphere: Statistical comparisons and scientific issues". In: *Journal of Geophysical Research: Space Physics* 107.A12 (2002), SIA–15.

[268] AI Pogoreltsev et al. "Planetary waves in coupling the lower and upper atmosphere". In: *Journal of Atmospheric and Solar-Terrestrial Physics* 69.17-18 (2007), pp. 2083–2101.

[269] Piero Poli and Nikolai M Shapiro. "Rapid characterization of large volcanic eruptions: measuring the impulse of the Hunga Tonga explosion from teleseismic waves". In: (2022).

[270] Hayden S. Porter, C. H. Jackman, and Alex E. S. Green. "Efficiencies for production of atomic nitrogen and oxygen by relativistic proton impact in air". In: *Journal of Chemical Physics* 65 (1976), pp. 154–167.

[271] Michael J Prather. "Ozone in the upper stratosphere and mesosphere". In: *Journal of Geophysical Research: Oceans* 86.C6 (1981), pp. 5325–5338.

[272] Frank Press and David Harkrider. "Propagation of acoustic-gravity waves in the atmosphere". In: *Journal of Geophysical Research* 67.10 (1962), pp. 3889–3908.

[273] Gerd W Prölss. *Physics of the Earth's space environment: An introduction*. Springer, 2004.

[274] Liying Qian et al. "The NCAR TIE-GCM: A community model of the coupled thermosphere/ionosphere system". In: *Modeling the ionosphere–thermosphere system* (2014), pp. 73–83.

[275] Liying Qian et al. "Variability of thermosphere and ionosphere responses to solar flares". In: *Journal of Geophysical Research: Space Physics* 116.A10 (2011).

[276] Y. P. Raizer. *Gas Discharge Physics*. New York, NY: Springer-Verlag, 1991.

[277] PK Rajesh et al. "Extreme poleward expanding super plasma bubbles over Asia-Pacific region triggered by Tonga volcano eruption during the recovery-phase of geomagnetic storm". In: *Geophysical Research Letters* 49.15 (2022), e2022GL099798.

[278] Karl Rawer. *Wave propagation in the ionosphere*. Vol. 5. Springer Science & Business Media, 1993.

[279] Manfred Hugh Rees. *Physics and chemistry of the upper atmosphere*. Cambridge University Press, 1989.

[280] MH Rees and RG Roble. "Observations and theory of the formation of stable auroral red arcs". In: *Reviews of Geophysics* 13.1 (1975), pp. 201–242.

[281] P. G. Richards and D G Torr. "A factor of 2 reduction in theoretical F2 peak electron density due to enhanced vibrational excitation of N_2 in summer at solar maximum". In: *Journal of Geophysical Research* 91.A10 (1986), p. 11331. ISSN: 0148-0227. DOI: 10.1029/JA091iA10p11331. URL: http://doi.wiley.com/10.1029/JA091iA10p11331.

[282] AD Richmond. "The ionospheric wind dynamo: Effects of its coupling with different atmospheric regions". In: *The Upper Mesosphere and Lower Thermosphere: A Review of Experiment and Theory, Geophys. Monogr. Ser* 87 (1995), pp. 49–65.

[283] AD Richmond, T-W Fang, and Astrid Maute. "Electrodynamics of the equatorial evening ionosphere: 1. Importance of winds in different regions". In: *Journal of Geophysical Research: Space Physics* 120.3 (2015), pp. 2118–2132.

[284] AD Richmond and S Matsushita. "Thermospheric response to a magnetic substorm". In: *Journal of Geophysical Research* 80.19 (1975), pp. 2839–2850.

[285] AD Richmond and RG Roble. "Electrodynamic effects of thermospheric winds from the NCAR thermospheric general circulation model". In: *Journal of Geophysical Research: Space Physics* 92.A11 (1987), pp. 12365–12376.

[286] Jadwiga H Richter, Fabrizio Sassi, and Rolando R Garcia. "Toward a physically based gravity wave source parameterization in a general circulation model". In: *Journal of the Atmospheric Sciences* 67.1 (2010), pp. 136–156.

[287] William Rideout and Anthea Coster. "Automated GPS processing for global total electron content data". In: *GPS solutions* 10 (2006), pp. 219–228.

[288] AJ Ridley et al. "A statistical study of the ionospheric convection response to changing interplanetary magnetic field conditions using the assimilative mapping of ionospheric electrodynamics technique". In: *Journal of Geophysical Research: Space Physics* 103.A3 (1998), pp. 4023–4039.

[289] Maurizio Ripepe et al. "Observation of infrasonic and gravity waves at Soufrière Hills Volcano, Montserrat". In: *Geophysical Research Letters* 37.19 (2010).

[290] H Rishbeth. "F-region links with the lower atmosphere?" In: *Journal of atmospheric and solar-terrestrial physics* 68.3-5 (2006), pp. 469–478.

[291] H Rishbeth. "Polarization fields produced by winds in the equatorial F-region". In: *Planetary and Space Science* 19.3 (1971), pp. 357–369.

[292] H Rishbeth. "The F-region dynamo". In: *Journal of Atmospheric and Terrestrial Physics* 43.5-6 (1981), pp. 387–392.

[293] H Rishbeth. "The ionospheric E-layer and F-layer dynamos: A tutorial review". In: *Journal of Atmospheric and Solar-Terrestrial Physics* 59.15 (1997), pp. 1873–1880.

[294] H Rishbeth and M Mendillo. "Patterns of F2-layer variability". In: *Journal of Atmospheric and Solar-Terrestrial Physics* 63.15 (2001), pp. 1661–1680.

[295] Henry Rishbeth and Owen K Garriott. "Introduction to ionospheric physics". In: *Introduction to ionospheric physics* (1969).

[296] FE Roach and JR Roach. "Stable 6300 Å auroral arcs in mid-latitudes". In: *Planetary and Space Science* 11.5 (1963), pp. 523–540.

[297] David H Roberts et al. "A large-amplitude traveling ionospheric disturbance produced by the May 18, 1980, explosion of Mount St. Helens". In: *Journal of Geophysical Research: Space Physics* 87.A8 (1982), pp. 6291–6301.

[298] RG Roble and BA Emery. "On the global mean temperature of the thermosphere". In: *Planetary and Space Science* 31.6 (1983), pp. 597–614.

[299] Alan Rodger. "The mid-latitude trough—Revisited". In: *Washington DC American geophysical union geophysical monograph series* 181 (2008), pp. 25–33.

[300] Alan S Rodger et al. "The poleward edge of the mid-latitude trough—Its formation, orientation and dynamics". In: *Journal of atmospheric and terrestrial physics* 48.8 (1986), pp. 715–728.

[301] Raquel Salmeron and Mark Wardle. "Magnetorotational instability in stratified, weakly ionized accretion discs". In: *Monthly Notices of the Royal Astronomical Society* 345.3 (2003), pp. 992–1008.

[302] L Scherliess and Bela G Fejer. "Radar and satellite global equatorial F region vertical drift model". In: *Journal of Geophysical Research: Space Physics* 104.A4 (1999), pp. 6829–6842.

[303] Robert Schunk and Andrew Nagy. *Ionospheres: Physics, plasma physics, and chemistry*. Cambridge university press, 2009.

[304] Robert W Schunk and Jan Josef Sojka. "Ionosphere-thermosphere space weather issues". In: *Journal of Atmospheric and Terrestrial Physics* 58.14 (1996), pp. 1527–1574.

[305] RW Schunk and JCG Walker. "Theoretical ion densities in the lower ionosphere". In: *Planetary and Space Science* 21.11 (1973), pp. 1875–1896.

[306] George Sebestyen et al. *Low Earth Orbit Satellite Design*. Springer, 2018.

[307] Joshua Semeter et al. "The mysterious green streaks below STEVE". In: *AGU Advances* 1.4 (2020), e2020AV000183.

[308] GW Sharp. "Midlatitude trough in the night ionosphere". In: *Journal of Geophysical Research* 71.5 (1966), pp. 1345–1356.

[309] Clint H Sheehan and J-P St. Maurice. "Dissociative recombination of N2+, O2+, and NO+: Rate coefficients for ground state and vibrationally excited ions". In: *Journal of Geophysical Research: Space Physics* 109.A3 (2004).

[310] EG Shelley. "The auroral acceleration region: The world of beams, conies, cavitons, and other plasma exotica". In: *Rev. Geophys.* 33.S1 (1995), pp. 709–714.

[311] Donald E Shemansky and Xianming Liu. "Evaluation of electron impact excitation of $N_2 X^1\Sigma_g^+(0)$ into the N_2^+ $X^2\Sigma_g^+(v)$, $A^2\Pi_u(v)$, and $B^2\Sigma_u^+(v)$ states". In: *J. Geophys. Res.: Space Phys.* 110.A7 (2005).

[312] Samuel A Shidler and Fabiano S Rodrigues. "An electrodynamics model for Data Interpretation and Numerical Analysis of ionospheric Missions and Observations (DINAMO)". In: *Progress in Earth and Planetary Science* 9.1 (2022), p. 7.

[313] Hiroyuki Shinagawa and Yasunobu Miyoshi. "Simulation study of atmosphere–ionosphere variations driven by the eruption of Hunga Tonga-Hunga Ha'apai on 15 January 2022". In: *Earth, Planets and Space* 76.1 (2024), p. 15.

[314] Atsuki Shinbori et al. "Electromagnetic conjugacy of ionospheric disturbances after the 2022 Hunga Tonga-Hunga Ha'apai volcanic eruption as seen in GNSS-TEC and SuperDARN Hokkaido pair of radars observations". In: *Earth, Planets and Space* 74.1 (2022), pp. 1–17.

[315] Ksenia Shults, Elvira Astafyeva, and Sévan Adourian. "Ionospheric detection and localization of volcano eruptions on the example of the April 2015 Calbuco events". In: *Journal of Geophysical Research: Space Physics* 121.10 (2016), pp. 10–303.

[316] M Simek. "Optical diagnostics of streamer discharges in atmospheric gases". In: *Journal of Physics D: Applied Physics* 47.46 (2014), p. 463001.

[317] Martin M Sirk et al. "Design and performance of the ICON EUV spectrograph". In: *Space science reviews* 212.1 (2017), pp. 631–643.

[318] Anne K Smith. "Global dynamics of the MLT". In: *Surveys in Geophysics* 33 (2012), pp. 1177–1230.

[319] Stanley Solomon. "Optical aeronomy". In: *Reviews of Geophysics Supplement* 29 (1991), pp. 1089–1109.

[320] Stanley C Solomon. "Global modeling of thermospheric airglow in the far ultraviolet". In: *Journal of Geophysical Research: Space Physics* 122.7 (2017), pp. 7834–7848.

[321] Stanley C Solomon and Vincent J Abreu. "The 630 nm dayglow". In: *Journal of Geophysical Research: Space Physics* 94.A6 (1989), pp. 6817–6824.

[322] VM Somsikov. "A spherical model of wave generation in the atmosphere by the solar terminator". In: *Journal of atmospheric and terrestrial physics* 49.5 (1987), pp. 433–438.

[323] VM Somsikov. "Solar terminator and dynamic phenomena in the atmosphere: A review". In: *Geomagnetism and Aeronomy* 51 (2011), pp. 707–719.

[324] VM Somsikov and B Ganguly. "On the formation of atmospheric inhomogeneities in the solar terminator region". In: *Journal of Atmospheric and Terrestrial Physics* 57.12 (1995), pp. 1513–1523.

[325] Qian Song et al. "Statistical study of large-scale traveling ionospheric disturbances generated by the solar terminator over China". In: *Journal of Geophysical Research: Space Physics* 118.7 (2013), pp. 4583–4593.

[326] E. Spanswick, E. Donovan, and D. Hampton. *Transition Region Explorer - Spectrograph Dataset [Data set].* 2023. DOI: https://doi.org/10.11575/2WNP-YC80.

[327] RW Spiro, RA Heelis, and WB Hanson. "Rapid subauroral ion drifts observed by Atmosphere Explorer C". In: *Geophysical Research Letters* 6.8 (1979), pp. 657–660.

[328] RW Spiro, RA Wolf, and BG Fejer. "Penetrating of high-latitude-electric-field effects to low latitudes during SUNDIAL 1984". In: *Annales Geophysicae*. Vol. 6. 1988, pp. 39–49.

[329] Andrew W Stephan et al. "Daytime ionosphere retrieval algorithm for the Ionospheric Connection Explorer (ICON)". In: *Space science reviews* 212.1 (2017), pp. 645–654.

[330] Andrew W Stephan et al. "Daytime O/N2 retrieval algorithm for the Ionospheric Connection Explorer (ICON)". In: *Space science reviews* 214.1 (2018), pp. 1–17.

[331] MH Stevens et al. "Temperatures in the upper mesosphere and lower thermosphere from O2 atmospheric band emission observed by ICON/MIGHTI". In: *Space Science Reviews* 218.8 (2022), p. 67.

[332] Michael H Stevens et al. "Retrieval of lower thermospheric temperatures from O_2 A band emission: The MIGHTI experiment on ICON". In: *Space Science Reviews* 214 (2018), pp. 1–9.

[333] DJ Strickland et al. "Atmospheric Ultraviolet Radiance Integrated Code (AURIC): Theory, software architecture, inputs, and selected results". In: *Journal of Quantitative Spectroscopy and Radiative Transfer* 62.6 (1999), pp. 689–742.

[334] P Stubbe and T Hagfors. "The Earth's ionosphere: A wall-less plasma laboratory". In: *Surveys in Geophysics* 18.1 (1997), pp. 57–127.

[335] Space Studies and National Research Council. *Severe space weather events: Understanding societal and economic impacts: A workshop report*. National Academies Press, 2009.

[336] Bruce R Sutherland. *Internal gravity waves*. Cambridge university press, 2010.

[337] Erwan Thébault et al. "International geomagnetic reference field: the 12th generation". In: *Earth, Planets and Space* 67 (2015), pp. 1–19.

[338] David R Themens et al. "Global propagation of ionospheric disturbances associated with the 2022 Tonga Volcanic Eruption". In: *Geophysical Research Letters* (2022), e2022GL098158.

[339] P Thirupathaiah and Vir Singh. "An updated model of atomic oxygen redline dayglow emission". In: *Advances in Space Research* 54.6 (2014), pp. 939–945.

[340] A. P. Thorne. *Spectrophysics*. London: Chapman and Hall, 1988. DOI: https://doi.org/10.1007/9789400911932.

[341] Richard M Thorne et al. "Scattering by chorus waves as the dominant cause of diffuse auroral precipitation". In: *Nature* 467.7318 (2010), pp. 943–946.

[342] DG Torr and Marsha R Torr. "Chemistry of the thermosphere and ionosphere". In: *Journal of Atmospheric and Terrestrial Physics* 41.7-8 (1979), pp. 797–839.

[343] Takuya Tsugawa et al. "Medium-scale traveling ionospheric disturbances detected with dense and wide TEC maps over North America". In: *Geophysical Research Letters* 34.22 (2007).

[344] NA Tsyganenko. "Modeling the Earth's magnetospheric magnetic field confined within a realistic magnetopause". In: *Journal of Geophysical Research: Space Physics* 100.A4 (1995), pp. 5599–5612.

[345] USGS. *M 5.8 Volcanic Eruption - 68 km NNW of Nuku'alofa, Tonga*. 2022. URL: https://earthquake.usgs.gov/earthquakes/eventpage/pt22015050/origin/detail (visited on 07/20/2022).

[346] Sharon L Vadas. "Compressible f-plane solutions to body forces, heatings, and coolings, and application to the primary and secondary gravity waves generated by a deep convective plume". In: *Journal of Geophysical Research: Space Physics* 118.5 (2013), pp. 2377–2397.

[347] Sharon L Vadas. "Horizontal and vertical propagation and dissipation of gravity waves in the thermosphere from lower atmospheric and thermospheric sources". In: *Journal of Geophysical Research: Space Physics* 112.A6 (2007).

[348] Sharon L Vadas and David C Fritts. "The importance of spatial variability in the generation of secondary gravity waves from local body forces". In: *Geophysical Research Letters* 29.20 (2002), pp. 45–1.

[349] Sharon L Vadas, David C Fritts, and M Joan Alexander. "Mechanism for the generation of secondary waves in wave breaking regions". In: *Journal of the Atmospheric Sciences* 60.1 (2003), pp. 194–214.

[350] Sharon L Vadas and Han-li Liu. "Generation of large-scale gravity waves and neutral winds in the thermosphere from the dissipation of convectively generated gravity waves". In: *Journal of Geophysical Research: Space Physics* 114.A10 (2009).

[351] Sharon L Vadas and Michael J Nicolls. "Temporal evolution of neutral, thermospheric winds and plasma response using PFISR measurements of gravity waves". In: *Journal of Atmospheric and Solar-Terrestrial Physics* 71.6-7 (2009), pp. 744–770.

[352] Sharon L Vadas et al. "Primary and secondary gravity waves and large-scale wind changes generated by the Tonga volcanic eruption on 15 January 2022: Modeling and comparison with ICON-MIGHTI winds". In: *Journal of Geophysical Research: Space Physics* 128.2 (2023), e2022JA031138.

[353] Alister Vallance Jones. *Aurora*. D. Reidel publishing company, 1974.

[354] Alexa R Van Eaton et al. "Lightning rings and gravity waves: Insights into the giant eruption plume from Tonga's Hunga Volcano on 15 January 2022". In: *Geophysical Research Letters* 50.12 (2023), e2022GL102341.

[355] J Vergoz et al. "IMS observations of infrasound and acoustic-gravity waves produced by the January 2022 volcanic eruption of Hunga, Tonga: A global analysis". In: *Earth and Planetary Science Letters* 591 (2022), p. 117639.

[356] A Viljanen, EI Tanskanen, and A Pulkkinen. "Relation between substorm characteristics and rapid temporal variations of the ground magnetic field". In: *Annales Geophysicae*. Vol. 24. 2. Copernicus Publications Göttingen, Germany. 2006, pp. 725–733.

[357] A Viljanen et al. "Time derivative of the horizontal geomagnetic field as an activity indicator". In: *Annales Geophysicae*. Vol. 19. 9. Copernicus Publications Göttingen, Germany. 2001, pp. 1107–1118.

[358] Robert A Vincent and M Joan Alexander. "Gravity waves in the tropical lower stratosphere: An observational study of seasonal and interannual variability". In: *Journal of Geophysical Research: Atmospheres* 105.D14 (2000), pp. 17971–17982.

[359] John M Wallace and Peter V Hobbs. *Atmospheric science: An introductory survey*. Vol. 92. Elsevier, 2006.

[360] RL Walterscheid, G Schubert, and DG Brinkman. "Acoustic waves in the upper mesosphere and lower thermosphere generated by deep tropical convection". In: *Journal of Geophysical Research: Space Physics* 108.A11 (2003).

[361] RL Walterscheid, G Schubert, and DG Brinkman. "Small-scale gravity waves in the upper mesosphere and lower thermosphere generated by deep tropical convection". In: *Journal of Geophysical Research: Atmospheres* 106.D23 (2001), pp. 31825–31832.

[362] Jack C Wang et al. "The Lower Thermospheric Winter-To-Summer Meridional Circulation: 1. Driving Mechanism". In: *Journal of Geophysical Research: Space Physics* 127.12 (2022), e2022JA030948.

[363] Lambert Wanninger. "Effects of the equatorial ionosphere on GPS". In: *GPS world* (1993).

[364] Ingo Wardinski et al. "Geomagnetic core field models and secular variation forecasts for the 13th International Geomagnetic Reference Field (IGRF-13)". In: *Earth, Planets and Space* 72.1 (2020), pp. 1–22.

[365] Mark Wardle. "Magnetic fields in protoplanetary disks". In: *Astrophysics and Space Science* 311 (2007), pp. 35–45.

[366] Mark Wardle. "The Balbus-Hawley instability in weakly ionized discs". In: *Monthly Notices of the Royal Astronomical Society* 307.4 (1999), pp. 849–856.

[367] Mark Wardle and Cindy Ng. "The conductivity of dense molecular gas". In: *Monthly Notices of the Royal Astronomical Society* 303.2 (1999), pp. 239–246.

[368] O Witasse et al. "Modeling the OI 630.0 and 557.7 nm thermospheric dayglow during EISCAT-WINDII coordinated measurements". In: *Journal of Geophysical Research: Space Physics* 104.A11 (1999), pp. 24639–24655.

[369] Ronald F Woodman and César La Hoz. "Radar observations of F region equatorial irregularities". In: *Journal of Geophysical Research* 81.31 (1976), pp. 5447–5466.

[370] Andrew W Woods and Stephen Self. "Thermal disequilibrium at the top of volcanic clouds and its effect on estimates of the column height". In: *Nature* 355.6361 (1992), pp. 628–630.

[371] Corwin J Wright et al. "Surface-to-space atmospheric waves from Hunga Tonga-Hunga Ha'apai eruption". In: *Nature* (2022), pp. 1–3.

[372] Haonan Wu et al. "Simulation of the Propagation and Effects of Gravity Waves Generated by Tonga Volcano Eruption in the Thermosphere and Ionosphere Using Nested-Grid TIEGCM". In: *Journal of Geophysical Research: Space Physics* (2023), e2023JA031354.

[373] Yen-Jung J Wu et al. "Cross-Validation of the Ionospheric Vertical Drift Measurements Based on ICON/IVM, Swarm, and the Ground-Based Radar at the Jicamarca Radio Observatory". In: *Space Science Reviews* 219.6 (2023), p. 47.

[374] Yen-Jung J Wu et al. "Errors from asymmetric emission rate in spaceborne, limb sounding Doppler interferometry: A correction algorithm with application to ICON/MIGHTI". In: *Earth and Space Science* 7.10 (2020), e2020EA001164.

[375] Sneha Yadav et al. "Multi-wavelength imaging observations of STEVE at Athabasca, Canada". In: *J. Geophys. Res.: Space Phys.* 126.2 (2021), 2020JA028622.

[376] Yosuke Yamazaki and Astrid Maute. "Sq and EEJ—A review on the daily variation of the geomagnetic field caused by ionospheric dynamo currents". In: *Space Science Reviews* 206.1-4 (2016), pp. 299–405.

[377] Yosuke Yamazaki, Gabriel Soares, and Jürgen Matzka. "Geomagnetic Detection of the Atmospheric Acoustic Resonance at 3.8 mHz During the Hunga Tonga Eruption Event on 15 January 2022". In: *Journal of Geophysical Research: Space Physics* 127.7 (2022), e2022JA030540.

[378] T Yonezawa. "Theory of formation of the ionosphere". In: *Space Science Reviews* 5.1 (1966), pp. 3–56.

[379] Justin D Yonker and Scott M Bailey. "$N_2(A)$ in the Terrestrial Thermosphere". In: *J. Geophys. Res.: Space Phys.* 125.1 (2020), e2019JA026508.

[380] MD Zettergren and JB Snively. "Latitude and longitude dependence of ionospheric TEC and magnetic perturbations from infrasonic-acoustic waves generated by strong seismic events". In: *Geophysical Research Letters* 46.3 (2019), pp. 1132–1140.

[381] MD Zettergren et al. "Nonlinear ionospheric responses to large-amplitude infrasonic-acoustic waves generated by undersea earthquakes". In: *Journal of Geophysical Research: Space Physics* 122.2 (2017), pp. 2272–2291.

[382] Shun-Rong Zhang. "Ionosphere and Thermosphere Coupling at Mid-and Subauroral Latitudes". In: *Ionosphere Dynamics and Applications* (2021), pp. 339–368.

[383] Shun-Rong Zhang et al. "2022 Tonga volcanic eruption induced global propagation of ionospheric disturbances via Lamb waves". In: *Frontiers in Astronomy and Space Sciences* 9 (2022), p. 871275.

[384] Shun-Rong Zhang et al. "Electrified postsunrise ionospheric perturbations at Millstone Hill". In: *Geophysical Research Letters* 48.18 (2021), e2021GL095151.

[385] Yongliang Zhang et al. "STEVE events with FUV emissions". In: *Journal of Geophysical Research: Space Physics* 129.2 (2024), e2023JA032017.

[386] Yongliang Zhang et al. "Thermospheric conditions associated with the loss of 40 Starlink satellites". In: *Space Weather* 20.10 (2022), e2022SW003168.

Appendix A

Appendix for Chapter 2

This appendix derives the expressions for the Hall, Pedersen, and parallel conductivity in the ionosphere as well as Ohm's law in the ionosphere. This derivation supplements the discussion of plasma transport presented in Chapter 2.

A.1 Derivation: Ionospheric Conductivity and Ohm's Law in the Ionosphere

Here, we will derive Ohm's law and the conductivity in a simplified ionosphere composed of electrons and one, singly-ionized ion species immersed in a neutral gas which has a much higher number density than the electrons or ions. We will thread this weakly-ionized plasma with a background magnetic field, and calculate the ease with which electric fields can generate currents in this medium both along and perpendicular to this background magnetic field. Effects from other forces, such as gravity or pressure gradients, will be ignored.

Much of this derivation replicates my response to a problem set given in Astronomy C202: Astrophysical Fluid Dynamics, which I took from Professor Eugene Chiang at the University of California, Berkeley in the spring of 2021. In the assigned problem set, the problem statement was inspired by developments in papers by astrophysicist Mark Wardle (e.g., Wardle 1999; Wardle & Ng 1999; Salmeron & Wardle 2003; Wardle 2007) [366, 367, 301, 365]. These papers primarily tackle conductivity in interstellar clouds, star-forming regions with scales far larger than our own solar system. However, these clouds, like Earth's ionosphere, are weakly ionized and threaded with a background magnetic field, so the derivation of conductivity proceeds remarkably similarly.

Proceeding in the rest frame of the neutral fluid, and assuming that the ions and electrons are in steady state, the equations of motion for the ions and electrons can be written as:

$$\begin{aligned} e\left(\vec{E}' + \vec{u}_i \times \vec{B}\right) - \nu_{in} m_i \vec{u}_i = 0 \\ -e\left(\vec{E}' + \vec{u}_e \times \vec{B}\right) - \nu_{en} m_e \vec{u}_e = 0 \end{aligned} \tag{A.1}$$

where e is the magnitude of the electron and ion charge, $\vec{E}'$ and $\vec{B}$ are the electric and magnetic fields in the rest frame of the neutral fluid, $\vec{u}_i$ and $\vec{u}_e$ are the ion and electron flow velocities relative to the neutral fluid, ν_{in} and ν_{en} are the ion- and electron-neutral collision frequencies, and m_i and m_e are the ion and electron masses. In a plasma with multiple ion species, we would have a separate force equation for each species. Additionally, we have ignored the effect of collisions between charged particles, known as Coulomb collisions. In the dynamo region of the ionosphere, which is the primarily focus of this dissertation, the Coulomb collision rate is much less than the collision rates between charged and neutral species. When considering the dynamics at higher altitudes, it would become more important to take Coulomb collisions into account.

Without loss of generality, we can work in a coordinate system in which the magnetic field lies along the z-axis and the component of the electric field perpendicular to the magnetic field lies along the x-axis. Thus, we can write these fields as $\vec{B} = (0, 0, B)$ and $\vec{E}' = \left(E'_\perp, 0, E'_\parallel\right)$. Working just with the ion force equation for a moment, let the ion velocity relative to the neutrals be written as $\vec{u}_i = (u_{i1}, u_{i2}, u_{i3})$. We can then rewrite it as a system of three equations, one for each component, as:

$$\begin{aligned} e\left(E'_\perp + u_{i2} B\right) - \nu_{in} m_i u_{i1} = 0 \\ -e u_{i1} B - \nu_{in} m_i u_{i2} = 0 \\ e E'_\parallel - \nu_{in} m_i u_{i3} = 0 \end{aligned} \tag{A.2}$$

From the equation for the third equation, we find:

$$u_{i3} = \frac{e E'_\parallel}{\nu_{in} m_i} \tag{A.3}$$

We can combine the equations for the first two equations to solve for u_{i1} and u_{i2}, finding:

$$\begin{aligned} u_{i1} = \frac{e E'_\perp}{m_i} \left(\frac{\nu_{in}}{\omega_i^2 + \nu_{in}^2}\right) \\ u_{i2} = -\frac{e E'_\perp}{m_i} \left(\frac{\omega_i}{\omega_i^2 + \nu_{in}^2}\right) \end{aligned} \tag{A.4}$$

where $\omega_i = eB/m_i$ is the ion gyrofrequency. Thus, we have found the ion velocity relative to the neutral gas to be:

$$\vec{u}_i = \left(\frac{eE'_\perp}{m_i} \left(\frac{\nu_{in}}{\omega_i^2 + \nu_{in}^2} \right), -\frac{eE'_\perp}{m_i} \left(\frac{\omega_i}{\omega_i^2 + \nu_{in}^2} \right), \frac{eE'_\parallel}{\nu_{in} m_i} \right) \tag{A.5}$$

Similarly, we can solve for the electron velocity relative to the neutral gas and find it to be:

$$\vec{u}_e = \left(-\frac{eE'_\perp}{m_e} \left(\frac{\nu_{en}}{\omega_e^2 + \nu_{en}^2} \right), -\frac{eE'_\perp}{m_e} \left(\frac{\omega_e}{\omega_e^2 + \nu_{en}^2} \right), -\frac{eE'_\parallel}{\nu_{en} m_e} \right) \tag{A.6}$$

The current density in a plasma, which arises from differences in the electron and ion motion, is calculated as $\vec{j} = ne\,(\vec{u}_i - \vec{u}_e)$, where we have considered the plasma to be quasi-neutral such that the ion and electron densities are the same on the scales we are interested in ($n_i = n_e = n$). Letting $\vec{j} = (j_1, j_2, j_3)$ and using the expressions for $\vec{u}_i$ and $\vec{u}_e$ calculated above, we can solve for each of the components of the current. Beginning with the component of the current parallel to the magnetic field, we find:

$$\begin{aligned} j_3 &= ne \left(\frac{eE'_\parallel}{\nu_{in} m_i} + \frac{eE'_\parallel}{\nu_{en} m_e} \right) \\ &= \frac{ne^2}{m_e} \left(\frac{1}{\nu_{en}} + \frac{m_e}{m_i} \frac{1}{\nu_{en}} \right) E'_\parallel \\ &= \sigma_\parallel E'_\parallel \end{aligned} \tag{A.7}$$

where we have defined the parallel conductivity $\sigma_\parallel$ to be:

$$\boxed{\sigma_\parallel = \frac{ne^2}{m_e} \left(\frac{1}{\nu_{en}} + \frac{m_e}{m_i} \frac{1}{\nu_{en}} \right)} \tag{A.8}$$

Next, examining the component of the current along the direction of the electric field component perpendicular to the magnetic field, we find:

$$\begin{aligned} j_1 &= ne \left(\frac{eE'_\perp}{m_i} \left(\frac{\nu_{in}}{\omega_i^2 + \nu_{in}^2} \right) + \frac{eE'_\perp}{m_e} \left(\frac{\nu_{en}}{\omega_e^2 + \nu_{en}^2} \right) \right) \\ &= \frac{ne^2}{m_e} \left(\frac{\nu_{en}}{\omega_e^2 + \nu_{en}^2} + \frac{m_e}{m_i} \frac{\nu_{in}}{\omega_i^2 + \nu_{in}^2} \right) E'_\perp \\ &= \sigma_P E'_\perp \end{aligned} \tag{A.9}$$

where we have defined the Pedersen conductivity σ_P to be:

$$\boxed{\sigma_P = \frac{ne^2}{m_e} \left(\frac{\nu_{en}}{\omega_e^2 + \nu_{en}^2} + \frac{m_e}{m_i} \frac{\nu_{in}}{\omega_i^2 + \nu_{in}^2} \right)} \tag{A.10}$$

Finally, examining the final component of the current, which is orthogonal to both the electric and magnetic fields, we find:

$$\begin{aligned} j_2 &= ne\left(-\frac{eE'_\perp}{m_i}\left(\frac{\omega_i}{\omega_i^2+\nu_{in}^2}\right)+\frac{eE'_\perp}{m_e}\left(\frac{\omega_e}{\omega_e^2+\nu_{en}^2}\right)\right) \\ &= \frac{ne^2}{m_e}\left(\frac{\omega_e}{\omega_e^2+\nu_{en}^2}-\frac{m_e}{m_i}\frac{\omega_i}{\omega_i^2+\nu_{in}^2}\right)E'_\perp \\ &= \sigma_H E'_\perp \end{aligned} \tag{A.11}$$

where we have defined the Hall conductivity σ_H to be:

$$\boxed{\sigma_H = \frac{ne^2}{m_e}\left(\frac{\omega_e}{\omega_e^2+\nu_{en}^2}-\frac{m_e}{m_i}\frac{\omega_i}{\omega_i^2+\nu_{in}^2}\right)} \tag{A.12}$$

Thus, we can write Ohm's law as:

$$\vec{j} = \sigma_\parallel \vec{E}'_\parallel + \sigma_H \hat{B}\times\vec{E}'_\perp + \sigma_P \vec{E}'_\perp = \overleftrightarrow{\sigma}\cdot\vec{E}' \tag{A.13}$$

Recall that the primes on the electric field vectors refer to the fact that we are performing our calculations in the rest frame of the neutral gas[1]. In the ionosphere, it is often more convenient to make measurements and perform calculations in an Earth-fixed frame. In this frame, the neutrals move with a bulk velocity $\vec{u}$ termed the *neutral wind*. Transforming Ohm's law to this frame, we can write Ohm's law in the ionosphere as:

$$\boxed{\vec{j} = \overleftrightarrow{\sigma}\cdot\left(\vec{E}+\vec{u}\times\vec{B}\right)} \tag{A.14}$$

[1]In the non-relativistic case we are considering here, the magnetic field vector $\vec{B}$ will not change between frames, so we did not include a prime on it.

Appendix B

Appendix for Chapter 3

This appendix expands on the work presented in Chapter 3 and published in Gasque et al. (2022) [108]. First, Appendix B.1 provides additional details on the Ionospheric Connection Explorer (ICON) mission and its Ion Velocity Meter (IVM), which was used to take the observations described in Chapter 3. Then Appendix B.2 steps through the ionospheric E Region dynamo calculation described in Chapter 3 to explain the observed plasma drifts. That section also details the assumptions that go into that calculation and evaluates their validity.

B.1 The Ionospheric Connection Explorer: Mission and Instrumentation

NASA's Ionospheric Connection Explorer (ICON) mission, launched on 10 October 2019, was designed to explore the dynamic equatorial-region coupling between the ionosphere and thermosphere (Immel et al., 2018) [156]. The study presented in Chapter 3 (Gasque et al., 2022) [108] displayed measurements from the Ion Velocity Meter (IVM) onboard ICON following the Tonga volcanic eruption. This section will provide additional details about the ICON mission as well as the IVM instrument and data products.

ICON: Mission Overview

ICON's primary science objective was to understand and quantify different sources of ionospheric variability by investigating energy and momentum inputs to the ionosphere from both the lower atmosphere below and the magnetosphere above (Immel et al., 2018) [156]. ICON's unique approach to sampling the coupled ionosphere-thermosphere system is depicted in Figure B.1. From its nearly circular, 27° inclination orbit at ∼575 km, ICON continuously makes in-situ measurements of ion densities, composition, and drifts within 30° of the magnetic equator. Simultaneously, ICON measures the neutral wind, temperature, and composition profiles as well as plasma density profiles near the base of the field line,

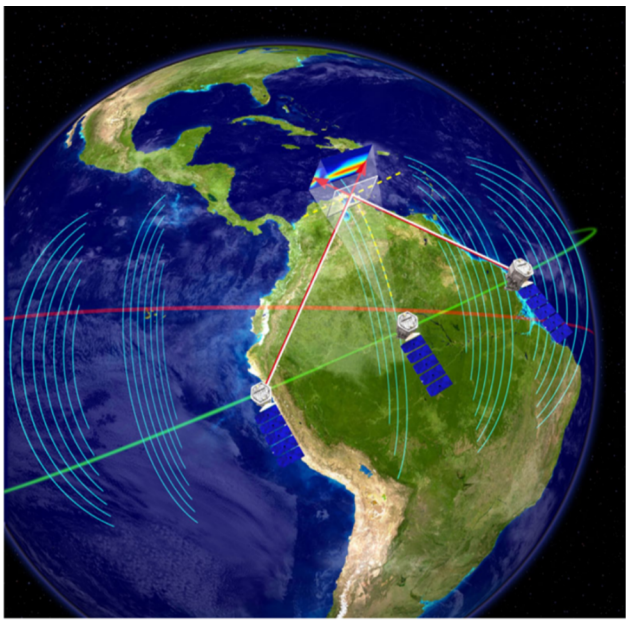

Figure B.1: Schematic of measurements made by the ICON satellite, reproduced from Immel et al., (2018) [156]. The satellite follows the orbit shown in green, making in situ plasma measurements near the apex of the equatorial field lines (shown in white). Simultaneously, ICON remotely measures the horizontal neutral wind profile, combining measurements ~ 7 minutes apart both ahead of and behind the satellite track to resolve the 2D vector winds.

covering the dynamo region (see Chapter 2.3). Notably, ICON measured each of the terms on the right hand side of the ionospheric Ohm's law (Equation A.14, derived in Appendix A.1), allowing it to investigate electrodynamic coupling in the I-T system in more detail than previously possible.

ICON carries a suite of four instruments: the Ion Velocity Meter (IVM) measures in-situ plasma parameters (Heelis et al., 2017) [134], the Michelson Interferometer for Global High-resolution Thermospheric Imaging (MIGHTI) remotely senses neutral wind and temperature profiles (Englert et al., 2017; Harlander et al., 2017; Harding et al., 2017; Stevens et al., 2018; Stevens et al., 2022; Englert et al., 2023) [75, 130, 125, 332, 331, 74], the Far-Ultraviolet Imager (FUV) senses the O/N_2 composition ratio during the day and O^+ ion density profile at night (Mende et al., 2017; Stephan et al., 2018; Kamalabadi et al., 2018) [230, 330, 165], and the Extreme Ultraviolet Spectrometer (EUV) measures O^+ ion density profiles during the day (Sirk et al., 2017; Stephan et al., 2017) [317, 329]. In the following section, we will further examine the IVM and its data products. MIGHTI, which we use extensively in Chapter 4 in studying the neutral wind signatures of solar terminator waves, will be reviewed in Appendix C.1.

Following an unexplained communications anomaly, the ICON ground team lost contact

with the satellite on 25 November 2022, shortly after the satellite had completed its prime mission. During its nearly 3-year mission lifetime, ICON observations enabled many important advances in the field, as summarized in Immel et al. (2023) [157]. Ongoing work with this dataset, some of which is outlined in Chapter 6 of this dissertation, will continue to address outstanding science questions.

ICON's Ion Velocity Meter

ICON's Ion Velocity Meter (IVM) comprises two sensors, a retarding potential analyzer (RPA) and an ion drift meter (IDM), both located on the ram side of the spacecraft. Their view is approximately aligned with the spacecraft velocity vector. Together, they provide continuous in situ measurements of ion drift, density, temperature, and major ion species composition at a 1-second cadence. For more detailed information on the IVM design, refer to Heelis et al. (2017) [134].

The RPA operates by allowing ions through an aperture and subjecting them to potentials ranging from 0 to 25.5 V. By sweeping through these potentials and measuring the resulting current from the detector, it is possible to determine the density and average energy of the incoming ion population. The shape of the resulting current-voltage curve (referred to as the *I-V curve*) also reveals the relative abundance of heavy and light ions. As the topside ionosphere, where the satellite resides, primarily contains O^+ and H^+ ions, fitting the I-V curve allows determination of the O^+ and H^+ compositional fractions. ICON traverses about 7.5 km during each measurement sweep, so structures with rapid density fluctuations over these spatial scales (such as equatorial plasma bubbles) lead to errors in these measurements.

The IDM measures the ion drift, both parallel and perpendicular to the local magnetic field, by measuring the angle of arrival of incoming O^+ ions. Since ICON lacks an onboard magnetometer, the local magnetic field direction is approximated using the International Geomagnetic Reference Field (Finlay et al., 2010) [84]. Perpendicular drifts are primarily due to $\vec{E} \times \vec{B}$ drift, making these measurements essentially a gauge of the perpendicular ionospheric electric field. Assuming magnetic field lines are equipotentials, the in situ perpendicular drift measurement therefore captures the drift and electric field at all points along the sampled magnetic field line (Heelis et al., 2017) [134]. This method for measuring plasma drifts is only viable when there are sufficient O^+ ions (>100 cm^{-3}) for a reliable signal. From the time of ICON's launch through October 2020, the deep solar minimum and associated low solar activity posed challenges for these measurements, especially during the night and early morning when the plasma density is at its lowest (Heelis et al., 2022) [135].

Figure B.2 shows representative IVM observations of the ion density, O^+ fraction, ion temperature, and field-aligned, meridional (vertical), and zonal ion drifts. These values are averaged with respect to solar local time for 8 - 13 January 2022, the period used to generate the climatologies compared with the conditions during the Tonga volcanic eruption in Chapter 3 (Gasque et al., 2022) [108].[1] The positive directions for ion drifts are defined

[1]It's worth noting that although the eruption occurred on 15 January 2022, a moderate geomagnetic

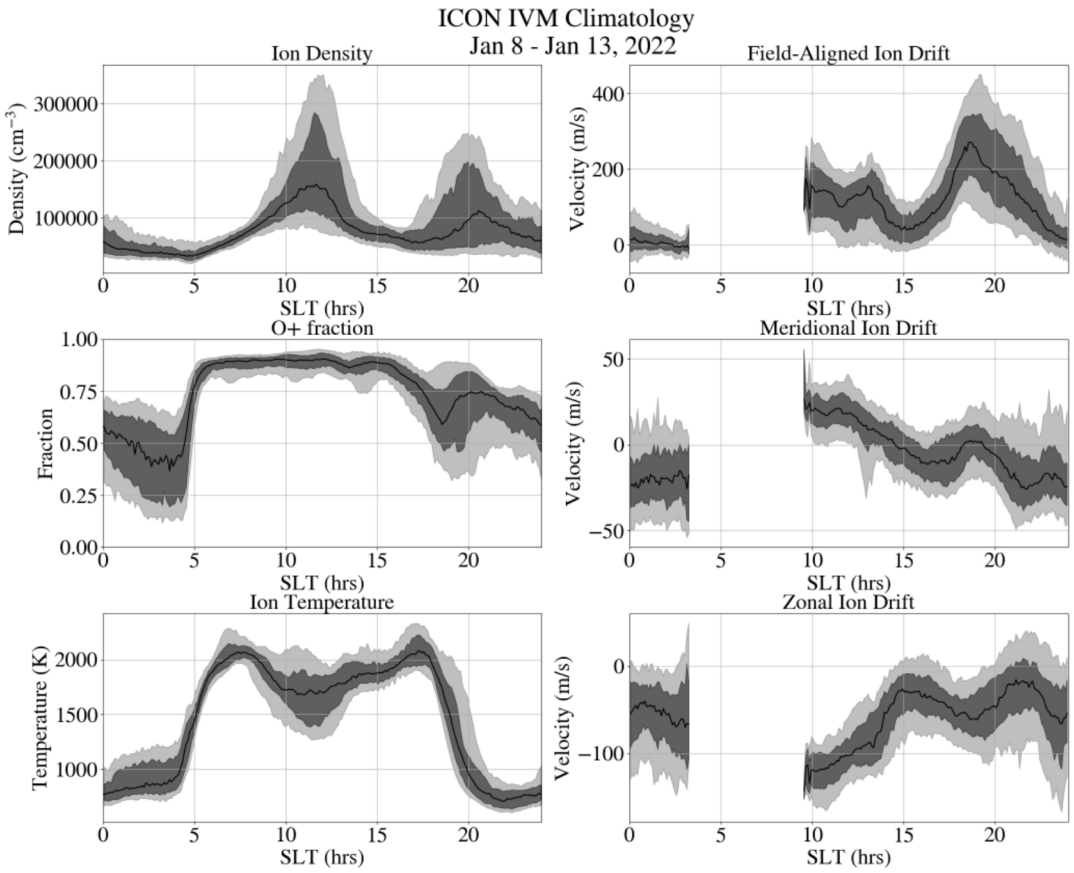

Figure B.2: ICON IVM climatologies for 8-13 January 2022, the period used to evaluate the background conditions in Gasque et al. (2022) [108]. Northward, upward, and eastward are defined to be positive for the ion drifts. The black line indicates the median at each solar local time (SLT), the dark grey shading spans the 25th to 75th percentiles, and the light grey shading spans the 10th to 90th percentiles.

as northward, upward, and eastward. The data are filtered for good quality using included quality flags and are then segmented into 0.1-hour solar local time bins. In each plot, the black line represents the median, the dark gray shading indicates the 25th to 75th percentiles, and the light gray shading indicates the 10th to 90th percentiles. Gaps in the drifts during the early morning are a result of the low plasma densities during these times.

B.2 Dynamo Calculation and Comparison with Whole-Atmosphere Model Results

Chapter 3 presents ICON observations of extreme vertical and zonal ion drifts conjugate to the ionosphere near the Tonga volcano within 45 minutes of the eruption. It described an E Region dynamo calculation which allowed prediction of the neutral winds which would have been required to produce such drifts, finding that these winds traveled with an effective propagation velocity of 600 ± 50 m/s and had an amplitude > 200 m/s. This appendix describes the dynamo calculation in greater detail and compares the results to the simulated neutral winds from the eruption modeled by Vadas et al. (2023) [352].

When the Tonga volcano erupted, the energy it released sent a broad spectrum of waves propagating through the atmosphere (e.g. Wright et al., 2022) [371]. In the neutral atmosphere, these waves are associated with perturbations in the background pressure, temperature, density, and wind. As explored in Chapter 2.3, neutral winds drive currents through the ionosphere in a process commonly referred to as the ionospheric dynamo. Having observed the extreme ion drifts in the conjugate hemisphere following the eruption, a dynamo calculation can be used to determine properties of the neutral winds triggered by the Tonga eruption.

The inspiration for the dynamo calculation described here comes from the ionospheric E and F Region dynamo models presented in Chapter 3 of Kelley (2009) [172]. The electric fields and ion drifts will be analyzed in a magnetic field-aligned slab of atmosphere, as shown schematically in Figure B.3. A slab with footpoints near the eruption site, $\sim 20°$ magnetic latitude from the magnetic equator, reaches an apex height[2] of ∼1,000 km, which lies near the boundary between the topside ionosphere and the plasmasphere.

In the absence of an externally-applied electric field, Ohm's law in the ionosphere (derived in Appendix A.1) can be written:

$$\vec{j} = \overleftrightarrow{\sigma} \cdot \left(\vec{u} \times \vec{B} \right) \tag{B.1}$$

where $\vec{j}$ is the current density, $\overleftrightarrow{\sigma}$ is the conductivity tensor, $\vec{u}$ is the neutral wind velocity, and $\vec{B}$ is the background magnetic field, all measured in an Earth-fixed frame.

storm occurred on 14 January 2022, so that day is excluded from the climatology. The days examined here are geomagnetically quiet.

[2]The *apex height* of a magnetic field line is the altitude of the field line at the magnetic equator, which is also the maximum altitude attained by a given field line.

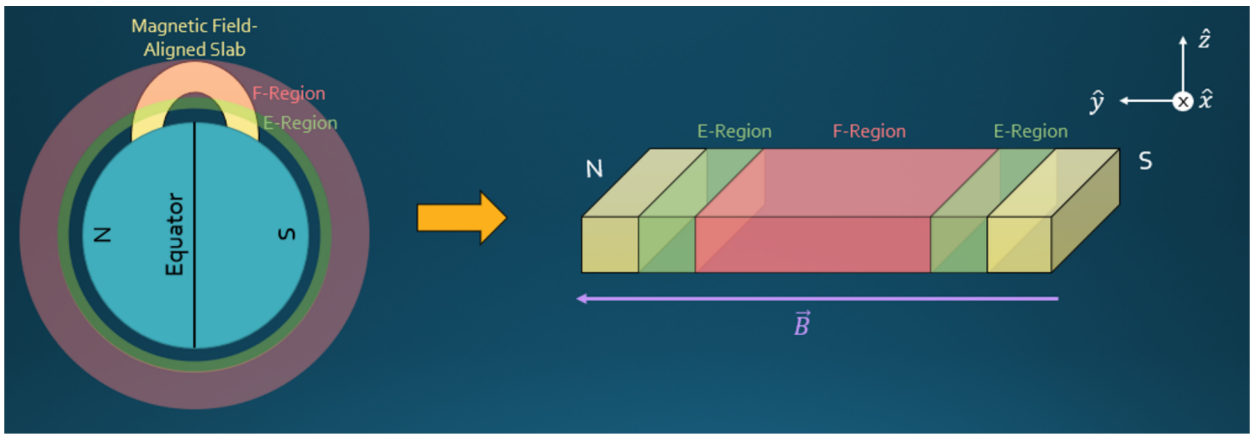

Figure B.3: Diagram of the slab geometry and coordinate system used in the dynamo calculation described in the text. We use a field-aligned slab of the atmosphere with footpoints $\sim 20°$ on either side of the equator. The coordinate system is aligned such that the y-axis points along the magnetic field direction, the z-axis points vertically at the magnetic equator, and the x-axis points eastward to complete the right-handed coordinate system.

The coordinate system is illustrated by the flattened slab on the right side of Figure B.3. The y-axis lies along the magnetic field line, the z-axis points vertically at the apex of the field line, and the x-axis points eastward, completing the right-handed coordinate system. In this coordinate system, the conductivity tensor will take the form:

$$\overleftrightarrow{\sigma} = \begin{pmatrix} \sigma_P & 0 & \sigma_H \\ 0 & \sigma_\parallel & 0 \\ -\sigma_H & 0 & \sigma_P \end{pmatrix} \tag{B.2}$$

where $\sigma_\parallel$, σ_P, and σ_H represent the parallel, Pedersen, and Hall conductivities, respectively, as defined in Equation 2.16 and derived in Appendix A.1.

The resulting Hall current is given by:

$$\vec{j}_H = \sigma_H \left(\left[\vec{u} \times \vec{B} \right]_z \hat{x} - \left[\vec{u} \times \vec{B} \right]_x \hat{z} \right) = \sigma_H \left(\hat{b} \times \left(\vec{u} \times \vec{B} \right) \right) \tag{B.3}$$

where the notation $\left[\vec{u} \times \vec{B} \right]_z$ refers to the z-component of the vector $\vec{u} \times \vec{B}$ and $\hat{b}$ is a unit vector in the direction of the magnetic field vector.

This current will result in a charge separation, which will in turn generate a polarization electric $\vec{E}_p$ field in the opposite direction: $\vec{E}_p = -\hat{b} \times \left(\vec{u} \times \vec{B} \right)$. This will then result in an $\vec{E} \times \vec{B}$ ion drift:

$$\vec{v_i} = \frac{\vec{E}_p \times \vec{B}}{B^2} = \frac{\left(-\hat{b} \times \left(\vec{u} \times \vec{B}\right)\right) \times \vec{B}}{B^2} = \hat{b} \times \vec{u} \tag{B.4}$$

where the vector triple product expansion $\vec{a} \times (\vec{b} \times \vec{c}) = (\vec{a} \cdot \vec{c})\vec{b} - (\vec{a} \cdot \vec{b})\vec{c}$ was used to simplify the result. Note that, for a wind that is perpendicular to the magnetic field, the magnitude of the ion drift is the same as the magnitude of the wind.

This result can be used to predict the direction of the drift given the direction of the initial wind. For example, given a westward wind (out of the page in the slab depicted in Figure B.3), the Hall current will be directed westward as well, generating an eastward polarization electric field which will then give rise to a vertical $\vec{E} \times \vec{B}$ drift. Given a northward wind at the northern footpoint (in the $+\hat{z}$-direction), the Hall current will be directed in the $+\hat{z}$-direction, generating a $-\hat{z}$ polarization electric field, which will result in an eastward $\vec{E} \times \vec{B}$ drift.

In performing this calculation, three assumptions were made implicitly, each of which will be examined in more detail below.

Assumption 1: The perturbation wind from the volcanic eruption is much larger than the background wind, and is therefore the main driver of observed variability

The dynamo calculation discussed above investigates drifts arising from a neutral wind driving a Hall current in the ionospheric E Region. Neutral wind perturbations induced by the volcano were not distinguished from the background winds. Consequently, in asserting that the calculation attributes the observed extreme drifts to the eruption, it is presupposed that the wind perturbation due to the eruption is significantly larger than the background winds and, hence, governs the dynamics. Several sources of evidence support the validity of this assumption.

According to the calculation, plasma drift magnitudes are expected to be comparable to or larger than[3] the driving neutral wind's magnitude. The observed maximum perturbation drift speed is 330 m/s, suggesting that the volcano likely induced neutral winds exceeding 330 m/s within the first hour post-eruption. Using ICON/MIGHTI, Harding et al. (2022) observed dynamo region winds of approximately 200 m/s over South America about 10 hours after the eruption, which were stronger than 99.9% of winds in that region between the launch of the ICON mission in December 2019 and 14 January 2022, the day prior to the eruption. This underscores that a dynamo-region neutral wind surpassing 330 m/s is extreme and significantly exceeds expected background winds.

Following the publication of Gasque et al., (2022) [108], several authors have published whole-atmosphere simulations investigating the effects of the eruption (Vadas et al., 2023; Liu et al., 2023; Wu et al., 2023; Shinagawa & Miyoshi, 2024) [352, 196, 372, 313]. Figure

[3]Our dynamo calculation assumed perfect dynamo driving efficiency, which is unlikely, suggesting that the winds may need to have higher velocities than the observed drifts.

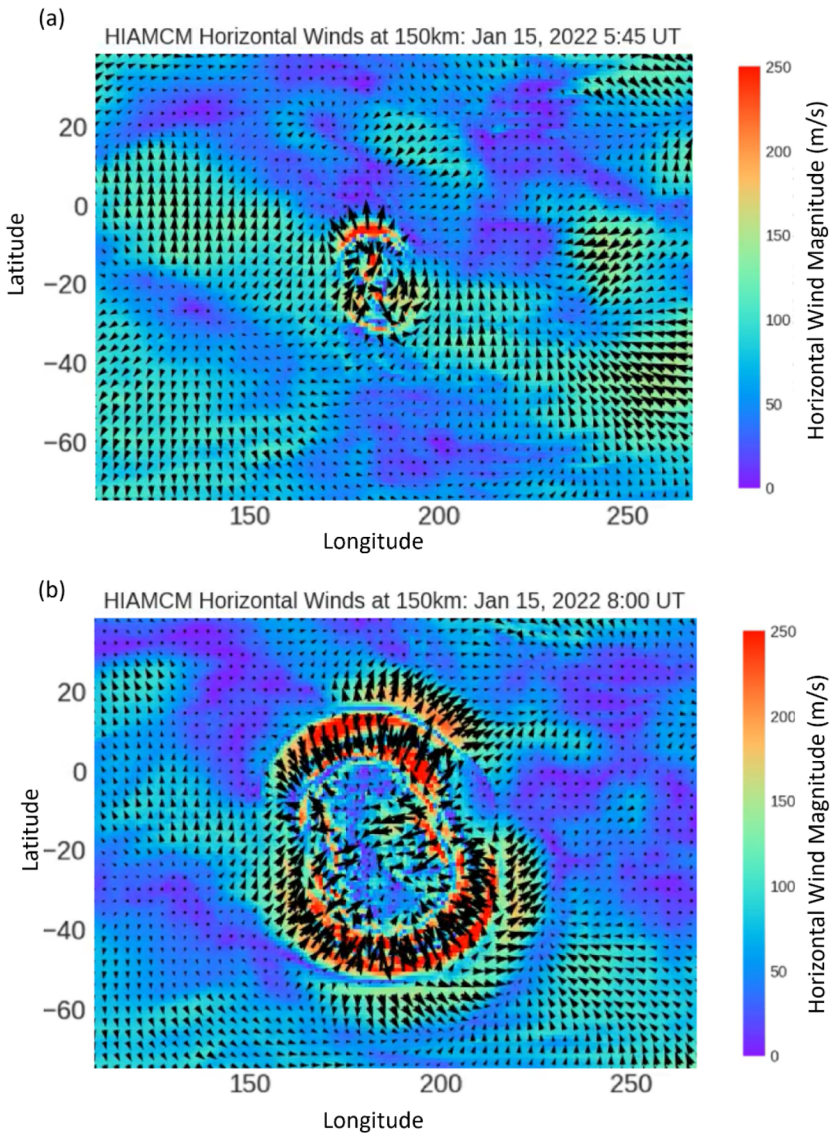

Figure B.4: Modeled horizontal winds following the Tonga volcanic eruption at 150 km at both (a) 5:15 UT and (b) 8:00 UT. The color bar displays the horizontal wind magnitude and the black arrows indicate the direction of the wind. The HIAMCM model simulation data is described in detail in Vadas et al., (2023) [346].

B.4 shows the simulated neutral wind perturbation due to secondary atmospheric gravity waves generated following the eruption as modeled by the HIgh Altitude Mechanistic general Circulation Model (HIAMCM) (Vadas et al., 2023) [352]. In the figure, which is centered on the location of the eruption, the color bar displays the horizontal neutral wind magnitude at 150 km while the black arrows signal the wind's direction.

Examining Figure B.4(a), which depicts the winds within an hour of the eruption, it is clear that the magnitude and direction of the winds are comparable to those deduced in Chapter 3. Along the northern part of the wind disturbance, where ICON's north footpoint sampled, the winds are directed radially away from the eruption site and have magnitudes of several hundred m/s. The simulated perturbation amplitudes are clearly much larger than the simulated background wind amplitudes, supporting the assumption made in the dynamo calculation. Several hours later, as depicted in Figure B.4(b), the perturbation winds are still much larger than the background winds, but the wind directions and presence of multiple wavefronts have made the geometry more complex, which would result in a different drift pattern from the one observed shortly after the eruption in Chapter 3.

Assumption 2: Magnetic field lines can be treated as equipotentials, so electric fields will map along the magnetic field lines

As discussed in Chapter 2.3, the ionospheric parallel conductivity is very high, meaning that charges can move freely along magnetic field lines. Since charges can easily redistribute in response to magnetic field-aligned electric fields, ionospheric magnetic field lines can often be treated as equipotentials, such that perpendicular electric fields are constant at all points along the magnetic field. In the electroquasistatic picture of the ionosphere, these perpendicular electric fields are transmitted rapidly along the magnetic field via Alfvén waves (e.g., Kelley, 2009) [172].

For the case considered in Chapter 3, Figure 3.1(b) depicts the magnetic field line[4] connected to the ICON satellite during its closest approach to the volcano about 45 minutes after the eruption. The Alfvén velocity along this field line can be calculated by using the magnitude of the magnetic field from the International Geomagnetic Reference Field, Version 13 model (Wardinski et al., 2020; Michael, 2021) [364, 231] and the plasma density and composition from the International Reference Ionosphere 2016 (Bilitza et al., 2017; Ilma, 2017) [31, 153]. From this, the total Alfvén travel time between the dynamo region of the ionosphere near the eruption and the spacecraft location is ~ 3.3 seconds. The drift variations occur on timescales on the order of several minutes, much longer than the time it takes for the electric field information to propagate along the magnetic field.

Although the validity of treating magnetic fields as equipotentials has recently been questioned (Cosgrove, 2016) [51], the electrostatic approach's success in capturing the broad strokes of ionospheric physics (e.g. Kelley, 2009) [172], and its success at explaining the

[4]The magnetic field line in Figure 3.1(b) is to scale, as calculated using the International Geomagnetic Reference Field, Version 13 model (Wardinski et al., 2020; Michael, 2021) [364, 231].

large-scale plasma motions we observed following the Tonga eruption (Gasque et al., 2022) [108] are sufficient to justify this assumption.

Assumption 3: The Hall conductivity is larger than the Pedersen conductivity, so the Hall current will dominate the dynamics

The dynamo calculation assumed that Hall currents would dominate the dynamics, explaining the extreme plasma drifts shortly after the eruption. Figure 2.3(a) illustrates that the Hall conductivity typically exceeds the Pedersen conductivity throughout the dynamo region, justifying its use as the primary dynamo driver. The good agreement between observed drifts and those predicted from the assumed radially expanding wind field using a Hall current model further supports this assumption.

However, idealized calculations inevitably have imperfections. A comprehensive treatment of the problem would consider the effects of Pedersen currents using a full solver for the dynamo equation (Richmond, 1995) [282], such as the one developed by Shidler & Rodrigues (2022) [312]. It's also noteworthy that papers published after Gasque et al. (2022) [108], such as Huba et al. (2023) and Liu et al. (2023) [146, 196], simulated ionospheric effects of the event. Although not specifically focusing on the dynamo effects of the volcanic eruption, these studies likely incorporate a full dynamo treatment, offering potential avenues for further investigation to support these results.

Appendix C

Appendix for Chapter 4

This appendix complements the research presented in Chapter 4 and published in Gasque et al. (2024) [106]. First, Appendix C.1 provides additional details on the underlying physical principles enabling neutral wind measurements on ICON, as well as considerations regarding instrumental effects which may influence the interpretation of the measurements. Following that, Appendix C.2 discusses the process used to determine the location of the solar terminator at different times and altitudes, also providing the Python code used for the calculations. Lastly, Appendix C.3, originally published as supplemental information to Gasque et al. (2024) [106], re-presents the primary findings of the paper, this time using the complete three years of ICON neutral wind observations.

C.1 MIGHTI Neutral Wind Observations

Chapter 4 presents observations collected by the Michelson Interferometer for Global High-resolution Thermospheric Imaging (MIGHTI) instrument on NASA's Ionospheric Connection Explorer (ICON) observatory (refer to Appendix B.1 for additional ICON mission details). This appendix provides more information about MIGHTI, including its operational principles and the physical parameters it measures.

MIGHTI generates interference patterns in thermospheric airglow emissions observed from Earth's limb.[1] Airglow is a faint atmospheric luminescence produced as a byproduct of chemical reactions in Earth's atmosphere. MIGHTI specifically detects three distinct emissions released when atomic or molecular oxygen in an excited state undergoes radiative relaxation, releasing a photon in the process.

Thermospheric winds above $\sim$ 170 km, the primary focus of the analysis in Chapter 4, are measured using Doppler shifts in the 630.0 nm emission of atomic oxygen. This emission occurs when oxygen atoms in the excited O(^{1}D) state radiatively relax to their ground state:

[1] The Earth's atmospheric *limb* is the horizon where the thin layer of the atmosphere can be observed against the backdrop of deeper space.

$$\mathrm{O}\left(^1\mathrm{D}\right) \rightarrow \mathrm{O}\left(^3\mathrm{P}\right) + h\nu_{\lambda=630.0\ \mathrm{nm}} \tag{C.1}$$

There are several natural pathways to excite atomic oxygen to the O(^{1}D) state. One of the major pathways, dominant at night, is through dissociative recombination of O_2^+ (as in Equation 2.9), an exothermic reaction which distributes its 7 eV excess energy to kinetic energy and electronic excitation of the resulting two neutral oxygen atoms (e.g., Solomon & Abreu, 1989) [321]. O(^{1}D) is also commonly produced via impact excitation with precipitating auroral particles or electrons in the energetic tail of the thermal distribution, via photodissociation of O_2, or via radiative relaxation from the O(^{1}S) excited state (e.g., Thirupathaiah & Singh, 2014) [339]. Once excited, the time it takes the excited atom to radiatively release a photon and relax to the ground state varies according to an exponential distribution with a mean of 110 s (e.g., Harding, 2017) [125]. Prior to releasing the photon, the O(^{1}D) state may be quenched, usually via collisions with N_2 or ground state oxygen atoms (e.g., Kalogerakis et al., 2009). Excited atoms are typically assumed to undergo multiple collisions with the ambient neutral gas prior to releasing a photon, allowing them to thermalize and adopt the bulk flow of the surrounding gas (e.g., Kharchenko et al., 2005) [173]. MIGHTI therefore measures the resulting Doppler shift in the 630.0 nm emissions from which the line-of-sight wind velocity can be estimated (Englert et al., 2017) [75].

Between about 90 and 170 km, MIGHTI operates using the same principle but by measuring the 557.7 nm green line emission of atomic oxygen, emitted when atoms in the excited O(^{1}S) state relax to the O(^{1}D) state:

$$\mathrm{O}\left(^1\mathrm{S}\right) \rightarrow \mathrm{O}\left(^1\mathrm{D}\right) + h\nu_{\lambda=557.7\mathrm{nm}} \tag{C.2}$$

At these altitudes, the O(^{1}D) state is quickly quenched, so radiative cascade from the O(^{1}S) state is not a dominant source of the 630.0 nm emissions discussed above. Sources of the excited O(^{1}S) state include electron impact excitation, dissociative recombination of O_2^+, collisions between atomic oxygen and the excited N_2 ($A^3\Sigma_u^+$),[2] and photoexcitation, among others (e.g., Witasse et al., 1999) [368]. This state has a mean radiative lifetime of ∼0.7 s (Itikawa & Ichimura, 1990) [159]. Although this lifetime is much shorter than that of O(^{1}D), collisions are also much more frequent at these lower altitudes where the neutral atmosphere is denser. Therefore, the excited O(^{1}S) atoms can also be assumed to thermalize and adopt the background bulk flow prior to emitting a photon, allowing an estimation of the line-of-sight wind velocity using the Doppler shift.

Upon reaching MIGHTI, the incoming photons traverse a series of apertures before being directed, collimated, and filtered by mirrors, lenses, and filters, as detailed in Englert et al. (2017) [75]. Within the interferometer, the beam is split, reflected off of tilted gratings, and combined to form an interference pattern. The phase of this fringe pattern is analyzed

[2]The 557.7 nm green line emissions are one of the most common auroral emissions and the dominant optical contributor to the picket fence spectrum, discussed in Chapter 5. Collisions between atomic oxygen and the N_2 ($A^3\Sigma_u^+$) state are the dominant source of O(^{1}S) in that case. Additional details are provided in Chapter 5 and Appendix D.4.

to determine the Doppler shift and, consequently, the wind velocity. The amplitude of the fringes correlates with the airglow volume emission rate. However, when there are insufficient electrons to excite the neutral gas through collisions, the emission rate decreases, rendering these measurements unreliable. This explains the observation gap between approximately 105 and 210 km at night, which is why the altitude profile of the solar terminator wave could not be displayed at those altitudes in Figure 4.7. Similarly, following the Tonga volcanic eruption, an ionospheric hole formed over the eruption location, reducing the plasma density and, consequently, diminishing the red-line airglow. This reduction in airglow prevented thermospheric wind measurements in the vicinity of the volcano for several hours after the eruption.

After measuring the fringe pattern, the raw interferograms are processed on the ground to correct for various effects, including thermal drift, stars in the field of view, and flat-fielding. The calibration process is detailed in Englert et al. (2017) [75] and Englert et al. (2023) [74]. To transform the calibrated interferograms into a neutral wind altitude profile, an iterative inversion process is employed, as described in Harding et al. (2017) [125]. The inversion assumes spherical symmetry in the atmospheric layers, a condition that may be compromised under the rapidly-changing conditions near the solar terminator. However, as discussed in Chapter 4, these errors are expected to be less than 1 m/s above 200 km, which does not significantly impact our conclusions (Wu et al., 2020) [374]. To obtain the full 2D horizontal vector wind, two MIGHTI instruments, one looking 45° ahead and the other 45° behind the plane orthogonal to ICON's velocity, simultaneously sample the line-of-sight winds. By sampling the same volume of space approximately 8 minutes apart, the line-of-sight profiles can be combined under the assumption that the winds do not change dramatically over that time period. In the nominal configuration, with the two MIGHTI instruments looking toward the northern side of the ICON observatory, the winds can be sampled between about -12° and +42° latitude, which is the range for which observations are reported in Chapter 4.

As detailed in Chapter 4, MIGHTI's horizontal resolution is influenced by various smearing effects, including the integration time (30 s during the day and 60 s at night), the horizontal field of view (approximately 75 km across the line-of-sight), the spacecraft velocity (around 7.1 km/s), and averaging along the line of sight, affected by the inversion and the natural airglow distribution (Harding et al., 2021) [129]. Figure C.1 is an extension of the analysis in Harding et al. (2021)'s [129] Appendix, illustrating the approximate horizontal averaging kernel for both the green and red line winds as a function of altitude. As discussed in Chapter 4, near 280 km, where the solar terminator wave amplitude and scale size are reported, the red line averaging kernels for both day and night modes are approximately 700 km, smaller than the expected solar terminator wave scale size of about 3,000 km.

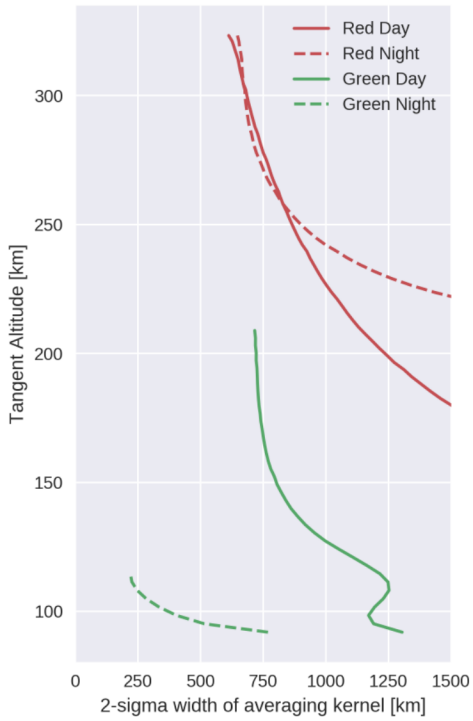

Figure C.1: MIGHTI green and red line horizontal averaging kernels for day (solid lines) and night (dashed lines) modes as a function of the tangent altitude of the observation. Figure courtesy of Brian Harding, using the same analysis described in the Appendix of Harding et al. (2021) [129].

C.2 Identifying the Solar Terminator as a Function of Altitude

To pinpoint the intersection between the solar terminator wave discussed in Chapter 4 and the evening solar terminator and calculate the angle between the two, it is essential to determine the solar terminator's location as a function of latitude, longitude, time, and altitude. This was achieved by adapting the method and code outlined in Colonna and Tramutoli (2021) [49], which presents a model to calculate the time- and location-dependent solar terminator height. This appendix details the adapted method, including the alterations made to align it with this study's specific objectives, and includes the Python functions used to perform the analysis.

In their work, Colonna and Tramutoli (2021) [49] calculate the solar terminator height under the assumption that solar rays travel parallel to each other and using the World Geodetic System (WGS) 84 model of the Earth. The Earth therefore casts an elliptical

shadow cylinder in space, and one can calculate the solar terminator height at a given latitude, longitude, and time by finding the intersection between the edge of that cylinder and a line normal to the Earth at that location on the surface.

To perform these calculations, it is first important to calculate three solar angles at the queried location and time: the local hour angle from sunset λ, the solar declination δ, and the solar elevation angle α. The equations used to determine these angles are detailed in Meeus (1998) [226]. The Python function `calculate_solar_angles` provided below calculates these angles at a given time, latitude, and longitude.

From these angles, as well as the ellipsoid parameters of the Earth, Colonna and Tramutoli (2021) [49] solve for the height of the solar terminator, given in their Equation 43. The Python function `ST_height`, included here, calculates this altitude as a function of time, latitude, and longitude. If the ground is sunlit at the given point, the terminator altitude is set to 0 km.

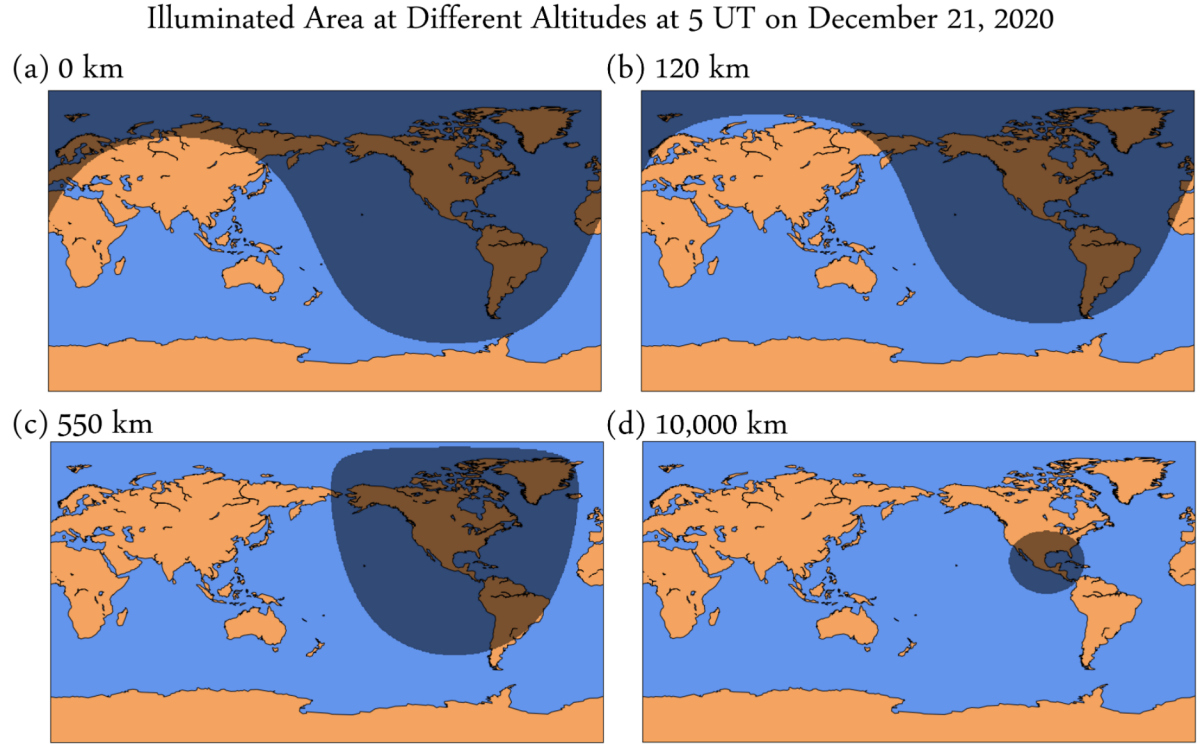

Figure C.2: World maps showing the illuminated and dark parts of the atmosphere at 5 UT on December 21, 2020 at (a) 0 km, (b) 120 km, (c) 550 km, and (d) 10,000 km, calculated using the Python functions included in the text.

```
def calculate_solar_angles(time,lat,lon):
    '''Calculate solar declination angle (delta), local hour angle
    from sunset (lamb), and solar elevation angle (alpha)
    time is a datetime object
    lat, lon are latitude, longitude in degrees'''

    pd_time = pd.Timestamp(time)
    T = (pd_time.to_julian_date() - 2451545)/36525 #Julian centuries
    ML = 280.46646 + T*(36000.76983 + 0.0003032*T) #Sun's mean longitude
    MA = 357.52911 + T*(35999.05029 - 0.0001537*T) #Sun's mean anomaly
    C = np.sin(np.deg2rad(MA))*(1.914602 - T*(0.004817 + 0.000014*T)) ...
        + np.sin(np.deg2rad(2*MA))*(0.019993 - 0.000101*T) ...
        + np.sin(np.deg2rad(3*MA))*0.000289 #Sun's equation of center
    TL = ML + C #Sun's true longitude
    AL = TL - 0.00478*np.sin(np.deg2rad(125.04 - 1934.136*T)) ...
        - 0.00569 #Sun's apparent longitude
    MOE = (23 + 26/60 + 21.406/3600) + (-46.836769*T - 0.0001831*T**2 ...
        + 0.00200340*T**3 - 0.576*10**(-6)*T**4 ...
        - 4.34*10**(-8)*T**5)/3600 #Mean obliquity of the ecliptic
    OC = MOE + 0.00256*np.cos(np.deg2rad(125.04 ...
        - 1934.136*T)) #Obliquity corrected
    delta = np.rad2deg(np.arcsin(np.sin(np.deg2rad(OC))...
        *np.sin(np.deg2rad(AL)))) #solar declination angle
    EEO = 0.016708634 - 0.000042037*T ...
        - 0.0000001267*T**2 #eccentricity of Earth's orbit
    y = np.tan(np.deg2rad(OC/2))**2 #coefficient y
    ET = 180/np.pi*(y*np.sin(np.deg2rad(2*ML)) ...
        - 2*EEO*np.sin(np.deg2rad(MA)) + 4*EEO*y...
        *np.sin(np.deg2rad(MA))*np.cos(np.deg2rad(2*ML)) ...
        - 0.5*y**2*np.sin(np.deg2rad(4*ML)) ...
        - 1.25*EEO**2*np.sin(np.deg2rad(2*MA)))*4 #equation of time (min)
    HD = time.hour*60 + time.minute + time.second/60 #Hour of Day (min)
    TST = (HD + ET + 4*lon)%1440 #True solar time (min/UTC)
    LHA = TST/4 - 180 #Local hour angle
    lamb = (LHA - 90)%360 #Local hour angle from sunset
    alpha = np.rad2deg(np.arcsin(np.sin(np.deg2rad(lat))...
        *np.sin(np.deg2rad(delta)) + np.cos(np.deg2rad(lat))...
        *np.cos(np.deg2rad(delta))*np.cos(np.deg2rad(LHA))))
        #solar elevation angle

    return delta, lamb, alpha
```

```
def ST_height(t,lat,lon):
    '''returns altitude of solar terminator at a given time,
    lat, and lon in km'''

    a = 6378137 #semi-major axis (m)
    c = 6356752.314 #semi-minor axis (m)
    e_squared = 1 - c**2/a**2 #eccentricity squared
    N = a/np.sqrt(1-e_squared*np.sin(np.deg2rad(lat))**2) #ellipsoid norm
    delta, lamb, alpha = calculate_solar_angles(t,lat,lon) #solar angles
    Z_P0 = -e_squared*N*np.sin(np.deg2rad(lat))*np.cos(np.deg2rad(delta))
    C1 = np.cos(np.deg2rad(lamb))/(np.sin(np.deg2rad(lamb))...
        *np.sin(np.deg2rad(delta)) + np.tan(np.deg2rad(lat))...
        *np.cos(np.deg2rad(delta)))
    C2 = (np.tan(np.deg2rad(delta))**2 + a**2/c**2)...
        /(np.cos(np.deg2rad(delta))*(1+np.tan(np.deg2rad(delta))**2))**2
    K1 = C1**2 + C2
    K2 = 2*Z_P0*C1**2
    K3 = Z_P0**2*C1**2 - a**2

    if delta+lat > 0:
        Z_H = (K2 + np.sqrt(K2**2 - 4*K1*K3))/(2*K1)
    else:
        Z_H = (K2 - np.sqrt(K2**2 - 4*K1*K3))/(2*K1)

    X_H = (Z_H - Z_P0)*C1

    if alpha < 0:
        h = X_H/(np.cos(np.deg2rad(lat))*np.cos(np.deg2rad(lamb))) - N
    else:
        h = 0

    if h < 0:
        if delta+lat > 0:
            Z_H = (K2 - np.sqrt(K2**2 - 4*K1*K3))/(2*K1)
        else:
            Z_H = (K2 + np.sqrt(K2**2 - 4*K1*K3))/(2*K1)

        X_H = (Z_H - Z_P0)*C1
        h = X_H/(np.cos(np.deg2rad(lat))*np.cos(np.deg2rad(lamb))) - N

    return h*10**(-3)
```

```
def daynight_terminator(date,nlats=290):
    '''Calculate solar terminator height on a latitude/longitude
    grid for a given datetime'''

    nlons = 2*nlats #number of longitudes:
    delta = 2*np.pi/(nlons-1)
    lats = (0.5*np.pi - delta*np.indices((nlats,nlons))[0,:,:])*180/np.pi
    lons = (delta*np.indices((nlats,nlons))[1,:,:])*180/np.pi

    h = np.zeros((nlats,nlons))

    for i in range(0,nlats):
        for j in range(0,nlons):
            h[i,j] = ST_height(date,lats[i,j],lons[i,j])

    return h, lats, lons
```

For this study's purposes, at a given altitude, it is necessary to determine the location of the solar terminator. Therefore, the function `daynight_terminator`, included above, calculates the altitude of the terminator on a grid of latitudes and longitudes. If the height of the terminator is above the altitude of interest, the point will be in darkness, while if the terminator height is below that altitude, the point will be illuminated.

These functions allow the production of maps like those shown in Figure C.2, finding the areas which are illuminated or in shadow at a given time as a function of altitude. For illustration purposes, Figure C.2 shows these maps at 5 UT on December 21, 2020 (the northern hemisphere winter solstice) at (a) ground level (0 km), (b) in the ionospheric dynamo region (120 km), (c) in the topside ionosphere near ICON's orbital altitude (550 km), and (d) in the magnetosphere at ∼1.5 earth radii above the surface (10,000 km). Note that, as you would expect, the entire north pole is perpetually in darkness at ground level during the solstice while the south pole is illuminated. At progressively higher altitudes, progressively less of the atmosphere is in the Earth's shadow.

From these maps, it is possible to extract the location of the solar terminator at a given altitude by finding the dividing line between illumination and darkness. This was the method used to determine the location of the solar terminator in Chapter 4.

C.3 Description of STW Parameters Using all Three Years of ICON Neutral Wind Data

In Chapter 4, the STW in ICON/MIGHTI neutral wind data is presented for the period from December 2019 to March 2021, corresponding to the period for which SD-WACCM-

X simulations were available for comparison. This appendix reproduces Figures 4.1, 4.2, and 4.3 of the main text, but uses data from the entire ICON mission (December 2019 to November 2022) for comparison. The analysis is identical to that described in Section 4.2 of the main article, but for this larger subset of data. The amplitudes and scale sizes of the reported STW features change slightly, but the qualitative results remain the same.

Figures C.3 and C.4 show the tidal decomposition for the winter meridional and zonal winds, respectively, for the full ICON mission.

Figure C.5 shows the MIGHTI meridional (left) and zonal (right) winds binned by latitude and SLT at ∼283 km for NH winter (top), combined equinox (middle) and NH summer (bottom), after removing the diurnal tide and using the entire MIGHTI data set. Black dotted lines identify the STW feature in the solstice cases. The NH winter STW is characterized by ∼55 m/s northward winds (Figure C.5(a)) and ∼55 m/s eastward winds on the nightside, although the zonal wind component diminishes on the dayside (Figure C.5(b)). In both meridional and zonal wind components, it has a ∼3200 km scale size, intersecting the ST between ∼15° to 20° latitude (∼18.6 SLT) with a ∼28° phase front inclination compared to the ST.

For the NH summer case, we observe a ∼35 m/s southward wind enhancement (Figure C.5(e)) and a ∼ 25 m/s eastward wind enhancement (Figure C.5(f)), whose phase fronts, when extrapolated down to lower latitudes, intersect the evening ST between ∼-20° to -25° latitude (∼18.6 SLT). The scale size of this feature is ∼ 2400 km, comparable to the NH winter STW, and its phase front is inclined ∼ 38° relative to the ST at the intersection point.

Compared with the subset of data presented in the main chapter, the amplitudes, scale sizes, and intersections with the ST do not change significantly.

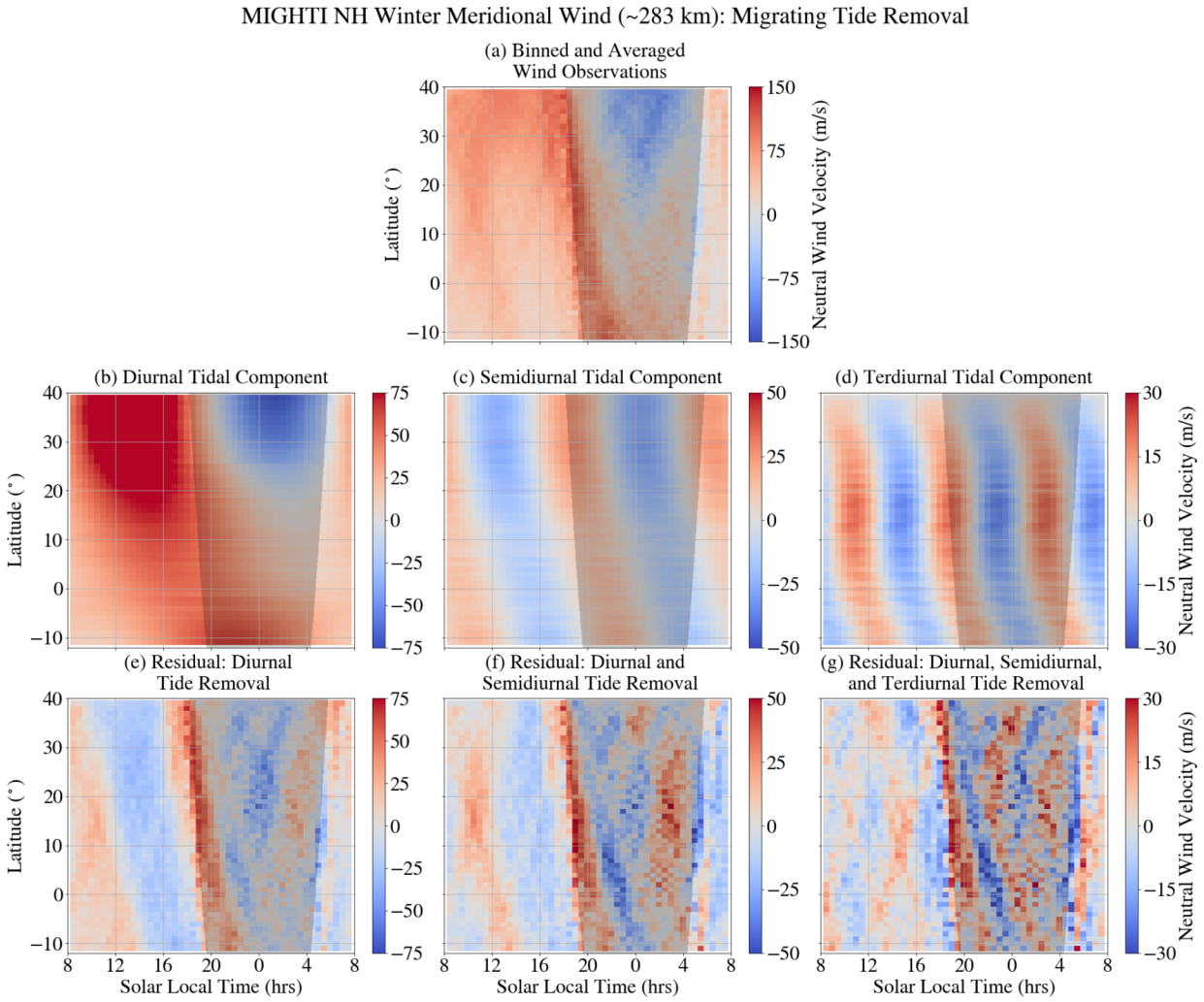

Figure C.3: Meridional winds during NH winter as observed by MIGHTI (full mission), presented as a function of latitude and SLT. In the first row, (a) shows the binned and averaged data prior to the removal of tidal components. The second row displays the fits for the (b) diurnal, (c) semidiurnal, and (d) terdiurnal tidal components. The final row shows the data residuals after successively removing the (e) diurnal, (f) semidiurnal, and (g) terdiurnal tides. Note that the colorbar amplitude varies between subfigures.

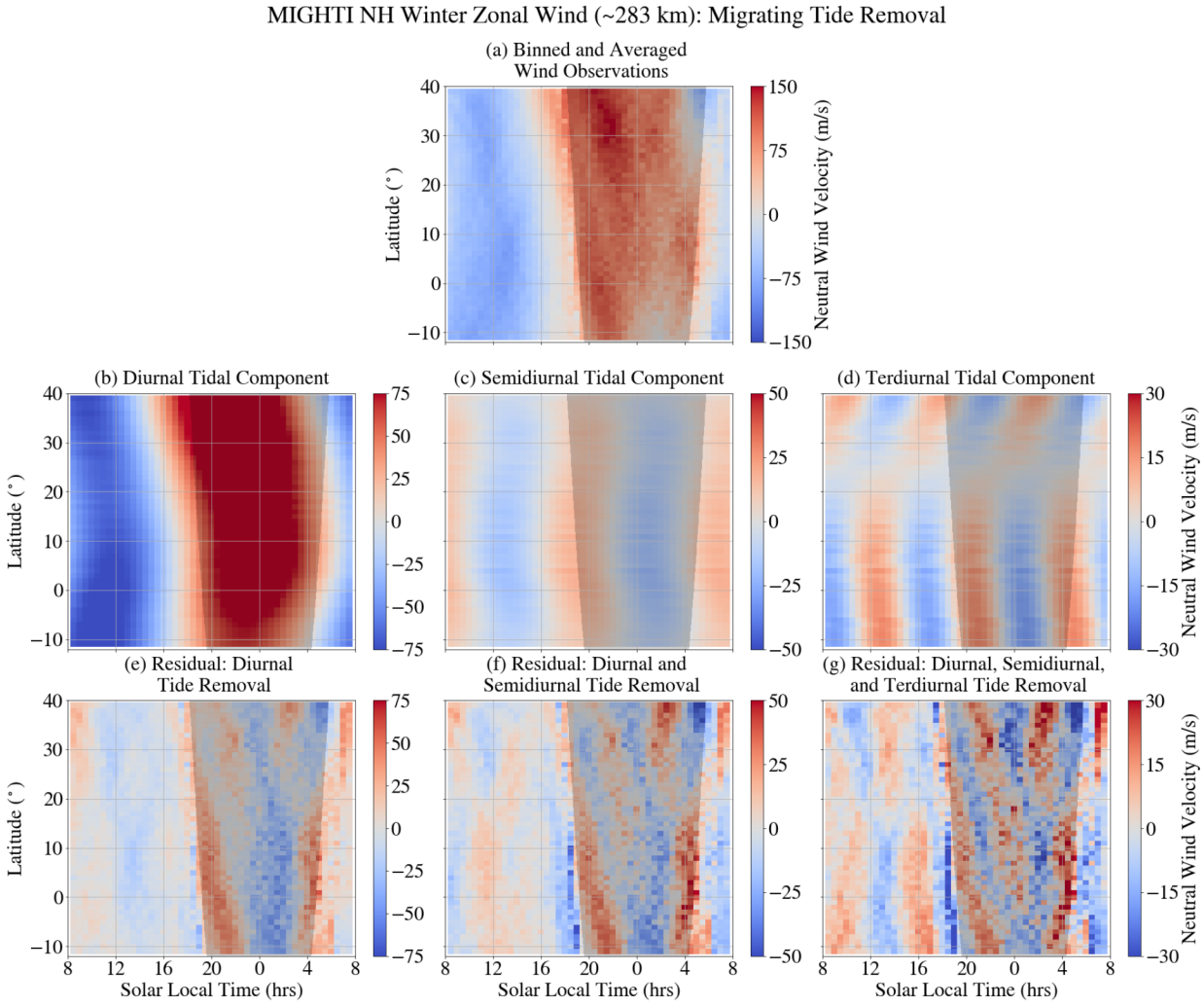

Figure C.4: Same as Figure C.3, but for the observed zonal wind component.

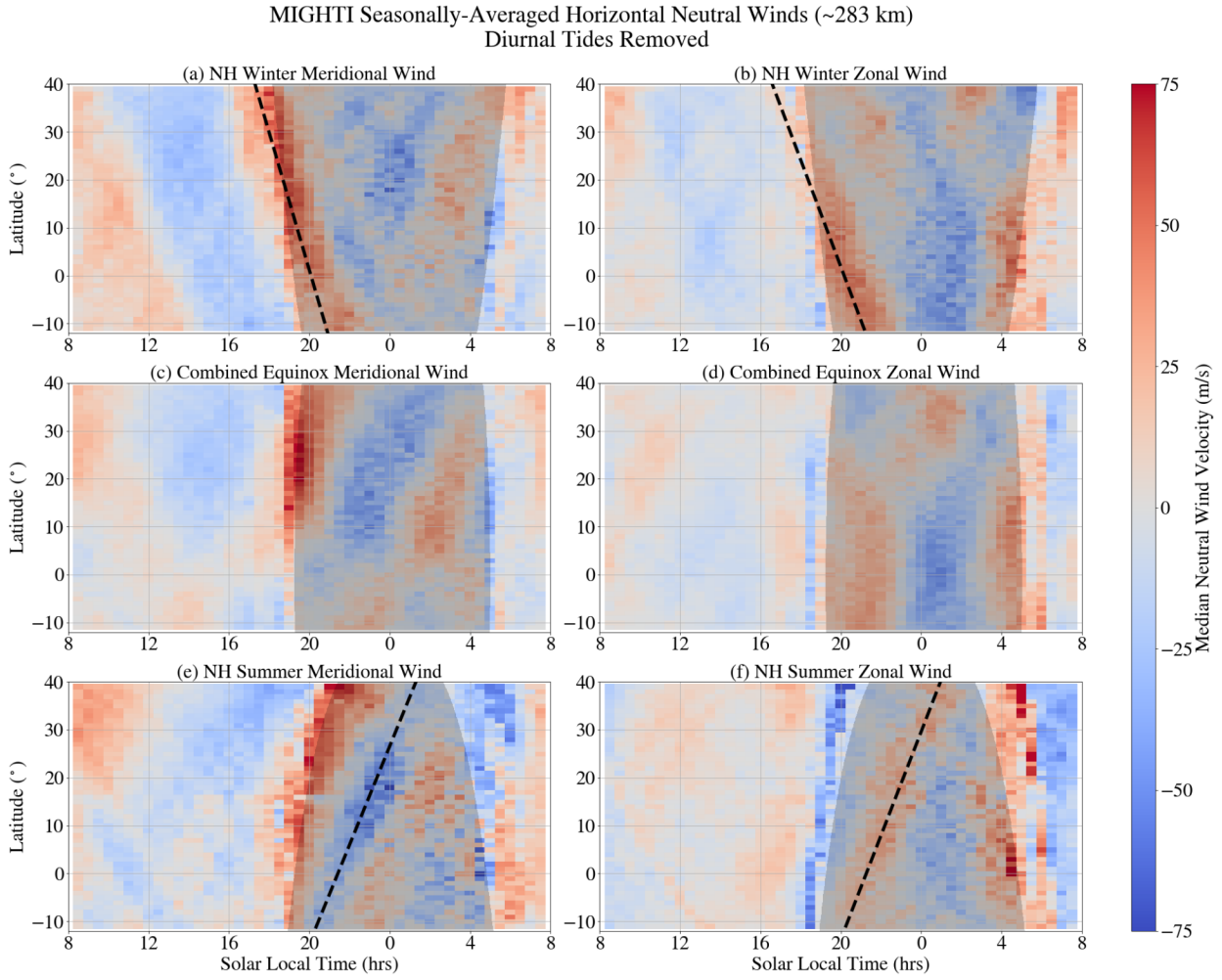

Figure C.5: Binned and averaged MIGHTI meridional (left column) and zonal (right column) neutral winds for NH winter (top row), combined equinox (middle row), and NH summer (bottom row) for the full ICON mission. Diurnal tides have been removed. Northward and eastward winds are positive. The gray shading shows the portion of the latitude/SLT space that is in darkness for each season. Clear STW features are marked by a black dotted line for the solstice cases ((a), (b), (e), and (f)).

Appendix D

Appendix for Chapter 5

This appendix supports the research presented in Chapter 5 and published in Gasque et al. (2023) [107]. First, Appendix D.1 provides additional details to describe the TREx spectrograph, which was used to gather the picket fence observations presented in Chapter 5. Appendix D.2 uses an electron transport model of precipitating particles to demonstrate that particle precipitation cannot replicate the picket fence's spectral features. Then, Appendix D.3 explains the method used to calculate electron impact excitation rates using the EEDFs obtained from BOLSIG+. Appendix D.4 describes the kinetic model used to determine volume emission rates (VERs) for various spectral features under the influence of electric fields parallel to the magnetic field in a realistic neutral atmosphere. In Appendix D.5, the kinetic model results are compared to those from the model described in Yonker and Bailey (2020) [379], which can resolve the vibrational states of N_2. Finally, Appendix D.6 describes an extension of this modeling to predict whether, under this mechanism, emission features in the ultra-violet (UV) spectral range might be observable in space-based observations of the picket fence. Appendices D.4 and D.6 were published as Supplemental Information to Gasque et al. (2023) [107].

D.1 The TREx Spectrograph

The Transition Region Explorer (TREx) is a ground-based array of instruments deployed across Canada with support from the Canadian Space Agency and developed by the University of Calgary. The TREx sensor array comprises various instruments, including all-sky imagers equipped with specific wavelength filters, riometers (measuring the opacity of the ionosphere to incoming cosmic radio sources), Global Navigation Satellite System (GNSS) receivers, and spectrographs. The auroral imagers and spectrographs aim to provide comprehensive information on magnetospheric processes at multiple scales, while the radio sensing capabilities help inform our understanding of space weather effects on climate and human infrastructure. In Chapter 5, we used data from the TREx spectrograph, which we will describe here in more detail.

A *spectrograph* is an instrument that disperses incoming electromagnetic radiation into its constituent wavelengths. As of the writing of this dissertation, the TREx array operates two spectrographs, situated at Rabbit Lake, Saskatchewan, and Lucky Lake, Saskatchewan (Spanswick et al., 2023) [326]. The latter, located farther south, typically near the subauroral region, provides the data used in this dissertation. The TREx spectrographs capture nighttime airglow and auroral emissions with wavelengths between ∼390 and 800 nm with a wavelength resolution of about 0.4 nm (Gillies et al., 2019; Gillies et al., 2023) [110, 111]. They image a narrow (∼2.1° wide) North/South latitudinal slice across the sky, dividing the image into about 200 elevation bins, each about 0.9° wide in elevation angle (Liang et al., 2023) [189]. Both the spectral and spatial resolutions vary slightly across the field of view (Gillies et al., 2023) [111].

The Lucky Lake TREx spectrograph collects light with a 13-second exposure time through a fisheye lens, which then passes through another lens focusing the light through a narrow slit. The remaining light is collimated and reflected off a grating, dispersing it according to wavelength. Further details regarding the optical elements are provided in Gillies et al. (2019) [110]. The resulting image undergoes flat-field correction, bias and dark signal subtraction, and unwarping (Thorne, 1988) [340]. Images are converted to physical units (Rayleighs) using calibration from a broadband 14C phosphor source and a National Institute of Standards and Technology (NIST)-traceable tungsten lamp (Gillies et al., 2019; Liang et al., 2023) [110, 189].

The study presented in Chapter 5 draws data from 10 April 2018, a single night of observations, and the same night as the data presented in Gillies et al. (2019) [110].

D.2 Are Picket Fence Emissions Consistent with Magnetospheric Particle Precipitation?

Chapter 5 demonstrated that the observed picket fence spectral features can be replicated by a kinetic model driven solely by local parallel electric fields. It also asserted that the picket fence spectrum is not consistent with magnetospheric particle precipitation. This is because precipitating particles and their secondaries would have sufficient energy to ionize N_2 and produce N_2^+ 1N emissions at picket fence altitudes, and these emission features are not detected in the picket fence. This appendix will show that spectral features from auroral emissions are not consistent with the picket fence spectrum. This section presents similar results to Mende and Turner (2019) [229], who investigated the color ratios in the aurora in comparison to those in STEVE and the picket fence.

To investigate the color ratios in the aurora as a function of the precipitating particle energy, this appendix uses the GLobal AirgLOW (GLOW) model (Solomon, 2017) [320], an electron transport model which can simulate emissions both from auroral precipitation and background airglow. Here, GLOW was used to simulate a series of precipitating monoenergetic electron beams, with characteristic energies (E_{char}) ranging from 1 eV to 100 keV,

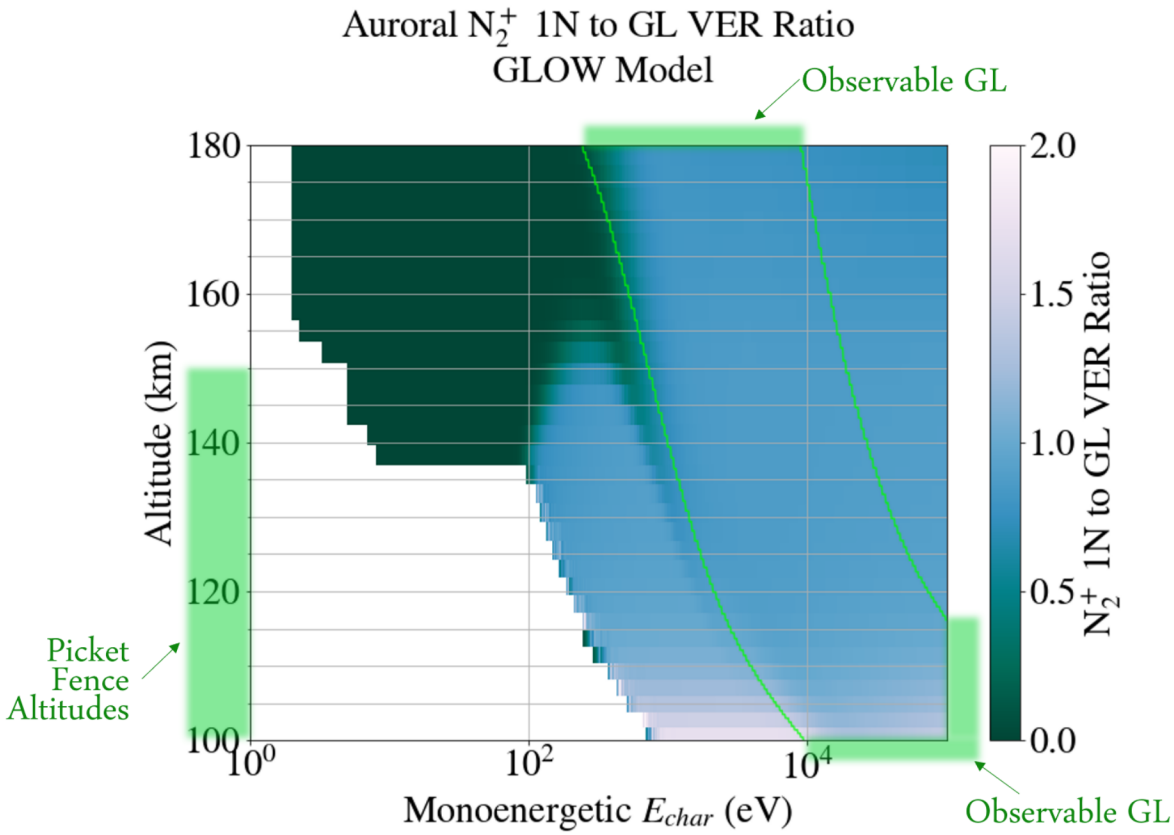

Figure D.1: GLOW model simulation results of the N_2^+ 1N to GL VER ratio as a function of altitude and characteristic electron beam energy. The region labelled 'Observable GL' is where the GL emissions are bright enough to be observed, as defined in the text. Since there is no electron beam energy for which GL emissions are produced without N_2^+ 1N emissions at picket fence altitudes, this shows that the picket fence cannot be replicated by particle precipitation models.

and an input energy flux of 50 erg/cm^2/s. The N_2^+ 1N and GL VERs resulting from each beam were modeled as a function of altitude and the background airglow was subtracted. Finally, VER ratios of N_2^+ 1N to GL emissions as a function of altitude were calculated for each incoming electron beam.

Figure D.1 displays the results as a function of altitude and the characteristic energy of the precipitating electron beam. Picket fence altitudes are highlighted in green on the y-axis (Archer et al., 2019) [10]. The white regions on the plot are regions for which no GL emissions are produced. The area labeled 'Observable GL' represents GL VER above

200 photons/cm^3/s (200 R for a 10 km thick layer), as the Chapter 5 analysis required GL emissions from observed picket fence spectra to exceed this threshold.

From Figure D.1, it is clear that at picket fence altitudes, there isn't a characteristic energy of a precipitating electron beam that would yield visible GL emissions without also generating N_2^+ 1N emissions. While not all types of aurora stem from monoenergetic energy beams (refer to the discussion in Chapter 2.4), any type of auroral precipitation can be constructed from a superposition of monoenergetic beams. Thus, this result applies to any form of auroral precipitation. Moreover, although the presented results pertain to a single incoming energy flux, altering the flux primarily affects the 'Observable GL' region, leaving the VER ratios unchanged, and the conclusions unaffected. It is therefore clear that the picket fence spectrum is incompatible with particle precipitation as its source.

D.3 Calculating Electron Impact Excitation Rate Constants

The kinetic modeling conducted in Chapter 5 aimed to determine the theoretical volume emission rate ratio for various spectral features observed (or not observed) in TREx observations of the picket fence, as driven by parallel electric fields of varying magnitudes. To do this, BOLSIG+ (version 12/2019) (Hagelaar & Pitchford, 2005) [120] was used to solve the Boltzmann equation in a realistic atmosphere under the influence of a parallel electric field and obtain the electron energy distribution function (EEDF).

As part of its output, BOLSIG+ also returns electron impact excitation rates for the states for which electron impact collisional cross sections are provided. For the majority of excited states considered, including the O(^1S) state and N_2 triplet states, our model used the electron impact excitation rate constants calculated by BOLSIG+. However, it's noteworthy that the cross section used by BOLSIG+ for the ionization of N_2 does not distinguish between electron impact ionization resulting in an excited ion and ionization that leaves the resulting ion in the ground state. It is important to consider the excited ionic states because N_2^+ 1N emissions are generated via the relaxation of the N_2^+ ($B^2\Sigma_u^+$) state to the ground N_2^+ $\left(X^2\Sigma_g^+\right)$ state, expressed as:

$$N_2^+\left(B^2\Sigma_u^+\right) \rightarrow N_2^+\left(X^2\Sigma_g^+\right) + h\nu_{N_2^+1N} \tag{D.1}$$

where h is Planck's constant and $\nu_{N_2^+1N}$ is the frequency of N_2^+ 1N emissions. It is therefore necessary to calculate the electron impact excitation rate for the N_2^+ ($B^2\Sigma_u^+$) state. This section describes the process by which the rate constant for this reaction (generalizable to any electron impact reaction) can be calculated from the cross section for the reaction and the EEDF. This section was developed using notes from and private communication with R. Janalizadeh.

Under given atmospheric conditions and parallel electric field strength, BOLSIG+ returns an EEDF $F_0(\epsilon)$ in units of $\mathrm{eV}^{-1.5}$, where ϵ is the electron energy in electron volts (eV). We can convert this EEDF into a probability distribution $P_0(\epsilon)$, with units of eV^{-1} as:

$$P_0(\epsilon) = \sqrt{\epsilon} F_0(\epsilon) \tag{D.2}$$

where $P_0(\epsilon)$ is normalized such that:

$$\int_{\epsilon=0}^{\inf} P_0(\epsilon)\, d\epsilon = 1 \tag{D.3}$$

The rate constant k (in cm^3/s) for an electron impact excitation reaction can then be calculated as:

$$k = \int_{\epsilon=0}^{\inf} P_0(\epsilon)\, \sigma(\epsilon)\, v d\epsilon \tag{D.4}$$

where $\sigma(\epsilon)$ is the electron impact cross section for the collision and v is the electron velocity, related to the energy as:

$$\epsilon = \frac{\frac{1}{2} m_e v^2}{q_e} \Rightarrow v^2 = 2\frac{q_e}{m_e}\epsilon \tag{D.5}$$

where m_e is the electron mass in kg and q_e is the elementary charge in C. Using this, the expression for the rate constant can be calculated as:

$$k = \sqrt{2\frac{q_e}{m_e}} \int_{\epsilon=0}^{\inf} P_0(\epsilon)\, \sqrt{\epsilon}\sigma(\epsilon)\, d\epsilon \tag{D.6}$$

In the absence of quenching or other loss processes, the resulting volume emission rate (VER) can be calculated by multiplying k by both the electron number density n_e and the number density of the relevant neutral species (n_{N_2} for the case of N_2^+ 1N emissions). When quenching or other loss processes are important, a more complicated model is needed, as described in the next section.

D.4 Detailed Steady State Kinetic Calculations of N_2 1P, GL, and N_2^+ 1N VERs

Atmospheric and ionospheric density profiles used in the modeling described in this section are shown in Figure D.2.

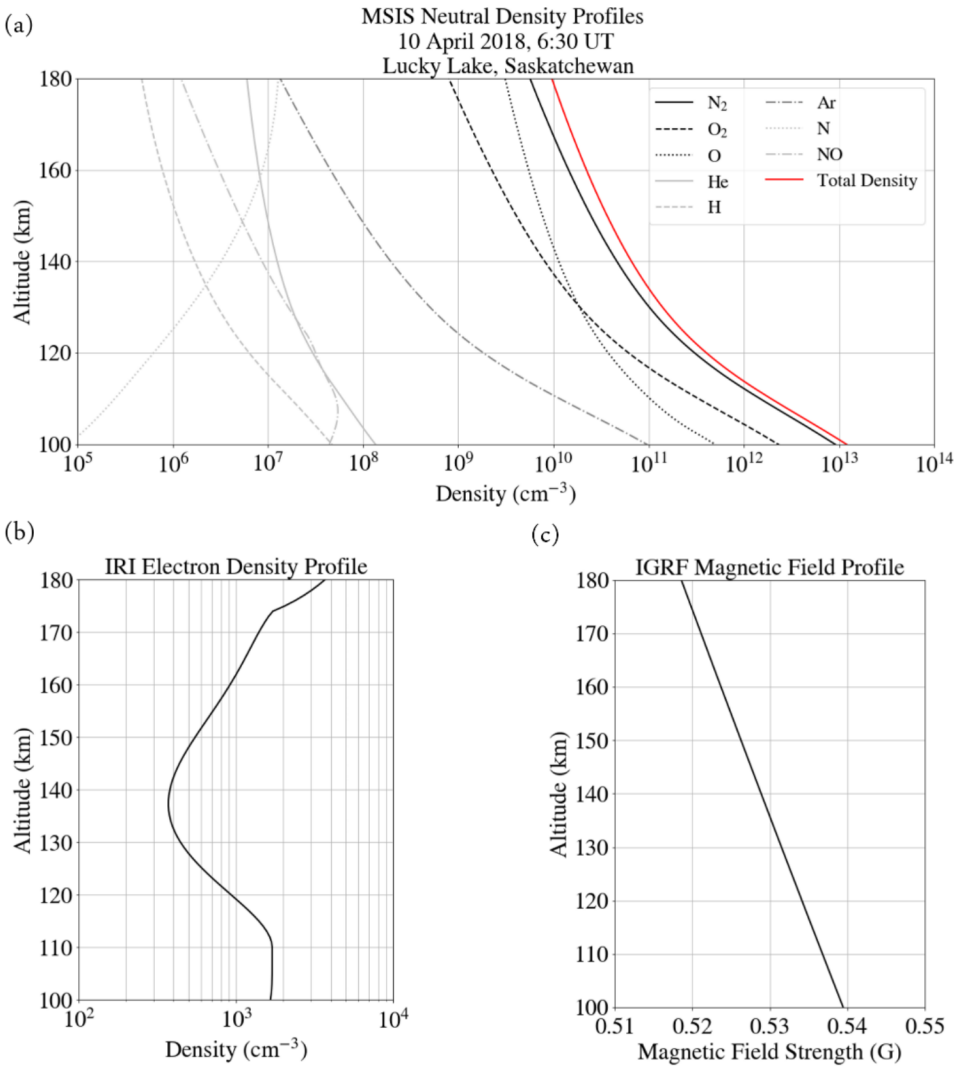

Figure D.2: Modeled atmospheric and ionospheric profiles from the time and location of the TREx observations. (a) Neutral atmospheric density profiles from MSIS. (b) Electron density profile from IRI. (c) Magnetic field strength profile obtained from IGRF.

Radiative Transition Reaction	Spectral Feature	Transition Rate (1/s)	Source
$N_2\,(B^3\Pi_g) \rightarrow N_2\,(A^3\Sigma_u^+) + h\nu_{N_2\ 1P}$	N_2 First Positive Bands	2×10^5	[77]
$N_2\,(A^3\Sigma_u^+) \rightarrow N_2\left(X^1\Pi_g^+\right) + h\nu_{VK}$	Vegard-Kaplan Bands	0.352	[116]
$O(^1S) \rightarrow O(^1D) + h\nu_{557.7\ \mathrm{nm}}$	O Green Line (557.7 nm)	1.26	[116]

Table D.1: Radiative Transition Rates. Transition rates were obtained from Eyler and Pipkin (1983) [77] and Grubbs et al. (2018) [116].

N_2 First Positive Emissions

N_2 1P emissions are produced through the rapid relaxation of the $N_2\,(B^3\Pi_g)$ state to the $N_2\,(A^3\Sigma_u^+)$ state. Atmospheric quenching effects are negligible above about 53 km (Vallance Jones, 1974) [353]. Radiative cascade from higher energy states, including $N_2\,(W^3\Delta_u)$, $N_2\,(B'^3\Sigma_u^-)$, and $N_2\,(C^3\Pi_u)$, significantly contribute to the total $N_2\,(B^3\Pi_g)$ population (Vallance Jones, 1974) [353]. Only half of the population excited by electron impact in the $N_2\,(C^3\Pi_u)$ state contributes to the cascade due to a pre-dissociation branching ratio of 0.5 (Porter et al., 1976) [270]. Contributions from the $N_2\left(E^3\Sigma_g^+\right)$ and $N_2\,(D^3\Sigma_u^+)$ states, which have small excitation cross sections, are omitted, following Meier (1991) [227]. Our modeling does not resolve individual vibrational levels of N_2, treating only the electronic states. As a result, contributions from reverse first positive transitions, which comprise the relaxation of higher vibrational levels of $N_2\,(A^3\Sigma_u^+)$ to lower vibrational levels of $N_2\,(B^3\Pi_g)$, are also omitted. However, as mentioned in the main chapter and shown in the next appendix, the results do not differ significantly from those obtained when comparing them to those from a vibrationally-resolved model (Yonker & Bailey, 2020) [379]. The N_2 1P VER is obtained by summing the direct electron impact excitation rate and the rate of radiative cascade to the $N_2\,(B^3\Pi_g)$ state. Balancing production and loss under the steady-state assumption allows us to calculate the total N_2 1P VER. This balance can be described by the equation:

$$n_e n_{N_2}\left(k_{e,N_2(B^3\Pi_g)} + k_{e,N_2\left(B'^3\Sigma_u^-\right)} + k_{e,N_2(W^3\Delta_u)} + 0.5k_{e,N_2(C^3\Pi_u)}\right) = n_{N_2(B^3\Pi_g)}k_{N_2\ 1P} \quad \text{(D.7)}$$

where n_X refers to the density of species or state X in cm^{-3}, $k_{e,Y}$ is the electron impact excitation of excited state Y from the ground state in cm^3/s (obtained from BOLSIG+), and $k_{N_2\ 1P}$ is the radiative transition frequency for the N_2 1P transition in units of 1/s (see Table D.1). The term on the right hand side represents the N_2 1P volume emission rate in units of photons/cm^3/s.

Atomic Oxygen Green Line Emissions

GL emissions occur via relaxation of the $O(^1S)$ state to the $O(^1D)$ state. The $O(^1S)$ state can be excited by electron impact and by O quenching of $N_2\,(A^3\Sigma_u^+)$. $N_2\,(A^3\Sigma_u^+)$ is

Reaction #	Quenching Reaction	Reaction Rate Constant (cm^3/s)	Source
Q1	$N_2\,(A^3\Sigma_u^+) + O \rightarrow N_2 + O(^1S)$	1×10^{-11}	[116]
Q2	$N_2\,(A^3\Sigma_u^+) + O \rightarrow N_2 + O$	1.8×10^{-11}	[116]
Q3	$N_2\,(A^3\Sigma_u^+) + O \rightarrow NO + N$	2×10^{-11}	[36]
Q4	$N_2\,(A^3\Sigma_u^+) + NO \rightarrow N_2 + NO$	8.9×10^{-11}	[116, 333]
Q5	$N_2\,(A^3\Sigma_u^+) + O_2 \rightarrow N_2 + O_2$	4×10^{-12}	[116, 333]
Q6	$O(^1S) + O \rightarrow O + O$	2×10^{-14}	[116]
Q7	$O(^1S) + O_2 \rightarrow O + O_2$	$1.6 \times 10^{-12}\chi$[a]	[116]
Q8	$O(^1S) + O_2 \rightarrow O(^1D) + O_2$	$7.2 \times 10^{-13}\chi$[a]	[116]
Q9	$O(^1S) + NO \rightarrow O(^1D) + NO$	5.12×10^{-11}	[116]
Q10	$O(^1S) + NO \rightarrow O(^1D) + NO$	2.88×10^{-11}	[116]

Table D.2: Quenching Reaction Rate Constants. Reaction rates were obtained from Grubbs et al. (2018) [116], Campbell et al. (2006) [36], and Strickland et al. (1999) [333].
[a] $\chi = e^{-\left(6750-0.0151T_n^2\right)/8.314T_n}$ where T_n is the neutral temperature in K.

formed through electron impact excitation and radiative cascade from the $N_2\,(B^3\Pi_g)$ state. The $N_2\,(A^3\Sigma_u^+)$ state undergoes radiative decay to the N_2 ground state and is additionally quenched through collisions with O and O_2 (Campbell et al., 2006) [36]. This process is described by the equation:

$$\begin{gathered} n_e n_{N_2} k_{e,N_2\left(A^3\Sigma_u^+\right)} + n_{N_2(B^3\Pi_g)} k_{N_2\,1P} = \\ n_{N_2\left(A^3\Sigma_u^+\right)} \left(k_{VK} + n_O\left(k_{Q1} + k_{Q2} + k_{Q3}\right) + n_{NO} k_{Q4} + n_{O_2} k_{Q5}\right) \end{gathered} \tag{D.8}$$

where k_{Qx} represents the rate coefficient for quenching reaction x in cm^3/s. These quenching reactions and their rates are listed in Table D.2. k_{VK} is the radiative transition rate for the Vegard-Kaplan bands, given in Table D.1. To determine the contribution of O quenching of $N_2\,(A^3\Sigma_u^+)$ to the GL VER, we solve Equation D.8 for the $N_2\,(A^3\Sigma_u^+)$ state density as:

$$n_{N_2\left(A^3\Sigma_u^+\right)} = \frac{n_e n_{N_2} k_{e,N_2\left(A^3\Sigma_u^+\right)} + n_{N_2(B^3\Pi_g)} k_{N_2\,1P}}{k_{VK} + n_O\left(k_{Q1} + k_{Q2} + k_{Q3}\right) + n_{NO} k_{Q4} + n_{O_2} k_{Q5}} \tag{D.9}$$

This density is directly dependent on the electron density n_e since both terms in the numerator are directly dependent on n_e. (It can be seen that the second term is directly dependent on n_e by examining Equation D.7.)

Quenching of the $O(^1S)$ state is mainly caused by collisions with O_2, while quenching from other species has a minimal effect (less than 10%) at picket fence altitudes. However, we also include quenching by O and NO. The balance for $O(^1S)$ is expressed as:

$$n_e n_O k_{e,O(^1S)} + n_{N_2\left(A^3\Sigma_u^+\right)} n_O k_{Q1} = n_{O(^1S)} \left(k_{557.7\text{ nm}} + n_O k_{Q6} + n_{O_2}\left(k_{Q7} + k_{Q8}\right) + n_{NO}\left(k_{Q9} + k_{Q10}\right)\right) \tag{D.10}$$

where, again, the quenching reaction rates are given in Table D.2 and the radiative transition rate $k_{557.7\text{ nm}}$ is given in Table D.2. The total GL VER is obtained by solving the above equation for $n_{O(^1S)} k_{557.7\text{ nm}}$:

$$n_{O(^1S)} k_{557.7\text{ nm}} = \frac{n_e n_O k_{e,O(^1S)} + n_{N_2\left(A^3\Sigma_u^+\right)} n_O k_{Q1}}{k_{557.7\text{ nm}} + n_O k_{Q6} + n_{O_2}\left(k_{Q7} + k_{Q8}\right) + n_{NO}\left(k_{Q9} + k_{Q10}\right)} k_{557.7\text{ nm}} \tag{D.11}$$

As can be seen from Equations D.7 and D.8, the GL VER is directly proportional to n_e. The ratio between the N_2 1P and GL VERs is given by:

$$\frac{\text{N}_2\text{ 1P VER}}{\text{GL VER}} = \frac{n_e n_{N_2}\left(k_{e,N_2(B^3\Pi_g)} + k_{e,N_2\left(B'^3\Sigma_u^-\right)} + k_{e,N_2(W^3\Delta_u)} + 0.5 k_{e,N_2(C^3\Pi_u)}\right)}{\left(\frac{n_e n_O k_{e,O(^1S)} + n_{N_2\left(A^3\Sigma_u^+\right)} n_O k_{Q1}}{k_{557.7\text{ nm}} + n_O k_{Q6} + n_{O_2}\left(k_{Q7}+k_{Q8}\right) + n_{NO}\left(k_{Q9}+k_{Q10}\right)} k_{557.7\text{ nm}}\right)} \tag{D.12}$$

Both the numerator and denominator are directly proportional to the electron density n_e (note that the $n_{N_2\left(A^3\Sigma_u^+\right)}$ is also proportional to n_e, as shown in Equations D.7 and D.9). As a result, the ratio between the two VERs is independent of n_e.

N_2^+ First Negative Emissions

N_2^+ 1N emissions occur through electron impact ionization of N_2, followed by rapid relaxation of the resulting N_2^+ ion in the excited $N_2^+\left(B^2\Sigma_u^+\right)$ state to the ground state. Quenching is negligible above about 48 km (Vallance Jones, 1974) [353]. Therefore, the electron impact excitation is the sole contributor to the N_2^+ 1N VER. We obtained electron impact excitation collisional cross sections for the $N_2^+\left(B^2\Sigma_u^+\right)$ state from Shemansky and Liu (2005) [311].

D.5 Comparison with the Results from Yonker and Bailey (2020) [379]

The kinetic modeling described in Appendix D.4 is a simplified approach that does not resolve the individual vibrational states of N_2 or collisions between different excited states. This appendix will compare the results from our model to outputs from the model presented by Yonker and Bailey (2020) [379], which accounts for both of these neglected effects.

As a diatomic molecule, N_2 comprises two nitrogen atoms which can vibrate by stretching and compressing the bond between them. These vibrations occur at several quantized

frequency levels, analogous to the energy levels in a simple harmonic oscillator. Different electronically excited states of N_2 have distinct bond lengths, leading to different sets of vibrational modes (e.g., Bayram & Freamat, 2012) [19].

The balance between different vibrational states can be important for some ionospheric chemical pathways, such as the creation of NO, which is believed to be generated by collisions between atomic oxygen and $N_2\,(A^3\Sigma_u^+)$ molecules with vibrational state $\nu > 2$ (Yonker & Bailey, 2020) [379]. It is also known that resolving the vibrational distribution of N_2 is important within SAIDs for modeling conductivity depletions (Richards & Torr, 1986) [281] and potentially 630.0 nm redline emissions (Mishin & Streltsov, 2019) [236]. The model for STEVE continuum emissions presented by Harding et al. (2020) [126] additionally depends on ground state N_2 being collisionally excited to vibrational states with $\nu > 11$. For this study's purposes, the proportion of N_2 in each triplet state can depend on vibrational state-dependent reactions, such as the reverse cascade reaction ($N_2\,(A^3\Sigma_u^+, \nu > 7) \rightarrow N_2\,(B^3\Pi_g)$). Furthermore, the spectrum of the N_2 1P emissions are dependent on the vibrational distribution of the $N_2\,(B^3\Pi_g)$ state, so it would be necessary to resolve the vibrational levels if one wanted to fully model the picket fence spectrum from our kinetic model.

The model presented by Yonker and Bailey (2020) [379] calculates the vibrational distribution for all of the N_2 triplet states, considering the various production and loss rates of each. It resolves 95 vibrational levels (ν=0-21 for A, B, B', and W states; ν=0-4 for the C state; and ν=0-1 for the E state). They account for excitation of the states by electron impact, as well as transitions between the states, which may occur due to radiative transitions as well as through collisions with O or O_2. Collisions with other N_2 molecules, called *intersystem collisions* can also change the balance of vibrational states.

The Yonker and Bailey (2020) [379] model is designed to model electron impact excitation rates based on the presence of photoelectrons or precipitating auroral electrons. This part of the model was bypassed for the tests performed here, which instead used the electron impact excitation rates for the A, B, B', C, and W N_2 triplet states obtained from BOLSIG+ as a function of altitude and parallel electric field strength to set the electron impact excitation rates in the model. The Yonker and Bailey (2020) [379] model then returns the vibrationally resolved $N_2\,(A^3\Sigma_u^+)$ and $N_2\,(B^3\Pi_g)$ state densities. The percentage difference[1] between the $N_2\,(A^3\Sigma_u^+)$ state density calculated using this study's kinetic model and that from Yonker and Bailey (2020) [379] is shown in Figure D.3.

At 110 km and above, the agreement between the two models is relatively good, with less than 20% difference between the two models. Below about 105 km, the Yonker and Bailey model predicts that the $N_2\,(A^3\Sigma_u^+)$ state density will be more than 50% larger than what this study's model predicted, likely due lower altitude effects including the increased importance of intersystem collisions at these altitudes.

Figure D.4 shows a comparison of the results for the total N_2 1P luminosity between the two models. The percentage difference between the two models, shown in Figure D.4(a)

[1]Here, a positive percentage difference indicates that the density from Yonker and Bailey (2020)'s [379] model is greater than that from the Gasque et al. (2023) [107] model.

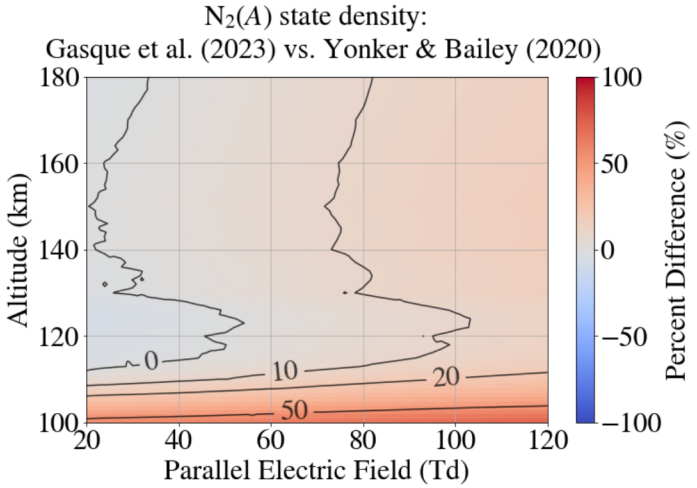

Figure D.3: Comparing the $N_2\,(A^3\Sigma_u^+)$ state density between our steady-state model and the model described in Yonker and Bailey (2020) [379] as a function of altitude and parallel electric field strength.

shows good agreement, with Yonker and Bailey (2020)'s [379] model predicting N_2 1P VERs between 5% and 30% higher than our VERs across the parameter space. Figure D.4(b) shows the N_2 1P VERs calculated by both models at 110 km, the most likely altitude of the picket fence, revealing excellent agreement.

Propagating these results through the remainder of the steady-state model described in Appendix D.4, it is possible to compare the final ratio between N_2 1P and GL emissions as obtained by Yonker and Bailey (2020)'s [379] vibrationally-resolved model and that in Gasque et al. (2023) [107]. These results are displayed in Figure D.5. At the nominal picket fence altitude of 110 km, the differences between the ratios are only a few percent, providing confidence that this study's results at these altitudes are not highly dependent on the vibrational kinetic and intersystem cascade. At lower altitudes, where collisions between N_2 in different vibrational states may become important, this study underestimates the ratio by up to about 40%. At higher altitudes, between 110 km and 180 km, the disagreement between models is less than 20%.

Furthermore, since Yonker and Bailey (2020)'s [379] resolves the individual vibrational levels of the excited N_2 triplet states, it is possible to use it to evaluate the resulting spectrum of the N_2 1P emissions. In Gasque et al. (2023) [107], it was assumed that the proportion of the N_2 1P emissions in the 642-700 nm wavelength band is 8%, as obtained from auroral observations presented in Vallance Jones (1974) [353]. The 642-700 nm portion of the N_2 1P spectrum represents the $\Delta\nu = +3$ transition for initial $N_2\,(B^3\Pi_g)$ vibrational states of $\nu' = (3-8)$ and the $\Delta\nu = +2$ transition for initial $N_2\,(B^3\Pi_g)$ vibrational states of

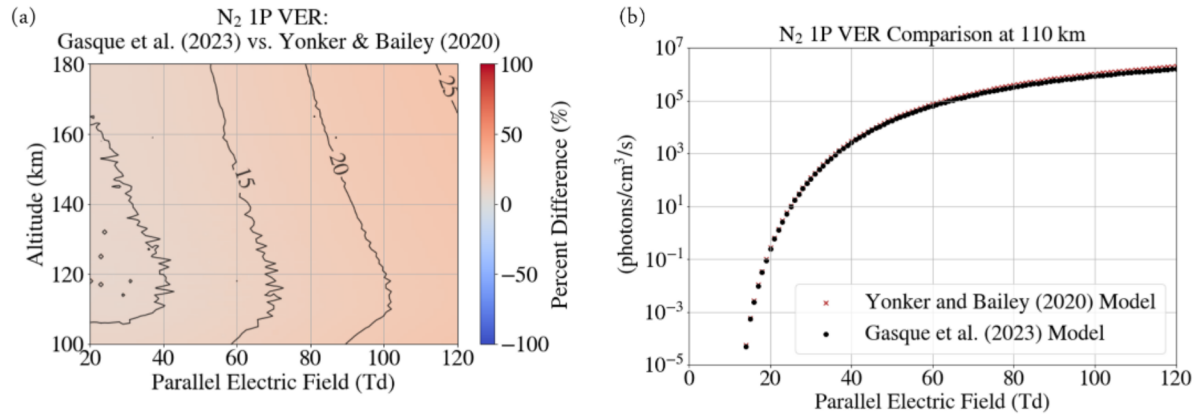

Figure D.4: Comparing the VER of N_2 1P emissions between our steady-state model and the model described in Yonker and Bailey (2020) [379], looking at (a) the percentage difference between the two models as a function of altitude and parallel electric field strength and (b) the modeled VERs as a function of parallel electric field strength at 110 km, a typical picket fence altitude.

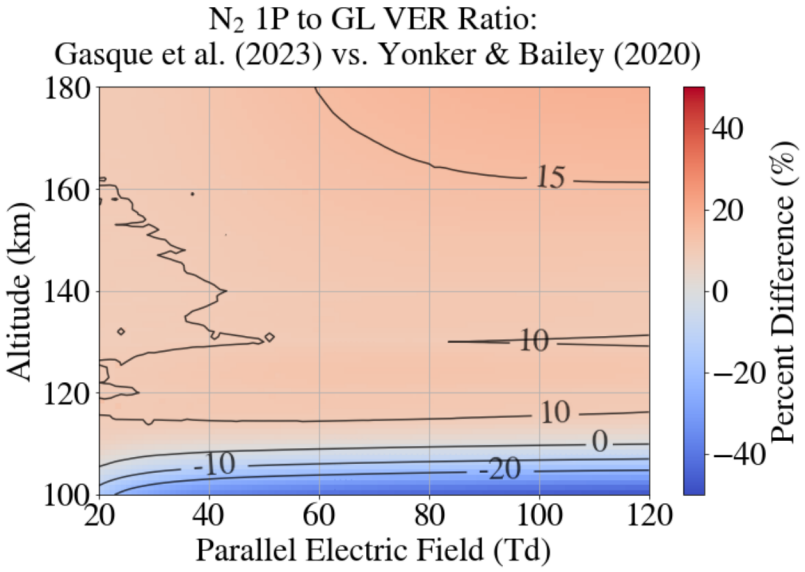

Figure D.5: Comparing the N_2 1P to GL VER ratio obtained by our steady-state model and the model described in Yonker and Bailey (2020) [379] as a function of altitude and parallel electric field strength.

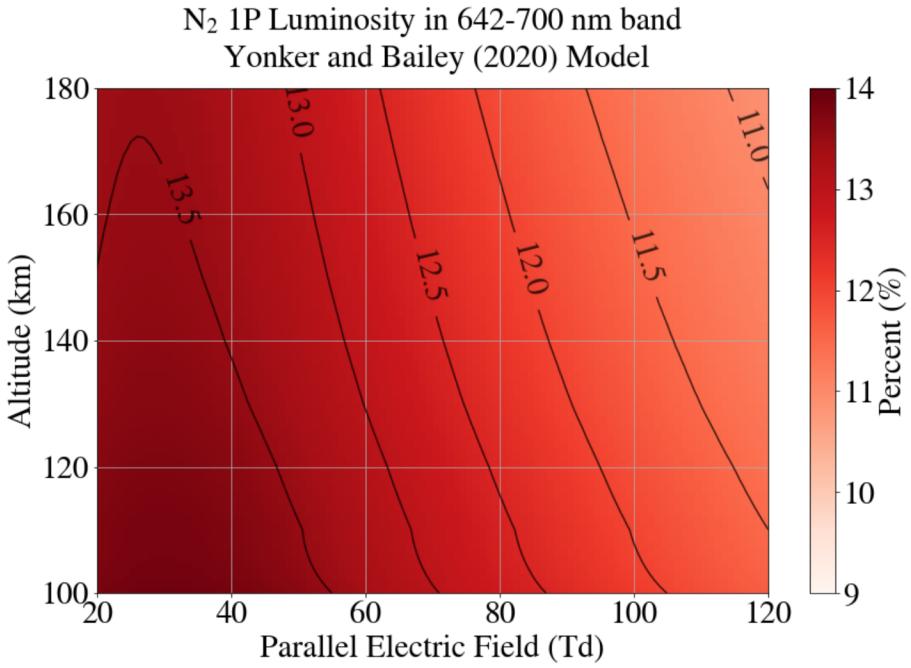

Figure D.6: N_2 1P fraction of emissions in the 642 - 700 nm band, as modeled by Yonker et al., (2020) [379]

$\nu' = (9 - 12)$, where $\Delta\nu$ represents the change in vibrational state between the upper and lower excited state (Simek, 2014) [316]. Since different excitation mechanisms and collisional chemistry will result in differences in the distribution among the vibrational states, it is possible that the N_2 1P spectrum in the aurora would differ from one arising from excitation driven by parallel electric fields.

The percentage of the N_2 1P luminosity in the 642-700 nm wavelength range for the parallel electric field excitation case using the Yonker and Bailey (2020) [379] model is displayed in Figure D.6. The results in the figure suggest that the 642-700 nm wavelength range may account for 12-14% of the total N_2 1P spectrum. Adopting this higher scale factor leads to a ∼50% reduction in this study's predicted parallel electric field strength at 110 km. However, it is difficult to evaluate the uncertainty in this modeling, so observationally obtaining a picket fence N_2 1P spectrum extending into the IR would enhance confidence in the quantitative estimates of parallel electric field strength, although the qualitative findings remain unchanged.

D.6 Calculating VERs for Various UV Emissions

This study's model can be extended to predict ultraviolet (UV) picket fence spectral features which may make good targets for future space-based observations. To do so, theoretical VERs are calculated for the N_2 Vegard-Kaplan (VK), Lyman-Birge-Hopfield (LBH), and Second Positive (2P) bands, as well as the 1356 Å atomic oxygen emission (Meier, 1991; Liu & Pasko, 2005; Eastes, 2000) [227, 200, 66]. The dominant source of each of these emissions is direct electronic excitation which is calculated from BOLSIG+, as described in Section 3.2, as well as some cascade contributions from higher energy states, described below. The 1304 Å atomic oxygen emission VER is not estimated due to complications arising from multiple scattering, which are beyond the scope of this study. Emissions from N and NO are not considered in this analysis.

The N_2 VK bands are generated by the relaxation of the $N_2\,(A^3\Sigma_u^+)$ state to the ground state, and the VK VER is obtained as part of our GL VER calculation (Equation D.8). The N_2 2P emissions result from the relaxation of the $N_2\,(C^3\Pi_u)$ state to the $N_2\,(B^3\Pi_g)$ state, which were determined while examining the radiative cascade contribution to the N_2 1P VER (Equation D.7).

The N_2 LBH bands (120-280 nm) form when the excited $N_2\,(a^1\Pi_g)$ state relaxes to the ground state. Since the quenching altitude for $N_2\,(a^1\Pi_g)$ is around 77 km, it is not significantly quenched at picket fence altitudes (Liu & Pasko, 2005) [200]. We do not consider the radiative and collisional cascades from $N_2\,(a'\,^1\Sigma_u)$ and $N_2\,(w^1\Delta_u)$, which could increase the LBH band system emissions by a factor of approximately 1.6 (Eastes, 2000) [66].

The 1356 Å atomic oxygen emission occurs when the $O(3s^5S)$ state relaxes to its ground state. The cascade contribution from the higher $O(3p^5P)$ state is considered, but cascade from other higher quintet states is disregarded. The effects of multiple scattering and absorption from O_2 are also neglected, both of which can significantly reduce the total observable emissions depending on the observation geometry (Meier, 1991) [227].

The full results of this modeling are shown in Figure D.7. At 110 km and 55 Td, the N_2 VK, N_2 LBH, N_2 2P, and O 1356 Å to GL ratios are 0.28, 0.24, 0.15, and 0.006, respectively. For the brightest observed picket fence event from this study, which is about 7 kR in the GL after accounting for atmospheric transmission, it is expected that N_2 VK, LBH, and N_2 2P bands may emit enough photons to be observed while O 1356 Å is likely not a good target for future observations.[2] Any observational comparisons will additionally need to account for viewing angle, absorption, multiple scattering, and instrumental effects.

[2]Recently, Zhang et al. (2024) [385] published the first space-based observations of STEVE with FUV emissions, reporting observable LBH bands and 1356 Å atomic oxygen emissions. These included a possible LBH band picket fence observation (see Figure 9(a) of Zhang et al. (2024) [385]). It was unclear whether the features were additionally visible in O 1356 Å emissions. Additional, more conclusive observations are still necessary to confirm these findings.

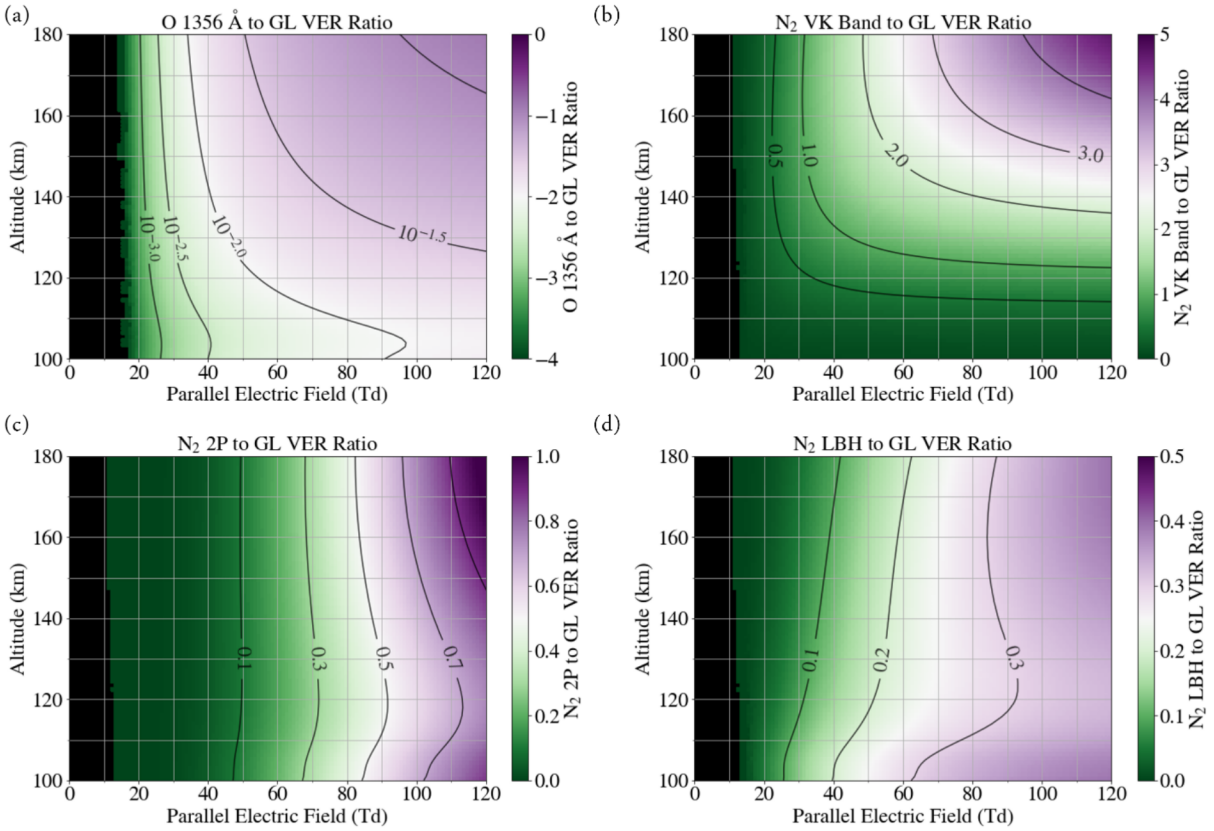

Figure D.7: Calculated VER Ratios of various UV emissions to GL as a function of altitude and parallel electric field strength. (a) O 1356 $\mathring{A}$ (b) VK Bands (c) N_2 2P (d) N_2 LBH.